



HAL
open science

Listening to the electrical noise for nanofluidic sensing

Adelchi Jacques Asta

► **To cite this version:**

Adelchi Jacques Asta. Listening to the electrical noise for nanofluidic sensing. Chemical Physics [physics.chem-ph]. Sorbonne Université, 2019. English. NNT : 2019SORUS444 . tel-02931882

HAL Id: tel-02931882

<https://theses.hal.science/tel-02931882>

Submitted on 7 Sep 2020

HAL is a multi-disciplinary open access archive for the deposit and dissemination of scientific research documents, whether they are published or not. The documents may come from teaching and research institutions in France or abroad, or from public or private research centers.

L'archive ouverte pluridisciplinaire **HAL**, est destinée au dépôt et à la diffusion de documents scientifiques de niveau recherche, publiés ou non, émanant des établissements d'enseignement et de recherche français ou étrangers, des laboratoires publics ou privés.



Thèse de doctorat

Pour l'obtention du grade de

Docteur de Sorbonne Université

École doctorale de Chimie Physique et Chimie Analytique de Paris Centre

Listening to the electrical noise for nanofluidic sensing

Adelchi Jacques ASTA

Directeur de thèse : Dr. Benjamin ROTENBERG

Soutenance prévue le 21/02/2019 devant un jury composé de :

Dr. Claire CHASSAGNE (Delft University, Delft) Rapportrice
Dr. Ignacio PAGONABARRAGA (CECAM - EPFL, Lausanne) Rapporteur
Dr. Lydéric BOCQUET (ENS, Paris) Examineur
Dr. Emmanuel TRIZAC (Université de Paris-Sud, Orsay) Examineur
Dr. Benjamin ROTENBERG (Sorbonne Université, Paris) Directeur de thèse

Contents

List of Figures	iv
List of Tables	xiii
Introduction	1
1.1 Coupling nanofluidics, electrokinetics and noise	2
1.1.1 Nanofluidics	2
1.1.2 Electrokinetics	3
1.1.3 What is noise?	8
1.2 Experiments using noise	11
1.3 Modelling charge, current and potential fluctuations at the nanoscale	14
1.4 Objectives of the present work	17
2 Lattice Boltzmann Electrokinetics	20
2.1 Governing Equations	21
2.1.1 Poisson-Nernst-Planck	21
2.1.2 Navier-Stokes	23
2.1.3 Discussion	24
2.2 Lattice Boltzmann	24
2.2.1 Kinetic theory	25
2.2.2 Boltzmann equation	26
2.2.3 BGK approximation	26
2.2.4 Equilibrium distribution	26
2.2.5 Conservation of Mass	27
2.2.6 Conservation of Momentum	27
2.2.7 Stress tensor	28
2.2.8 Lattice Boltzmann Equation	28
2.2.9 Algorithm	31
2.2.10 Boundaries	31
2.2.11 Concluding remarks and summary of the method	33
2.3 Link-flux method	33
2.3.1 Solute transport: diffusion-migration	33
2.3.2 Solute transport: advection	35
2.3.3 Solute transport: force on the fluid	35
2.3.4 Solute transport: electrostatic potential	36
2.3.5 Solute transport: boundary conditions	36
2.4 Summary of the algorithm	36
2.5 Results	37
2.5.1 Poiseuille Flow	37
2.5.2 Poisson-Boltzmann theory	41

2.5.3	Electro-osmotic flow	55
2.6	Conclusion	60
3	Moment propagation method for adsorbing/desorbing charged species	61
3.1	Model and adsorption/desorption equation	62
3.2	Algorithm - Moment Propagation	63
3.3	Results and Discussion	66
3.3.1	Dispersion of charged adsorbing tracers by an electro-osmotic flow	66
3.3.2	Validation	67
3.3.3	Simulation parameters	70
3.3.4	Fraction of adsorbed tracers	71
3.3.5	Electro-osmotic flow profile	72
3.3.6	Average tracer velocity	72
3.3.7	Diffusion coefficient	74
3.3.8	Dispersion coefficient	76
3.4	Conclusion	78
4	From Surface Charge to Constant Potential Simulations in LBE	80
4.1	Ion distribution on the microscopic scale	81
4.2	Capacitor imposing a surface charge $\pm\sigma$	81
4.2.1	No salt solution	81
4.2.2	Added salt solution	83
4.2.3	Electro-osmotic flow	86
4.3	Capacitor with a constant potential difference	87
4.3.1	Boundary conditions	88
4.3.2	Case of a slit channel	89
4.3.3	Case of a coaxial cylindrical channel	97
4.4	Conclusion	102
5	Transient regime in constant potential simulations	105
5.1	Debye relaxation time	106
5.1.1	Macroscopic point of view	107
5.1.2	Microscopic point of view	108
5.1.3	From bulk to confined electrolytes	109
5.2	Case of a slit channel	110
5.2.1	Results	110
5.3	Case of a coaxial cylindrical channel	116
5.3.1	Results	116
5.4	Conclusion	117
6	Transient hydrodynamic finite size effects in simulations under periodic boundary conditions	119
6.1	Diffusion and mobility	121
6.2	Perturbation in a fluid and its linear response	124
6.3	Algorithm	125
6.4	Validation of the method	126

Contents

6.5	Finite size effects in the transient regime	127
6.5.1	Velocity auto-correlation of the local velocity field	127
6.5.2	Propagation of acoustic modes	129
6.6	Conclusion	131
General Conclusion		133
6.7	Perspectives	134
Appendix		135
A Mathematical derivations and algorithms		136
A.1	Successive Over Relaxation Algorithm	136
A.2	Ions dynamics and relaxation times, linear regime - slit channel case	137
A.3	Ions dynamics and relaxation times - cylindrical channel case	143
Bibliography		146

List of Figures

1.1	Various length scales at play in nanofluidics ^[9]	2
1.2	Electric double layer formed at a negatively charged solid surface	3
1.3	EOF in a slit channel bearing a uniform negative surface charge inducing an electrostatic potential $\psi(y)$	4
1.4	Electrophoretic motion of a negatively charged particle.	5
1.5	Sketch of the electric dipole moment created by two opposite charges	5
1.6	Negative dielectrophoresis of an uncharged particle under an external AC E-field	6
1.7	Schematics of induced-charge electroosmosis around a conducting particle . . .	7
1.8	Sketch of the influence of slippage on the electro-osmotic transport. Slippage reduces the viscous friction in the electric Debye layer, as the hydrodynamic velocity gradient occurs on a length $b + \lambda_D$, instead of l without slippage. Flow is accordingly enhanced by a factor $1 + b/\lambda_D$. Sketch taken from Ref. 9.	7
1.9	Electrochemical single-molecule detection. (a) Basic concept of redox cycling. (b) Nanoelectrode encased in wax and positioned near a metallic surface. (c) Recessed glass-encased nanoelectrode immersed in mercury. (d) Lithographically fabricated nanogap device (Figure taken from Ref. 66)	12
1.10	(a) Principle of operation of the device. Redox-active molecules undergoing Brownian motion are repeatedly oxidized and reduced at two parallel electrodes separated by a distance of 70 nm, leading to a measurable current. (b) Optical micrograph of a device (top view). Visible are the top electrode and its contacting wires (orange), the access holes (black squares), and the nanochannel connecting the active region of the device to the access holes (colored magenta for clarity). The active region of the device is connected to an outside fluid reservoir via the nanochannel, allowing the target molecules to freely diffuse between these compartments. The bottom electrode is hidden below the top electrode and the nanochannel such that only its contacting wires are visible (dark orange). The dashed white line represents the cut in (c). (c) Scanning electron microscope image of the cross-section of a device. The device was cut open using a focused ion beam. (Figure taken from Ref. 67)	13
2.1	D3Q19 model	30
2.2	Bounce-Back step	31
2.3	Collision step	32
2.4	Streaming step	32
2.5	Shifted cell by a velocity v . The quantity of solutes transferred to the neighbouring nodes during a time step Δt is proportional to the intersection between the neighbouring cells as well as the shifted cell. In LB units $\Delta x = \Delta t = 1$ the quantity of transferred solute from node 5 to node 6 during a time step is proportional to $v_x(1 - v_y)$, where v is the speed of the fluid at node 5. The solvent quantity that stays at node 5 is proportional to $(1 - v_x)(1 - v_y)$. The notations differ from ours as the sketch is taken from Ref. 131	35

List of Figures

2.6	Velocity profile in a slit channel. The flow is induced by a pressure gradient resulting in a Poiseuille flow. The velocity u is normalized with respect to the maximum velocity u_{max} , whereas the position z in the fluid region is normalized with respect to L the distance between the walls.	38
2.7	Coordinate system.	39
2.8	Box of simulation in a charged cylindrical pore with a distribution of the charge on the interfacial nodes only (in green). Fluid nodes are in black. PBCs are used in the x, y and z -directions. w denotes the amount of solid nodes between the interfacial nodes and on of the edges of the box of simulation.	40
2.9	Velocity profile in a cylindrical channel. The flow is induced by a pressure gradient resulting in a Poiseuille flow. The velocity u is normalized with respect to the maximum velocity u_{max} , whereas r , which denotes the position in the fluid region, is normalized with respect to $2R$ the cylinder diameter.	40
2.10	Sketch of the slit geometry. The walls are negatively charged and counterions are inserted in order to preserve electroneutrality. The system may or may not have added salt. An external electric field parallel to the walls couples hydrodynamic and electrostatic effects, resulting in an electro-osmotic flow.	42
2.11	Electrostatic potential in a slit channel due to the surface charge density $\sigma\Delta x^2/e = -0.0125$, for a distance $L/\Delta x = 120$ between the walls, when salt is added at a concentration corresponding to a Debye screening length $\lambda_D/\Delta x = 6.0$. The potential is non-dimensionalized with $\beta e = e/k_B T$ and z is normalized with respect to L	44
2.12	Ionic concentration profile in a slit channel due to the surface charge density $\sigma\Delta x^2/e = -0.0125$, for a distance $L/\Delta x = 120$ between the walls, when salt is added at a concentration corresponding to a Debye screening length $\lambda_D/\Delta x = 6.0$. The ions density is in LB units of $\rho_{\pm}\Delta x^3$ and z is normalized with respect to L	45
2.13	Electrostatic potential in a slit channel due to the surface charge density $\sigma\Delta x^2/e = -0.0125$, for a distance $L/\Delta x = 120$ between the walls, when only counterions are present. The potential is non-dimensionalized with $\beta e = e/k_B T$ and z is normalized with respect to L	48
2.14	Concentration profile of cations in a slit channel due to the surface charge density $\sigma\Delta x^2/e = -0.0125$, for a distance $L/\Delta x = 120$ between the walls, when only counterions are present. The cations density is in LB units of $\rho_+\Delta x^3$ and $z/\Delta x$ is normalized with respect to $L/\Delta x$	49
2.15	Electrostatic potential in a cylindrical channel due to the surface charge density $\sigma\Delta x^2/e = -0.1$, for a diameter $2R/\Delta x = 61$, in the presence of added salt at a concentration corresponding to a Debye screening length $\lambda_D/\Delta x = 4.0$. The potential is non-dimensionalized with $\beta e = e/k_B T$ and z is normalized with respect to L	50
2.16	Ionic concentration profile in a cylindrical channel due to the surface charge density $\sigma\Delta x^2/e = -0.1$, for a diameter $2R/\Delta x = 61$, when salt is added. The ions density is in LB units of $\rho_{\pm}\Delta x^3$ and r is normalized with respect to $2R$	51

List of Figures

2.17	Electrostatic potential in a cylindrical channel due to the surface charge density $\sigma\Delta x^2/e = -2.0$, for a distance diameter $2R/\Delta x = 61$, when only counterions are present. The potential is non-dimensionalized with $\beta e = e/k_B T$ and r is normalized with respect to $2R$	53
2.18	Concentration profile of cations in a cylindrical channel due to the surface charge density $\sigma\Delta x^2/e = -2.0$, for a diameter $2R/\Delta x = 61$, when only counterions are present. The cations density is in LB units of $\rho_+\Delta x^3$ and $r/\Delta x$ is normalized with respect to $2R/\Delta x$	54
2.19	Relative error on the counterions density when compared to the analytical solution. The radius of the pore is $R = 5 \text{ nm}$, no salt is present and the walls bear a surface charge of $\sigma = -8 \times 10^{16} \text{ m}^{-2}$. The separation between the boundary of the channel and the box of simulation is $w = 1\Delta x$	55
2.20	Relative error on the counterions density when compared to the analytical solution. The radius of the pore is $R = 5 \text{ nm}$, no salt is present and the walls bear a surface charge of $\sigma = -8 \times 10^{16} \text{ m}^{-2}$. The separation between the boundary of the channel and the box of simulation is $w = 50\Delta x$	55
2.21	Electro-osmotic flow profile in a slit channel with added salt. The flow is induced by an external electric field $\beta e\Delta x E = 0.025$ parallel to the walls (resulting in an EOF). The velocity u is normalized with respect to the maximum velocity $u_{max} = eE_x\sigma/[\eta\kappa \sinh(\kappa L/2)]$, whereas z , which denotes the position in the fluid region, is normalized with respect to L the distance between the walls. The theoretical profile is given Eq. 2.130.	56
2.22	Electro-osmotic flow profile in a slit channel with only counterions. The flow is induced by an external electric field $\beta e\Delta x E = 0.025$ parallel to the walls resulting in an EOF. The velocity u is normalized with respect to the maximum velocity $u_{ref} = eE_x/[2\pi\eta l_B]$, whereas z , which denotes the fluid region, is normalized with respect to L , the distance between the walls. The theoretical profile is given Eq. 2.131.	57
2.23	Electro-osmotic flow profile in a cylindrical channel with added salt. The flow is induced by an external electric field $\beta e\Delta x E = 0.005$ parallel to the walls resulting in an EOF. The velocity u is normalized with respect to the reference velocity $u_{ref} = \sigma eE_x/(\kappa\eta) \times I_0(\kappa R)/I_1(\kappa R)$, whereas r , which denotes the position in the fluid region, is normalized with respect to the channel diameter $2R$. The theoretical profile is given by Eq. 2.130.	58
2.24	Electro-osmotic flow profile in a cylindrical channel with counterions only. The flow is induced by an external electric field $\beta e\Delta x E = 0.005$ parallel to the walls resulting in an EOF. The velocity u is normalized with respect to the reference velocity $u_{ref} = eE_z/(2\pi\eta l_B)$, whereas r , which denotes the position in the fluid region, is normalized with respect to the channel diameter $2R$. The theoretical profile is given by Eq. 2.131.	59
3.1	Electro-osmotic flow in a slit pore between negatively charged walls.	66
3.2	Time-dependent diffusion coefficient in the direction normal to the surfaces $D_z(t) = \int_0^t dt' Z_z(t')$ for anions, neutral and cations for $\alpha L = 1.98$. The red line is analytical result for neutral tracers as given by Eq. 3.21.	68

List of Figures

3.3	Dispersion coefficient by an EOF (see text for details) from moment propagation (symbols) and Eq. 3.24 (line). Anions are less dispersed than neutral and cations, because they are concentrated in the centre of the slit, where the flow is more homogeneous. Increasing the charge density increases both the dispersion coefficient and the difference between tracers of different charge.	69
3.4	Dispersion coefficient of neutral tracers in a slit pore in the direction of the flux, normalized by the bulk diffusion coefficient, as a function of the Péclet number, as extracted from our LB scheme (symbols) and from the exact results (lines). Several fractions of adsorbed tracers, or sorption strength, f_a , defined in Eq. 3.25, are presented: blue circles, 16%; red squares, 66%; and black upward triangles, 95%.	70
3.5	Fraction of adsorbed tracers f_{ads} with valency $q = +1$ (top), 0 (middle) and -1 (bottom), as a function of αL which quantifies the strength of electrostatic interactions with the walls (see section 3.3.1). In each panel, we consider a finite adsorption rate $k_a \Delta t / \Delta x = 10^{-1}$ and three desorption rates: $k_d \Delta t = 10^{-2}$ (red), 10^{-3} (blue) and 10^{-4} (green). In the last case simulated in the present work (without adsorption), obviously $f_{ads} = 0$ regardless of the tracer valency (not shown). The lines are computed from Eq. 3.15 and the symbols indicate the values of αL corresponding to the simulated systems.	71
3.6	On the left: electro-osmotic flow profile in a slit pore with uniformly charged walls and no added salt (counterions only, in the presence of an applied electric field along the surfaces (see text for details). The Lattice-Boltzmann Electrokinetics simulations, normalized by the reference velocity $u_{ref} = eE_y / 2\pi\eta l_B$, are compared with the analytical solution Eq. 3.14. On the right: average fluid velocity \bar{u} , normalized by the reference velocity u_{ref} , as a function of αL	72
3.7	Average tracer velocity, adimensionalized as a Péclet number $\bar{v}_{y,q} L / D$ as a function of the actual Péclet number $Pe = \bar{u} L / D$ with \bar{u} the average fluid velocity, for tracers with valency $q \in \{-1, 0, 1\}$, for a surface charge density corresponding to $\alpha L = 2.63$ and adsorption/desorption rates $(k_a \Delta t / \Delta x, k_d \Delta t) = (10^{-1}, 10^{-3})$. The simulation results (symbols) are compared to the analytical results Eq. 3.17 (solid line). In each case, the analytical solution without adsorption (dashed line).	73
3.8	Average tracer velocity $\bar{v}_{y,q}$, normalized by the average flow velocity \bar{u} , for charged adsorbing tracers with valency $q = +1$ (top), 0 (middle) and -1 (bottom), as a function of the strength of electrostatic interactions with the walls (αL). In each case, simulation results (symbols) for various adsorption/desorption rates are compared with the analytical results Eq. 3.17 (lines).	74
3.9	Time-dependent diffusion coefficient in the direction normal to the surfaces $D_z(t) = \int_0^t dt' Z_z(t')$ for neutral tracers, for $\alpha L = 0.96$ and $\beta e E_y \Delta x = 0.1$. The adsorption/desorption rates are $k_a \Delta t / \Delta x = 10^{-1}$ and $k_d \Delta t = 10^{-2}, 10^{-3}$ and 10^{-4}	75
3.10	Time-dependent diffusion coefficient in the direction normal to the surfaces $D_z(t) = \int_0^t dt' Z_z(t')$ for positive tracers, for $\alpha L = 0.96$ (left figure), 2.2 (centre figure) and 2.6 (right figure) and $\beta e E_y \Delta x = 0.1$. The adsorption/desorption rates are $k_a \Delta t / \Delta x = 10^{-1}$ and $k_d \Delta t = 10^{-2}, 10^{-3}$ and 10^{-4}	75

List of Figures

3.11	Time-dependent diffusion coefficient in the direction normal to the surfaces $D_z(t) = \int_0^t dt' Z_z(t')$ for negative tracers, for $\alpha L = 0.96$ (left figure), 2.2 (centre figure) and 2.6 (right figure) and $\beta e E_y \Delta x = 0.1$. The adsorption/desorption rates are $k_a \Delta t / \Delta x = 10^{-1}$ and $k_d \Delta t = 10^{-2}, 10^{-3}$ and 10^{-4}	76
3.12	Dispersion coefficient, normalized by the diffusion coefficient, $D_{y,q} L / D$ as a function of the Péclet number $\bar{u} L / D$, for tracers with valency $q \in \{-1, 0, 1\}$, for a surface charge density corresponding to $\alpha L = 2.63$, without adsorption (dashed lines) and with adsorption/desorption rates $(k_a \Delta t / \Delta x, k_d \Delta t) = (10^{-1}, 10^{-3})$ (solid lines). The simulation results are shown as symbols, while the lines correspond to the quadratic form Eq. 3.22. In this equation, the value at zero-field $f_{mob} = 1 - f_{ads}$ corresponds to Figure 3.5; the curvature is known analytically in the no-adsorption case, see Eq. 3.24 and fitted numerically in the presence of adsorption/desorption. Results of this fitting are discussed in Figure 3.13. . . .	77
3.13	Prefactor of the dispersion coefficient vs Péclet number, $f(\alpha L, q)$ defined by Eq. 3.22, for $q = +1$ (top), 0 (middle) and -1 (bottom). In the no-adsorption case (black), simulation results are compared to the analytical expression Eq. 3.24 (solid line). The other simulation results are for finite adsorption rate $k_a \Delta t / \Delta x = 10^{-1}$ and three desorption rates: $k_d \Delta t = 10^{-2}$ (red), 10^{-3} (blue) and 10^{-4} (green). The dashed-lines are only guide for the eyes.	78
4.1	Electrostatic potential in a slit channel due to the surface charge density $\pm \sigma \Delta x^2 / e = \pm 0.11111$, for a distance $L / \Delta x = 89$ between the walls in the absence of salt. The potential is non-dimensionalized with $\beta e = e / k_B T$ and z is normalized with respect to L . The theoretical solution under PBCs is given by Eq. 4.7	82
4.2	Sketch of PBC corrections for no-salt case	83
4.3	Electrostatic potential in a slit channel due to the surface charge density $\pm \sigma \Delta x^2 / e = \pm 0.05$, for a distance $L / \Delta x = 89$ between the walls, when salt is added. The salt concentration corresponds to a Debye screening length $\lambda_D / \Delta x = 8.0$. The potential is non-dimensionalized with $\beta e = e / k_B T$ and z is normalized with respect to L	84
4.4	Sketch of PBC corrections	85
4.5	Electro-osmotic flow profile in a slit channel with added salt due to the surface charge density $\pm \sigma \Delta x^2 / e = \pm 0.05$. The flow is induced by an external electric field $\beta e \Delta x E = 1 \times 10^{-3}$ parallel to the walls. The velocity u is normalized with respect to the reference velocity $u_{ref} = \varepsilon E_y / \eta$, whereas z , which denotes the position in the fluid region, is normalized with respect to the distance L between the walls.	86
4.6	Sketch of a capacitor	87
4.7	Electrostatic potential values as a function of the position. The discretized green region denotes the solid part, whereas the remaining region on the right corresponds to the fluid region, where the Poisson equation is solved. The potential of one electrode is fixed at a constant value ϕ_1 . The wall is located half-way between the discretized solid region and liquid region. The resolution is Δx	88
4.8	Electrostatic potential profile in a slit channel of separation $L / \Delta x = 82$ without salt. The resolution is fixed by the Bjerrum length $l_B / \Delta x = 1.44$ and $\Delta V = 0.1$	89

List of Figures

- 4.9 Electrostatic potential profile in a slit channel of separation $L/\Delta x = 82$ with added salt. The resolution is fixed by the Bjerrum length $l_B/\Delta x = 1.44$, the salt concentration corresponds to a Debye screening length $\lambda_D/\Delta x = 6.0$ and $\Delta V = 0.1$ 90
- 4.10 Ion concentration profile in a capacitor of width $L/\Delta x = 82$ with added salt under a reduced voltage $\Delta V = \beta e \Delta \psi = 0.1$ (cations are in black and red and anions are in blue and green). The resolution is fixed by the Bjerrum length $l_B/\Delta x = 1.44$ and the salt concentration corresponds to a Debye screening length $\lambda_D/\Delta x = 6.0$. 91
- 4.11 Effect of the resolution on the relative error of the anions concentration profile. The error is defined as $\frac{\delta \rho}{\rho} = \sqrt{\frac{1}{N} \sum_{\omega} \left(\frac{\rho_n}{\rho_a} - 1 \right)^2}$, where ρ_n and ρ_a denote the numerical and analytical concentration respectively. The study was carried out by fixing the distance $L = 3.7 \times 10^{-8}$ m between the walls and varying the Debye screening length λ_D (nm) from a curve to another (see Table 4.2). The fit is $f(x) = \frac{ALx}{2\lambda_D} + B$ where A and B are the fitting parameters, whose numerical values are illustrated in Table 4.3. 91
- 4.12 Effect of the Debye screening length λ_D on the relative error of the anions concentration profile. The error is defined as $\frac{\delta \rho}{\rho} = \sqrt{\frac{1}{N} \sum_{\omega} \left(\frac{\rho_n}{\rho_a} - 1 \right)^2}$, where ρ_n and ρ_a denote the numerical and analytical error respectively. The study was carried out by fixing the distance L (nm) between the walls and varying the Debye screening length λ_D , as shown in Table 4.2. 92
- 4.13 Effect of the resolution $\Delta x/l_B$ on the relative error of the anions concentration profile. The error is defined as $\frac{\delta \rho}{\rho} = \sqrt{\frac{1}{N} \sum_{\omega} \left(\frac{\rho_n}{\rho_a} - 1 \right)^2}$, where ρ_n and ρ_a denote the numerical and analytical concentrations respectively. The study was carried out by fixing the distance $\lambda_D = 1.1 \times 10^{-9}$ m between the walls and varying L (nm) from a curve to another, as shown in Table 4.4. The fit is $f(x) = \frac{ALx}{2\lambda_D}$, where A is the fitting parameter. 94
- 4.14 Effect of the Debye screening length λ_D on the relative error of the anions concentration profile. The error is defined as $\frac{\delta \rho}{\rho} = \sqrt{\frac{1}{N} \sum_{\omega} \left(\frac{\rho_n}{\rho_a} - 1 \right)^2}$, where ρ_n and ρ_a denote the numerical and analytical concentrations respectively. The study was carried out by fixing the distance $\lambda_D = 1.1 \times 10^{-9}$ m and varying the distance L between the walls, as shown in Table 4.4. 94
- 4.15 Effect of the concentration (*i.e* λ_D) on the capacitance error $\frac{\delta C}{C} = \frac{C_n}{C_a} - 1$ for a fixed distance $L = 7.35 \times 10^{-8}$ m between the walls and fixed $l_B/\Delta x = 1.2$. $\delta C/C$ scales linearly following $\delta C/C = \Delta x/2\lambda_D$. The fit is shown in red and the numerical simulations are shown as black dots. 95
- 4.16 Scaling of the slope of $\delta C/C$ vs. $\Delta x/(2\lambda_D)$ as a function of λ_D/l_B . The numerical data obeys to Eq. 4.39. The fit is shown in red and the numerical simulations are in shown as black dots. 96

List of Figures

4.17	Electro-osmotic flow profile in a slit channel of width $L/\Delta x = 82$ with added salt. The salt concentration corresponds to a Debye screening length $\lambda_D/\Delta x = 6.0$ and a reduced voltage $\Delta V = 0.1$ is applied. The EOF flow is induced by an external electric field $\beta e \Delta x E_y = 0.01$ parallel to the walls. The resolution is fixed by the Bjerrum length $l_B/\Delta x = 1.44$	96
4.18	Sketch of a coaxial cylindrical channel	97
4.19	Electrostatic potential profile in a coaxial cylindrical channel with radii $R_1/\Delta x = 2$ and $R_2/\Delta x = 35$ without salt. The resolution is fixed by the Bjerrum length $l_B/\Delta x = 1.2$ and a potential difference $\Delta V = 0.1$ was imposed between the two cylinders. The separation between the external boundary of the outer cylinder and the box of simulation is $w = 4\Delta x$	98
4.20	Electrostatic potential profile in a coaxial cylindrical channel with radii $R_1/\Delta x = 2$ and $R_2/\Delta x = 35$ with added salt. The resolution is fixed by the Bjerrum length $l_B/\Delta x = 1.2$ and a reduced potential difference $\Delta V = 0.1$ was imposed between the two cylinders. The separation between the external boundary of the outer cylinder and the box of simulation is $w = 4\Delta x$. The salt concentration corresponds to a Debye screening length $\lambda_D/\Delta x = 9.0$	99
4.21	Velocity profile in a coaxial cylindrical channel with radii $R_1/\Delta x = 2$ and $R_2/\Delta x = 35$ with added salt, corresponding to a Debye screening length $\lambda_D/\Delta x = 9.0$. The flow is induced by an external electric field $\beta e \Delta x E = 0.0001$ parallel to the walls resulting in an EOF. The resolution is fixed by the Bjerrum length $l_B/\Delta x = 1.2$	102
5.1	Evolution of the electrode charge for a capacitor, submitted to a voltage step $\psi(t) = \psi_0 \theta(t)$, with θ denoting the Heaviside step function. The charge accumulates in a monoexponential manner analog to a RC circuit. The distance between the solid-liquid interfaces is $L = 253\Delta x$. The resolution is fixed with the Bjerrum length $l_B/\Delta x = 4.8$. The reduced potential difference applied at the walls is $\Delta V = 0.1$, the salt concentration corresponds to a Debye screening length of $\lambda_D/\Delta x = 35.0$ and the ions have a bulk diffusion coefficient $D = 0.05 (\Delta x^2/\Delta t)$	110
5.2	Natural logarithm of the temporal charge evolution of Fig. 5.1 as described by Eq. 5.38. The inverse of the slope of the straight line corresponds to the characteristic time at which the capacitor relaxes (see Eq. 5.39).	112
5.3	Characteristic time in a slit when varying $\epsilon := 2\lambda_D/L$. The simulations were carried out under a reduced potential difference of $\Delta V = 0.1$ with a fixed L while λ_D varies so that $L/\Delta x = 253$ and the concentration corresponds to Debye screening lengths $\lambda_D/\Delta x = 8, 12, 20$ and 35 . The analytical results described in Appendix A.2 is shown with a green solid line, our numerical results with red triangles and Bazant's results <i>i.e.</i> Eq. 5.32 with a blue solid line.	113
5.4	Relative error on the characteristic time τ for $l_B/\Delta x = 1.44, 2.88$ and 4.8 , for a fixed L/l_B ratio. Four different values of $\epsilon := 2\lambda_D/L$ were tested: $0.06, 0.09, 0.16, 0.28$	114
5.5	Relative error on the characteristic time τ for $\lambda_D/\Delta x = 8, 12, 20$ and 35 , for a fixed L/l_B ratio. Four different values of $\epsilon := 2\lambda_D/L$ were tested: $0.06, 0.09, 0.16, 0.28$	114

List of Figures

- 5.6 Characteristic time in a slit when varying the reduced potential $\Delta V = 0.5, 1, 2, 3, 4, 5, 6, 8, 10$ and 20. The distance between the solid-liquid interfaces is $L = 253\Delta x$. The resolution is fixed with the Bjerrum length $l_B/\Delta x = 4.8$. The salt concentration corresponds to a Debye screening length of $\lambda_D/\Delta x = 35.0$ and the ions have a bulk diffusion coefficient $D = 0.05 (\Delta x^2/\Delta t)$. The time for the electrolyte to relax increases for $\Delta V \leq 6/\beta e$, whereas it decreases for higher values. 115
- 5.7 Steady-state electrostatic potential profile for $\Delta V = 1, 2, 6, 10, 20$ and 30. As ΔV increases the potential profile becomes more and more linear and therefore resembles the case where no salt is added. 115
- 5.8 Steady-state cation density profiles for $\Delta V = 1, 2, 6, 10, 20$ and 30. As ΔV increases, the ions move away from the bulk region, eventually leaving almost no salt, to stick to the walls. The initial salt concentration is shown with a black solid line. 116
- 5.9 Temporal charge evolution at one electrode of a coaxial channel. The charge accumulates in a monoexponential manner analog to a RC circuit. The distance between the electrodes is $L/\Delta x = (R_2 - R_1)/\Delta x = 40$, with the inner and outer cylinder $R_1 = 2\Delta x$ and $R_2 = 42\Delta x$ respectively. The resolution is fixed by $l_B/\Delta x = 1.2$. The reduced potential difference applied at the walls is $\Delta V = 0.1$, the salt concentration corresponds to a Debye screening length $\lambda_D/\Delta x = 8.0$ and the ions have a bulk diffusion coefficient $D = 0.05 (\Delta x^2/\Delta t)$ 116
- 5.10 Characteristic time in a coaxial cylindrical channel when varying $\epsilon := 2\lambda_D/L$. The simulations were carried out under a reduced potential difference of $\Delta V = 0.1$ with a fixed L while λ_D varies so that the inner and outer cylinder are $R_1 = 2\Delta x$ and $R_2 = 42\Delta x$ respectively. The salt concentration corresponds to Debye screening lengths $\lambda_D/\Delta x = 4, 6, 8, 12, 16$ and 26. 117
- 6.1 a. A bulk fluid in an orthorhombic cell with one length different from the other two is submitted to a perturbation Eq. 6.20 which corresponds to a singular point force (in one of the two relevant directions indicated by red arrows) and a uniform compensating background. Both elongated ($L_\perp > L_\parallel$, as shown) and flat ($L_\perp < L_\parallel$) boxes are considered. b. Velocity at point \mathbf{r} where the perturbation is applied, as a function of time, from Lattice Boltzmann simulations with various cubic boxes of size $L = L_{\perp,\parallel}$. The inset shows the scaling at long times used to extrapolate the steady-state velocity, for the largest system. 126
- 6.2 Scaling functions $h_{\parallel,\perp} = (D_{\parallel,\perp} - D_\infty)/(k_B T/6\pi\eta L_\parallel)$ defined in Eq. 6.30 as a function of the aspect ratio L_\perp/L_\parallel . Lattice Boltzmann results (symbols) are compared to analytical results (lines) from Ref. 207. Note the logarithmic scale on the x -axis. Each point corresponds to the slope of a scaling with system size at fixed aspect ratio, as illustrated in the inset for a cubic box ($L = L_{\perp,\parallel}$), where the line again corresponds to Eq. 6.30. 127

List of Figures

6.3 Local velocity auto-correlation function (LVACF) computed from Lattice Boltzmann simulations in a cubic cell, for various cell sizes $L/\Delta x$. The double logarithmic scale underlines the algebraic decay expected from hydrodynamics in an unbounded fluid, Eq. 6.31. The finite size results in a cross-over to an exponential decay, analyzed in further detail in Figure 6.4. The arrows indicate the diffusion time for the slowest mode, $\tau_L = 1/\nu k_L^2$, with $k_L = 2\pi/L$, which corresponds to the exponential decay rate and is also typical of the cross-over between the algebraic and exponential regimes. 129

6.4 LVACF computed from Lattice Boltzmann simulations in a cubic cell, for various cell sizes $L/\Delta x$, normalized by the expected exponential scaling at long times $A_L e^{-\nu k_L^2 t}$ with $k_L = 2\pi/L$ and A_L given by Eq. 6.32, as a function of time rescaled by the frequency $\omega_L = kc_s \sqrt{1 - \nu^2 k^2 / c_s^2}$. The oscillations are due to the small compressibility of the LB fluid, which results in damped acoustic waves. For the larger systems the contribution of faster modes nk_L is still visible on the time scale of the simulations. 130

A.1 On the left, poles s_n and corresponding relaxation times τ_n for $\epsilon = 0.1$; the first pole is $s_0 = -1.057$ and the longest relaxation time is $\tau_0 = -s_0^{-1} = 0.946$. On the right, the same thing for $\epsilon = 10$; in this case the first pole is $s_0 = -24.693 = -10.008 \frac{\pi^2}{4}$ and the longest relaxation time is $\tau_0 = -s_0^{-1} = 0.04050$ 141

A.2 In continuous lines, τ as a function of ϵ , for different values of η . In dotted blue lines, the circuit-model approximation for τ (Eq. A.57), for the same values of η . 144

List of Tables

2.1	Physical data for the simulation of a Poiseuille flow in a slit. L is the length of the channel separating the walls, ν is the kinematic viscosity, l_B the Bjerrum length, λ_D the Debye screening length, σ the surface charge and dp/dx the pressure gradient.	38
2.2	Physical data for the simulation of a Poiseuille flow in a cylinder. R is the radius of the pore and L its length. ν is the kinematic viscosity, l_B the Bjerrum length, λ_D the Debye length, σ the surface charge and dp/dz the pressure gradient. . .	41
2.3	Physical data for an electrolyte with added salt in a slit channel (counterions and co-ions). L is the length of the channel separating the walls, ν is the kinematic viscosity, l_B the Bjerrum length, λ_D the Debye length and σ the surface charge.	43
2.4	Physical data for a fluid without added salt (<i>i.e.</i> counterions only) in a slit channel. L is the length of the channel separating the walls, ν is the kinematic viscosity, l_B the Bjerrum length and σ the surface charge.	48
2.5	Physical data for an electrolyte with added salt (counterions and coions) in a cylindrical channel. R is the radius of the pore and L its length. ν is the kinematic viscosity, l_B the Bjerrum length, λ_D the Debye screening length and σ the surface charge.	50
2.6	Physical data for an electrolyte with only counterions in a cylindrical channel. R is the radius of the pore and L its length. ν is the kinematic viscosity, l_B the Bjerrum length, σ the surface charge.	52
2.7	Physical data for a cylindrical channel with only counterions. R is the radius of the pore and L its length. ν is the kinematic viscosity, l_B the Bjerrum length and σ the surface charge	54
4.1	Physical data for an Electro-osmotic flow without salt in a slit channel. L is the length of the channel separating the walls, ν is the kinematic viscosity, l_B the Bjerrum length, σ the surface charge.	82
4.2	Simulations parameters used to obtain the results shown in Fig. 4.11. All of the simulations were carried out for $l_B/\Delta x = 1.44, 2.88$ and 4.8 , under a reduced voltage $\Delta V = 0.1$, to ensure that the distance between the wall is always the same $L = 3.7 \times 10^{-8} m$	92
4.3	Fitting parameters corresponding to the fit $f(x) = \frac{ALx}{2\lambda_D} + B$ as illustrated in Fig. 4.11.	92
4.4	Simulations were carried out for $l_B/\Delta x = 1.44, 2.88$ and 4.8 , to ensure that the Debye screening length is always the same, <i>i.e.</i> $\lambda_D = 1.17 \times 10^{-9} m$	93
4.5	Fitting parameters corresponding to the fit $f(x) = \frac{ALx}{2\lambda_D}$ as illustrated in Fig. 4.13.	93
4.6	Physical data for a coaxial cylindrical channel with a constant reduced potential difference of $\Delta V = 0.1$. R_1 and R_2 are the inner and outer cylinder radii respectively. ν and l_B denote the dynamic viscosity and the Bjerrum length. . .	99
4.7	Error the capacitance for a coaxial cylindrical channel with added salt (see Eq. 4.66), when varying λ_D (see text for details on parameters).	101

List of Tables

5.1	Error on Q_∞ and $Q(0)$ when varying λ_D (see text for details on parameters) . .	111
5.2	Error on Q_∞ and $Q(0)$ when varying L , for a fixed resolution $l_B/\Delta x = 4.8$ and salt concentration corresponding to $\lambda_D/\Delta x = 8$	111
6.1	The simulated systems correspond to orthorhombic boxes with $L_x = L_y = L_\parallel$ and $L_z = L_\perp$. For each size ratio $\alpha = L_\perp/L_\parallel$, we compute the steady-state velocity as a function of $k_B T/6\pi\eta L_\parallel$, for a singular force applied either in the x or z directions. The corresponding slopes provide the scaling functions $h_{\parallel,\perp}$ reported in Figure 6.2.	128

"If . . . all of scientific knowledge were to be destroyed, and only one sentence passed on to the next generations of creatures . . . it is . . . all things are made of atoms"
- Richard Feynman

Introduction

DURING the last decade, technological developments in nanosciences saw a rapid improvement in the design and tailoring of new devices with specific geometries. They are characterised by specific lengths, whose size is below of the micrometer, and with adjustable surface properties. Hence, it has been possible to manipulate fluids at the nanometric scale and thus create new applications in different technological fields. For instance the transport of solutions through a nanotube with charged interfaces offers simple analytical tools, which can detect single molecules ("pore blockade" during DNA^[1,2] or ion^[3] translocation), as well as new technologies for water purification and energy production^[4]. The possibility to control and monitor the electrodes surface charge at the interface of nanofluidic devices opens new paths, such as nano-electrochemistry or new original detection techniques at the molecular level (redox cycling and Electron Correlation Spectroscopy^[5-7]) or improved sensors (*e.g.* Nanoscale Ion Sensitive Field Effect transistors, nanoISFET^[8]). The unique properties of these systems come from the presence of charged interfaces between a solid and a liquid for scales ranging from 1 to a few 100 *nm*. Experimentalists and engineers are thus limited to the possibility to understand and predict the experimental properties, preventing them to fully exploit these new technologies beyond the current state-of-the-art and thus anticipate future technological developments.

Moving from microfluidics, which is now a well-established field, to nanofluidics requires a paradigm change. Current understanding and interpretation of the experiments mentioned above is limited to the macroscopic descriptions of mean-field theories. However, the nanometric scale requires taking into account phenomena which are often neglected at larger scales. Indeed, due to the small number of particles involved, thermal fluctuations are here essential in the understanding of the dynamics of the system. Furthermore, due to confinement we observe strong electric potential gradients and strong coupling between electrostatics and hydrodynamics. In fact confinement of the order of the nanometer reveals the discreteness of matter and its molecular nature. It is important to point out that these aspects are intrinsic properties of the system due to its confinement and are not created by experimental limitations.

The charge of an electrode in contact with a liquid is kept at a constant potential value inducing thermal fluctuations, which provide information on microscopic interfacial processes. Other common applications involving interfaces make use of the electrode capacitance to acquire a mean charge when applying a voltage. It is thus necessary that we better understand fluctuations, which are often wrongly considered as a source of nuisance. Unfortunately experimentalists rarely exploit the potential of noise for measurements at the nanoscale. Instead of merely trying to reduce the signal-to-noise ratio, "listening" to this electrical noise would open a wide range of applications. Even though we are limited by the available theories to interpret the signal we can still extract information on the underlying mechanisms present. We here focus on the noise arising from charged fluids confined by electrodes or any general charged surface.

1.1 Coupling nanofluidics, electrokinetics and noise

1.1.1 Nanofluidics

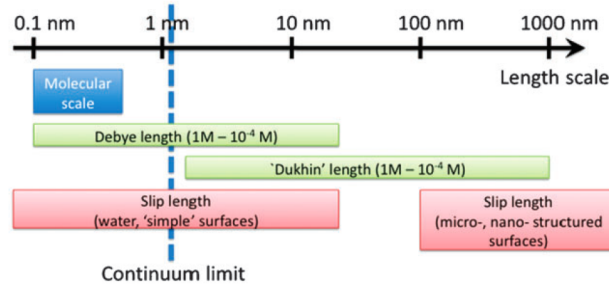


Figure 1.1 – Various length scales at play in nanofluidics^[9].

Nanofluidics can be defined in different ways, according to the many different scientific communities. In the context of this work, we consider nanofluidics as the study of fluidic transport at nanometer scales. It emerged rather recently and proved to be successful in a great number of technological areas, for instance in biotechnology ("lab on a chip") allowing the study of individual macromolecules^[10–12]. Furthermore, it was possible to develop nanofluidic transistors^[13,14], as well as nanofluidic diodes^[15,16]. On the other hand, their study enables the development of bio-mimetic membranes, which would allow permeability or selectivity^[17]. A great example are aquaporin channels, which are excellent water filters across biological membranes: they are both permeable to water, yet extremely selective to other species^[17,18]. Despite the recent development of this field, scientists were already working on confined fluids when dealing with electrokinetics (*e.g.* electro-osmosis, electrophoresis ... see Section 1.1.2), soil science, membrane science (*e.g.* ultra-filtration, fuel cells, reverse osmosis ...), colloid chemistry and the study of physiology and biological channels^[10]. Such fundamental studies allow us to design nanofluidic devices and study them with new techniques such as Surface Force Apparatus (SFA), Atomic Force Microscopy (AFM) and nano-Particle Image Velocimetry (nano-PIV) coupling PIV to TIRF set-up (Total Internal Reflection Fluorescence). A great effort was also done in the progress of computational techniques such as Molecular Dynamics, which allows us to understand, design and observe such devices.

On the other hand, the community rightfully wondered how to describe theoretically nanofluidic devices. Indeed, as we can see in Fig. 1.1, depending on the considered scale, available theories usually apply in a given range of length scales. Nonetheless, despite being developed in the 19th century, the Navier-Stokes equation proved to be efficient even for confined fluids, down to ~ 1 nm. This was verified experimentally initially by Chan and Horn^[19] and later, using Surface Force Apparatus, by Georges *et al.*^[20]. Similarly Klein *et al.*^[21] and E. Riedo *et al.*^[22] showed that water keeps its bulk viscosity down to 1–2 nm. However they also observed a drastic change in behaviour for stronger confinement, where the wettability of the confining walls becomes important, showing how water can produce exotic behaviour different from the common known picture and theory. Analog studies on different fluids such as octamethylcyclotetrasiloxane were also carried out^[23,24] and similar observations were made. On the computational side the 1 nm value was confirmed on several

Introduction

studies^[25-27]. Beyond viscosity, the self-diffusion coefficient was found to deviate from the classical Stokes-Einstein prediction given by

$$D = \frac{k_B T}{3\pi\eta\sigma}, \quad (1.1)$$

where σ is the molecule diameter, because of confinement. More specifically the diffusion coefficient depends algebraically on the confinement width^[28,29], showing that Eq. 1.1 is not a correct measure of the viscosity η as previously assumed. The structuring and ordering of a fluid at the confining walls was found to play an important role in nanofluidics. It was shown experimentally that it induces an oscillatory dissipation in liquid films with a width of several molecule diameters^[23,24]. Furthermore, non-local effects were observed to impact the rheology of the confined fluid and depend on the specific nature of the surfaces^[30].

Electrokinetic effects also play an important role in the rheology of nanofluids. Before we discuss them into details let us introduce the most common electrokinetic effects.

1.1.2 Electrokinetics

Solid surfaces in contact with electrolytes have a tendency to gain surface charges. This phenomenon mainly arises from adsorption or dissociation of chemical groups. As a result, because of electrostatic forces, the charged surface attracts the counterions present in the solution and repels the co-ions. Eventually this will form a thin layer made of counterions, which are adsorbed at the walls. This layer is often referred to as the electric double layer (EDL), which is shown schematically in Fig. 1.2. It is made of two layers: the Stern and diffuse layers.

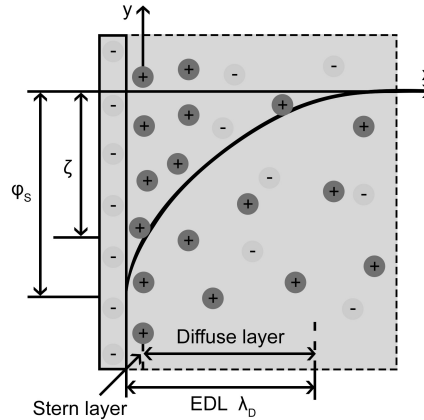


Figure 1.2 – Electric double layer formed at a negatively charged solid surface

The remaining ions then distribute according to Boltzmann statistics. We shall discuss more in details the derivation of the governing equations of these phenomena and in particular of the electro-osmotic flow, in Chapter 2.

Introduction

1.1.2.1 Electroosmosis

If an external electric field is applied parallel to the walls, a force acting upon the ions will be generated, which in turn will induce a characteristic flow called electro-osmotic flow or EOF. This is shown in Fig. 1.3.

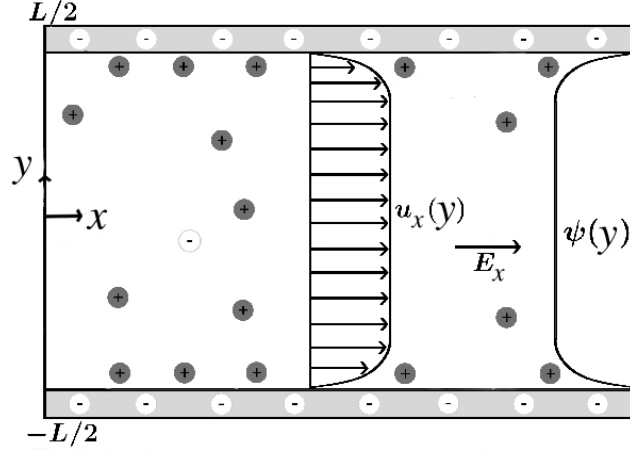


Figure 1.3 – EOF in a slit channel bearing a uniform negative surface charge inducing an electrostatic potential $\psi(y)$.

The EOF velocity profile $u(y)$ in a microchannel is almost uniform, and is usually referred to as a plug-like flow, as shown in Fig. 1.3. Therefore, one can use the constant velocity to describe the EOF velocity outside the EDL, which is known as the Smoluchowski slip velocity.

1.1.2.2 Electrophoresis

Another electrokinetic phenomenon is electrophoresis where the external applied electric field is responsible for the migration of charged suspended particles. For sufficiently small applied fields (corresponding to the linear response regime), the velocity v_p of a particle subjected to an electric field \mathbf{E} reads

$$\mathbf{U}_p = \mu_E \mathbf{E} \quad (1.2)$$

which defines the electrophoretic mobility μ_E .

Consider the zeta potential ζ defined as the potential taken at the interface between the Stern layer and the diffuse layer, as illustrated in Fig. 1.2 and 1.3. When the zeta potential of the particle is relatively small (*i.e.* $\zeta \ll k_B T/e$) the surface conduction within the EDL is negligible.

Given a to be the characteristic size of the particle, for a thin EDL (*i.e.* $\lambda_D \ll a$) the electrophoretic mobility of a particle suspended in an unbounded medium can be written as^[31]

$$\mu_E = \frac{\varepsilon \zeta}{\eta}, \quad (1.3)$$

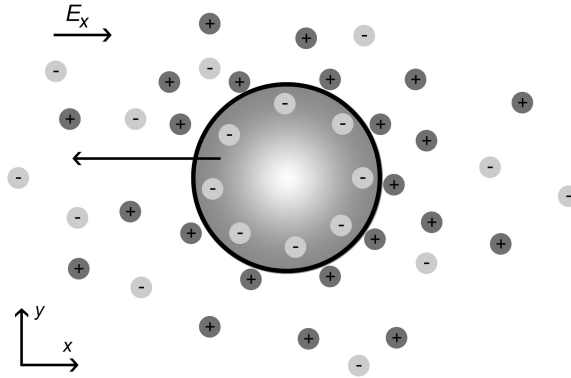


Figure 1.4 – Electrophoretic motion of a negatively charged particle.

which is often referred as the Helmholtz-Smoluchowski law and where $\varepsilon = \varepsilon_0\varepsilon_r$ is the permittivity. Conversely, for $\lambda_D \gg a$, Hückel found that the particle mobility reads:

$$\mu_E = \frac{2\varepsilon\zeta}{3\eta}. \quad (1.4)$$

For intermediate cases, Henry’s function accounts for the effect of finite EDL with an arbitrary thickness on electrophoresis of a sphere in an unbounded medium^[32].

1.1.2.3 Dielectrophoresis

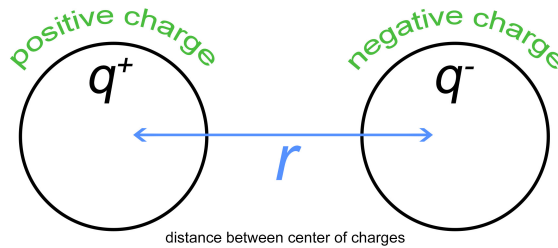


Figure 1.5 – Sketch of the electric dipole moment created by two opposite charges

Dielectrophoresis is an electrostatic phenomenon (sometimes related to electrophoresis) which describes the motion of suspended particles resulting from polarisation forces produced by an inhomogeneous electric field. This is because in some special cases, particles have both positive and negative charges, thus forming a dipole moment $\mu_D = q \cdot r$ (see Fig. 1.5). Therefore, they experience a force in an inhomogeneous external electric field. This also applies for dipoles induced by the external field itself^[33]. This is shown schematically in Fig. 1.6.

The direction of the dielectrophoretic (DEP) force is determined by the ratio of the polarizability of particles to that of the electrolyte solution. For an AC field, when averaging over

Introduction

time, the dielectrophoretic force can be expressed as^[34]

$$\mathbf{F}_{DEP} = 2\pi r^3 \epsilon \operatorname{Re}[K(\omega)] \nabla |E_{rms}|^2 \quad (1.5)$$

where ω and E_{rms} refer to the AC electric field frequency current and the root mean square electric field strength respectively. $\operatorname{Re}[K(\omega)]$ accounts for the real part of the Claussius-Mossotti factor, given by

$$K(\omega) = \frac{\bar{\epsilon}_p - \bar{\epsilon}_f}{\bar{\epsilon}_p + 2\bar{\epsilon}_f} \quad (1.6)$$

where $\bar{\epsilon}_k = \epsilon_k - i\frac{\sigma_k}{\omega}$ is the complex permittivity, with σ_k denoting the corresponding conductivity.

The force of Eq. 1.5 is acting on a sphere of radius r : a positive dielectrophoresis refers to a DEP force directed toward the region with a higher electric field and vice versa.

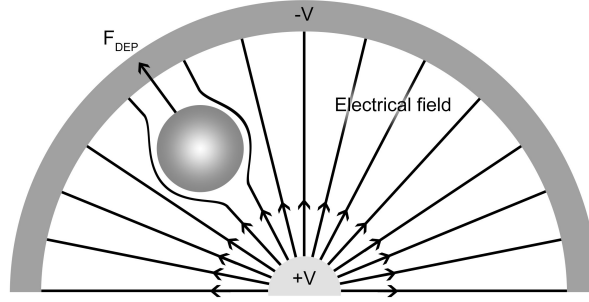


Figure 1.6 – Negative dielectrophoresis of an uncharged particle under an external AC E-field

Eq. 1.5 is only valid when the presence of the particle does not significantly affect the electric field and the particle size is much smaller than the characteristic length of the system. However, when nanopores are considered, the characteristic length can be roughly of the same order of the particle size, meaning that the theory is inaccurate. Al Jarro *et al.*^[35] showed that a better derivation for the force calculation is to directly integrate the Maxwell stress tensor (MST) over the particle surface.

1.1.2.4 Induced charge electrokinetics

Induced charge electrokinetic (ICEK) occur around any polarizable (metal or dielectric) surface in the presence of any (DC or low-frequency AC) electric field. This leads to a special type of electrokinetic flow, which is often denoted as ICEK flow. The main difference between conventional electrokinetics and ICEK is the origin of the surface charges. For the former case, the surface charge is acquired via adsorption or dissociation of specific chemical groups, whilst for the latter the surface charge arises from material polarization.

Fig. 1.7 shows schematically the flow field around a conducting spherical particle, which is a quadrupolar EOF, moving toward the particle, in the direction of the electric field, and eventually leaving the particle in perpendicular directions.

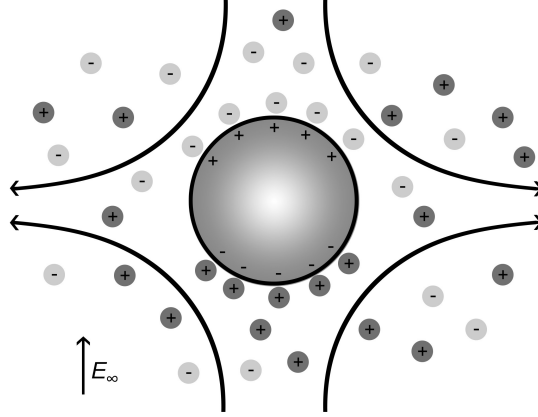


Figure 1.7 – Schematics of induced-charge electroosmosis around a conducting particle

Therefore, now that electrokinetic effects were introduced, we understand that the Debye length $\lambda_D = (8\pi l_B n_s)^{-1/2}$ (with n_s denoting the salt concentration), as depicted in Fig. 1.3, is an important length scale in nanofluids. Indeed, it was found to play a pivotal role when the two Debye layers overlap in a nanopore (*i.e.* when the nanopore is of the order of twice the Debye length), thereby affecting the fluidic transport in the channel^[36]. This leads to new fluidic phenomena, such as permselectivity^[13,14], nanofluidic diodes^[15,16] or surface dominated ion transport^[37].

If we consider the slip length b defined as

$$b\partial_n v_t = v_t, \quad (1.7)$$

where n and t denote the normal and tangential directions of the surface respectively, experimentalists observed that b strongly affects ion transport at charged surfaces^[38]. This is shown in Fig. 1.8.

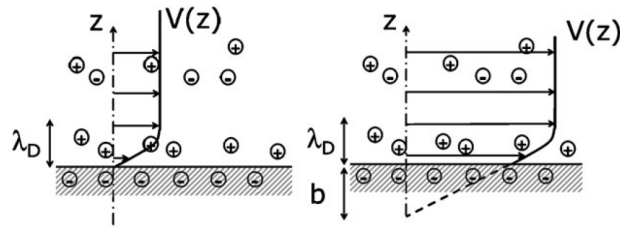


Figure 1.8 – Sketch of the influence of slippage on the electro-osmotic transport. Slippage reduces the viscous friction in the electric Debye layer, as the hydrodynamic velocity gradient occurs on a length $b + \lambda_D$, instead of l without slippage. Flow is accordingly enhanced by a factor $1 + b/\lambda_D$. Sketch taken from Ref. 9.

In the recent years, colloidal particles were electrophoretically driven through a nanopore in order to give rise to a detectable change in the ionic current through the slit. This type of technique was further developed to achieve affordable and high-throughput nanopore-based DNA sequencing^[39,40]. Furthermore, dielectrophoresis proved to be a great tool to allow nanoparticles separation^[41]. The microfluidic/nanofluidic community started to draw more

Introduction

attention to the ICEK in the last fifteen years in order to develop a theoretical framework^[42,43], to account for these phenomena. Until today, ICEK was already successfully used to generate circulating flows for fluid stirring and mixing in microfluidics^[5,44–46]. Particle trapping and enrichment were also experimentally achieved using ICEK in microchannels^[47,48].

It is thus clear that in the context of electrolytes confined at the nanoscale, electrokinetic effects are essential for an accurate description of the physical phenomena. We now turn to the origin of noise, which as we said is essential in the understanding of microscopic processes, and define it in the context of nanofluids.

1.1.3 What is noise?

It was not before the early 18th century that humans started considering matter as composed of discrete objects instead of a continuous media, as perceived by our senses. One of the early scientific thinkers of the "atomist" picture was Bernoulli^[49], although Democritus was the first to make use of the word "atom". More specifically, it was in 1738 that Bernoulli tried to use science to explain something about atoms. Seventy years earlier, Boyle had shown that air exerts pressure and that it is inversely related to volume, leading to the question of how does air exert pressure^[49]. Boyle himself tried to explain that in a certain way particles repel each other. Newton made use of his idea to develop the "repulsion theory" of a gas. He then combined it with the then-prevailing idea that heat is a fluid. On the other hand, Bernoulli understood that if the gas consists of little balls, then pressure would arise from the force with which they hit the sides. He could then derive Boyle's law using this idea. However the idea was not taken seriously and was forgotten for a while.

On the other hand, Lavoisier understood that substances react to form new substances in given mass proportions. This was the beginning of stoichiometry, which led Dalton, in 1803, to propose "atoms" as a solution to the question of why should things always react in the same way? He claimed that substances are fixed combinations of atoms and as they react they maintain the same proportions^[49]. Similarly, Gay-Lussac carried out studies of how things combine when the volumes of the reacting gases are considered^[49].

In 1811 Avogadro argued that, in a fixed volume, the number of little balls of a gas is the same for all substances, independently of the mass, size, or nature of the substance. This was the birth of Avogadro's number, but once again he was not taken seriously until Einstein and more particularly Perrin came in the picture. Indeed, it was Perrin who coined the term "Avogadro's number"^[50]. Still, during the late 19th century, people were trying to estimate the speed of the molecules in gases and concluded it must be very high. Thus, they wondered why it takes time for someone across the room to smell food when someone starts cooking at the other end. Indeed, if molecules moved so fast we should smell almost instantaneously. However, despite their fast motion, molecules are hindered in their forward progress because they collide. Clausius wondered about the average time that a molecule goes before colliding with another, which is the birth of the concept of mean free path. In fact, Clausius assumed particles to be moving at the same speed for a given temperature. Maxwell, proved Clausius wrong and came out with the idea that for a given temperature, molecules move with all speeds (zero to infinity), yet the proportion of each velocity behaves according to a Gaussian distribution (*i.e.* the now called Maxwell-Boltzmann distribution). Then Clausius claimed that temperature is proportional to the average kinetic energy, which is the variance of the

Introduction

distribution, giving a stochastic picture to the problem in 1860.

Another key character in the pursuit of atoms was Boltzmann. He doubted the Maxwellian distribution to be the correct distribution and realized that collisions are at the root of the answer to his query^[51]. He could then derive the Boltzmann equation, which became essential in different areas of physics, astronomy, chemistry, and plasma physics. It is an equation of evolution for the probability density of position and velocity, $f(\mathbf{r}, \mathbf{v}, t)$

$$\frac{\partial f}{\partial t} + \mathbf{v} \cdot \nabla_{\mathbf{r}} f + F \cdot \nabla_{\mathbf{v}} f = \left(\frac{\delta f}{\delta t} \right)_{\text{coll}} \quad (1.8)$$

where F is the external force. $\left(\frac{\delta f}{\delta t} \right)_{\text{coll}}$ denotes the so-called collision term, which is the change in the distribution due to collisions. Boltzmann derived it originally for a dilute gas^[51]. The collision term makes the process irreversible and is responsible for the Maxwellian distribution. Boltzmann was the first to fully understand the concepts of stochastic processes and in particular the idea of an evolving probability distribution. Nevertheless his work was not sufficient to convince the community of the existence of atoms. It was Einstein who really did so in his seminal paper of 1905^[52], his "miracle" year. In order to achieve it, he had to use the concept of "noise".

When we talk about noise, we often talk about Brownian motion. In fact, Einstein introduced these words in his 1905 paper: "It is possible that the movements described here are identical with the so-called Brownian motion; however the information available to me [...] is so imprecise that I could not form a definite opinion on this matter". Later, in 1908, he wrote another paper on "The Elementary Theory of the Brownian Motion"^[53], which begins with "Prof. R. Lorentz has called to my attention, in a verbal communication, that an elementary theory of the Brownian motion would be welcomed by a number of chemists." He could develop the link with diffusion in an explicit way. Lorentz was among the greatest physicists of his time, hence the phrase "Brownian motion" became standard.

Thanks to the work of Einstein^[52], Perrin could verify his prediction that noise could be used to calculate Avogadro's number N_A ^[50]. Three years afterwards, Langevin started the field of stochastic differential equations, even though atoms were not his initial motivation. Einstein maintained a strong interest in noise. Actually, he is the first to define the auto-correlation function. Indeed in Ref. 54 he introduces a quantity $\chi(\Delta)$, which is called the "characteristic" and is defined as:

$$\chi(\Delta) = \overline{F(t)F(t+\Delta)} = \lim_{T \rightarrow \infty} \frac{1}{T} \int_0^T F(t)F(t+\Delta)dt \quad (1.9)$$

He claimed that there exists a simple dependence between the characteristic and the intensity curve, *i.e.* between the autocorrelation function and the power spectrum. Einstein concluded (leaving out the constant of integration) that

$$2\chi(\Delta) = \int_0^\infty I(x) \cos(x\Delta)dx \quad (1.10)$$

where $I(x)$ denotes the spectral intensity, which he derived from the Fourier series. Eq. 1.9 is the so-called Wiener-Khinchin theorem, one of Einstein's many contributions to noise signal analysis.

Introduction

A different approach to noise analysis was introduced by Langevin, a student of Pierre Curie, which makes use of Newton's equation. Starting from Stokes law, which is given by

$$F = -6\pi\eta a\xi \quad (1.11)$$

where ξ (using his notation) is the velocity, a is the radius and μ the viscosity, Langevin claimed that, in addition to friction, there is another force because. In his own words^[55]: "in reality [...] the Stokes force is only an average, and because of the irregularity of the collisions of the surrounding molecules". Therefore the total force is the friction force plus an irregular force X . Using Newton's equation he could finally obtain the same result as Einstein.

After the use of noise in the proof of the existence of atoms, it became again important with the arrival of electronics and, more specifically, with the arrival of the vacuum tube. Indeed, it initiated the study of noise in electrical engineering in both theory and practice. The vacuum tube became available thanks to Fleming who, in 1904, invented the vacuum diode. Initially its purpose was to convert AC into DC. The first contributors in the understanding of noise in electrical circuits were Schottky, Johnson, and Nyquist.

Schottky was a physicist who, in a milestone paper of 1918, was the first to consider both shot noise and thermal noise^[56]. The term "shot noise" denotes any stochastic process that is a sum of discrete events, meaning that shot noise are the fluctuations around the mean value of the process. Besides, the mere existence of shot noise in a vacuum tube shows that electricity consists of small fluctuating particles, namely electrons. On the other hand, thermal noise is caused by the fact that some electrons in a conductor are free to move in random directions. On average, the current vanishes if no voltage is imposed. Nevertheless, fluctuations appear, meaning that at any given time there could be more electrons moving to the right than to the left and producing a momentary current. The electrons, like atoms, have a velocity distribution and the wider the distribution, the larger the fluctuations. This distribution width is proportional to the temperature; thus the term thermal noise.

John B. Johnson and Harry Nyquist, who worked at the Bell Laboratories, independently published papers on the same effect in 1928^[57,58]. Johnson reported the experimental results and Nyquist produced an elegant derivation of the effect. His idea was to relate the fluctuations to the temperature. He thus obtained (in his notations)

$$E^2 d\nu = 4RkTd\nu \quad (1.12)$$

where $E^2 d\nu$ is the square of the voltage in the frequency interval $d\nu$, and R denotes the resistance. Nyquist used Planck's law to get (using angular frequency)

$$E^2 = \frac{2R}{\pi} \left(\frac{\hbar\omega}{e^{\hbar\omega/kT} - 1} \right) \quad (1.13)$$

which reduces to Eq. 1.12 when $\hbar\omega \ll k_B T$.

Therefore after Einstein's paper on Brownian motion, where he first postulated the idea of spontaneous irregular motion of electricity in electrical circuits^[59], the fundamental role of intrinsic thermal fluctuations in electronics was recognised in 1928 with the pioneering works of Nyquist and Johnson. Thermal noise is the fluctuation counterpart of the dissipative resistance of the circuit and was recently examined in the context of fluctuation theorems^[60]. Finally, flicker noise or $1/f$ noise, shows a universal power density spectrum which varies as the

inverse of the frequency, despite various possible microscopic origins. One such mechanism, relevant to the cases considered here (involving confined charged fluids), is the fluctuations in the number of charge carriers in the system of interest. Landauer understood the importance of noise in the context of electrical circuits to understand microscopic mechanisms. In his Nature paper he stated that "The noise is the signal"^[61], which led to exciting developments^[62]. Although the condensed matter community has drawn a lot of interest to the development of noise based techniques and further worked on noise analysis little attention among physical chemists and electrochemists or in the microfluidics/nanofluidics community was drawn.

1.2 Experiments using noise

In recent years, experimentalists in the nanofluidics community are beginning to focus on noise based techniques. Instead of considering it a spurious signal, they develop new techniques which extract microscopic information on nano-confined electrolytes.

Only few electrochemists use noise analysis to extract information on the redox reaction rates and corrosion processes^[63]. In addition it was shown that electrical potential fluctuations of redox active species play a major role on the rate of electro-chemical reactions^[64]. These local (Madelung) potential fluctuations of the species, fundamentally differ from the mean (Poisson) potential and are intrinsically linked to the redox properties of the species^[65]. Such fluctuations thus play a wider role on in the electrochemical field, including batteries. When a potential difference is applied, a motion of the charged species is enabled, thereby, inducing a polarization current. In addition, redox-active species may be oxidized or reduced, resulting in a Faradaic current, which leads to a redox cycling device (see Fig. 1.9 (a)).

Despite electrodes being widely used, knowledge of the physical chemistry at the molecular level still remains limited. Furthermore, as we are interested in systems such as nanopores, the signal generated by this device becomes very noisy, due to thermal fluctuations of the charged species, *i.e.* Brownian motion. Lemay *et al.*^[67] tried to interpret this noise in order to quantify the amount of adsorbed and desorbed molecules at the walls. This was achieved using a model which gave good results compared to experimental data available. However, the model makes several non-physical assumptions, as only Brownian motion between the analyte molecules is considered. This means that collisions between the molecules are ignored, which eludes the possibility to exchange electrons during those collisions, and the motion established by the charged walls is also ignored. The size of the system may be the reason why the experimental results are in agreement with the model: thermal fluctuations might be much more important than the electrical forces driving the molecules. Another reason might also be that the authors worked only in the low-frequency regime.

Similarly, Lemay and co-workers^[68] decided to use noise analysis in order to detect the passage of single molecules entering and leaving a nanochannel (see Fig. 1.10). Their procedure is as follows: a solution is used, so that it cannot be affected by the potential difference applied at the walls. A current noise, merely due to thermal fluctuations, can then be measured and whenever a redox species (*e.g.* ferrocene) is inserted within the solution, a change in the background noise is observed. This change was verified to be generated only by the redox species and therefore reveals the method to be efficient in order to detect the passage of a single type of molecules. More specifically, cross-correlation analysis of the current noise signal gives a unique footprint for each type of studied species. Nonetheless, the method only

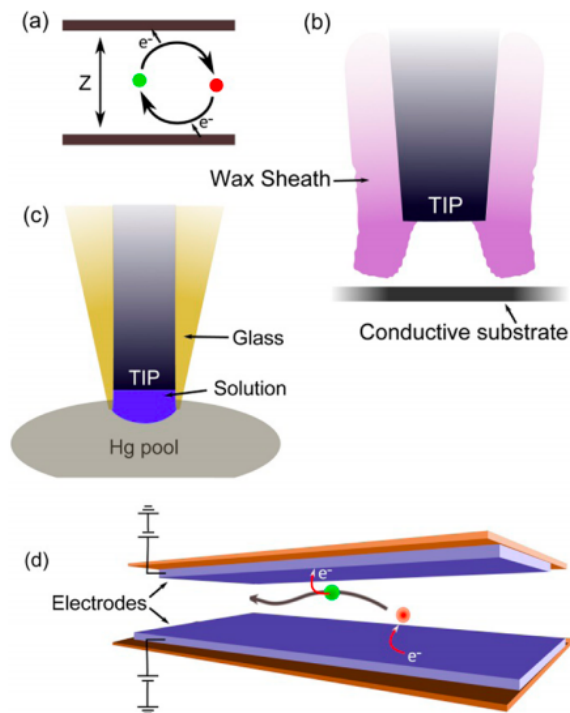


Figure 1.9 – Electrochemical single-molecule detection. (a) Basic concept of redox cycling. (b) Nanoelectrode encased in wax and positioned near a metallic surface. (c) Recessed glass-encased nanoelectrode immersed in mercury. (d) Lithographically fabricated nanogap device (Figure taken from Ref. 66)

applies to redox molecules and is sensitive to the type of walls used as well as the voltage difference applied. Another interesting result from their study is that as the concentration of those molecules increases, the current distribution becomes a Gaussian^[67]. These examples of experiments show that the experimental reality of the ions dynamics at charged solid/liquid interfaces, in particular in porous media, results from a complex interplay between diffusion, advection by the fluid flow, electrostatic interactions as well as adsorption/desorption phenomena. The coupling between all of these phenomena is often neglected.

Indeed, one of the main issues when dealing with adsorption/desorption dynamics at the electrodes, is that it strongly depends on the electronic structure of the metal interface, on the adsorbate, on the nature of the supporting electrolyte and on the potential applied^[69,70]. On the other hand, the motion of ions also influences the local charge distribution, hence the electrical force acting on the fluid. Such electrokinetic effects, which are encountered from energy conversion exploiting couplings on the scale of interfaces^[71,72] to large scales applications in Earth Sciences^[73] have been the subject of extensive theoretical and numerical studies (see *e.g.* Refs^[28,74–79]) and a number of simulation tools have been proposed to model them at various levels, from the molecular to the macroscopic ones (see *e.g.* Refs.^[80,81] for reviews).

Even without electrokinetic couplings, specific effects play an important role on the dynamics of charged species. For example, the diffusion of ions in porous materials depends not only on their charge but also on their chemical nature. An illustration can be found

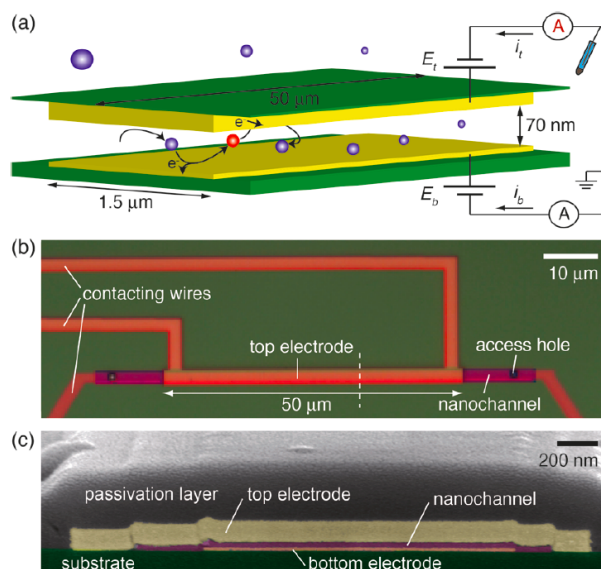


Figure 1.10 – (a) Principle of operation of the device. Redox-active molecules undergoing Brownian motion are repeatedly oxidized and reduced at two parallel electrodes separated by a distance of 70 nm , leading to a measurable current. (b) Optical micrograph of a device (top view). Visible are the top electrode and its contacting wires (orange), the access holes (black squares), and the nanochannel connecting the active region of the device to the access holes (colored magenta for clarity). The active region of the device is connected to an outside fluid reservoir via the nanochannel, allowing the target molecules to freely diffuse between these compartments. The bottom electrode is hidden below the top electrode and the nanochannel such that only its contacting wires are visible (dark orange). The dashed white line represents the cut in (c). (c) Scanning electron microscope image of the cross-section of a device. The device was cut open using a focused ion beam. (Figure taken from Ref. 67)

e.g. with the different properties of Na^+ and Cs^+ tracers in clays, which go beyond their different behaviour in the bulk.^[82] Of course, charged tracers also experience the effects of hydrodynamics and electrokinetic couplings in the fluid as a whole, in addition to their own dynamics and interactions with the solid surfaces. This is exploited in practice in analytical chemistry *e.g.* in chromatography or electrophoresis experiments.^[83] It is well known *e.g.* in the chemical engineering community that even in the case of uncharged solids and solutes, the coupling between pore-scale motion and surface adsorption may result in intricate macroscopic transport properties^[84]. Surface charge and charged solutes only increase the difficulty to understand and predict the emerging behaviour.

At the coarse-grained or macroscopic levels, specific interactions with the surfaces are usually introduced via adsorption and desorption reactions, with corresponding rates. Such reactions are usually assumed to be of first-order, even though in principle the description can be improved to account for more complex features such as the saturation of surface sites.

Adsorption phenomena at the electrodes strongly depend on the electronic structure of the metal interface, on the adsorbate, on the nature of the supporting electrolyte and on the potential applied^[69,70]. Unfortunately, most experimentalists tend to neglect these phenomena, as well as electrokinetic effects in general, and model their experiments using only Brownian motion. Nonetheless, an experimental method^[85], which does not require any knowledge of the diffusion constant of the molecules or of the exact geometry of the electrodes, was pro-

posed. Measuring the oxidizing and reducing current, they could link them to the amount of redox molecules present in the solution, and thus quantify the amount of adsorbed species. The experiment showed that adsorption is detected through a decrease in the amplitude of the fluctuations in the current, proving once again the usefulness of these fluctuations in determining transport coefficients. Nevertheless, the method presents some drawbacks: adsorption can only be detected if the molecules can undergo a redox cycle; furthermore the residence time in the active region must be significantly longer than the shuttling time between the electrodes (*i.e.* the geometry of the system needs to be adapted in order to achieve that) and finally the current has to be measured sufficiently fast for the full spectrum of the diffusive fluctuations to be captured. Both results in Ref. 85 and 86 are in agreement, but the frequency based method is somehow weaker as it necessitates extra numerical calculations (finite differences), in order to compute the escape rate and estimate the rate of adsorption present in the system. On the contrary, the former study gives a direct experimental method, which enables quantification of adsorption rates. Furthermore, it does not require prior knowledge of the diffusion constant of the molecules or the exact geometry of the electrodes. Once again, the issue with both these methods is that they assume free diffusion of molecules caused only by Brownian motion and hence do not take into account all of the electrokinetic phenomena or the effect of the local electric field on the charged species. Despite these theoretical issues, noise based techniques showed high potential in determining highly precise flow measurements. Indeed Lemay *et al.* [87] used the simple idea that the electrical current measured in a nanogap is a time-dependent quantity proportional to the number of electrochemically active molecules in the volume between the electrodes. Then, using cross-correlation spectroscopy, they could detect the same noise footprint of analyte molecules entering and leaving the pore. By means of this technique, given the length of the pore and the time period time taken by the analyte molecules to go through the nanochannel, they were able to detect flow rates below $10 \text{ pL} \cdot \text{min}^{-1}$, pushing the limit of ultra-low flow rate measurements. Electrokinetic effects were also neglected, however the choice was justified as they are negligible for flow rate with low Péclet number ($Pe < 0.1$). The method is an analogue to fluorescence cross-correlation spectroscopy, which is widely used for instance in DNA detection [88,89]. The method can be extended to another class of molecules (electrochemically active instead of fluorescent).

We have thus shown how the description of these experiments involves many different physical phenomena, which require coupling different dynamics (*e.g.* hydrodynamic, electrokinetic or sorption effects) and thus cannot be done via simple model. This is why a more detailed model/algorithm should be carried out, in order to account for these physical chemical phenomena, which are obviously present within the system. This would provide a computational tool that is as close as possible to what is observed experimentally.

1.3 Modelling charge, current and potential fluctuations at the nanoscale

In spite of the many improvements during the last century in the description of interfacial science the canonical picture of Gouy and Chapman prevails in the fields of electrochemistry and micro/nanofluidics [90]. Although the theory was extended to capture the effects of packing

Introduction

and ion correlations at the interface, as it is very important in the context of ionic liquids^[91,92], the theory usually lies on a mean-field approach of the ionic correlations, with only a few exceptions (*e.g.* field theories^[93] or in the strong coupling approach^[94,95]). This is why most of the advances on the understanding of ions dynamics at interfaces make use of numerical methods.

Among the successful numerical methods to simulate complex fluids we find Molecular Dynamics (MD). MD simulates the motion of molecules (*i.e.* particles) according to the equations of motion leading to applications to both thermodynamic equilibrium and non-equilibrium phenomena. MD yields a correct description of fluids on microscopic and hydrodynamic scales. One of the drawbacks is that typical length scale is of the order of a few tens of nanometer and the time scales are about a few hundred nanoseconds for simulations of dense liquids. Furthermore, its computational cost is prohibitively high such that it cannot be used for practical fluid flow simulations in micro and nano scales, except for free molecular regimes. This is because it starts from the integration of Newton's second law and using integral methods, such as Verlet method algorithm, the basic dynamics parameters such as position, velocity, and interaction force can be determined. All of the macroscopic physical properties are then computed averaging all of the configurations, using statistical mechanics.

Contrary to MD, the Monte Carlo method (MC) produces a series of microscopic states according to a stochastic law and is thus irrespective of the equations of motion. Hence, it does not include the concept of explicit time and is thus used for phenomena in thermodynamic equilibrium. Therefore it is a suitable method for time dependent dynamical properties of a given system. However, it is limited to high concentration scenarios, if electrolytes are considered.

These methods due to their high computational cost are limited to the dimension of the system we wish to simulate. For larger systems ~ 100 nm mesoscopic method become natural candidates. Among these we find the Dissipative Particle Dynamics (DPD), where the fluid is considered as a set of "particles" (fluid volumes) which interact with each other via conservative forces, whose principle is very close to the Smooth Profile Hydrodynamics (SPH). We also have the Stochastic Rotation Dynamics (SRD), also called Multi-Particle Collision Dynamics (MPCD), where we consider particles whose motion is simulated by collisions steps (where the particles velocity is modified by random rotations) and flow steps. Furthermore, we have Brownian Dynamics (BD) where we consider particles animated by a random motion, with hydrodynamic interactions which induce the general motion of the fluid. Finally the Lattice Boltzmann (LB) method, which we shall introduce in great details in Chapter 2 focuses on the probability density to find a particle in a phase space (position and velocity) which evolves according to a discretized version of Boltzmann equation.

While MD allows to better account for ionic correlations (all ions are explicit) and naturally includes thermal fluctuations, it is limited by its computational cost when simulating systems closer to the experimental literature. Succi^[96] showed that for a very fine resolution of $\Delta x = \sigma/4$ (where σ in the Lennard-Jones potential is the inter-particle distance where the inter-particle potential is zero) LB is about a factor of 2000 faster than MD. All of the other mesoscopic methods can be used to simulate ions transport within charged interfaces, but they remain close to MD and present a higher computational cost. The LB method can be easily coupled to other dynamics and because of its low computational cost it is more adapted to systems in our range of interest. Besides, it is able to account for the coupling of the ions

Introduction

with the solvent flow.

All of these methods helped in understanding the structure and the dynamics at interfaces. However, although fluctuations can be neglected at the micron scale, they can no longer be ignored at the nanoscale. Very few studies showed the importance and advantages of noise analysis. For instance, we can find that Wolfrum *et al.*^[97] developed a numerical model that accounts for noise phenomena present in nanopores, during redox cycles pointing out that most software codes use finite differences, whenever diffusion processes need to be described. However, they present several drawbacks, when modeling noise, as they are methods which use probability densities to account for the location of analyte molecules. Therefore, they are not convenient for noise descriptions: only averaged currents are present in the calculations. Two sources of noise are considered: number of fluctuations (which vary between the two electrodes) and redox cycling shot noise (due to diffusive shuttling of molecules). They used a Monte Carlo algorithm, on a cubic lattice, to account for random motion, based on three main assumptions: analyte molecules perform random walks, according to the diffusion equation, and reflect upon collision with the walls; whenever a wall is hit, the molecule may change its state to reduced or oxidized; finally, redox molecules do not interact with each other nor with the electric field. Statistical physics and the connection between fluctuations and observable properties have been applied to electrical phenomena in bulk liquids, taking in particular advantage of the possibility to compute microscopic observables using molecular simulations. The Green-Kubo formalism, which we will discuss extensively in Chapter 6, allows computing transport coefficients (*e.g.* electrical conductivity) from time correlation functions (*e.g.* of the electric current).

Marcus won the Chemistry Nobel prize in 1992, for underlining the role of the potential, induced by the solvents, and the electric field fluctuations on redox processes^[65]. The role of fluctuations on a polar solvent was tackled using liquid state theory^[98–100] and Gaussian field theory^[101]. We could also mention the link between the Nuclear Magnetic Relaxation (NMR) relaxation time of quadrupolar nuclei and fluctuations of the electric field gradient (EFG) at the nucleus^[102]. However, applications to charged interfaces between a fluid and a charged or conducting solid are rather scarce, despite their importance in the contexts introduced in the previous section. For instance, Dünweg and Schmitz^[77] analyzed the effects of flow field around a single colloidal sphere, such as the ones present in electrolyte solutions. A lot of attention was brought on electrophoretic effects, and thus on the competition between electrostatic and hydrodynamic effects. Furthermore, the current modulation through nanopores caused by a polyelectrolyte (*e.g.* DNA) entering the channel was modeled taking into account electrokinetic effects using the Poisson-Nernst-Planck theory (PNP) (see Chapter 2)^[103] or with mesoscopic simulations^[104,105]. As mentioned in the previous section, most models are based on a combination of BD or PNP or a combination of the two^[106,107]. Neglecting electrostatic effects can for instance lead to a wrong description at low concentrations in the electrolytes^[5,108].

The role of electrical fluctuations at the interface between an electrode and an electrolyte has only recently attracted attention. Jardat *et al.*^[109], from the PHENIX lab, computed the relaxation time of the electric double layer after an electron transfer event at the surface using Brownian Dynamics simulation of electrolytes between uniformly charged electrodes^[109]. A major step forward was achieved when charge fluctuations of electrode atoms, in response to the thermal fluctuations of the electrolyte in their vicinity, could be taken into account in

classical MD^[110–112].

We note that although the literature has different approaches to model charge, current and potential fluctuations at the nanoscale, experimentalists often neglect electrokinetic phenomena and simply uses Brownian dynamics. However, since the interplay between hydrodynamic and electrokinetic effect proved to be important in the interpretation of noise based experiments, it is essential for us to be able to model in a compact form (*i.e.* in a single algorithm) all of these phenomena. The LB method is a suitable candidate for this task.

1.4 Objectives of the present work

The overall objective of the present thesis is to develop the theoretical framework and the simulation tools necessary to simulate electrolytes confined at the nanometric scale which are subject to external perturbations (*e.g.* a disturbing potential). The method should then be able to measure the response to the perturbation from which an analysis of the underlying fluctuations can be carried out. This would provide a useful tool for experimentalists and engineers to push their setups beyond the current state-of-the-art, *e.g.* at low ionic strength, and to anticipate future technological developments, *e.g.* working at higher frequencies or with smaller devices. Hence, we are hoping to contribute and enhance the fields of nano-electrochemistry and single molecule detection. We consider systems where the characteristic lengths are much larger than the molecular one. Using continuous solvent models, we can focus on key aspects induced by the large surface to volume ratio and leading to electrical fluctuations (small number of charge carriers, as well as coupling between hydrodynamics, electrostatics and adsorption/desorption). Our approach should in the long run allow rationalizing the manipulation of fluids at the nanoscale that is nowadays feasible but limited by the ability to interpret such fluctuations.

In order to do so, we extended a Lattice Boltzmann Electrokinetics code originally developed by M. Levesque and B. Rotenberg at the PHENIX laboratories in order to include the different physical phenomena important at this scale. The code only included the hydrodynamics in the LB part and a sorption dynamics of neutral tracers in the moment propagation method, which we will introduce in more details in Chapter 3.

In Chapter 2 we couple the hydrodynamics with the ions dynamics to understand the interplay between hydrodynamic and electrokinetic effects. We simulate with boundaries bearing an imposed surface charge at the solid-liquid interface. We introduce the theory and algorithm behind the method and validate our modification with known analytical results with or without added salt.

In Chapter 3 we extend the moment propagation method for the sorption dynamics to the case of charged tracers. We introduce the theory and validate our results with analytical results for simple geometries and with previous works available in the literature^[113,114].

In Chapter 4 we change the boundary conditions at the solid-liquid interface to simulate nano-capacitors, which is the common device in the experiments described in this Introduction. As previously we impose a surface charge density on the electrodes and then extend the algorithm to simulate an applied constant potential difference between the two electrodes. This is closer to the experimental reality and allows us to study more in details the charge at the electrode. We derive and validate the modifications with analytical results in simple geometries.

Introduction

In Chapter 5 we study the charge response at the electrode under a perturbing potential and how it evolves during the transient regime. This temporal response can be linked to the underlying fluctuations using linear response theory.

In Chapter 6 we test linear response theory on our LB method, in the context of ion diffusion in a box of simulation, allowing us to analyse the finite size effects due to periodic boundary conditions in the transient regime.

Finally in the **General Conclusion** chapter we summarize the main achievements of this PhD and discuss what could be done in the future, in the context of fluctuations, and to extend the approach to more complex problems.

*"A method is more important than a discovery, since the right method will lead to
new and even more important discoveries"*
- Lev Landau

Lattice Boltzmann Electrokinetics

Contents

2.1	Governing Equations	21
2.1.1	Poisson-Nernst-Planck	21
2.1.2	Navier-Stokes	23
2.1.3	Discussion	24
2.2	Lattice Boltzmann	24
2.2.1	Kinetic theory	25
2.2.2	Boltzmann equation	26
2.2.3	BGK approximation	26
2.2.4	Equilibrium distribution	26
2.2.5	Conservation of Mass	27
2.2.6	Conservation of Momentum	27
2.2.7	Stress tensor	28
2.2.8	Lattice Boltzmann Equation	28
2.2.9	Algorithm	31
2.2.10	Boundaries	31
2.2.11	Concluding remarks and summary of the method	33
2.3	Link-flux method	33
2.3.1	Solute transport: diffusion-migration	33
2.3.2	Solute transport: advection	35
2.3.3	Solute transport: force on the fluid	35
2.3.4	Solute transport: electrostatic potential	36
2.3.5	Solute transport: boundary conditions	36
2.4	Summary of the algorithm	36
2.5	Results	37
2.5.1	Poiseuille Flow	37
2.5.1.1	Slit pore	37
2.5.1.2	Cylindrical pore	39
2.5.2	Poisson-Boltzmann theory	41
2.5.2.1	Slit pore	43
2.5.2.2	Cylindrical pore	49
2.5.2.3	Effect of PBCs	53
2.5.3	Electro-osmotic flow	55
2.5.3.1	Microscopic origin and Helmholtz-Smoluchowski theory	55
2.5.3.2	Slit pore	56
2.5.3.3	Cylindrical pore	58
2.6	Conclusion	60

IN this chapter we ought to present the Lattice Boltzmann Electrokinetics (LBE) method and the underlying theory to validate its implementation in a code by comparison with analytical results in simple geometries. In order to do that we consider the electrokinetic transport of a confined fluid, which bears a surface charge at the solid interface. We consider here two types of geometries: slit and cylindrical. The governing equations at the continuous level of description, namely the Poisson-Nernst Planck (PNP) and Navier-Stokes (NS) equations, are presented in Section 2.1. Analytical solutions may be recovered (see Section 2.5) both when no salt is added, meaning that only counterions are present, and in the presence of salt but in low potential condition, in which case a linearization of PNP is possible. The first solution is exact and is thus needed in order to validate the Lattice Boltzmann electrokinetics algorithm (LBE). LBE works also in the non-linear regime, *i.e.* in the high potential regime. Section 2.2 shows how the macroscopic NS equation is recovered from the Boltzmann equation and how the Lattice Boltzmann algorithm is implemented. Then, Section 2.3 introduces the link-flux algorithm (LF) needed for the coupling with the electrostatic interactions. Finally, Section 2.4 summarizes the main steps of the algorithm and Section 2.5 is the validation of the algorithm by means of known analytical results, which are presented along.

2.1 Governing Equations

The Navier-Stokes (NS) equation, which is required to describe the hydrodynamics of the system, has to be coupled with the Poisson-Nernst-Planck (PNP) equation, in order to include electrokinetic effects. More specifically, we consider a fluid confined in a certain region, which is bounded by solid walls, constituting the interface. The system studied is then made of two parts.

The first is a non-mobile solid phase, which could represent a porous material saturated by water. Clays are for instance common examples. Besides, when solid phases are in contact with electrolytes, electric charges may appear at the surface. This electric charge is partly screened by the counterions present in the liquid phase, which adsorb at the interface, forming the so-called Stern layer. For the time being we neglect adsorption-desorption phenomena as well as any diffusion in this layer. Thus, the solid phase possesses a surface charge density $\sigma(\mathbf{r})$ ($e m^{-2}$, where e is the electric charge), for all \mathbf{r} in the solid part. We consider that the surface does not change with time.

The second part is made of a liquid phase, in other words the electrolyte, which is made of dissociated ionic species in a continuous solvent with permittivity $\varepsilon = \varepsilon_r \varepsilon_0$, where ε_r is the relative permittivity and ε_0 is the permittivity in vacuum. The fluid viscosity η and temperature T are assumed to be uniform. The ionic species are point-like particles with charge $q_k = z_k e$ and valence z_k . Hence, no excluded volume effects are considered. Likewise, water molecule deformation, due to electrostatic interactions are also neglected. Finally, no chemical reaction is taken into consideration.

2.1.1 Poisson-Nernst-Planck

The Nernst-Planck Equation is a conservation of mass equation that describes the influence of an ionic concentration gradient and that of an electric field on the flux of chemical species,

Chapter 2. Lattice Boltzmann Electrokinetics

specifically ions. Starting from the conservation of mass equation and considering an incompressible fluid, *i.e.* $\nabla \cdot \mathbf{u} = 0$, where \mathbf{u} is the fluid velocity, we have for each species k ,

$$\frac{D\rho_k}{Dt} + \nabla \cdot \mathbf{j}_k = 0 \quad (2.1)$$

where $\frac{D(\cdot)}{Dt} = \frac{\partial(\cdot)}{\partial t} + \mathbf{u} \cdot \nabla(\cdot)$ is the material derivative; ρ_k and \mathbf{j}_k are the ionic concentration and the flux, respectively. Thus, the equation becomes:

$$\frac{\partial\rho_k}{\partial t} + \mathbf{u} \cdot \nabla\rho_k + \nabla \cdot \mathbf{j}_k = 0. \quad (2.2)$$

$\mathbf{u} \cdot \nabla\rho_k$ represents the advection term. The flux for the Nernst-Planck equation is usually expressed as:

$$\mathbf{j}_k = -M_k\rho_k\nabla\mu_k, \quad (2.3)$$

with M_k the mobility and where the local electrochemical potential μ_k is the sum of an ideal term and an excess term:

$$\mu_k = k_B T \ln(\rho_k/\rho_k^0) + \mu_k^{\text{ex}}, \quad (2.4)$$

where ρ_k^0 is the concentration of reference. The excess part is written as an electrostatic term:

$$\mu_k^{\text{ex}} = z_k e \psi, \quad (2.5)$$

where e is the elementary charge and ψ the electrostatic potential. The electrochemical potential gradient is given by:

$$\nabla\mu_k = \frac{k_B T}{\rho_k} \nabla\rho_k + z_k e \nabla\psi \quad (2.6)$$

Then the mobility is given by the Einstein's relation

$$M_k = \frac{D_k}{k_B T}, \quad (2.7)$$

where D_k denotes the diffusion coefficient of the k -th ionic species and k_B and T denote the Boltzmann constant and the temperature respectively. The flux can therefore be expressed as:

$$\mathbf{j}_k = -D_k \left(\nabla\rho_k + \frac{z_k e}{k_B T} \rho_k \nabla\psi \right). \quad (2.8)$$

The first term on the right hand side of Eq. 2.8 is the flux due to diffusion (Fick's law), whilst the second term is the flux due to electromigration. Plugging this expression in Eq. 2.1 we obtain the Nernst-Planck Equation for a dilute solution, *i.e.*

$$\boxed{\frac{\partial\rho_k}{\partial t} + \mathbf{u} \cdot \nabla\rho_k + \nabla \cdot \left[-D_k \left(\nabla\rho_k + \frac{z_k e}{k_B T} \rho_k \nabla\psi \right) \right]} = 0 \quad (2.9)$$

It is important to notice that Nernst-Planck Equation gives N equations with $N + 1$ unknowns. In order to solve the system of equations one more equation is needed. At the

Chapter 2. Lattice Boltzmann Electrokinetics

mean field level this can be achieved describing the electrostatic potential via the Poisson Equation

$$\rho_f = \nabla \cdot \mathbf{D} \quad (2.10)$$

ρ_f is the free charge density and \mathbf{D} is the electric displacement. For a linear dielectric material we can express \mathbf{D} as

$$\mathbf{D} = \varepsilon \mathbf{E} \quad (2.11)$$

where $\varepsilon = \varepsilon_r \varepsilon_0$ is the permittivity of the material, in this case the solvent. \mathbf{E} is the electric field generated by the charges present within the system. We may then write $\mathbf{E} = -\nabla\psi$. Thus,

$$\mathbf{D} = -\varepsilon \nabla\psi \quad (2.12)$$

Plugging this expression in the Poisson equation

$$\rho_f = -\nabla \cdot (\varepsilon \nabla\psi) = -\varepsilon \Delta\psi \quad (2.13)$$

if the permittivity is uniform. Using a mean field approximation, the free charge density can be defined in terms of the local ion concentrations

$$\rho_f(\mathbf{r}) = \sum_{i=1}^N z_k e \rho_k(\mathbf{r}). \quad (2.14)$$

Therefore, the PNP equations are written

$$\boxed{\begin{cases} \frac{\partial \rho_k}{\partial t} + \mathbf{u} \cdot \nabla \rho_k - \nabla \cdot \left[D_k \left(\nabla \rho_k + \frac{z_k e}{k_B T} \rho_k \nabla \psi \right) \right] = 0 \\ \varepsilon \Delta \psi = -\rho_f = -\sum_{i=1}^N z_k e \rho_k \end{cases}} \quad (2.15)$$

the system has identical number of equations and unknowns.

2.1.2 Navier-Stokes

The fluid considered is a binary electrolyte (1:1) diluted in a solvent, *i.e.* an aqueous solution with a monovalent salt (*e.g.* KCl, NaCl...). We consider only flows at low Reynolds (Re) number, which can be perturbed by external constraints such as a pressure gradient or an external electric field. The solvent velocity $\mathbf{u}(\mathbf{r}, t)$, as shown in Eq. 2.15, is then computed using NS equation

$$\boxed{\rho \left(\frac{\partial \mathbf{u}}{\partial t} + \mathbf{u} \cdot \nabla \mathbf{u} \right) = \eta \nabla^2 \mathbf{u} - \sum_k \rho_k \nabla \mu_k + \mathbf{f}_V^{\text{ext}}} \quad (2.16)$$

where η is the viscosity, ρ the fluid density, $\mathbf{f}_V^{\text{ext}}$ is the external force density and where the second term on the right-hand side corresponds to the thermodynamic force, which is expressed from the pressure gradient using the Gibbs-Duhem equation.

Using the excess part of Eq. 2.4 with the contribution of the external force we recover the usual electric force density $e(\sum_k z_k \rho_k)(\mathbf{E}_{app} - \nabla\psi)$, where \mathbf{E}_{app} is an applied external electric field.

At equilibrium, the Gibbs-Duhem equation at constant pressure and temperature reads

$$\sum_{k=1}^N \rho_k \nabla \mu_k = 0 \quad (2.17)$$

The force density \mathbf{f}_v^{int} imposed by the solutes on the fluid is computed according to

$$\mathbf{f}_v^{int} = - \sum_{k=1}^N \rho_k \nabla \mu_k^{ex} \quad (2.18)$$

This forcing term is responsible for the coupling between the ions and the solvent dynamics, together with the advection of the ions (*i.e.* $\mathbf{u} \cdot \nabla \rho_k$ in Eq. 2.15).

2.1.3 Discussion

Therefore, Eq. 2.15 and Eq. 2.16 are the governing equations for our system. The model is thus limited by the prior assumptions of NS and PNP. They are indeed both continuous equations, which cannot resolve the molecular details of the system. Nonetheless, NS was shown^[9] to hold down to length scales of the order of 1 *nm*. On the other hand, PNP relies on a mean field approach meaning that all quantities are averaged and thus ionic correlations are not taken into account. Furthermore, since the theory was derived considering point-like charges for ions, excluded volume effects are neglected, so that the description of the system breaks down at high concentrations. Similarly, excluded volume effects taking place at the solid-liquid interface are neglected.

As described in the introduction, a good candidate to solve numerically NS-PNP is the Lattice Boltzmann Electrokinetics (LBE). The LBE scheme couples the Lattice Boltzmann method (LB), which takes care of the hydrodynamics of the problem, with the link-flux (LF) method, which tackles the electrostatic interactions. During this thesis we have further developed an existing code called *Laboetie*, which prior to this work included only the Lattice Boltzmann part. Thus no electrostatic interactions were involved in the calculations. LBE codes have been previously developed (*e.g.* 115 and 116), hence our first aim was to recover previous known analytical and numerical results in order to validate this part. In the next two sections I introduce the theory behind LB and LF and how they are implemented.

2.2 Lattice Boltzmann

The Lattice Boltzmann Method is a grid based method with spacing Δx and time step Δt . In contrast to the traditional numerical schemes such as finite difference method (FDM), finite volume method (FVM), finite element method (FEM) or spectral element methods (SEM), which are based on the discretization of macroscopic continuum equations, the LB method is rooted in microscopic models and mesoscopic kinetic equations. Mesoscopic models, and notably those arising from kinetic theory such as LB, are natural candidates for intermediate

scales between the atomistic and continuum levels as they are computationally inexpensive when compared to Molecular Dynamics (MD) simulations.

The LB method was initially developed as an extension of the lattice gas automaton (LGA), which was proposed by Pommeau, Hasslacher, Frisch and Wolfram^[117,118]. Their idea was to create a very simplistic MD model which evolves on a two-dimensional triangular lattice. Particles move from one site to another in discrete time steps. The LGA could then be a form of MD with structureless particles with perfect conservation laws and could even process basic symmetries to simulate hydrodynamics. However, the method presented some shortcomings as the simulations are very noisy due to large fluctuations of particles, forcing a spatial and temporal average in order to obtain statistically converged results. One way to overcome these shortcomings is to leave the boolean world of LGA and work at the level of continuous probabilities. The LB method is indeed an algorithm based on a discretized kinetic equation.

2.2.1 Kinetic theory

In this section we show how the macroscopic NS equation is recovered from the Boltzmann equation. Generally speaking, it is possible to view a fluid in a statistical physics framework, by considering a quantity $f(\mathbf{r}, \mathbf{v}, t) d\mathbf{r} d\mathbf{v}$, at a specific time t , located in a volume $d\mathbf{r} = dx dy dz$, which surrounds the position $\mathbf{r} = [x, y, z]$ with a velocity, within $d\mathbf{v} = dv_x dv_y dv_z$, of $\mathbf{v} = [v_x, v_y, v_z]$. Both \mathbf{r} and \mathbf{v} are independent variables, and the ensemble-averaged hydrodynamic variables are derived from the distribution function $f(\mathbf{r}, \mathbf{v}, t)$ by integrating over all possible velocities, *i.e.* the local mass density is obtained as:

$$\rho(\mathbf{r}, t) := \iiint f(\mathbf{r}, \mathbf{v}, t) d\mathbf{v}. \quad (2.1)$$

The notation $\iiint(\dots)d\mathbf{v}$ corresponds to the definite integral $\iiint_{-\infty}^{\infty}(\dots)dv_x dv_y dv_z$. We shall now use index notation and adopt the Einstein summation convention of implicit summation over repeated indices. The local average velocity is obtained using

$$u_\alpha(\mathbf{r}, t) := \frac{1}{\rho(\mathbf{r}, t)} \iiint v_\alpha f(\mathbf{r}, \mathbf{v}, t) d\mathbf{v}, \quad (2.2)$$

and the internal energy density

$$\frac{3}{2}\rho(\mathbf{r}, t)U^2(\mathbf{r}, t) := \iiint \frac{1}{2}|\mathbf{v} - \mathbf{u}(\mathbf{r}, t)|^2 f(\mathbf{r}, \mathbf{v}, t) d\mathbf{v}, \quad (2.3)$$

with $U^2(\mathbf{r}, t) = k_B T(\mathbf{r}, t)/m$ and where the factor 3/2 is due to the three dimensions of the physical space. In 2D it would be 2/2 and 1/2 in 1D. The velocity in Eq. 2.3 is the thermal agitation velocity. The total energy density reads

$$\rho(\mathbf{r}, t)E_{\text{tot}}(\mathbf{r}, t) := \iiint \frac{1}{2}|\mathbf{v}|^2 f(\mathbf{r}, \mathbf{v}, t) d\mathbf{v} = \frac{1}{2}\rho(\mathbf{r}, t)|\mathbf{u}(\mathbf{r}, t)|^2 + \frac{3}{2}\rho(\mathbf{r}, t)U^2(\mathbf{r}, t), \quad (2.4)$$

The right hand side of the equation was obtained using Eq. 2.2 and Eq. 2.3, as well as the identity $|\mathbf{v} - \mathbf{u}|^2 = |\mathbf{v}|^2 - 2\mathbf{v} \cdot \mathbf{u} + |\mathbf{u}|^2$. The energy flux may be computed using

$$q_\alpha(\mathbf{r}, t) := \iiint \frac{1}{2}|\mathbf{v} - \mathbf{u}(\mathbf{r}, t)|^2 (v_\alpha - u_\alpha(\mathbf{r}, t)) f(\mathbf{r}, \mathbf{v}, t) d\mathbf{v} \quad (2.5)$$

Finally the stress tensor is written as

$$\Pi_{\alpha\beta}(\mathbf{r}, t) := \iiint (v_\alpha - u_\alpha(\mathbf{r}, t))(v_\beta - u_\beta(\mathbf{r}, t)) f(\mathbf{r}, \mathbf{v}, t) d\mathbf{v} \quad (2.6)$$

2.2.2 Boltzmann equation

The temporal evolution of the mass probability distribution is given by the Boltzmann equation

$$\frac{\partial f}{\partial t} + v_\alpha \frac{\partial f}{\partial x_\alpha} + \frac{F_\alpha}{m} \frac{\partial f}{\partial v_\alpha} = \mathcal{C}(f) \quad (2.7)$$

where F_α are the components of an external force applied upon the fluid, m is the mass of the fluid particles and $\mathcal{C}(f)$ is called the collision operator. Eq. 2.7 means that f is advected in physical space by the particle velocities. On the other hand, its velocity space is modified by the acceleration term and redistributed by the collision operator.

2.2.3 BGK approximation

A possible solution for Eq. 2.7 was carried out in 1959 by Bhatnagar, Gross and Krook, who noticed that the main effect of the collision term is to bring the velocity distribution function closer to the equilibrium distribution f^{eq} . They proposed to approximate the collision kernel as:

$$\mathcal{C}(f) = \frac{1}{\tau} (f^{eq} - f) \quad (2.8)$$

This is the so-called BGK formulation^[119], where τ represents the relaxation time. Introducing Eq. 2.7 in Eq. 2.8 we obtain the Boltzmann-BGK equation

$$\boxed{\frac{\partial f}{\partial t} + v_\alpha \frac{\partial f}{\partial x_\alpha} + a_\alpha \frac{\partial f}{\partial v_\alpha} = \frac{1}{\tau} (f^{eq} - f)} \quad (2.9)$$

with $a_\alpha = F_\alpha/m$ the acceleration. We shall now discuss more in details which equilibrium solution is best for the purpose of our analysis.

2.2.4 Equilibrium distribution

Ludwig Boltzmann^[120] considered gas particles to be animated by Brownian motion and contributed to the derivation of the Maxwell-Boltzmann distribution f^{eq} written as:

$$f^{eq}(\mathbf{r}, \mathbf{v}, t) = \frac{\rho(\mathbf{r}, t)}{(2\pi)^{3/2} U^3(\mathbf{r}, t)} \exp\left(-\frac{|\mathbf{v} - \mathbf{u}(\mathbf{r}, t)|^2}{2U^2(\mathbf{r}, t)}\right) \quad (2.10)$$

which is merely a Gaussian distribution of velocities v_α centred in their averages u_α with standard deviation U . In order to ensure that the collision operator conserves mass, momentum and energy, f^{eq} must obey to Eq. 2.1, 2.2 and 2.3. The Maxwell-Boltzmann distribution satisfies these conditions.

Conservation of mass, momentum and energy can be derived using zeroth, first and second moments of the Boltzmann-BGK Equation respectively.

2.2.5 Conservation of Mass

Mass conservation is obtained by considering the zeroth moment of Eq. 2.9, *i.e.* integrating over the velocity space

$$\iiint \left\{ \frac{\partial f}{\partial t} + v_\alpha \frac{\partial f}{\partial x_\alpha} + a_\alpha \frac{\partial f}{\partial v_\alpha} \right\} d\mathbf{v} = \iiint \left\{ \frac{1}{\tau} (f^{eq} - f) \right\} d\mathbf{v} \quad (2.11)$$

Temporal and spatial derivatives are independent variables and thus commute with the velocity integrations. Furthermore, because of the integrability of f we have $f \rightarrow 0$ as $v_\alpha \rightarrow \pm\infty$ and thus the acceleration term (*e.g.* gravity) cancels out. Moreover, both distributions f and f^{eq} satisfy Eq. 2.1. Therefore the integral of $f^{eq} - f$ vanishes, meaning that collisions conserve mass. Then, using Eq. 2.1 and 2.2, Eq. 2.11 reduces to

$$\boxed{\frac{\partial \rho}{\partial t} + \frac{\partial}{\partial x_\alpha} (\rho u_\alpha) = 0} \quad (2.12)$$

which is the continuity equation.

2.2.6 Conservation of Momentum

First order moments of Eq. 2.9 leads to the momentum equations, *i.e.*

$$\iiint v_\beta \left\{ \frac{\partial f}{\partial t} + v_\alpha \frac{\partial f}{\partial x_\alpha} + a_\alpha \frac{\partial f}{\partial v_\alpha} \right\} d\mathbf{v} = \iiint v_\beta \left\{ \frac{1}{\tau} (f^{eq} - f) \right\} d\mathbf{v} \quad (2.13)$$

Expanding the term $v_\alpha v_\beta$ as:

$$v_\alpha v_\beta = (v_\alpha - u_\alpha)(v_\beta - u_\beta) + v_\alpha u_\beta + v_\beta u_\alpha - u_\alpha u_\beta, \quad (2.14)$$

the advective term is then written as:

$$\begin{aligned} \frac{\partial}{\partial x_\alpha} \iiint v_\alpha v_\beta f d\mathbf{v} &= \frac{\partial}{\partial x_\alpha} \iiint (v_\alpha - u_\alpha)(v_\beta - u_\beta) f d\mathbf{v} \\ &+ \frac{\partial}{\partial x_\alpha} \iiint (v_\alpha u_\beta + v_\beta u_\alpha - u_\alpha u_\beta) f d\mathbf{v} \end{aligned} \quad (2.15)$$

The first term on the right-hand side may be recognized as the stress tensor, *i.e.* $\Pi_{\alpha\beta}$, whereas the second term corresponds to $\rho u_\alpha u_\beta$. The acceleration term is computed using $v_\alpha \frac{\partial f}{\partial v_\alpha} = \frac{\partial(v_\alpha f)}{\partial v_\alpha} - f$ and the fact that $v_\alpha f \rightarrow 0$ as $v_\alpha \rightarrow \pm\infty$. Since collisions conserve momentum, the distributions satisfy Eq. 2.2 and thus the term $f^{eq} - f$ vanishes. Plugging Eq. 2.15 in Eq. 2.13 gives the Cauchy momentum equation

$$\boxed{\frac{\partial}{\partial t} (\rho u_\beta) + \frac{\partial}{\partial x_\alpha} (\rho u_\alpha u_\beta) + \frac{\partial \Pi_{\alpha\beta}}{\partial x_\alpha} = \rho a_\alpha} \quad (2.16)$$

2.2.7 Stress tensor

Assuming a short relaxation time τ , the stress tensor can be derived using a Chapman-Enskog expansion. However, since this proof is not the main goal of this PhD thesis, we shall send the reader to the following references for the mathematical details^[121–125]. Introducing the ideal gas pressure $p = \rho U^2$ the stress tensor may be written as:

$$\Pi_{\alpha\beta} = p\delta_{\alpha\beta} + \tau_{\alpha\beta} \quad (2.17)$$

where $\tau_{\alpha\beta}$ corresponds to the deviatoric component of the stress tensor.

The deviatoric stress tensor or shear stress tensor can be further evaluated in order to recover a more classical form, *i.e.*

$$\tau_{\alpha\beta} = \rho\tau U^2 \left[\left(\frac{\partial u_\alpha}{\partial x_\beta} + \frac{\partial u_\beta}{\partial x_\alpha} \right) - \frac{2}{3} \left(\frac{\partial u_\gamma}{\partial x_\gamma} \right) \delta_{\alpha\beta} \right] \quad (2.18)$$

which is the constitutive equation for a compressible Newtonian fluid with viscosity

$$\eta = \rho\tau U^2 = \rho U \lambda \quad (2.19)$$

where λ is the mean free path. Plugging Eq. 2.18 and 2.19 in Eq. 2.16 we recover the compressible flow Navier-Stokes (NS) equation. Therefore the NS equation can be derived from the Boltzmann equation.

The Boltzmann equation can thus correctly describe Newtonian hydrodynamics. If an incompressible fluid without thermal fluctuations is considered it is necessary to impose two closing relations on the pressure p and on the kinematic viscosity $\nu = \eta/\rho$

$$p = \rho c_s^2 \quad \text{and} \quad \nu = \tau c_s^2 \quad (2.20)$$

with c_s denoting the speed of sound in the fluid. The first relation corresponds to the equation of state for a perfect gas.

2.2.8 Lattice Boltzmann Equation

The time discretisation is done introducing the time step Δt . This allows us to discretize the Boltzmann equation using the BGK approximation:

$$f(\mathbf{r} + \mathbf{v}\Delta t, \mathbf{v}, t + \Delta t) = f(\mathbf{r}, \mathbf{v}, t) + \frac{\Delta t}{\tau} [f^{eq}(\mathbf{r}, \mathbf{v}, t) - f(\mathbf{r}, \mathbf{v}, t)] \quad (2.21)$$

From this, a numerical scheme can be devised with a precision of Δt^2 . Furthermore, a discretization in space is done via an evenly spaced grid, often cubic. Particles then move from a node to another during the time step Δt . Each node is separated by a lattice spacing Δx and the lattice velocity is thus obtained using $|\mathbf{v}| = \Delta x/\Delta t$. Nodes can either have a solid or a fluid nature. There have been other LB algorithms developed with irregular meshes, but since it is not the case of the Laboetie code we shall refer the reader to Ref. 126. Finally the velocity space is discretized to a finite number of velocity vectors \mathbf{c}_i such that $\mathbf{r} + \mathbf{c}_i\Delta t$ is always a lattice position. The choice of velocities needs to ensure that the isotropy given by the Boltzmann equation is conserved.

Chapter 2. Lattice Boltzmann Electrokinetics

The equilibrium distribution f^{eq} can be expressed with Hermite polynomials $H_n(x) = (-1)^n e^{x^2} \partial_x^n e^{-x^2}$, which form an orthonormal basis for the functions space with an expansion up to order m . The equilibrium distribution then reads:

$$f^{\text{eq}}(\mathbf{r}, \mathbf{u}, t) = \frac{\rho(\mathbf{r}, t)}{(2\pi c_s^2)^{\frac{3}{2}}} \exp\left(-\frac{|\mathbf{v}|^2}{2c_s^2}\right) \prod_{\alpha=x,y,z} \left[\sum_{n=0}^m \frac{1}{n!} \left(\frac{u_\alpha}{c_s}\right)^n H_n(v_\alpha) \right]. \quad (2.22)$$

This corresponds to a development of the velocity dependence at low Mach (Ma) number $|\mathbf{u}|/c_s$. Without loss of generality, a non-zero moment M_k reads

$$\begin{aligned} M_k &= \int v_x^{k_x} v_y^{k_y} v_z^{k_z} f^{\text{eq}} d\mathbf{u} \\ &= \frac{\rho}{(2\pi c_s^2)^{\frac{3}{2}}} \prod_{\alpha=x,y,z} \left[\sum_{n=0}^m \frac{1}{n!} \left(\frac{u_\alpha}{c_s}\right)^n \int v_\alpha^{k_\alpha} \exp\left(-\frac{v_\alpha^2}{2c_s^2}\right) H_n(v_\alpha) dv \right] \end{aligned} \quad (2.23)$$

where $m \geq \max(k_x, k_y, k_z)$. The integrals can be evaluated using a finite number of velocities as Gaussian-Hermite quadrature, which computes the integral with a sum

$$\sum_{k=0}^{n_q-1} w_k^{m_\alpha} H_{n_q}(\xi_k), \quad (2.24)$$

where ξ_k are the roots of $H_{n_q}(\xi_k) = 0$ and n_q are their corresponding number, which have corresponding weights

$$w_k = \frac{2^{n_q-1} n_q! \sqrt{\pi}}{n_q^2 H_{n_q-1}(\xi_k)} \quad (2.25)$$

of the quadrature. From these roots the discretized weights can be obtained

$$w_i = \frac{1}{(2\pi)^{3/2}} w_{i_x} w_{i_y} w_{i_z} \exp\left(-\frac{|\mathbf{c}_i|^2}{2c_s^2}\right) \quad (2.26)$$

where $\mathbf{c}_i = (\xi_{i_x}, \xi_{i_y}, \xi_{i_z})$ is a discretized velocity. The number of discretized velocities depends on the chosen model. The velocity of sound in the D3Q19 model is written in LB units as:

$$c_s = \frac{1}{\sqrt{3}} \frac{\Delta x}{\Delta t} \quad (2.27)$$

Let $f_i(\mathbf{r}, t) := w_i f(\mathbf{r}, \mathbf{c}_i, t)$, called the populations, then Eq. 2.21 may be rearranged as

$$f_i(\mathbf{r} + \mathbf{c}_i \Delta t, t + \Delta t) = f_i(\mathbf{r}, t) - \frac{\Delta t}{\tau} [f_i(\mathbf{r}, t) - f_i^{\text{eq}}(\mathbf{r}, t)] + F_i(\mathbf{r}) \quad (2.28)$$

The term F_i takes into account the action of an external force \mathbf{F} , as well as the internal forces described by the Gibbs-Duhem equation (see Eq. 2.17). The forcing term satisfies $\sum_i F_i = 0$ and $\sum_i \mathbf{c}_i F_i = \mathbf{F}$.

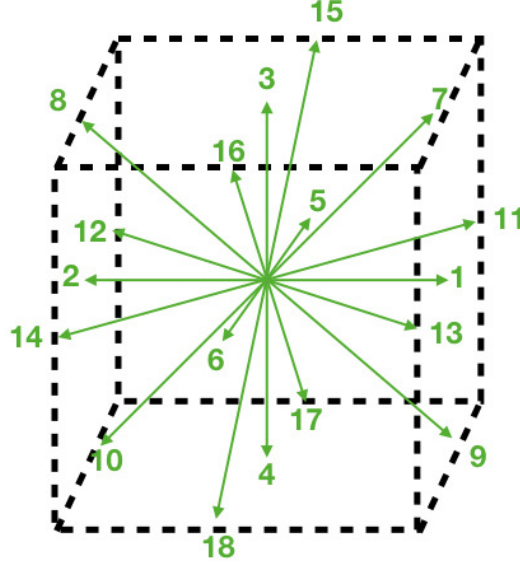


Figure 2.1 – D3Q19 model

The equilibrium distribution for the D3Q19 model (which is a 3D model including 19 different velocities, as shown in Fig. 2.1) which corresponds to a quadrature with $n_q = 3$ and a truncation at order $m = 2$ reads

$$f_i^{eq} = \rho w_i \left[1 + \frac{\mathbf{u} \cdot \mathbf{c}_i}{c_s^2} + \frac{(\mathbf{u} \cdot \mathbf{c}_i)^2}{2c_s^4} - \frac{\mathbf{u} \cdot \mathbf{u}}{2c_s^2} \right] \quad (2.29)$$

the velocities $\mathbf{c}_i = \Delta x / \Delta t$ for the D3Q19 model are

$$|\mathbf{c}_i| = \begin{cases} 0 & \text{for } i = 0 \\ c & \text{for } i = 1 - 6 \\ \sqrt{2}c & \text{for } i = 7 - 18 \end{cases} \quad (2.30)$$

Their corresponding weights w_i are

$$w_i = \begin{cases} 1/3 & i = 0 \\ 1/18 & i = 1 - 6 \\ 1/36 & i = 7 - 18 \end{cases} \quad (2.31)$$

The D3Q19 proved to be a good compromise in terms of computational cost and accuracy and was thus chosen for the purpose of this thesis. The macroscopic quantities are then recovered with

$$\rho(\mathbf{r}, t) = \sum_i f_i(\mathbf{r}, t) \quad (2.32)$$

$$\rho \mathbf{u}(\mathbf{r}, t) = \sum_i \mathbf{c}_i f_i(\mathbf{r}, t), \quad (2.33)$$

2.2.9 Algorithm

Let us define $\tilde{f}_i(\mathbf{r}, t)$ as:

$$\tilde{f}_i(\mathbf{r}, t) := f_i(\mathbf{r}, t) - \frac{\Delta t}{\tau} [f_i(\mathbf{r}, t) - f_i^{\text{eq}}(\mathbf{r}, t)] + F_i(\mathbf{r}), \quad (2.34)$$

which correspond to the populations after the collision step. We consider $\tau = \Delta t$. Then, the propagation step moves particles along the nodes as

$$f_i(\mathbf{r} + \mathbf{c}_i \Delta t, t + \Delta t) = \tilde{f}_i(\mathbf{r}, t) \quad (2.35)$$

The algorithm, may be summarised as follows:

- Set appropriate fluid velocities $\mathbf{u}(\mathbf{r}, t)$ and densities $\rho(\mathbf{r}, t)$ at each lattice site.
- Calculate equilibrium densities f_i^{eq} ($i = 0, 1, \dots, 18$) at each lattice site from Eq. 2.29 and regard these distributions as the initial distributions $f_i = f_i^{\text{eq}}$ ($i = 0, 1, \dots, 18$).
- Collision step: compute \tilde{f}_i using Eq. 2.34.
- Streaming step: update the distribution at the neighbouring site in the i -direction $f_i(\mathbf{r} + \mathbf{c}_i \Delta t, t + \Delta t)$ as \tilde{f}_i .
- Calculate the macroscopic densities and velocities using $\rho(\mathbf{r}, t) = \sum_i f_i(\mathbf{r}, t)$ and $\rho(\mathbf{r}, t)\mathbf{u}(\mathbf{r}, t) = \sum_i f_i(\mathbf{r}, t)\mathbf{c}_i$, and repeat the procedure from the second step.

Convergence is finally reached when

$$\max_{\mathbf{r}} (|j_{\alpha}^{t+1} - j_{\alpha}^t|) < C \quad (2.36)$$

where j is the mass flux in the x , y or z -direction and C is the convergence criterion which is set by the user.

2.2.10 Boundaries

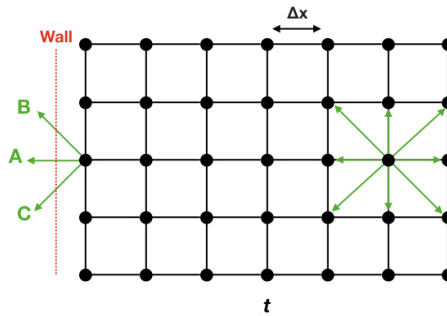


Figure 2.2 – Bounce-Back step

A final key factor is boundaries, as we are interested in modelling confined fluids. No-slip boundary conditions are often adopted when dealing with walls, even though slip velocities may be present for very small pores ($\sim 1 \text{ nm}$). Nonetheless, as we are interested in larger

systems, up to 100 nm, we shall not consider such effects. The simplest yet efficient way to implement such a boundary is to draw the boundary and then mark all links that are cut by this boundary. As mentioned earlier the LB is a grid-based method and thus the nodes have either a fluid or a solid nature. In early implementations of LB, the interface was merely drawn on the lattice nodes and the method was called the fullway bounce back rule. The densities that were streamed into the solid were bounced-back during the collision step, at time t instead of being streamed from a node to another.

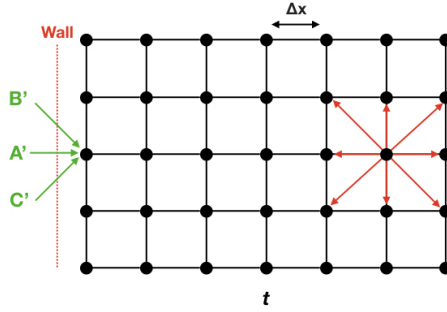


Figure 2.3 – Collision step

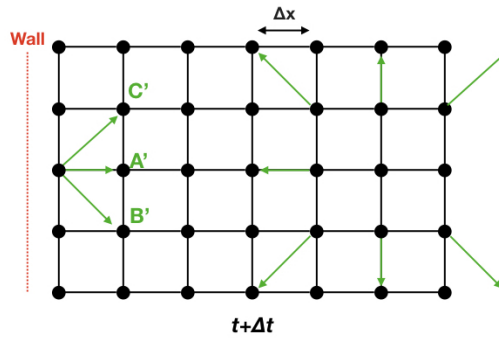


Figure 2.4 – Streaming step

The information was then passed to the bulk during the streaming step, after which the time was increased by Δt . Thus, we have

$$f_i(\mathbf{r}, t + \Delta t) = f_{-i}(\mathbf{r}, t) \quad (2.37)$$

where the velocity index $-i$ is defined through $\mathbf{c}_{-i} = -\mathbf{c}_i$. Mass is conserved by the bounce-back rule, whereas energy and stress tensor $\Pi = \sum_i \mathbf{c}_i \mathbf{c}_i f_i$ are related to the second order moment of lattice velocity and cannot be conserved since the unknown distribution functions are modified directly to those in the opposite direction, without taking the conservation of energy into consideration.

The fullway bounce back rule is simple but it achieves only first order spatial accuracy^[127]. This would definitely limit the advantage of LBM, which essentially performs with second order spatial accuracy. In order to obtain the second order accuracy, the halfway bounce back rule was introduced. The idea is that the boundary lies between the nodes so that the wall is placed in the middle of the solid boundary nodes and bulk nodes, as shown in Fig. 2.2. Fig. 2.2 to 2.4 show the three main steps experienced: in the first step densities are streamed

in the solid at time t (Fig. 2.2), they are then bounced-back in the fluid during the same time step (Fig. 2.3) and finally quantities are allowed stream in the other lattice nodes at $t + \Delta t$ (Fig. 2.4).

This approach has been extended to the case of moving boundaries^[128]. However, since we did not need such feature we will not discuss this here.

2.2.11 Concluding remarks and summary of the method

The expansion used to derive the algorithm implies that the LBM is valid only for small velocities, *i.e.* at low Mach number, although it was shown that it can be adapted in order to simulate more complex phenomena such as turbulence for higher speeds^[129]. In most cases, LB is restricted to micro-scale flows with a Knudsen number, $Kn < 0.1$, even though Meghdadi Isfahani *et al.*^[130] proposed a modification of the algorithm in order to extend the ability of LBM to simulate a wider range of Knudsen flow regimes. When comparing with a purely hydrodynamic description, LB offers some advantages such as providing the fluid pressure locally available site by site, with no need of solving a computationally demanding Poisson problem or simply having the momentum diffusion not represented by second-order spatial derivatives; indeed it merely emerges from the first-order LB relaxation-propagation dynamics. As we are interested in more complex fluids, we need to couple the LB method to the thermodynamics of the system via the free energy. Local chemical potential gradients induce fluxes of the various species (see Eq. 2.3), but also forces which drive the fluid (see Eq. 2.16). This can be achieved with the link-flux method.

2.3 Link-flux method

In this part the numerical algorithm used to describe the coupling between the solvent and the ions is presented. This method is coupled with the LB part in order to ensure momentum conservation in the fluid. It also includes the time dependent density functional theory (DFT) in order to take into account the local evolution of the local ionic composition. The version of the LF method used is the one introduced by Capuani *et al.*^[131], which aimed at removing spurious fluxes across the fluid-solid interface, which appeared at steady state in the previous versions of the algorithm^[132], where LB method was directly used in order to model electroviscous transport problems. More specifically, the Stokes equations was obtained from the standard lattice Boltzmann equation, the Smoluchowski equations were computed as a simple extension of the moment propagation method for convective diffusion problems (see Chapter 3), and the Poisson equation was solved on a lattice by a standard finite difference scheme.

2.3.1 Solute transport: diffusion-migration

As we said, the first attempts at coupling the LBM for the solvent dynamics with another algorithm for the ions dynamics were only partly successful. The moment propagation method was developed and coupled with the LBM^[113,132-137] in order to compute statical mechanical quantities (*e.g.* the velocity autocorrelation function) of tracers dispersed in a fluid. We shall discuss more in details this method, which we contributed to improve in Chapter 3. However, the methods which aimed at solving the PNP equation, introduced spurious fluxes from fluid

Chapter 2. Lattice Boltzmann Electrokinetics

to solid nodes which would appear at steady state. In order to solve this problem Capuani *et al.*^[131] developed the link-flux (LF) method, which focuses on the solute fluxes between each node rather than the solutes fluxes at each node. The continuity equation can be written in its integral form:

$$\partial_t \mathcal{N}_k(\mathbf{r}, t) = - \int_{\Omega} \nabla \cdot \mathbf{j}_k(\mathbf{r}, t) d\Omega, \quad (2.38)$$

where $\mathcal{N}_k(\mathbf{r}, t)$ is the number of ions in a cell Ω centered on a node \mathbf{r} and bounded by a surface $\partial\Omega$. Such a cell corresponds to the closest volume to a node rather than another node. The integral is then on all the volume of such cell. The LF method deals with the diffusive and migration fluxes (see Section 2.3.2 for advection). Thus, we have

$$\mathbf{j}_k(\mathbf{r}, t) = -D_k \rho_k \nabla \ln \rho_k - z_k e D_k \rho_k \nabla \psi. \quad (2.39)$$

Thanks to the Green-Ostrogradski theorem we can rewrite the integral in the following manner:

$$\partial_t \mathcal{N}_k(\mathbf{r}, t) = - \oint_{\partial\Omega} \mathbf{j}_k(\mathbf{r}, t) \cdot \mathbf{n} d\Omega, \quad (2.40)$$

where the integral is computed along the cell surface and the unit vector \mathbf{n} is perpendicular to this surface and pointing outside the cell. The integral is here the sum of the ions fluxes leaving the cell. The concentrations are then updated according to the following discretized equation:

$$\frac{\rho_k(\mathbf{r}, t + \Delta t) - \rho_k(\mathbf{r}, t)}{\Delta t} \Delta x^3 = -A_0 \sum_i j_k^i(\mathbf{r}, t). \quad (2.41)$$

The i -index refers to the discrete velocity directions and j_k^i corresponds to the contribution of the i -link between \mathbf{r} and $\mathbf{r} + \mathbf{c}_i \Delta t$ to the flux of species k through the cell surface around node \mathbf{r} . A_0 is a coefficient which depends on the geometry of the lattice. For the D3Q19 model, $A_0 = 1 + 2\sqrt{2}$ (see Ref. 131 for more details). In order to ensure that the ions follow a Boltzmann distribution at equilibrium, the ions fluxes are first rewritten as:

$$\mathbf{j}_k = -D_k e^{-\beta \mu_k^{\text{ex}}} \nabla \left[\rho_k e^{\beta \mu_k^{\text{ex}}} \right]. \quad (2.42)$$

where $\beta := 1/k_B T$. An excess part of the electrochemical potential $\beta \mu_k^{\text{ex}}(\mathbf{r}) = z_k e \psi(\mathbf{r})$ was here introduced. This allows to discretize them in a symmetric way. The fluxes passing through the i -links are computed in the LBE algorithm according to

$$j_k^i(\mathbf{r}) = -d_k \frac{e^{-\beta \mu_k^{\text{ex}}(\mathbf{r})} + e^{-\beta \mu_k^{\text{ex}}(\mathbf{r} + \mathbf{c}_i \Delta t)}}{2} \left[\frac{\rho_k(\mathbf{r} + \mathbf{c}_i \Delta t) e^{\beta \mu_k^{\text{ex}}(\mathbf{r} + \mathbf{c}_i \Delta t)} - \rho_k(\mathbf{r}) e^{\beta \mu_k^{\text{ex}}(\mathbf{r})}}{\Delta_i} \right] \quad (2.43)$$

where $d_k = D_k/A_0$ and $\Delta_i = \|\mathbf{c}_i \Delta t\|$. This symmetric form ensures the solute conservation. Hence, we have $j_k^i(\mathbf{r}) = -j_k^{i'}(\mathbf{r} + \mathbf{c}_i \Delta t)$ between each link, with $\mathbf{c}_{i'}$ denoting the velocity opposed to \mathbf{c}_i . The flux j_k^i is set to zero for the links between liquid and solid nodes. This ensures that solutes are not transported into the solid.

2.3.2 Solute transport: advection

The advective fluxes $\rho_k \mathbf{u}$ are treated separately^[131]. The amount of advected particles is proportional to the overlap between the cell shifted virtually by $\mathbf{u}\Delta t$ and all of the neighbouring cells (see Fig. 2.5). Note that densities used for the diffusive flux computation are modified by the advection which triggers an artificial diffusion. More precisely, the spurious diffusion coefficient due to advection results in

$$D^{\text{ad}} = \frac{1}{2} \sum_{\alpha=x,y,z} u_\alpha (1 - u_\alpha) \quad (2.44)$$

which is written in LB units. By choosing a large diffusion coefficient D_k and a small velocity, this artificial diffusion coefficient D_{ad} is negligible.

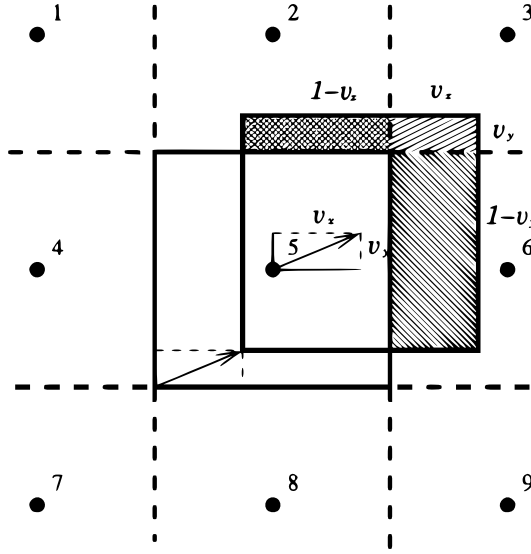


Figure 2.5 – Shifted cell by a velocity v . The quantity of solutes transferred to the neighbouring nodes during a time step Δt is proportional to the intersection between the neighbouring cells as well as the shifted cell. In LB units $\Delta x = \Delta t = 1$ the quantity of transferred solute from node 5 to node 6 during a time step is proportional to $v_x (1 - v_y)$, where v is the speed of the fluid at node 5. The solvent quantity that stays at node 5 is proportional to $(1 - v_x)(1 - v_y)$. The notations differ from ours as the sketch is taken from Ref. 131

2.3.3 Solute transport: force on the fluid

The forcing term given in Eq. 2.18 can be easily computed numerically from the fluxes

$$F_i(\mathbf{r}) = -c_s^2 \Delta t w_i \left[\frac{j_+^i(\mathbf{r})}{d_+} - \frac{\rho_+(\mathbf{r} + \mathbf{c}_i \Delta t) - \rho_+(\mathbf{r})}{\Delta_i} + \frac{j_-^i(\mathbf{r})}{d_-} - \frac{\rho_-(\mathbf{r} + \mathbf{c}_i \Delta t) - \rho_-(\mathbf{r})}{\Delta_i} \right]. \quad (2.45)$$

with j_\pm given by Eq. 2.43. This force has an influence on the fluid dynamics and enters in the LB algorithm as described in Eq. 2.28.

2.3.4 Solute transport: electrostatic potential

The electrostatic potential ψ is computed by means of the charges distribution on the lattice grid, which is obtained solving Poisson equation. This is achieved using the successive over-relaxation (SOR) routine^[138], which is a standard solver similar to a Gauss-Seidel solver. The mathematical details of the method are summarized in Appendix A.1.

The matrix system solved leads to a solution of the Laplacian of ψ , which is computed in the following manner

$$\nabla^2 \psi(\mathbf{r}) = \frac{2}{\Delta t^2} \sum_i \frac{w_i}{c_s^2} [\psi(\mathbf{r} + \mathbf{c}_i \Delta t) - \psi(\mathbf{r})] \quad (2.46)$$

The potential is then updated at each time step in an iterative way. Convergence is finally reached when

$$\sum_{\mathbf{r}} \left| \frac{\psi^{l+1}(\mathbf{r}) - \psi^l(\mathbf{r})}{\psi^l(\mathbf{r})} \right| < C \quad (2.47)$$

for all $\psi > 0$ and where C is a convergence criterion set by the user (typically $C = 10^{-10}$).

2.3.5 Solute transport: boundary conditions

We use periodic boundary conditions (PBC) in the three directions of space. At the solid-liquid interface, boundary conditions need to be specified for the solvent (LB part) and for the ions (LF part). As mentioned before the LB part has no-slip boundary conditions through the bounce-back rule and the LF part requires the ions fluxes penetrating the walls to be canceled (i.e. $j_k^i = 0$).

2.4 Summary of the algorithm

The Lattice Boltzmann Electrokinetics is a hybrid method coupling LB and LF: the dynamics of the solvent is simulated with LB and the one of the ions with LF. In the LB part the distribution function $f_i(\mathbf{r}, t)$ is updated, using Eq. 2.28, in two steps: a collision and a propagation step. The collision operator $\tilde{f}_i(\mathbf{r}, t)$ corresponds to an intermediate distribution function

$$\tilde{f}_i(\mathbf{r}, t) = f_i(\mathbf{r}, t) - \frac{\Delta t}{\tau} (f_i(\mathbf{r}, t) - f_i^{\text{eq}}(\mathbf{r}, t)) + F_i(\mathbf{r}, t). \quad (2.48)$$

This step aims at relaxing the system locally in order to obtain the equilibrium distribution $f_i^{\text{eq}}(\mathbf{r}, t)$ in a time equal to the relaxation time τ . Secondly, fluid particles are moved along the nodes according to

$$f_i(\mathbf{r} + \mathbf{c}_i \Delta t, t + \Delta t) = \tilde{f}_i(\mathbf{r}, t). \quad (2.49)$$

Once the streaming step is over, the particles in \mathbf{r} , which are moving from this node to a neighbouring node $\mathbf{r} + \mathbf{c}_i \Delta t$, conserve the same velocity at the new node after the time step Δt . The distribution function is here modified by the forcing term, which takes into account the force (Eq. 2.45) applied by the ions on the fluid, as well as the applied pressure gradient. The fluid internal forces are computed at each time step from the ions fluxes (Eq. 2.43) between

each link. This requires the ions density to be updated according to Eq. 2.41, taking into account the effects of advection as well as the computation of the new electric potential on all the nodes. The algorithm also requires an initial step whose aim is to bring the solvent and the ions at equilibrium in the absence of external perturbation. Only then, an external pressure gradient or external electric field can be applied.

The LBE algorithm is implemented in the *Laboetie* code via:

1) Definition of the nodes: distinguish solid nodes from fluid nodes in the simulation box. A surface charge is imposed on each interfacial solid node according to the total electric charge of the solid region. A study on the comparison between imposing charges on the surface nodes only, with respect to imposing charges on all the solid nodes, in a cylindrical pore, was carried out by Obliger *et al.*^[139]. See Section 2.5.2.3 for further details.

2) The initial cation and anion concentrations $\rho_k(\mathbf{r}, t = 0)$ are defined. For simplicity they are taken as homogeneous, but a specific profile corresponding to the solution at equilibrium can be used to avoid step 3, if the solution is known previously.

3) Computation of the ion distributions at equilibrium solving iteratively the PNP equation via the SOR algorithm for the potential. The ionic densities are updated at each iteration in LF until all of the ions fluxes vanish. Here no advection is considered. The LB part, which includes the dynamics of the fluid is not yet activated. Once convergence is reached the concentrations and potential correspond to the Poisson-Boltzmann equilibrium.

4) The LB part is initialized by choosing a homogeneous distribution function $f_i(\mathbf{r}, t = 0)$. The LBE algorithm now couples the fluid and the ions dynamics together without imposing external forces. This enable the code to verify whether the ions state of equilibrium is stable. No flux should appear.

5) External forces (*e.g.* ∇P or $\nabla\psi$) are applied. Steady state is reached once the flow no longer evolves according to a convergence criterion.

2.5 Results

The LBE method is available in different open source codes, *e.g.* Ref. 115 and 116. During this PhD an initial part of the work was to implement the LF method and the SOR routine needed to solve the Poisson equation. The *Laboetie* code was initially developed in the PHENIX laboratory by B. Rotenberg and M. Levesque. In order to validate these new parts of the code, comparison with known analytical solutions is necessary. In the next Chapters we shall introduce new features that were added in the code, which are not available in other implementations of LBE. The following sections show the available results in two different geometries: a slit pore and a cylindrical pore.

2.5.1 Poiseuille Flow

2.5.1.1 Slit pore

As a first test of the LBE method as implemented in the code, we verified that even the past features of the code were not corrupted by our modifications. Here we consider the simple case of a Poiseuille flow in a slit pore. A uniform pressure gradient $-dp/dx$ was applied and the resulting flow in the slit is shown in Fig. 2.6.

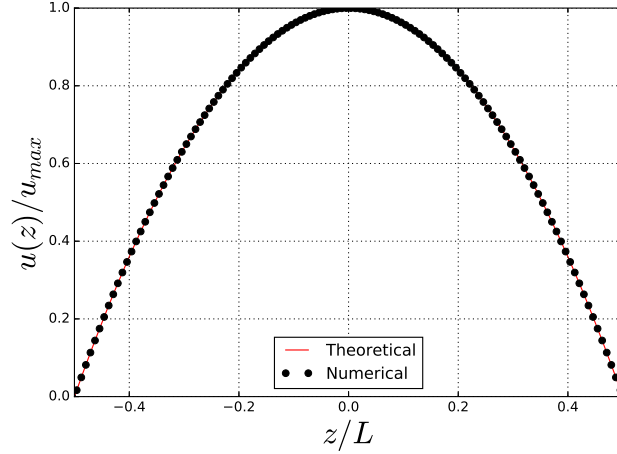


Figure 2.6 – Velocity profile in a slit channel. The flow is induced by a pressure gradient resulting in a Poiseuille flow. The velocity u is normalized with respect to the maximum velocity u_{max} , whereas the position z in the fluid region is normalized with respect to L the distance between the walls.

The analytical solution at steady state, assuming a laminar flow and no-slip boundary conditions at the surfaces is:

$$u_x(z) = -\frac{L^2}{8\eta} \frac{dp}{dx} \left[1 - \left(\frac{2z}{L} \right)^2 \right]. \quad (2.50)$$

The maximum velocity of the fluid is given by

$$u_{max} := -\frac{L^2}{8\eta} \frac{dp}{dx} \quad (2.51)$$

Fig. 2.6 shows the profile of the velocity flow. Here the grid was constructed with $N_z = 126$ nodes and $N_x = N_y = 5$ nodes. The fluid region is made of $N_f = 120$ layers of fluid nodes with three layers of solid nodes on each side (*i.e.* $N_s = 6$ layers of solid nodes). Given a fluid such as water, which has a Bjerrum length $l_B = 0.7 \text{ nm}$ at room temperature, we picked a resolution of $\Delta x = 8.75 \times 10^{-10} \text{ m}$. The walls have a surface charge density $\sigma \Delta x^2 / e = -0.0125$ and the salt concentration corresponds to a Debye screening length $\lambda_D / \Delta x = 6.0$. λ_D and l_B are defined in Section 2.5.2. The corresponding physical data is presented in Table 2.1.

L	$1.10 \times 10^{-7} \text{ m}$
$L_x = L_y$	$4.38 \times 10^{-9} \text{ m}$
ν	$1.0 \times 10^{-6} \text{ m}^2/\text{s}$
l_B	$0.7 \times 10^{-9} \text{ m}$
λ_D	$5.25 \times 10^{-9} \text{ m}$
σ	$-3.27 \times 10^{14} \text{ m}^{-2}$
dp/dx	$-2.11 \times 10^{11} \text{ Pa/m}$

Table 2.1 – Physical data for the simulation of a Poiseuille flow in a slit. L is the length of the channel separating the walls, ν is the kinematic viscosity, l_B the Bjerrum length, λ_D the Debye screening length, σ the surface charge and dp/dx the pressure gradient.

The numerical data as illustrated in Fig. 2.6 reproduces perfectly the exact solution given by Eq. 2.50. In order to achieve this result, it is important that the fluid is sufficiently discretized, as it is here, and that the force is sufficiently low in order to allow a correct laminar flow as mentioned in the initial assumptions of the problem. It is worthwhile to mention that although 5 nodes were used in the x and y -directions, a single node would suffice in order to recover the correct solution. We use periodic boundary conditions (PBC) to simulate infinite walls. The velocity goes to zero at the walls, which are located half-way between the solid and liquid planes (as enforced by the Bounce-Back rule). This gives then a distance between the planes equal to $L = N_f \Delta x = (N_z - N_s) \Delta x$.

2.5.1.2 Cylindrical pore

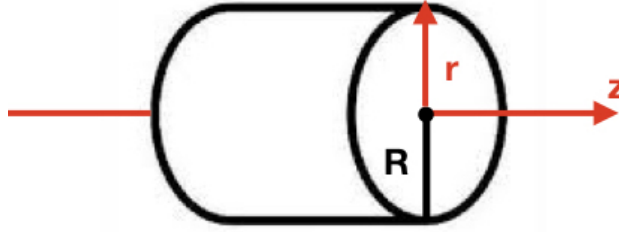


Figure 2.7 – Coordinate system.

As in the slit case, we now consider a viscous flow of a fluid through a pipe with a circular cross-section, given by $r = R$ under the constant and uniform pressure gradient $\frac{dp}{dz}$. We also consider a laminar flow ($Re \ll 1$) and no-slip boundary conditions. The solution for the velocity profile reads in cylindrical coordinates (see Fig. 2.7):

$$u_z(r) = -\frac{dp}{dz} \frac{1}{4\eta} (R^2 - r^2) \quad (2.52)$$

with $u_r = u_\theta = 0$. Introducing the maximum speed u_{\max} :

$$u_{\max} := -\frac{dp}{dz} \frac{R^2}{4\eta}, \quad (2.53)$$

we have

$$\boxed{u_z(r) = u_{\max} \left[1 - \left(\frac{r}{R} \right)^2 \right]} \quad (2.54)$$

Fig. 2.9 shows the numerical result obtained. Due to the symmetry of the problem, it is sufficient to look at the profiles along a specific plane (*e.g.* at $N_x/2$). Here the grid was constructed with $w = 100$ nodes, $N_z = 3$ nodes and $N_x = N_y = 161$ nodes. The w -parameter allows us to have N_s solid nodes outside the fluid region, so that $N_f = N_y - w$, where N_f denotes the number of fluid nodes in the plane of interest (see Fig. 2.8). We chose a resolution of $\Delta x = 1.75 \times 10^{-9} m$. The walls have a surface charge density $\sigma \Delta x^2 / e = -2.0$ and the salt concentration corresponds to a Debye screening length $\lambda_D / \Delta x = 4.0$. The *Laboetie* code

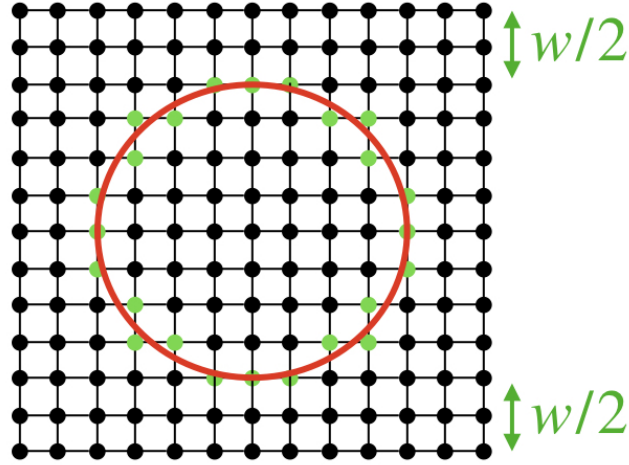


Figure 2.8 – Box of simulation in a charged cylindrical pore with a distribution of the charge on the interfacial nodes only (in green). Fluid nodes are in black. PBCs are used in the x, y and z -directions. w denotes the amount of solid nodes between the interfacial nodes and on of the edges of the box of simulation.

distributes the charge only on the interfacial solid nodes. The pressure gradient inducing the flow is $\frac{dp}{dz}\Delta t^2/(\rho\Delta x) = 1.0 \times 10^{-5}$. The corresponding physical data is presented in Table 2.2. Once again, as in the slit case, due to the symmetry of the problem and thanks to the PBCs, a single node in the z -direction would have been enough in order to recover the correct solution. As we can see in Fig. 2.9, there is perfect agreement between the numerical data and Eq. 2.54. $r = 0$ denotes the centre of the channel and the solid nodes are located at $r = \pm 0.5$. The walls are again half way between the last liquid plane and the first solid plane.

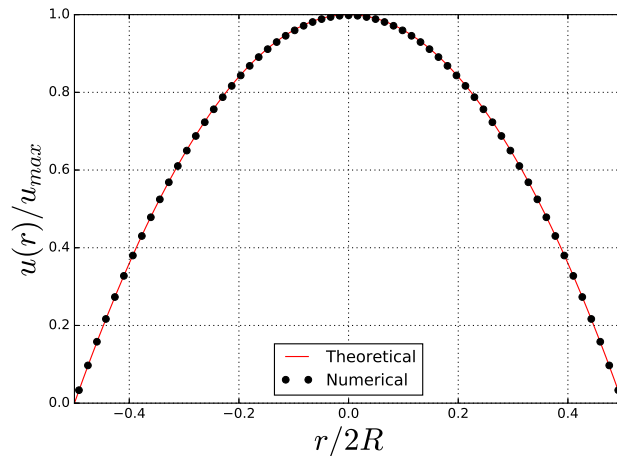


Figure 2.9 – Velocity profile in a cylindrical channel. The flow is induced by a pressure gradient resulting in a Poiseuille flow. The velocity u is normalized with respect to the maximum velocity u_{max} , whereas r , which denotes the position in the fluid region, is normalized with respect to $2R$ the cylinder diameter.

Now that the hydrodynamic part of the code is validated, we test the implementation of the

R	$5.34 \times 10^{-8} \text{ m}$
L_{PBC}	$5.25 \times 10^{-9} \text{ m}$
ν	$1.0 \times 10^{-6} \text{ m}^2/\text{s}$
l_B	$0.7 \times 10^{-9} \text{ m}$
λ_D	$7 \times 10^{-9} \text{ m}$
σ	$-1.14 \times 10^{15} \text{ m}^{-2}$
dp/dz	$-13.16 \times 10^9 \text{ Pa/m}$

Table 2.2 – Physical data for the simulation of a Poiseuille flow in a cylinder. R is the radius of the pore and L its length. ν is the kinematic viscosity, l_B the Bjerrum length, λ_D the Debye length, σ the surface charge and dp/dz the pressure gradient.

transport of ions, involving both the LF and SOR methods. We first examine the equilibrium state corresponding to the Poisson-Boltzmann solution for which analytical solutions can be obtained in both slit and cylindrical pores in two different scenarios:

1. Debye Hückel theory: charged surfaces in low potential condition (*i.e.* $\psi \ll k_B T/e$) with a symmetric monovalent salt and counterions
2. Gouy Chapman theory: with charged surfaces without salt, where only counterions are present, even for high potentials.

2.5.2 Poisson-Boltzmann theory

The Poisson-Boltzmann (PB) equation gives the configuration of the physical system at equilibrium. The system is made of chemical species diluted in a solvent, and are supposed to follow Boltzmann statistics. The system can be described via Poisson equation, *i.e.*

$$\Delta\psi = -\frac{\rho_f}{\varepsilon} \quad (2.55)$$

where $\varepsilon = \varepsilon_r \varepsilon_0$ is the permittivity, ψ is the electric potential and ρ_f is the charge density.

Given the assumption that the charge follows a Boltzmann distribution, the local charge density ρ_k is written as

$$\rho_k(\mathbf{r}) = n_k \exp\left(-\frac{z_k e \psi(\mathbf{r})}{k_B T}\right). \quad (2.56)$$

Note that ρ_k is a position dependent function, whereas n_k is a constant corresponding to the concentration where the potential reference was taken. Plugging Eq. 2.56 and Eq. 2.14 in Eq. 2.55 yields,

$$\varepsilon \Delta\psi = -\sum_{k=1}^N z_k e n_k \exp\left(-\frac{z_k e \psi}{k_B T}\right) \quad (2.57)$$

This is the so-called Poisson-Boltzmann (PB) equation, whose solution is the electric potential distribution in the diffuse ionic layer.

Chapter 2. Lattice Boltzmann Electrokinetics

If the potential is low, *i.e.* $e\psi/k_B T \ll 1$, the PB equation can be linearised via Taylor expansion. Since $\exp(X) \simeq 1 + X$, we have

$$\varepsilon \Delta \psi = - \sum_{k=1}^N z_k e n_k \left(1 - \frac{z_k e \psi}{k_B T} \right) \quad (2.58)$$

Because of electroneutrality condition $\sum_{k=1}^N z_k n_k = 0$, the first contribution vanishes and we obtain

$$\varepsilon \Delta \psi = \left(\sum_{k=1}^N n_k z_k^2 \right) \beta e^2 \psi \quad (2.59)$$

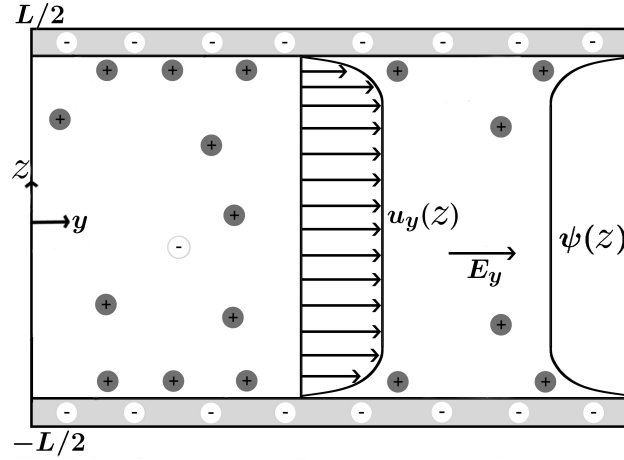


Figure 2.10 – Sketch of the slit geometry. The walls are negatively charged and counterions are inserted in order to preserve electroneutrality. The system may or may not have added salt. An external electric field parallel to the walls couples hydrodynamic and electrostatic effects, resulting in an electro-osmotic flow.

The inverse of the Debye screening length $\kappa := 1/\lambda_D$ is defined as,

$$\kappa^2 = 4\pi l_B \sum_{k=1}^N n_k z_k^2 \quad (2.60)$$

where the Bjerrum length l_B is defined as

$$l_B = \frac{e^2}{4\pi \varepsilon k_B T}. \quad (2.61)$$

In the case of a binary symmetric electrolyte gives

$$\kappa^2 = \frac{\beta e^2}{\varepsilon} n_s z^2 \quad (2.62)$$

with $n_s := n_+ + n_-$ the salt concentration and $z := z_{\pm}$ the valency of the ions. The linearized PB equation obtained by Debye-Hückel finally reads:

$$\Delta \psi = \kappa^2 \psi \quad (2.63)$$

It is worth mentioning that our LBE code is in the canonical ensemble, meaning that our λ_D does not correspond to the actual physical Debye screening length; instead it is used to fix the initial concentration of added salt in the system via the following equation:

$$n_s = \frac{1}{8\pi l_B \lambda_D^2}. \quad (2.64)$$

2.5.2.1 Slit pore

Debye-Hückel solution

Consider a slit whose surfaces bear a negative surface charge $-\sigma$ in m^{-2} , as shown in Fig 2.10, and suppose that a symmetric, binary, monovalent (1:1) salt, such as KCl or NaCl, is inserted in the channel. Once steady state is reached, the ions will have a potential ψ according to the PB equation (Eq. 2.57) and distribute according to a Boltzmann distribution.

L	$1.10 \times 10^{-7} \text{ m}$
$L_x = L_y$	$4.38 \times 10^{-9} \text{ m}$
ν	$1.0 \times 10^{-6} \text{ m}^2/\text{s}$
l_B	$0.7 \times 10^{-9} \text{ m}$
λ_D	$5.25 \times 10^{-9} \text{ m}$
σ	$-3.27 \times 10^{14} \text{ m}^{-2}$

Table 2.3 – Physical data for an electrolyte with added salt in a slit channel (counterions and cations). L is the length of the channel separating the walls, ν is the kinematic viscosity, l_B the Bjerrum length, λ_D the Debye length and σ the surface charge.

Because of the symmetry of the problem, the potential $\psi(z)$ and the concentrations $\rho_k(z)$ only depend on the position z in the direction perpendicular to the walls.

$$\varepsilon \frac{d^2\psi}{dz^2} = \frac{z^2 e^2 \psi}{k_B T} (n_+ + n_-) \quad (2.65)$$

The solutions for Eq. 2.63 are of the form

$$\psi(z) = A \exp(\kappa z) + B \exp(-\kappa z) \quad (2.66)$$

with A and B two constants determined by the boundary conditions

$$\pm \beta e \frac{d\psi}{dz} \Big|_{z=\mp L/2} = -4\pi l_B \sigma \quad (2.67)$$

and the symmetry condition

$$\frac{d\psi}{dz} \Big|_{z=0} = 0 \quad (2.68)$$

Since

$$\frac{d\psi}{dz} = A\kappa \exp(\kappa z) - B\kappa \exp(-\kappa z) \quad (2.69)$$

the symmetry condition gives,

$$A = B \quad (2.70)$$

and the boundary conditions yield

$$A = \frac{4\pi l_B \sigma}{2\kappa \sinh(\frac{\kappa L}{2})} \quad (2.71)$$

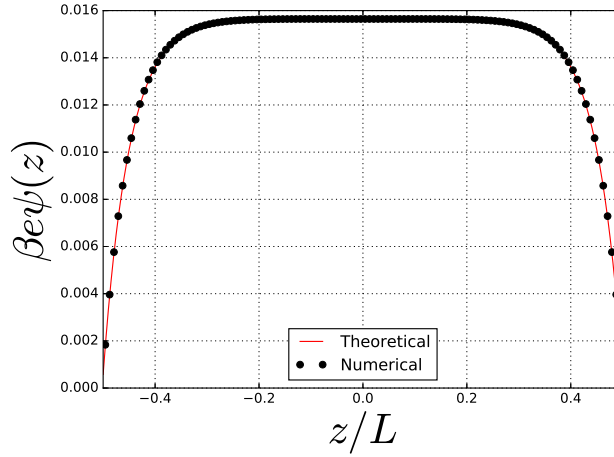


Figure 2.11 – Electrostatic potential in a slit channel due to the surface charge density $\sigma\Delta x^2/e = -0.0125$, for a distance $L/\Delta x = 120$ between the walls, when salt is added at a concentration corresponding to a Debye screening length $\lambda_D/\Delta x = 6.0$. The potential is non-dimensionalized with $\beta e = e/k_B T$ and z is normalized with respect to L

Hence the solution for the reduced electrostatic potential is:

$$\phi(z) = \beta e \psi(z) = \frac{4\pi l_B \sigma}{\kappa \sinh(\frac{\kappa L}{2})} \cosh(\kappa z) \quad (2.72)$$

For a symmetric electrolyte the concentrations read

$$\rho_{\pm}(z) = n_{\pm} [1 \mp \phi(z)] \quad (2.73)$$

Then, using $n_{\pm} = n_s/2 = \kappa^2/(8\pi l_B)$ we recover the final expression for the concentration

$$\rho_{\pm}(z) = \frac{\kappa^2}{8\pi l_B} \left(1 \mp \frac{4\pi l_B \sigma}{\kappa \sinh(\frac{\kappa L}{2})} \cosh(\kappa z) \right) \quad (2.74)$$

A simulation was run in the *Laboetic* code, in order to see if we could recover the solution for the electrostatic potential and the ionic concentration. We used the same parameters and resolution as in the simulations given in Section 2.5.1.1 unless specified. The diffusion coefficients of the ionic species are $D_{\pm}\Delta t/\Delta x^2 = 0.05$. The corresponding physical data of the system is presented in Table 2.3.

Fig. 2.11 shows that the correct solution for the electrostatic potential is recovered. More specifically we can observe the exponential decay of the potential across the electric double layer (EDL) at the wall. This means that the parameters for σ and λ_D were correctly chosen according the low potential condition and the other prior assumptions of the theory. Furthermore a perfect agreement is also observed between the numerical results and theoretical predictions for the ionic densities as illustrated in Fig. 2.12. However, the theoretical results in Fig. 2.11 and 2.12 do not correspond exactly to Eq. 2.72 and 2.74. Indeed, some modifications, which we shall now discuss more in details, had to be done.

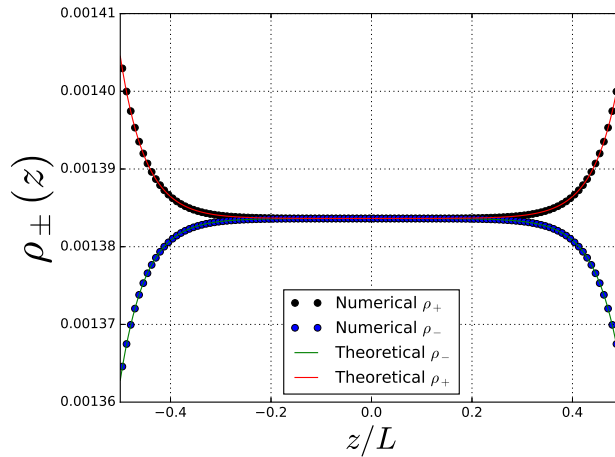


Figure 2.12 – Ionic concentration profile in a slit channel due to the surface charge density $\sigma\Delta x^2/e = -0.0125$, for a distance $L/\Delta x = 120$ between the walls, when salt is added at a concentration corresponding to a Debye screening length $\lambda_D/\Delta x = 6.0$. The ions density is in LB units of $\rho_{\pm}\Delta x^3$ and z is normalized with respect to L

Canonical corrections

As mentioned earlier the LBE method is performed in the canonical ensemble, meaning that we fix the initial concentration in salt n_s , in the slit, instead of fixing the chemical potential. This induces a small difference in the electrostatic potential since the results for the PB theory were derived in the grand-canonical ensemble. This difference becomes more apparent in the concentration profiles. Indeed, we need to link our salt concentration n_s to the concentration n_0 of reference in the reservoir. Therefore, in order to compute the correction to apply to our theoretical results, let us define the concentration profile in a more general manner so that

$$\rho_+ = A \exp[-\phi(z)] \approx A[1 - \phi(z)] \quad (2.75)$$

$$\rho_- = B \exp[\phi(z)] \approx B[1 + \phi(z)] \quad (2.76)$$

where A and B are constants to be determined. Then, from Poisson equation we can write

$$\psi''(z) = \frac{\beta e^2}{\varepsilon}(\rho_+ - \rho_-). \quad (2.77)$$

Chapter 2. Lattice Boltzmann Electrokinetics

Using the definition of the Bjerrum length (see Eq. 2.61) we obtain

$$\phi''(z) = -4\pi l_B(A + B)\phi(z) + 4\pi l_B(B - A). \quad (2.78)$$

Thus, we have $\kappa^2 = 4\pi l_B(A + B)$. A solution for this equation is

$$\phi(z) = \frac{B - A}{A + B} + \alpha \cosh(\kappa z) \quad (2.79)$$

where α is a constant that is determined from the boundary conditions

$$\phi'(L/2) = \alpha \kappa \sinh(\kappa L/2) = -4\pi l_B \sigma \quad (2.80)$$

which leads to

$$\phi(z) = \frac{B - A}{A + B} - \frac{4\pi l_B \sigma}{\kappa \sinh(\kappa L/2)} \cosh(\kappa z) \quad (2.81)$$

Consider the average potential

$$\bar{\phi} = \frac{1}{L} \int_{-L/2}^{L/2} \phi(z) dz \quad (2.82)$$

Then we may write the corresponding concentration profiles

$$\bar{\rho}_+ = \frac{1}{L} \int_{-L/2}^{L/2} \rho_+(z) dz = A[1 - \bar{\phi}] \quad (2.83)$$

$$\bar{\rho}_- = \frac{1}{L} \int_{-L/2}^{L/2} \rho_-(z) dz = B[1 + \bar{\phi}] \quad (2.84)$$

Because we are in the canonical ensemble we know how much salt we insert and thus we have

$$\bar{\rho}_+ = n_s + \frac{2\sigma}{L} \quad (2.85)$$

$$\bar{\rho}_- = n_s \quad (2.86)$$

We now introduce the Donnan potential ϕ_D to write the constants A and B as

$$A = n_0 \exp[-\phi_D] \approx n_0(1 - \phi_D) \quad (2.87)$$

$$B = n_0 \exp[\phi_D] \approx n_0(1 + \phi_D) \quad (2.88)$$

with n_0 a reference concentration. Using that $AB = n_0^2$, we then write the product $\bar{\rho}_+ \bar{\rho}_-$ as

$$\bar{\rho}_+ \bar{\rho}_- = n_s \left(n_s + \frac{2\sigma}{L} \right) = AB[1 - \bar{\phi}^2] \quad (2.89)$$

$$= n_0^2 [1 - \bar{\phi}^2] \approx n_0^2 \quad (2.90)$$

Chapter 2. Lattice Boltzmann Electrokinetics

to linear order in $\bar{\phi}$. Hence we obtain a closing relation for the concentration n_0 in the reservoir, *i.e.*

$$\boxed{n_0 = \sqrt{n_s(n_s + \frac{2\sigma}{L})} \approx n_s + \frac{\sigma}{L}} \quad (2.91)$$

In order to obtain an expression for the Donnan potential ϕ_D we take the ratio of the average concentrations

$$\frac{\bar{\rho}_+}{\bar{\rho}_-} = \frac{A[1 - \bar{\phi}]}{B[1 + \bar{\phi}]} \quad (2.92)$$

Using Eq. 2.87 and 2.88 we can write

$$\frac{A}{B} = \exp[-2\phi_D] \quad (2.93)$$

Hence,

$$\frac{\bar{\rho}_+}{\bar{\rho}_-} = \exp[-2\phi_D] \left(\frac{1 - \bar{\phi}}{1 + \bar{\phi}} \right) \quad (2.94)$$

$$= 1 + \frac{2\sigma}{n_s L} \quad (2.95)$$

from which a closing relation for ϕ_D reads

$$\phi_D = -\frac{1}{2} \left[\ln \left(1 + \frac{2\sigma}{n_s L} \right) + \ln \left(\frac{1 - \bar{\phi}}{1 + \bar{\phi}} \right) \right] \quad (2.96)$$

$$\approx -\frac{\sigma}{n_s L} + \bar{\phi} \quad (2.97)$$

The second term on the right hand side, $\bar{\phi}$, may be neglected, as we are in the low potential condition regime, and thus

$$\boxed{\phi_D = -\frac{\sigma}{n_s L}} \quad (2.98)$$

Using again Eq. 2.87 and 2.88 we can write

$$\frac{A - B}{A + B} = \frac{\exp[-2\phi_D] - 1}{\exp[-2\phi_D] + 1} \approx -\phi_D \quad (2.99)$$

which yields to the final solution for the corrected potential

$$\boxed{\phi(z) = \frac{\sigma}{n_s L} - \frac{4\pi l_B \sigma}{\kappa} \frac{\cosh(\kappa z)}{\sinh(\kappa L/2)}} \quad (2.100)$$

with $\kappa^2 = 4\pi l_B(2n_s + 2\sigma/L)$. Eq. 2.100 is thus the correct solution for the electrostatic potential, which corresponds more closely to our simulations. Plugging the derived expressions for A and B in Eq. 2.75 and 2.76 yields to the correct concentration profiles.

Gouy-Chapman solution

The solution carried out with the Debye-Hückel approximation, required an approximation which showed differences when compared to the numerical solution. On the contrary, the Gouy-Chapman solution is obtained when only counterions are present and is an exact solution of the PB equation. The walls are again negatively charged.

L	$1.10 \times 10^{-7} \text{ m}$
$L_x = L_y$	$4.38 \times 10^{-9} \text{ m}$
ν	$1.0 \times 10^{-6} \text{ m}^2/\text{s}$
l_B	$0.7 \times 10^{-9} \text{ m}$
σ	$-3.27 \times 10^{14} \text{ m}^{-2}$

Table 2.4 – Physical data for a fluid without added salt (*i.e.* counterions only) in a slit channel. L is the length of the channel separating the walls, ν is the kinematic viscosity, l_B the Bjerrum length and σ the surface charge.

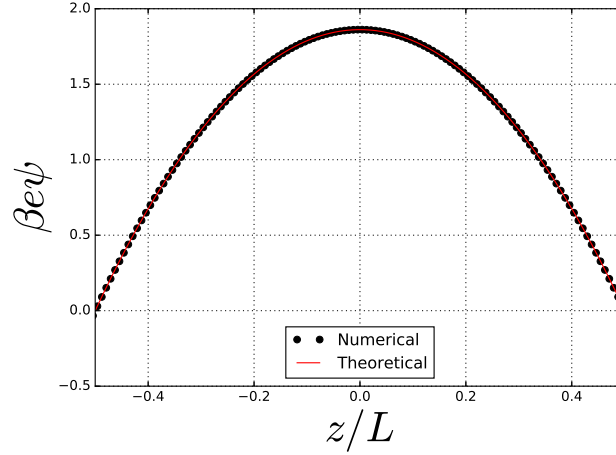


Figure 2.13 – Electrostatic potential in a slit channel due to the surface charge density $\sigma\Delta x^2/e = -0.0125$, for a distance $L/\Delta x = 120$ between the walls, when only counterions are present. The potential is non-dimensionalized with $\beta e = e/k_B T$ and z is normalized with respect to L

Using the PB equation as shown in Eq. 2.57 and given that only cations are present we may write

$$\frac{d^2\phi}{dz^2} = -\frac{e^2}{\epsilon k_B T} \rho_+ = -\frac{e^2 n_+}{\epsilon k_B T} \exp[-\phi] \quad (2.101)$$

Given that the electrostatic potential is defined with respect to a reference potential, we may take $\phi(z=0) = 0$ and because of the symmetry of the problem we have again $d\phi/dz = 0$, the final expression for the electric potential is:

$$\boxed{\phi(z) = -2 \ln [\cos(\alpha z)]}, \quad (2.102)$$

where α^{-1} is the analog of the Debye screening length defined by:

$$\pi L l_B |\sigma| = \frac{\alpha L}{2} \tan\left(\frac{\alpha L}{2}\right) \quad (2.103)$$

Chapter 2. Lattice Boltzmann Electrokinetics

In order to determine the concentration profile, we use

$$\rho_+ = n_+ \exp(-\phi) \quad (2.104)$$

and Eq. 2.102 to write:

$$\rho_+(z) = \frac{n_+}{\cos^2(\alpha z)}. \quad (2.105)$$

Then, from electroneutrality we determine n_+ using

$$\int_{-L/2}^{L/2} \rho_+(z) dz = -2\sigma \quad (2.106)$$

with the definition of α we obtain

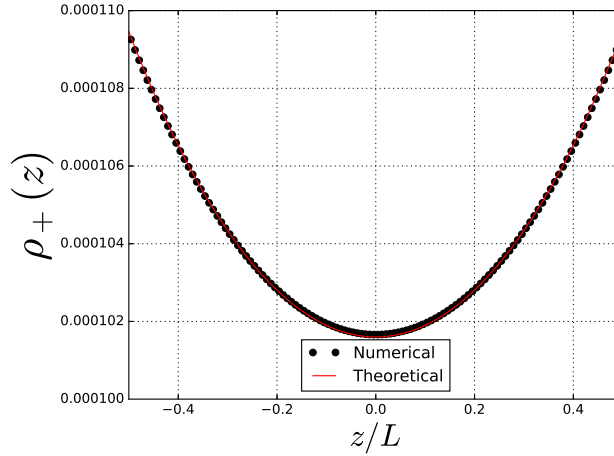


Figure 2.14 – Concentration profile of cations in a slit channel due to the surface charge density $\sigma\Delta x^2/e = -0.0125$, for a distance $L/\Delta x = 120$ between the walls, when only counterions are present. The cations density is in LB units of $\rho_+\Delta x^3$ and $z/\Delta x$ is normalized with respect to $L/\Delta x$

$$\rho_+(z) = \frac{\alpha^2}{2\pi l_B} \frac{1}{\cos^2(\alpha z)} \quad (2.107)$$

The simulation results for both the electrostatic potential and the concentration profiles, shown in Fig. 2.13 and 2.14 respectively, perfectly reproduce the exact analytical result. This completes the validation of the code for the equilibrium of the electrostatic problem in this geometry.

2.5.2.2 Cylindrical pore

The Poisson-Boltzmann solution is now tested in two new different scenarios:

1. A cylindrical pore with charged surfaces in low potential condition ($\psi \ll k_B T/e$) with a symmetric monovalent salt inside the channel
2. A cylindrical pore with charged surfaces without salt, where only counterions are present, in order to preserve electroneutrality.

Similarly to the slit case, a simulation was run in the *Laboetie* code, in order to recover the solution for the electrostatic potential and the concentration. We used the same parameters and resolution as in the simulations given in Section 2.5.1.2 unless specified. The diffusion coefficients of the ionic species are $D_{\pm}\Delta t/\Delta x^2 = 0.05$. The corresponding physical data of the system is presented in Table 2.5.

Debye-Hückel solution

R	$5.34 \times 10^{-8} \text{ m}$
L_{PBC}	$5.25 \times 10^{-9} \text{ m}$
ν	$1.0 \times 10^{-6} \text{ m}^2/\text{s}$
l_B	$0.7 \times 10^{-9} \text{ m}$
λ_D	$7 \times 10^{-9} \text{ m}$
σ	$-5.68 \times 10^{13} \text{ m}^{-2}$

Table 2.5 – Physical data for an electrolyte with added salt (counterions and coions) in a cylindrical channel. R is the radius of the pore and L its length. ν is the kinematic viscosity, l_B the Bjerrum length, λ_D the Debye screening length and σ the surface charge.

Similarly to the slit geometry, if the potential is small compared to the thermal energy, the PB equation can be linearized. In a cylindrical geometry the equation becomes

$$\nabla^2\psi = \frac{\partial_r (r\partial_r\psi)}{\partial r} = \kappa^2\psi \quad (2.108)$$

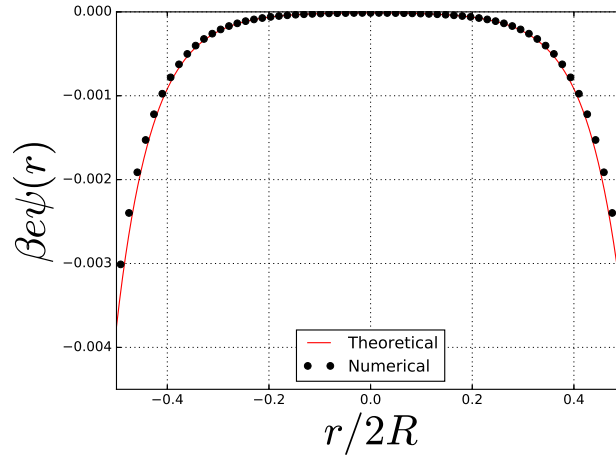


Figure 2.15 – Electrostatic potential in a cylindrical channel due to the surface charge density $\sigma\Delta x^2/e = -0.1$, for a diameter $2R/\Delta x = 61$, in the presence of added salt at a concentration corresponding to a Debye screening length $\lambda_D/\Delta x = 4.0$. The potential is non-dimensionalized with $\beta e = e/k_B T$ and z is normalized with respect to L

The boundary conditions are

- $\beta e \partial_r \psi|_R = 4\pi l_B \sigma$

- $\beta e \partial_r \psi|_{r=0} = 0$ (because of the symmetry of the problem)

The solution is then:

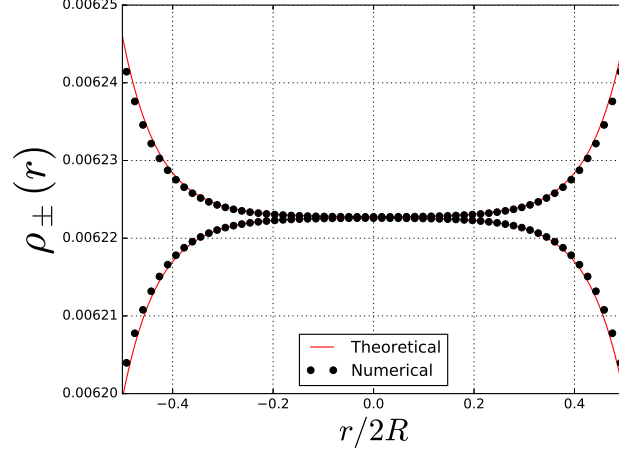


Figure 2.16 – Ionic concentration profile in a cylindrical channel due to the surface charge density $\sigma \Delta x^2/e = -0.1$, for a diameter $2R/\Delta x = 61$, when salt is added. The ions density is in LB units of $\rho_{\pm} \Delta x^3$ and r is normalized with respect to $2R$.

$$\phi(r) = \frac{4\pi l_B \sigma}{\kappa} \frac{I_0(\kappa r)}{I_1(\kappa R)} \quad (2.109)$$

where I_n correspond to modified Bessel functions of the first kind, which are defined as

$$I_n(x) = \sum_m^{\infty} \frac{1}{m!(m+n)!} \left(\frac{x}{2}\right)^{2m+n}, \forall x \in \mathbb{R} \quad (2.110)$$

The corresponding ionic concentrations are

$$\rho_{\pm}(r) = \frac{\kappa^2}{8\pi l_B} \left(1 \mp \frac{4\pi \sigma l_B}{\kappa} \frac{I_0(\kappa r)}{I_1(\kappa R)} \right) \quad (2.111)$$

A simulation was carried out in order to recover $\psi(r)$ and $\rho_{\pm}(r)$, with the same parameters as in Section 2.5.1.2 except for the surface charge density, which was set to $\sigma \Delta x^2/e = -0.1$ in order to be in the low potential condition needed to recover the analytical solution. The corresponding physical data is shown in Table 2.5. The solution for the electric potential is correctly reproduced as illustrated in Fig. 2.15. Actually, the potential and concentration solutions were subjected to the canonical corrections, in a similar fashion as in the slit case (see next paragraph **Canonical corrections**). By doing so we recover the correct concentrations of cations and anions (see Fig. 2.16), although we can see a discrepancy between analytical and numerical results close to the walls. However, this discrepancy could be merely due to the way cylindrical boundaries are drawn (see Fig. 2.8), which can introduce errors due to the periodic boundary conditions (PBCs) of the simulation box. We shall address this issue in more details in Section 2.5.2.3.

Canonical corrections

Similarly to the slit case one can correct the potential profile solution deriving the Donnan potential and the reference concentration n_0 . The general solution in this geometry reads

$$\phi(r) = \frac{A - B}{A + B} - \frac{4\pi l_B \sigma}{\kappa} \frac{I_0(\kappa r)}{I_1(\kappa R)} \quad (2.112)$$

Using,

$$\bar{\phi} = \frac{2}{R} \int_0^R 2\pi r \phi(r) dr \quad (2.113)$$

with

$$\bar{\rho}_+ = A[1 - \bar{\phi}] \quad (2.114)$$

$$\bar{\rho}_- = B[1 + \bar{\phi}] \quad (2.115)$$

with A and B defined as in the slit case. Because we are in the canonical ensemble the cations concentration compensating the surface charge is $\sigma 2\pi R / (\pi R^2) = 2\sigma / R$ and thus we have

$$\bar{\rho}_+ = n_s + \frac{2\sigma}{R} \quad (2.116)$$

$$\bar{\rho}_- = n_s \quad (2.117)$$

We then obtain

$$\boxed{n_0 = \sqrt{n_s(n_s + 2\sigma/R)}} \quad (2.118)$$

and the Donnan potential

$$\phi_D = -\frac{2\sigma}{n_s 2R}. \quad (2.119)$$

Therefore the corrected potential reads,

$$\boxed{\phi(r) = \frac{2\sigma}{n_s 2R} - \frac{4\pi l_B \sigma}{\kappa} \frac{I_0(\kappa r)}{I_1(\kappa R)}} \quad (2.120)$$

Gouy-Chapman solution

R	$5.34 \times 10^{-8} \text{ m}$
L	$5.25 \times 10^{-9} \text{ m}$
ν	$1.0 \times 10^{-6} \text{ m}^2/\text{s}$
l_B	$0.7 \times 10^{-9} \text{ m}$
σ	$-1.14 \times 10^{15} \text{ m}^{-2}$

Table 2.6 – Physical data for an electrolyte with only counterions in a cylindrical channel. R is the radius of the pore and L its length. ν is the kinematic viscosity, l_B the Bjerrum length, σ the surface charge.

Chapter 2. Lattice Boltzmann Electrokinetics

When no salt is added and only counterions are present, if $\sigma < 0$ then the solution for the PB equation reads:

$$\Delta\phi = -\frac{e^2 n_+}{k_B T} \exp[-\phi] \quad (2.121)$$

and the exact solution for the electrostatic potential profile is

$$\boxed{\phi(r) = 2 \ln(1 - \alpha^2 r^2)} \quad (2.122)$$

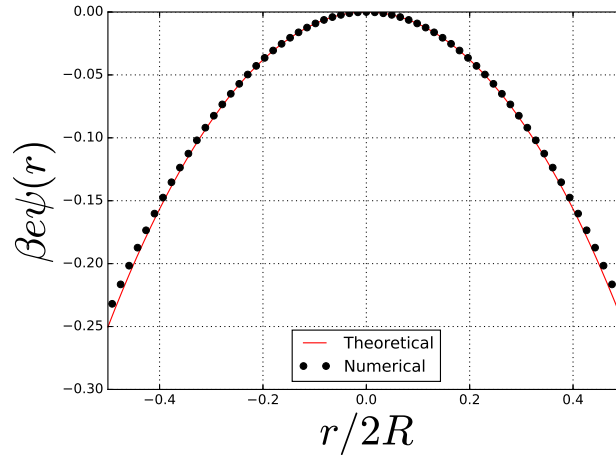


Figure 2.17 – Electrostatic potential in a cylindrical channel due to the surface charge density $\sigma\Delta x^2/e = -2.0$, for a distance diameter $2R/\Delta x = 61$, when only counterions are present. The potential is non-dimensionalized with $\beta e = e/k_B T$ and r is normalized with respect to $2R$

where α^{-1} is analogous to the Debye screening length, which can be computed numerically using the electroneutrality condition, as the solution of

$$\alpha^2 R^2 = \frac{\pi R |\sigma| l_B}{1 + \pi R |\sigma| l_B} \quad (2.123)$$

The corresponding counterions profile may then be written as

$$\boxed{\rho_+(r) = \frac{2\alpha^2}{\pi l_B} \frac{1}{(1 - \alpha^2 r^2)^2}} \quad (2.124)$$

Eq. 2.122 and 2.124 are exact solutions and indeed, as we can see in Fig. 2.17 and 2.18 they are perfectly reproduced by our numerical data. Nonetheless, we still observe a discrepancy between the two solutions close to the walls.

We shall now discuss more in details the errors arising from this type of geometry.

2.5.2.3 Effect of PBCs

This problem was previously tackled by Amaël Obliger^[139]. As a further way to validate our new code, we reproduced the exact system that he simulated. Specifically, he ran simulations

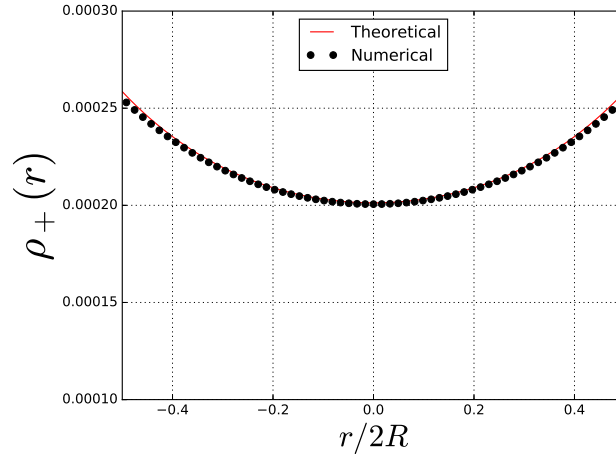


Figure 2.18 – Concentration profile of cations in a cylindrical channel due to the surface charge density $\sigma\Delta x^2/e = -2.0$, for a diameter $2R/\Delta x = 61$, when only counterions are present. The cations density is in LB units of $\rho_+\Delta x^3$ and $r/\Delta x$ is normalized with respect to $2R/\Delta x$

with a solvent mass density $\rho = 10^3 \text{ kg/m}^3$, a dynamic viscosity $\eta = 0.001 \text{ Pa} \cdot \text{s}$, a radius $R = 5 \times 10^{-9} \text{ m}$ and a surface charge $\sigma = 8 \times 10^{16} \text{ m}^{-2}$. The resolution he adopted was $\Delta x = 0.208 \times 10^{-9} \text{ m}$. The corresponding physical data is shown in Table 2.7.

R	$5.04 \times 10^{-9} \text{ m}$
L_{PBC}	$5.25 \times 10^{-9} \text{ m}$
ν	$1.0 \times 10^{-6} \text{ m}^2/\text{s}$
l_B	$0.7 \times 10^{-9} \text{ m}$
σ	$-8.02 \times 10^{16} \text{ m}^{-2}$

Table 2.7 – Physical data for a cylindrical channel with only counterions . R is the radius of the pore and L its length. ν is the kinematic viscosity, l_B the Bjerrum length and σ the surface charge

Errors arise due to periodic boundary conditions because the simulation box is an orthorhombic cell in which the cylinder boundaries are drawn approximately using the lattice nodes inside. Thus the cylinder may be affected by the PBC in different ways, depending on how far the solid nodes are from the boundaries of the box of simulation, as shown in Fig. 2.8. The parameter w determines the distance of the circle with the boundaries of the box. Depending on the value of w , more or less errors appear in the final solution. Following this previous study, we consider two scenarios, with $w = 1\Delta x$ and $w = 50\Delta x$. The relative error for the charge concentration, $\delta\rho_+ = (\rho_+^{sim} - \rho_+^{ana})/\rho_+^{ana}$, was computed and presented in Fig. 2.19 and 2.20 for $w = 1\Delta x$ and $w = 50\Delta x$ respectively.

Maximum error values decrease from 8% to 5% when w is increased. The error maps clearly show that errors are positive along with the main diagonal (orange/red regions) and negative along with the vertical and horizontal diameter (blue regions). In other words in the former case the numerical data overestimates the analytical solution whereas, in the latter case, the numerical data underestimates the analytical solution. Furthermore, the positive errors on the main diagonal are smaller than the ones on the horizontal and vertical diameters. This is due to the fact that the number of solid nodes is higher along with the main diagonal,

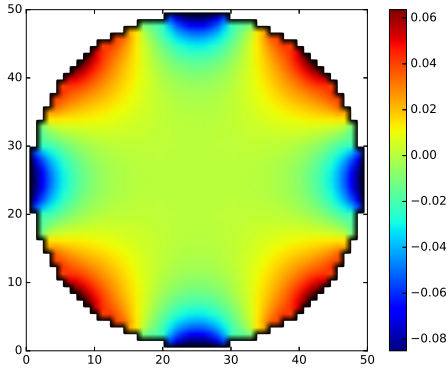


Figure 2.19 – Relative error on the counterions density when compared to the analytical solution. The radius of the pore is $R = 5 \text{ nm}$, no salt is present and the walls bear a surface charge of $\sigma = -8 \times 10^{16} \text{ m}^{-2}$. The separation between the boundary of the channel and the box of simulation is $w = 1\Delta x$

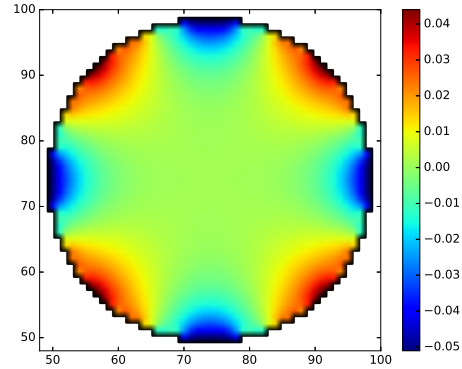


Figure 2.20 – Relative error on the counterions density when compared to the analytical solution. The radius of the pore is $R = 5 \text{ nm}$, no salt is present and the walls bear a surface charge of $\sigma = -8 \times 10^{16} \text{ m}^{-2}$. The separation between the boundary of the channel and the box of simulation is $w = 50\Delta x$

rather than on the vertical and horizontal diameters. The results are in accordance with what Amaël Obliger observed. This validates once more our implementation of the LF and SOR algorithms.

2.5.3 Electro-osmotic flow

After validating independently the hydrodynamic (see Section 2.5.1) and the electrostatic (see Section 2.5.2) parts, we finally consider their coupling by simulating an electro-osmotic flow (EOF).

2.5.3.1 Microscopic origin and Helmholtz-Smoluchowski theory

An electro-osmotic flow (EOF) is a type of flow induced by an external applied electric field tangential to a charged solid-fluid interface. They were first reported in 1809 by F. F. Reuss in Ref. 140, who showed that water could flow through a plug of clay by applying an electric voltage. This is because clay is composed of closely packed charged aluminosilicate particles. Water can then flow through the narrow spaces between these particles. More generally, any combination of an electrolyte confined by charged walls would generate electro-osmotic flows. For water/silica interfaces the effect is particularly large, due to high surface charge densities. The reason why such flow takes place is that the mobile ions present in the electrical double layer (EDL), which forms in the region near the interface, are moved by the Coulombic force exerted by the electric field applied to the fluid (usually via electrodes placed at inlets and outlets). This force acting per unit volume of the fluid can be written as:

$$\mathbf{f}_V = \mathbf{E} \sum_{k=1}^N z_k \rho_k e = -(\varepsilon \nabla^2 \phi) \mathbf{E} \quad (2.125)$$

where \mathbf{E} is the applied electric field.

Therefore, the fluid motion is governed by the the Navier-Stokes (NS) equation, *i.e.*

$$\rho \left(\frac{\partial \mathbf{u}}{\partial t} + \mathbf{u} \cdot \nabla \mathbf{u} \right) = -\nabla p + \eta \nabla^2 \mathbf{u} - (\varepsilon \nabla^2 \phi) \mathbf{E} \quad (2.126)$$

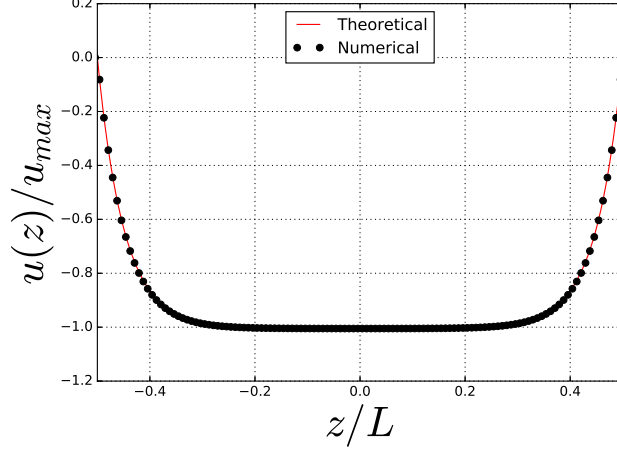


Figure 2.21 – Electro-osmotic flow profile in a slit channel with added salt. The flow is induced by an external electric field $\beta e \Delta x E = 0.025$ parallel to the walls (resulting in an EOF). The velocity u is normalized with respect to the maximum velocity $u_{max} = e E_x \sigma / [\eta \kappa \sinh(\kappa L / 2)]$, whereas z , which denotes the position in the fluid region, is normalized with respect to L the distance between the walls. The theoretical profile is given Eq. 2.130.

with the incompressibility condition

$$\nabla \cdot \mathbf{u} = 0. \quad (2.127)$$

ρ , \mathbf{u} , p and η denote the density, velocity, pressure and fluid dynamic viscosity respectively.

2.5.3.2 Slit pore

As in Section 2.5.2.1, we consider a slit whose surfaces bear a negative surface charge density $-\sigma e$ in $e \cdot m^{-2}$ and a symmetric, binary, monovalent (1:1) salt. Assuming the external applied electric field to be much weaker than the one induced by the surface charge of the solid surface, one can consider that the ionic concentrations near the walls are not affected by the external electric field and thus the induced EOF.

When the EOF is fully developed, *i.e.* $d\mathbf{u}/dt = \mathbf{0}$, with no external pressure gradient across the charged surface and in the limit of low Reynolds number ($\Rightarrow (\mathbf{u} \cdot \nabla) \mathbf{u} = \mathbf{0}$) Eq. 2.126 and 2.127 may be simply written as:

$$\eta \frac{d^2 u}{dz^2} = \varepsilon \frac{d^2 \psi}{dz^2} E_x. \quad (2.128)$$

Integration yields

$$u(z) = \frac{\varepsilon}{\eta} E_x \psi(z) + Az + B \quad (2.129)$$

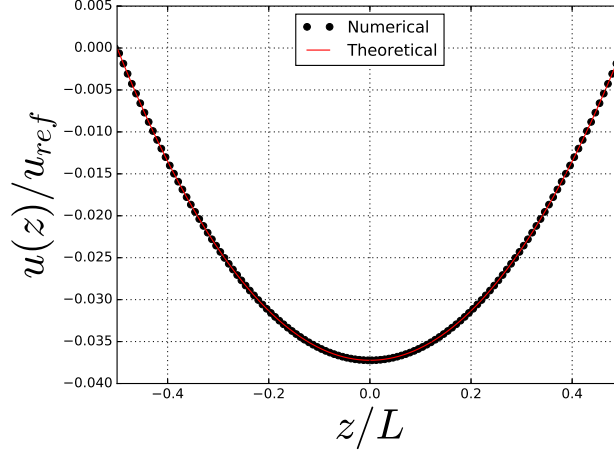


Figure 2.22 – Electro-osmotic flow profile in a slit channel with only counterions. The flow is induced by an external electric field $\beta e \Delta x E = 0.025$ parallel to the walls resulting in an EOF. The velocity u is normalized with respect to the maximum velocity $u_{ref} = eE_x / [2\pi\eta l_B]$, whereas z , which denotes the fluid region, is normalized with respect to L , the distance between the walls. The theoretical profile is given Eq. 2.131.

where A and B are constants to be determined and $\psi(z)$ is given by Eq. 2.100 or 2.102 depending on whether salt is inserted or not.

The EDL thickness is on the order of nanometers, which is much smaller than the characteristic length of microfluidic devices. The EOF velocity profile in a microchannel is almost uniform and is referred to as a "plug-like flow". Therefore, one can use the constant velocity to describe the EOF velocity outside the EDL, which is known as the Smoluchowski slip velocity^[141].

In the presence of salt and under the low potential assumption (*i.e.* Debye-Hückel regime) the boundary conditions are:

- $u(z = \pm L/2) = 0$
- $\psi(z = \pm L/2) = -\frac{4\pi l_B \sigma}{\kappa} \tanh(\kappa L/2)$

and the solution for the velocity profile is given by:

$$u(z) = u_{max} [\cosh(\kappa z) - 1] \quad (2.130)$$

where $u_{max} := \frac{eE_x \sigma}{\eta \kappa \sinh(\kappa L/2)}$.

On the other hand, when no salt is added the exact solution of the non-linear problem (*i.e.* Gouy-Chapman regime) reads:

$$u(z) = u_{ref} \ln \left[\cos \left(\frac{\alpha z}{\alpha L/2} \right) \right] \quad (2.131)$$

where $u_{ref} := \frac{eE_x}{2\pi\eta l_B}$.

Simulations results for these two regimes are presented in Fig. 2.21 and 2.22 respectively and compared to the analytical solutions given in Eq. 2.130 and 2.131. The simulations

are performed with the same parameters as in Section 2.5.1.1 and thus correspond to the potential showed in Fig. 2.11 and 2.13, respectively. The applied electric field was chosen to be $\beta e \Delta x E = 0.025$. Both solutions are correctly reproduced and we observe in the presence of salt the plug-like type of flow characteristic of EOF, which differentiates it from a classical parabolic shape of pressure driven flows (Poiseuille).

2.5.3.3 Cylindrical pore

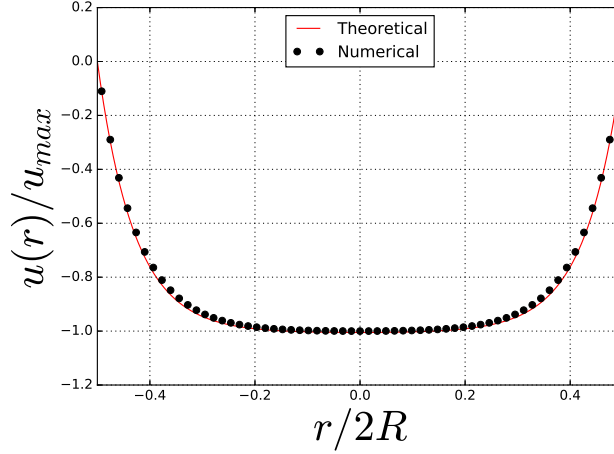


Figure 2.23 – Electro-osmotic flow profile in a cylindrical channel with added salt. The flow is induced by an external electric field $\beta e \Delta x E = 0.005$ parallel to the walls resulting in an EOF. The velocity u is normalized with respect to the reference velocity $u_{ref} = \sigma e E_x / (\kappa \eta) \times I_0(\kappa R) / I_1(\kappa R)$, whereas r , which denotes the position in the fluid region, is normalized with respect to the channel diameter $2R$. The theoretical profile is given by Eq. 2.130.

As in the slit pore case, we consider the NS equation and we express the term $\eta \nabla^2 u_z$ in cylindrical coordinates as:

$$\eta \nabla^2 u_z = \eta \left[\frac{1}{r} \frac{\partial}{\partial r} \left(r \frac{\partial u_z}{\partial r} \right) + \frac{1}{r^2} \frac{\partial^2 u_z}{\partial \theta^2} + \frac{\partial^2 u_z}{\partial z^2} \right] \quad (2.132)$$

Given our assumptions,

- the radial and swirl components of the velocity are zero, *i.e.* $u_r = u_\theta = 0$
- steady state is reached, *i.e.* $\partial u_z / \partial t = 0$
- the flow is axisymmetric, *i.e.* $\partial(\cdot) / \partial \theta = 0$
- translational invariance, *i.e.* $\partial(\cdot) / \partial z = 0$

Thus,

$$\eta \nabla^2 u_z = \eta \left[\frac{1}{r} \frac{\partial}{\partial r} \left(r \frac{\partial u_z}{\partial r} \right) \right] \quad (2.133)$$

Hence, NS equation can be simplified as,

$$\eta \left[\frac{1}{r} \frac{\partial}{\partial r} \left(r \frac{\partial u_z}{\partial r} \right) \right] = \varepsilon E \left[\frac{1}{r} \frac{\partial}{\partial r} \left(r \frac{\partial \psi}{\partial r} \right) \right] \quad (2.134)$$

In a cylinder $u(r = R) = 0$ and $\psi(r = R)$ can be determined using Eq. 2.109 or 2.122 depending on whether or not salt is added to the system. Integration for the velocity profile yields:

$$u(r) = \frac{\varepsilon E_x}{\eta} [\psi(r) + A \ln(r) + B] \quad (2.135)$$

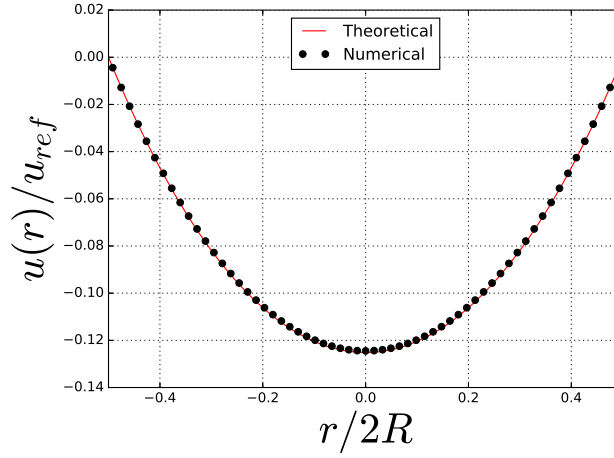


Figure 2.24 – Electro-osmotic flow profile in a cylindrical channel with counterions only. The flow is induced by an external electric field $\beta e \Delta x E = 0.005$ parallel to the walls resulting in an EOF. The velocity u is normalized with respect to the reference velocity $u_{ref} = e E_z / (2\pi\eta l_B)$, whereas r , which denotes the position in the fluid region, is normalized with respect to the channel diameter $2R$. The theoretical profile is given by Eq. 2.131.

If salt is added under the assumption of low potential (Debye-Hückel regime) the velocity profile is written

$$u(r) = -\frac{\sigma e}{\kappa\eta} \left(\frac{I_0(\kappa r) - I_0(\kappa R)}{I_1(\kappa R)} \right) E_z. \quad (2.136)$$

On the other hand, if no salt is added the corresponding exact solution of the non-linear problem, in the Gouy-Chapman regime is:

$$u(r) = -\frac{e}{2\pi\eta l_B} \ln \left(\frac{1 - \alpha^2 r^2}{1 - \alpha^2 R^2} \right) E_z, \quad (2.137)$$

with α as defined in Eq. 2.123. The parameters of the simulation are the same as in Section 2.5.1.2. Fig. 2.23 and 2.24 correspond to the potential profiles of Fig. 2.15 and 2.17 respectively. An electric field $\beta e \Delta x E = 0.005$ parallel to the walls, which induces an EOF, was applied. The resulting numerical data for the two cases studied, perfectly reproduces the analytical solutions (see Fig. 2.24 and Fig. 2.23). Coupling between the hydrodynamics and electrostatics was thus successfully achieved.

2.6 Conclusion

In this chapter, we introduced the Lattice Boltzmann Electrokinetics method. The governing equation of the problem were set and their corresponding discretized form, as implemented in the algorithm, were illustrated. We showed how the NS equation is recovered from the Boltzmann equation and how it is then coupled with the LF method to couple the solvent with the ions dynamics.

The hydrodynamics part of the code was validated for two geometries (*i.e.* a slit and a cylinder) simulating a Poiseuille flow, whose analytical solution is known. Similarly, we validated the electrostatics part of the code by comparing our results with analytical solutions of the PB equation, which were derived for two geometries (slit and cylindrical pores) in the cases where no salt is added, which is an exact solution of the problem, or in the presence of salt under the assumption of low potential. Finally the coupling of electrostatics and hydrodynamics was validated by perturbing the system with an external electric field, which induces an electro-osmotic flow and comparing with analytical solutions for the two geometries.

The overall code was thus successfully validated. In the next Chapters we will introduce new features to the code, which introduce new physics, not available to our knowledge in other LBE codes. In Chapter 3 we introduce the moment propagation method for charged tracers, which may also experience adsorption/desorption dynamics. Then, in Chapter 4 and 5 we introduce the major novelty of this thesis, which is the change of boundary conditions from surface charges to fixed potentials at the solid-boundaries. Finally Chapter 6 discusses how the formalism of linear response theory can be applied to LBM.

Moment propagation method for adsorbing/desorbing charged species

Contents

3.1	Model and adsorption/desorption equation	62
3.2	Algorithm - Moment Propagation	63
3.3	Results and Discussion	66
3.3.1	Dispersion of charged adsorbing tracers by an electro-osmotic flow	66
3.3.2	Validation	67
3.3.3	Simulation parameters	70
3.3.4	Fraction of adsorbed tracers	71
3.3.5	Electro-osmotic flow profile	72
3.3.6	Average tracer velocity	72
3.3.7	Diffusion coefficient	74
3.3.8	Dispersion coefficient	76
3.4	Conclusion	78

Chapter 3. Moment propagation method for adsorbing/desorbing charged species

IT HAS also become obvious recently that the behaviour of charged solid/liquid interfaces does not only depend on the electrostatic interactions between the ions and the wall, but also on their chemical nature, which modifies their short-range interactions, *e.g.* via the solvation properties of the ions.^[142,143] Molecular simulations have clarified such ion-specific effects, as well as the consequences on the electrokinetic effects on both hydrophilic and hydrophobic surfaces.^[144] Details of the electronic properties of the walls also have strong effects on the interaction with solutes: Density Functional Theory (DFT) calculations suggest for example that differences in the interactions between the hydroxide ions and either carbon or boron nitride nanotubes, which have the same geometry but different electronic structures^[145], may be at the origin of the dramatically different hydrodynamic behaviour observed on larger scale for the flow of water through these tubes.^[4,146] At a more coarse-grained level, specific effects can be introduced in mean-field theories such as Poisson-Boltzmann via Potentials of Mean Force (PMF), which can be computed using molecular simulations.^[147] In the present thesis, we aim at extracting microscopic information on the dynamics of individual mobile species, which may involve diffusion, advection and migration, but also adsorption and desorption from surfaces. To that end, we follow the Moment Propagation (MP) approach^[113,132–137], which is not limited to the mere computation of average fluxes but allows the computation of observables which reflect the statistical properties, averaged over all possible trajectories, of their dynamics, such as their velocity auto-correlation function (VACF).

Section 3.1 presents the theoretical basis for the description of the transport of solvent and ions as well as their adsorption/desorption at solid/liquid interfaces. The lattice-based algorithm is then presented in Section 3.2. It extends previous works treating either the effect of electrostatics and electrokinetics, or that of adsorption/desorption at the walls. Results are then presented in Section 3.3 which is divided in two parts. The first one validates the implementation of the algorithm using two previous works^[113,114]. The second one finally considers the case of dispersion of neutral and charged adsorbing/desorbing tracers, by an electro-osmotic flow in a slit-pore with charged walls and counterions in the absence of added salt, for which some properties can be determined analytically. The algorithm is validated by examining the average velocity of tracers as a function of surface charge, of the tracer valency and of the adsorption/desorption rates. We then illustrate the ability of the MP method to estimate properties for which no analytical results are available, by considering their dispersion coefficient.

3.1 Model and adsorption/desorption equation

The combination of the Poisson and Nernst-Planck equations, as given in Eq. 2.15, with the Navier-Stokes equation (Eq. 2.16) provides a simple yet reasonably accurate description of the coupled ionic and solvent dynamics. They must be supplemented by electrostatic and hydrodynamic boundary conditions. We will focus here on fixed surface charge density $\sigma\epsilon$ (with σ per unit surface), which may in principle depend on the position on the surface, and no-slip ($\mathbf{u} = 0$) boundary conditions at the fluid-solid interface.

We will further investigate the dynamics of charged tracers within such an ionic solution. Tracers follow the same evolution of Eq. 2.9 as the major ions, *i.e.* experience diffusion, advection and migration, but they do not influence in return the electrostatic potential ψ or the fluid velocity \mathbf{u} (or the other ionic densities). However, we will also consider the adsorp-

Chapter 3. Moment propagation method for adsorbing/desorbing charged species

tion and desorption of such tracers at the surface of solid walls. Introducing Γ_k the surface concentration of species k (length⁻²) and assuming first-order kinetics for both processes, the evolution of the adsorbed and mobile tracers at the surfaces follow:

$$\partial_t \Gamma_k(\mathbf{r}, t) = -k_d \Gamma_k(\mathbf{r}, t) + k_a \rho_k(\mathbf{r}, t) \quad (3.1)$$

where k_d (time⁻¹) and k_a (length·time⁻¹) are the desorption and adsorption rates, respectively. In equilibrium, this results in the Henry law adsorption isotherm.

These coupled non-linear equations, namely Eq. 2.15 and 2.16 for the dynamics of the major species and of the fluid and Eq. 2.9+3.1 for the adsorbing/desorbing charged tracers should then be solved, in general numerically, to predict the evolution of the system. At this mean-field level, however, such a solution does not provide information on the dynamics of individual tracers and how they explore the fluid and the interface under the combined effects of all microscopic processes. Here we extend the Moment Propagation method, which allows the computation of observables which reflect the statistical properties, averaged over all possible trajectories, of their dynamics, such as their velocity auto-correlation function (VACF).

3.2 Algorithm - Moment Propagation

In order to compute the VACF of tracers within such electrokinetic flows, we take advantage of the probabilistic description underlying the LB method via the Moment Propagation (MP) approach introduced by Lowe and Frenkel^[133,148]. Several descriptions and extensions of this method have since been proposed for various applications, see Ref. 113,114,132,137,149–151. In the present work, we show that this method can be used for charged mobile (hence experiencing diffusion, advection and migration) and adsorbing/desorbing species – a combination of features which had to date not been investigated previously despite its relevance in the many contexts described in the introduction. We first show how the MP method can be implemented to propagate any quantity related to the transport of tracers under the combined effect of all the above-mentioned processes. Then, we show how a particular choice of propagated quantity can be made to compute the VACF, before finally expressing averaged quantities such as the average velocity or dispersion coefficient of tracers from their VACF.

We consider here the propagation of an arbitrary quantity $P(\mathbf{r}, t)$ defined on the same lattice as the one used for the LB/link-flux simulations. In the absence of adsorption/desorption processes, it is updated in steps according to $P(\mathbf{r}, t + \Delta t) = P^*(\mathbf{r}, t + \Delta t)$ with:

$$P^*(\mathbf{r}, t + \Delta t) = P(\mathbf{r}, t) \left[1 - \sum_i p_i(\mathbf{r}, t) \right] + \sum_i P(\mathbf{r} - \mathbf{c}_i \Delta t, t) p_i(\mathbf{r} - \mathbf{c}_i \Delta t, t) \quad (3.2)$$

where the sums run over discrete velocities and $p_i(\mathbf{r}, t)$ stands for the probability of leaving a node \mathbf{r} with velocity \mathbf{c}_i . The first term therefore corresponds to particles that have not left \mathbf{r} between t and $t + \Delta t$. All the dynamics is then encompassed in the definition of these probabilities, which are designed to capture the relevant physical processes^[113]:

Chapter 3. Moment propagation method for adsorbing/desorbing charged species

$$p_i(\mathbf{r}, t) = p_i^{adv}(\mathbf{r}, t) + \lambda w_i \left\{ \frac{1}{4} \beta e q \mathbf{E} \cdot \mathbf{c}_i \Delta t + \frac{1}{1 + e^{\beta \Delta \mu_i^{ex}(\mathbf{r}, t)}} \right\} \quad (3.3)$$

with w_i the weight associated with velocity \mathbf{c}_i in the underlying LB lattice^[152] and $\Delta \mu_i^{ex}(\mathbf{r}, t) = \mu^{ex}(\mathbf{r} + \mathbf{c}_i \Delta t, t) - \mu^{ex}(\mathbf{r}, t)$ if $\mathbf{r} + \mathbf{c}_i \Delta t$ belongs to the fluid phase, while $p_i(\mathbf{r}, t) = 0$ otherwise. The first term accounts for advection by the fluid, whereas the term between curly brackets is specific to the tracer and includes both the effect of diffusion and migration under the influence of the external and internal electric fields (at the present level of description, $\mu^{ex} = qe\psi$ with q the valence of the tracer and ψ the potential arising from the surface charges and major ions). More precisely, the advective contribution is computed from the LB populations as:

$$p_i^{adv}(\mathbf{r}, t) = \frac{f_i(\mathbf{r}, t)}{\rho(\mathbf{r}, t)} - w_i \quad (3.4)$$

where $\rho(\mathbf{r}, t) = \sum_i w_i f_i(\mathbf{r}, t)$ is the local density of the fluid, and the λ parameter in Eq. 3.3 is related to the diffusion coefficient D of the tracer via:

$$\lambda = \frac{4D}{c_s^2 \Delta t} \quad (3.5)$$

with c_s the speed of sound associated with the LB lattice. As a result, any property P will be propagated following the same dynamics as Eq. 2.9. We now complement this algorithm with the approach of Ref. 114 for adsorption/desorption at the solid-liquid interface. To that end, we introduce for interfacial fluid nodes a propagated quantity $P_{\text{ads}}(\mathbf{r}, t)$ associated with adsorbed particles. It is updated according to:

$$P_{\text{ads}}(\mathbf{r}, t + \Delta t) = P_{\text{ads}}(\mathbf{r}, t)(1 - p_d) + P(\mathbf{r}, t)p_a \quad (3.6)$$

where $p_a = k_a \Delta t / \Delta x$ and $p_d = k_d \Delta t$, with k_a and k_d the rates defined in Eq. 3.1. Conversely, the evolution of the propagated quantity for mobile species is modified to:

$$P(\mathbf{r}, t + \Delta t) = P^*(\mathbf{r}, t + \Delta t) - P(\mathbf{r}, t)p_a + P_{\text{ads}}(\mathbf{r}, t)p_d \quad (3.7)$$

with P^* defined in Eq. 3.2.

The combination of Eqs. 3.2-3.7 therefore corresponds to the evolution of particles according to the coupled diffusion-advection-migration and adsorption/desorption equations 2.9 and 3.1 for tracers. However, one can propagate properties beyond the mere density of particles. Indeed, a proper choice of P (and corresponding P_{ads}), defined by the initialization discussed below, allows the computation of the VACF. We briefly recall here the derivation of Ref. 113. The starting point is the definition of the VACF for the $\gamma \in \{x, y, z\}$ component of the velocity, which in the present case where the velocities of particles can only assume discrete values reads:

$$\begin{aligned} Z_\gamma(t) &= \langle v_\gamma^0 v_\gamma^t \rangle = \sum_{\mathbf{r}^0, c_\gamma^0} \pi(\mathbf{r}^0, c_\gamma^0) \pi(c_\gamma^t | \mathbf{r}^0, c_\gamma^0) c_\gamma^t c_\gamma^0 \\ &= \sum_{\mathbf{r}^0, c_\gamma^0} \pi(\mathbf{r}^0, c_\gamma^0) c_\gamma^0 \sum_{\mathbf{r}^t} \pi(\mathbf{r}^t, c_\gamma^t | \mathbf{r}^0, c_\gamma^0) c_\gamma^t \end{aligned} \quad (3.8)$$

Chapter 3. Moment propagation method for adsorbing/desorbing charged species

where the superscripts refer to times 0 and t and the discrete sums run over nodes and set of velocities associated with the chosen lattice. Moreover, $\pi(\mathbf{r}^0, c_\gamma^0)$ is the probability of being at node \mathbf{r}^0 , with velocity c_γ^0 and $\pi(c_\gamma^t|\mathbf{r}^0, c_\gamma^0)$ the probability to have a velocity c_γ^t , given that the particle was initially at node \mathbf{r}^0 with velocity c_γ^0 (and similarly for the joint distribution in the sum over \mathbf{r}^t). Eq. 3.8 can be rewritten by replacing $\pi(\mathbf{r}^t, c_\gamma^t|\mathbf{r}^0, c_\gamma^0)c_\gamma^t$ by the post-collisional average $\pi(\mathbf{r}^t, c_\gamma^t|\mathbf{r}^0, c_\gamma^0)\sum_i p_i(\mathbf{r}, t)c_{i\gamma} = \pi(\mathbf{r}^t, c_\gamma^t|\mathbf{r}^0, c_\gamma^0)u_\gamma^*(\mathbf{r}, t)$, with the local average tracer velocity defined by:

$$\mathbf{u}^*(\mathbf{r}, t) = \sum_i p_i(\mathbf{r}, t)\mathbf{c}_i \quad (3.9)$$

which to first order in $\beta\|\mathbf{c}_i \cdot \nabla\mu^{ex}\|\Delta t$ reduces to $\mathbf{u}^* \approx \mathbf{u} + \beta D(qe\mathbf{E} - \nabla\mu^{ex}) = \mathbf{u} + \beta Dqe(\mathbf{E} - \nabla\psi)$. We can then rewrite the VACF as a sum over all lattice nodes at time t :

$$Z_\gamma(t) = \sum_{\mathbf{r}^t} \left[\sum_{\mathbf{r}^0, c_\gamma^0} \pi(\mathbf{r}^0, c_\gamma^0)c_\gamma^0 \pi(\mathbf{r}^t|\mathbf{r}^0, c_\gamma^0) \right] u_\gamma^*(\mathbf{r}, t) = \sum_{\mathbf{r}} P(\mathbf{r}, t, \gamma)u_\gamma^*(\mathbf{r}, t) \quad (3.10)$$

which also defines the relevant probability $P(\mathbf{r}, t, \gamma)$ to be propagated for each component γ of the VACF, namely the probability to arrive at node \mathbf{r} at time t , weighted by the initial velocity of the particle. Since the particles adsorbed at the solid-liquid interface are considered as immobile (*i.e.* we neglect here surface diffusion), they do not enter directly in \mathbf{u}^* . However, the adsorption and desorption processes do contribute to the VACF via the evolution of P in Eq. 3.10, which is coupled to that of the corresponding P_{ads} – see Eqs. 3.6 and 3.7. The crucial step is then the definition of the initial values of both propagated quantities. Specifically, this is achieved by the following choice:

$$P(\mathbf{r}, 1, \gamma) = \sum_i \frac{e^{-\beta\mu^{ex}(\mathbf{r}-\mathbf{c}_i\Delta t)}}{Q} p_i(\mathbf{r}-\mathbf{c}_i\Delta t, 0)c_{i\gamma} \quad (3.11)$$

for all fluid (F) nodes, including interfacial (I) ones, with Q the partition function of the tracers, which also includes the adsorbed ones:

$$Q = \sum_{\mathbf{r} \in F \setminus I} e^{-\beta\mu^{ex}(\mathbf{r})} + \sum_{\mathbf{r} \in I} e^{-\beta\mu^{ex}(\mathbf{r})} \left(1 + e^{-\beta\Delta\mu_{\text{ads}}(\mathbf{r})} \right) \quad (3.12)$$

where $e^{-\beta\Delta\mu_{\text{ads}}} = k_a/k_d\Delta x$ defines the tracer sorption free energy. We further initialize the corresponding propagated quantity for adsorbed tracers to 0, because of their vanishing velocity.

The initial value of the VACF is simply given by

$$Z_\gamma(0) = \sum_i \frac{e^{-\beta\mu^{ex}(\mathbf{r})}}{Q} p_i(\mathbf{r}, 0)c_{i\gamma} \quad (3.13)$$

and subsequent values are computed with Eq. 3.10 where the propagated quantity is initialized via Eq. 3.11 and evolved according to Eqs. 3.2, 3.6 and 3.7. This completes the description of the algorithm. Note that this should be applied separately for each direction γ and of course for each tracer, defined in the present case by its valency q (which enters in μ^{ex}), its diffusion coefficient D (which enters in the transition probabilities p_i) and the adsorption/desorption rates k_a and k_d .

All the above algorithms have been implemented in the *Laboetie* code.

3.3 Results and Discussion

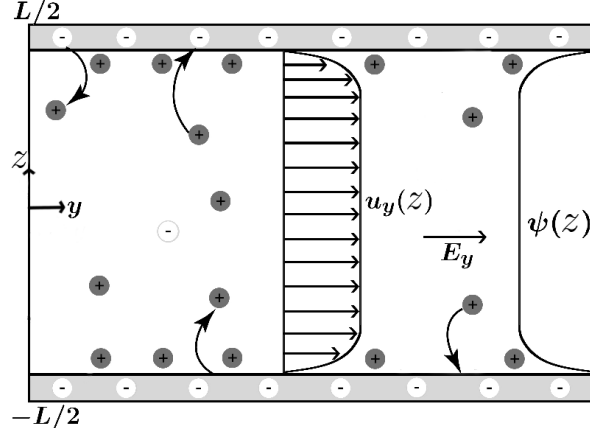


Figure 3.1 – Electro-osmotic flow in a slit pore between negatively charged walls.

The moment propagation method starts once the EOF reaches steady state, as described in Chapter 2. The *Laboetie* code was previously implemented in order to take into account the effect adsorption/desorption of only neutral tracers. We extended the code to capture the effect of electrostatic forces coupled with adsorption/desorption. This is shown schematically in Fig. 3.1. In order to validate this new methodological development, we first validate it by reproducing the results of Rotenberg *et al.*^[113] for the moment propagation method with neutral, positive and negative tracers without adsorption/desorption. Furthermore, we validate the adsorption/desorption dynamics with neutral tracers reproducing the results obtained by Levesque *et al.*^[114].

3.3.1 Dispersion of charged adsorbing tracers by an electro-osmotic flow

The system showed in Fig. 3.1 is useful to show the ability of the moment propagation method to capture the combined effects of adsorption/desorption, in addition to that of advection, electro-migration and diffusion. Specifically, we investigate the dispersion of tracers with valency $q \in \{-1, 0, +1\}$ by an electro-osmotic flow in a slit pore with parallel walls of surface charge density $\sigma e < 0$ separated by a distance L , with monovalent counterions. This system has the advantage that a number of properties can be computed analytically in the absence of added salt (see Chapter 2). In particular, the electrostatic potential in the direction perpendicular to the surfaces is given by: $\psi(z) = \psi(L/2) + \frac{k_B T}{e} \ln [\cos^2(\alpha z) / \cos^2(\alpha L/2)]$, with $z \in [-L/2, +L/2]$ and where the characteristic length α^{-1} is the solution of $\frac{\alpha L}{2} \tan \frac{\alpha L}{2} = \pi |\sigma| L l_B$ with the Bjerrum length $l_B = e^2 / 4\pi \epsilon_0 \epsilon_r k_B T$. In the presence of an applied electric field E_y parallel to the surfaces, the steady-state profile is governed by the balance between the electrostatic force $e\rho_+(z)E_y$ (since only monovalent cations are present in the fluid) and viscous force $\eta u_y''(z)$, resulting in the electro-osmotic flow:

$$u_y(z) = \frac{eE_y}{2\pi\eta l_B} \ln \frac{\cos(\alpha z)}{\cos(\alpha L/2)} \equiv u_{ref} h(z) \quad (3.14)$$

which also defines the reference velocity $u_{ref} := eE_y / 2\pi\eta l_B$ and the scaling function h . For small surface charge density ($\alpha L \rightarrow 0$), the velocity profile is almost parabolic, $u_y(z) \sim$

Chapter 3. Moment propagation method for adsorbing/desorbing charged species

$u_{ref} \frac{(\alpha L)^2}{8} \left[1 - \frac{4z^2}{L^2} \right]$, as in the case of a Poiseuille flow (applied pressure gradient instead of electric field, which corresponds of course to a different prefactor).

The fraction of adsorbed tracers f_{ads} (or equivalently of mobile tracers $f_{mob} = 1 - f_{ads}$) depends on the surface charge and distance between surfaces via the product αL , as well as on their valency q and the ratio $k_a/k_d L$. More generally, the equilibrium distribution of tracers within the pore is given by the normalized Boltzmann weights:

$$B_q(\xi) = \frac{B_q^*(\xi)}{\int_{-1/2}^{1/2} B_q^*(\xi) d\xi + \frac{k_a}{k_d L} [B_q^*(\frac{1}{2}) + B_q^*(-\frac{1}{2})]} \quad (3.15)$$

with $\xi = z/L \in [-1/2, +1/2]$ and

$$B_q^*(\xi) = e^{-qe\psi(\xi)/k_B T} = \left[\frac{\cos(\alpha L \xi)}{\cos(\alpha L/2)} \right]^{-2q} \quad (3.16)$$

The integral in the denominator of Eq. 3.15 can be performed analytically for $q \in \{-1, 0, +1\}$, with the results $(1 + \frac{\sin \alpha L}{\alpha L}) / (1 + \cos \alpha L)$, 1 and $\frac{\sin \alpha L}{\alpha L}$ respectively. The variation of the fraction of adsorbed tracers with αL and $k_a/k_d L$ will be discussed below.

From the dynamical point of view, we will analyze two properties relevant in practice for the transport of tracers, namely the average velocity and the dispersion coefficient, in the direction of the flow:

$$\bar{v}_{y,q} = \int_{-1/2}^{1/2} B_q(\xi) [\beta D q E_y + u_{ref} h(\xi)] d\xi \quad (3.17)$$

and

$$D_{y,q} = \int_0^\infty \langle [v_{y,q}(0) - \bar{v}_{y,q}] [v_{y,q}(t) - \bar{v}_{y,q}] \rangle dt \quad (3.18)$$

Both can be determined from the VACF (computed in the following with the moment propagation method) as $\bar{v}_{y,q} = \sqrt{Z_y(\infty)}$ and

$$D_{y,q} = \int_0^\infty [Z_{y,q}(t) - Z_{y,q}(\infty)] dt \quad (3.19)$$

for each tracer q with $Z_{y,q}(\infty) = \lim_{t \rightarrow \infty} Z_{y,q}(t)$.

3.3.2 Validation

We first reproduced the simulation of Ref. 113, in the absence of adsorption for charged tracers, which were performed with D3Q19 lattice for $c_s^2 = 1/3(\Delta x/\Delta t)^2$ on $N_x \times N_y \times N_z = 5 \times 5 \times 66$ lattice points which have three solid sheets on each side, for $\alpha L = 1.98$. The distance between walls is thus $L = N_z - 6 = 60\Delta x$. A Bjerrum length $l_B/\Delta x = 0.4$, a bulk diffusion $D = 0.05 (\Delta x^2/\Delta t)$ were chosen. An electric field parallel to the walls with $\beta e E_y \Delta x = 0.05, 0.1$ and 0.15 was applied. Once steady state is achieved we recover the EOF as discussed in Chapter 2. The moment propagation method allows us to compute easily the VACF, which can then be linked to the time-dependent diffusion coefficient via

$$D_z(t) = \int_0^t dt' Z_z(t'). \quad (3.20)$$

Chapter 3. Moment propagation method for adsorbing/desorbing charged species

$D_z(t)$ is a quantity which can be easily measured using NMR thanks to pulsed field gradients and it is often applied to quantify the surface-to-volume ratio of porous media^[153]. In the case of neutral tracers, an analytical solution exists, namely

$$D_z(t)/D = \frac{8}{\pi^2} \sum_{n=0}^{\infty} \frac{1}{(2n+1)^2} \exp \left[-(2n+1)^2 \frac{\pi^2 D t}{L^2} \right]. \quad (3.21)$$

The corresponding numerical results are illustrated with black upward triangles in Fig. 3.2 and good agreement is found between the theory and the simulation. Moreover, we notice that the time dependent diffusion coefficient decays faster for anions than for neutral tracers. This is due to the repulsion from the negatively charged walls which confine the tracers in a smaller region resulting in a faster memory loss of their initial velocity. Finally, $D_z(t)$ for the cations exhibits a long time tail. Indeed, the initial part of the decay is explained via the confinement in the vicinity of one surface, whereas the longer tail is due to the escape from one surface to the other.

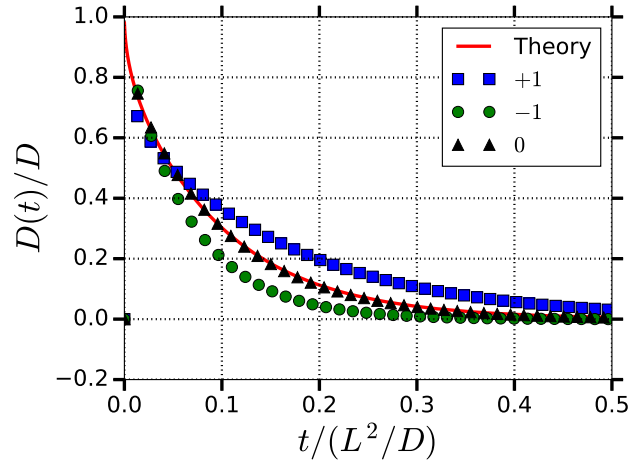


Figure 3.2 – Time-dependent diffusion coefficient in the direction normal to the surfaces $D_z(t) = \int_0^t dt' Z_z(t')$ for anions, neutral and cations for $\alpha L = 1.98$. The red line is analytical result for neutral tracers as given by Eq. 3.21.

The dispersion coefficient in the direction of the flow is computed using Eq. 3.19. In this geometry, for all cases the dispersion coefficient increases quadratically with the Péclet number Pe , more precisely as:

$$\frac{D_y}{D} = f_{mob} + f(\alpha L, q) \times Pe^2 \quad (3.22)$$

which defines the prefactor $f(\alpha L, q)$, which also depends on the adsorption/desorption rates k_a and k_d , and where $Pe = L\bar{u}/D$. The average velocity \bar{u} is defined as:

$$\bar{u} = \frac{1}{L} \int_{-L/2}^{L/2} u_y(z) dz. \quad (3.23)$$

Then, following De Leebeck and Sinton for the case of a cylindrical channel^[154], one can

Chapter 3. Moment propagation method for adsorbing/desorbing charged species

obtain (see Ref. 113) the expression for the dispersion factor for a slit pore in the no-adsorption case:

$$f(\alpha L, q, k_a = 0) = - \int_{-1/2}^{1/2} d\xi B_q(\xi) g_q(\xi) \int_0^\xi d\xi' \frac{1}{B_q(\xi')} \int_0^{\xi'} d\xi'' B_q(\xi'') g_q(\xi'') \quad (3.24)$$

where $g_q(\xi) = [u_y(\xi) + \beta D q e E_y - \bar{v}_{y,q}] / \bar{u}$ measures the local deviation from the average velocity. Comparison between the numerical results carried out with *Laboetie* (symbols) and solution of Eq. 3.24 (line) is presented in Fig. 3.3. The good agreement between the numerical and analytical results validates the correct implementation of the method in the *Laboetie* code without adsorption/desorption. We now turn to the validation of the latter for neutral tracers in a Poiseuille (*i.e.* pressure driven) flow as in Ref. 114.

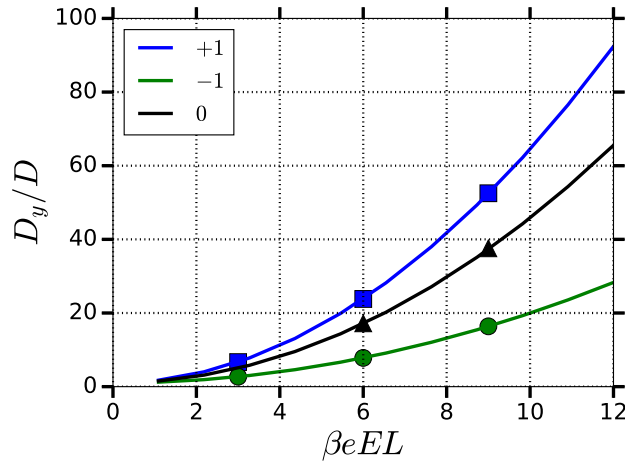


Figure 3.3 – Dispersion coefficient by an EOF (see text for details) from moment propagation (symbols) and Eq. 3.24 (line). Anions are less dispersed than neutral and cations, because they are concentrated in the centre of the slit, where the flow is more homogeneous. Increasing the charge density increases both the dispersion coefficient and the difference between tracers of different charge.

We carried out the same simulations as in Ref. 114, where the slit pore has a width $L = 100\Delta x$, with no surface charge at the walls and a bulk diffusion coefficient $D = 10^{-2}\Delta x^2/\Delta t$. The adsorption rate $k_a = 10^{-1}\Delta x/\Delta t$ and decreasing desorption rates $k_d\Delta t = 10^{-2}, 10^{-3}$, and 10^{-4} . This results in an increasing fraction of adsorbed tracers f_a of approximately 16%, 66%, and 95%, respectively. This fraction is defined for neutral tracers as

$$f_a = \left(1 + \frac{k_d L}{2k_a}\right)^{-1} \quad (3.25)$$

The effect of a pressure gradient was studied on the system. The Poiseuille flow induces a Taylor-Aris dispersion^[155,156] of the tracers with a dispersion coefficient D_y , which is known exactly in the presence of adsorption and desorption in the simple slit geometry

$$\frac{D_y}{D} = 1 + Pe^2 \left[\frac{102\chi^2 + 18\chi + 1}{210(1 + 2\chi)^3} + \frac{D}{L^2 k_d} \frac{2\chi}{(1 + 2\chi)^3} \right] \quad (3.26)$$

where $\chi := k_a/k_d L$. Fig. 3.4 shows that there is perfect agreement between Eq. 3.26 and the numerical results, as it was also found in Ref. 114.

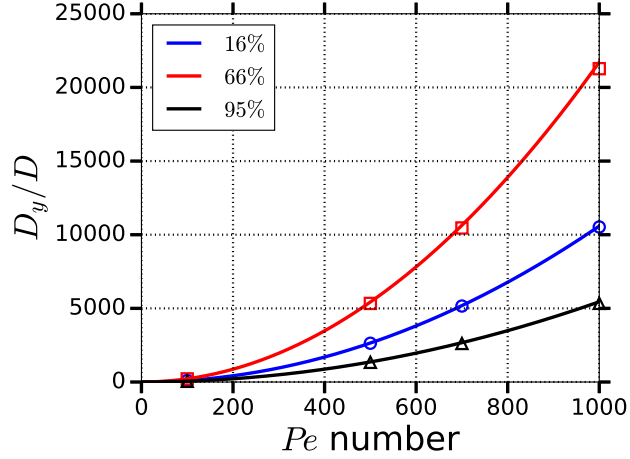


Figure 3.4 – Dispersion coefficient of neutral tracers in a slit pore in the direction of the flux, normalized by the bulk diffusion coefficient, as a function of the Péclet number, as extracted from our LB scheme (symbols) and from the exact results (lines). Several fractions of adsorbed tracers, or sorption strength, f_a , defined in Eq. 3.25, are presented: blue circles, 16%; red squares, 66%; and black upward triangles, 95%.

The adsorption/desorption dynamics of the code was thus validated. We can now turn to the study of the effect of adsorption/desorption effects on neutral or charged adsorbing/desorbing tracers, which experience electrostatic interactions and the effect of electrokinetic flows.

3.3.3 Simulation parameters

We use the standard D3Q19 lattice, (see Chapter 2). The associated speed of sound is $c_s^2 = \frac{1}{3} \left(\frac{\Delta x}{\Delta t}\right)^2$.^[125] We use $N_x \times N_y \times N_z = 5 \times 5 \times 106$ lattice points, with three layers of solid nodes on each side. The distance between the solid-liquid interfaces is thus $L = (N_z - 6)\Delta x = 100\Delta x$. Periodic boundary conditions are used in all directions. The relaxation time in the collision operator of the LB scheme is chosen as $\tau = \Delta t$ (with Δt the time step); this corresponds to a kinematic viscosity $\nu = \frac{1}{6} \frac{\Delta x^2}{\Delta t}$. The diffusion coefficient of the counterions and all the tracers is $D = 0.05 \frac{\Delta x^2}{\Delta t}$, which ensures that the Schmidt number $Sc = \nu/D$ is large, as in the case for small ions in water. In order to resolve the variations of the electrostatic potential, ionic concentrations and velocities over a distance α^{-1} , we use a lattice spacing $\Delta x = 2.5 l_B$. Since the Bjerrum length in water at room temperature is $l_B \approx 7\text{\AA}$, the distance between walls is $L = 100\Delta x \approx 175\text{ nm}$. Simulations are performed for 4 surface charge densities, namely $2N_x N_y \sigma \Delta x^2 = -0.1, -1.0, -2.0$ and -5.0 corresponding to $\alpha L = 0.96, 2.29, 2.63$ and 2.91 . For each case, the electric field is applied in the y direction with magnitude $\beta e E_y \Delta x = 0.0$ to 0.15 in reduced units.

Finally, once the steady-state is reached in each case with LBE, the populations f_i are used in the moment propagation equations (see Eq. 3.3 and 3.4) for 3 different tracers with valency $q \in \{-1, 0, +1\}$ to obtain the corresponding VACFs, from which the average velocity $\bar{v}_{y,q}$

Chapter 3. Moment propagation method for adsorbing/desorbing charged species

and dispersion coefficient $D_{y,q}$ are obtained as explained above. For each tracer, 4 different simulations were carried out to investigate the effect of adsorption/desorption. In addition to the reference case without adsorption ($k_a\Delta t/\Delta x = 0$), we consider a finite adsorption rate $k_a\Delta t/\Delta x = 10^{-1}$ and three desorption rates $k_d\Delta t = 10^{-2}, 10^{-3}$ and 10^{-4} .

3.3.4 Fraction of adsorbed tracers

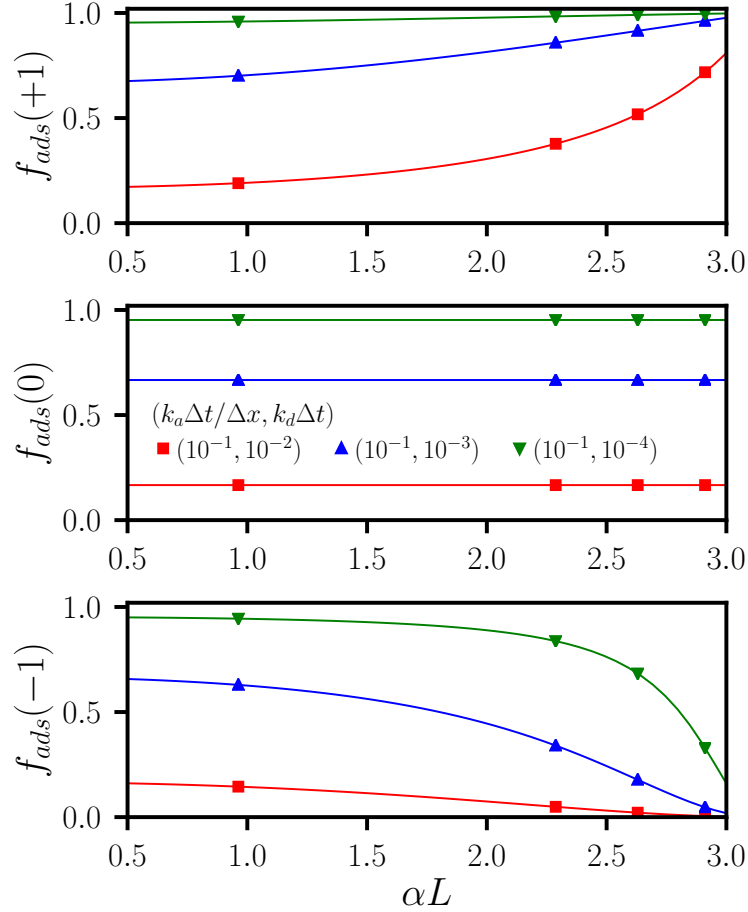


Figure 3.5 – Fraction of adsorbed tracers f_{ads} with valency $q = +1$ (top), 0 (middle) and -1 (bottom), as a function of αL which quantifies the strength of electrostatic interactions with the walls (see section 3.3.1). In each panel, we consider a finite adsorption rate $k_a\Delta t/\Delta x = 10^{-1}$ and three desorption rates: $k_d\Delta t = 10^{-2}$ (red), 10^{-3} (blue) and 10^{-4} (green). In the last case simulated in the present work (without adsorption), obviously $f_{ads} = 0$ regardless of the tracer valency (not shown). The lines are computed from Eq. 3.15 and the symbols indicate the values of αL corresponding to the simulated systems.

Before discussing the dynamical properties, we first summarize the equilibrium fraction of adsorbed tracers for the considered systems in Figure 3.5, which is calculated from the analytical expression Eq. 3.15. For given electrostatic conditions (fixed αL), f_{ads} increases with increasing k_a/k_d for all tracers. For fixed k_a/k_d , the variation of f_{ads} with the electrostatic conditions depends on the valency of the tracer: f_{ads} does not depend on αL for neutral tracers, while for the present case of a negatively charged surface it increases (resp. decreases)

with αL for cations (resp. anions). This is a direct consequence of the effect of the surface charge density on the concentration of mobile tracers at the surface, which are in equilibrium with the adsorbed ones.

3.3.5 Electro-osmotic flow profile

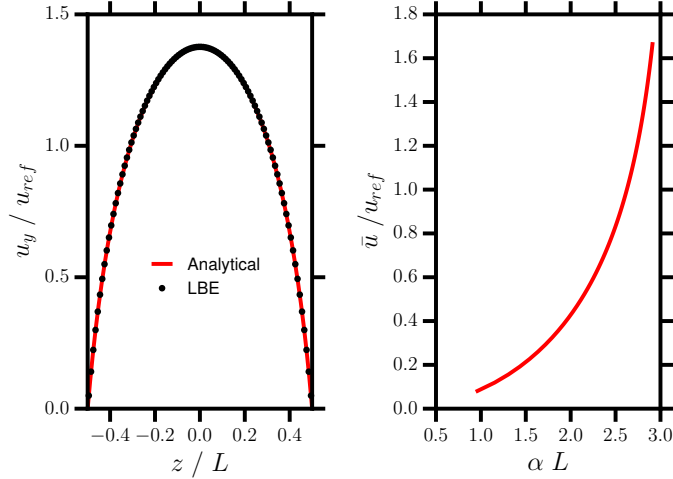


Figure 3.6 – On the left: electro-osmotic flow profile in a slit pore with uniformly charged walls and no added salt (counterions only, in the presence of an applied electric field along the surfaces (see text for details). The Lattice-Boltzmann Electrokinetics simulations, normalized by the reference velocity $u_{ref} = eE_y / 2\pi\eta l_B$, are compared with the analytical solution Eq. 3.14. On the right: average fluid velocity \bar{u} , normalized by the reference velocity u_{ref} , as a function of αL .

Figure 3.6a reports the electro-osmotic flow profile for an applied electric field $\beta e E_y \Delta x = 0.1$ and a surface charge density $2N_x N_y \sigma \Delta x^2 = -2.0$. Together with the above simulation parameters, this corresponds to $\alpha L = 2.63$. As expected from previous work on a nearly identical system^[113], the LBE results are in excellent agreement with the analytical solution Eq. 3.14. The fluid velocity is maximal near the center and more inhomogeneous near the walls (where it vanishes). Figure 3.6b then shows the variation of the average velocity:

$$\bar{u} = \frac{1}{L} \int_{-L/2}^{L/2} u_y(z) dz \quad (3.27)$$

with $u_y(z)$ given by Eq. 3.14, as a function of αL . As expected, the average electro-osmotic flow increases with increasing surface charge density. In particular, it vanishes as $u_{ref} \frac{(\alpha L)^2}{12}$ in the limit of small surface charges ($\alpha L \rightarrow 0$).

3.3.6 Average tracer velocity

Figure 3.7 indicates the average velocity $\bar{v}_{y,q}$ of tracers with valency $q \in \{-1, 0, 1\}$ as a function of the Péclet number $Pe = \bar{u}L/D$ with \bar{u} the average fluid velocity, for a surface charge density corresponding to $\alpha L = 2.63$ and adsorption/desorption rates ($k_a \Delta t / \Delta x, k_d \Delta t$) =

($10^{-1}, 10^{-3}$). We first note the excellent agreement between the simulation (LBE/MP) results and the analytical solution Eq. 3.17 for all tracers. Even though the average velocity depends only on the limit of the VACF at long times, this provides a first validation of the proposed MP algorithm combining electrokinetics and adsorption/desorption. We further note that the latter decreases the average velocity, by an amount which depends on the charge of the tracer. More precisely, it follows from Eqs. 3.15 and 3.17 that the average velocity is simply equal to the product of the average velocity without adsorption/desorption (previously studied in Ref. [113]) and the fraction of mobile tracers, $f_{mob} = 1 - f_{ads}$. The proportionality between the average tracer velocity and average fluid velocity suggests to investigate how the ratio $\bar{v}_{y,q}/\bar{u}$ depends on the surface charge and the adsorption properties. This is illustrated in Figure 3.8. The good agreement with analytical results in all cases (varying αL , q , k_a and k_d) further validates the present MP scheme.

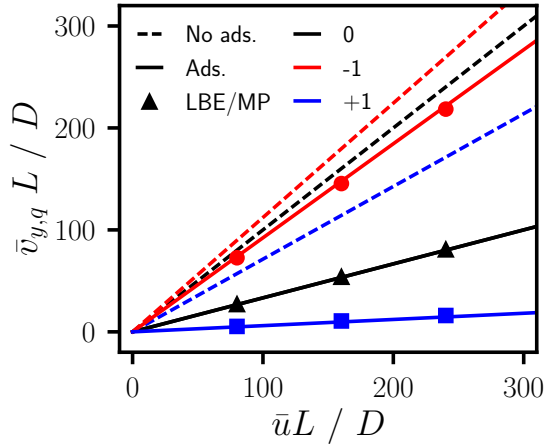


Figure 3.7 – Average tracer velocity, adimensionalized as a Péclet number $\bar{v}_{y,q}L/D$ as a function of the actual Péclet number $Pe = \bar{u}L/D$ with \bar{u} the average fluid velocity, for tracers with valency $q \in \{-1, 0, 1\}$, for a surface charge density corresponding to $\alpha L = 2.63$ and adsorption/desorption rates $(k_a\Delta t/\Delta x, k_d\Delta t) = (10^{-1}, 10^{-3})$. The simulation results (symbols) are compared to the analytical results Eq. 3.17 (solid line). In each case, the analytical solution without adsorption (dashed line).

In the simpler case of neutral tracers, the average tracer velocity without adsorption is equal to the average fluid velocity. In the presence of adsorption, the ratio $\bar{v}_{y,0}/\bar{u}$ is independent of the surface charge and simply equal to the fraction of mobile tracers, which decreases as k_d increases for fixed k_a . Similarly, the ratio $\bar{v}_{y,q}/\bar{u}$ also decreases with increasing adsorption in the case of positive and negative tracers. However, the behaviour is more complicated since the mobile fraction as well as the distribution of charged tracers within the pores (hence the flow) depends on the surface charge.

For positive tracers, which are located closer to the surface where the fluid is slower than near the center of the pore, the ratio $\bar{v}_{y,+1}/\bar{u}$ decreases with increasing surface charge (αL). This ratio is larger than 1 for small surface charge, because the motion of the counterions ($q = +1$) is dominated by the direct effect of the electric field. Specifically, in this regime $\bar{v}_{y,+1} \sim \beta D e E_y$, while $\bar{u} \sim \frac{e E_y}{2\pi\eta l_B} \frac{(\alpha L)^2}{12}$ so that their ratio diverges as $(\alpha L)^{-2}$. It gradually vanishes as the surface charge increases, because the motion becomes dominated by the advection by

the electro-osmotic flow, which is more efficient for the fluid as a whole than for the cations located on average closer to the surface.

In contrast, co-ions ($q = -1$) are located on average closer to the center of the pore and the direct effect of the electric field is to drive them in the direction opposite to the electro-osmotic flow. As a result, the ratio $\bar{v}_{y,-1}/\bar{u}$ is negative for small surface charge and diverges as $-(\alpha L)^{-2}$ for $\alpha L \rightarrow 0$, but is positive for large αL as the motion of co-ions becomes dominated by advection by the electro-osmotic flow. This ratio tends to 1 as $\alpha L \rightarrow \pi$ regardless of adsorption, since the fraction of mobile co-ions also goes to 1 in this limit where both $\bar{v}_{y,-1}$ and \bar{u} are dominated by the flow near the center of the pore.

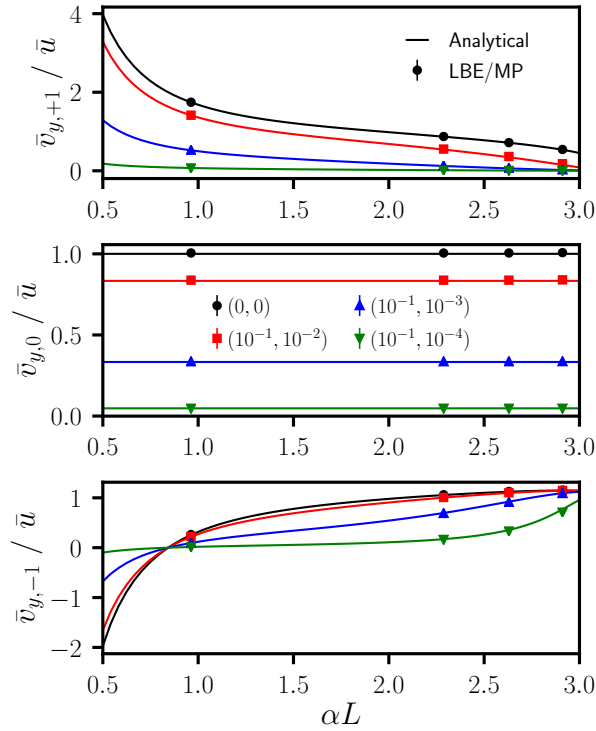


Figure 3.8 – Average tracer velocity $\bar{v}_{y,q}$, normalized by the average flow velocity \bar{u} , for charged adsorbing tracers with valency $q = +1$ (top), 0 (middle) and -1 (bottom), as a function of the strength of electrostatic interactions with the walls (αL). In each case, simulation results (symbols) for various adsorption/desorption rates are compared with the analytical results Eq. 3.17 (lines).

3.3.7 Diffusion coefficient

We now consider the dynamics of tracers in the direction perpendicular to the surfaces by considering $D_z(t)$. We verified that results for neutral tracers are independent of the surface charge and we present how $D_z(t)$ decays when $k_a \Delta t / \Delta x = 10^{-1}$ and $k_d \Delta t = 10^{-2}, 10^{-3}$ and 10^{-4} change for a given surface charge value corresponding to $\alpha L = 0.96$. This is shown in Fig. 3.9. We verified that at $t = 0$, $D_z(t)/D$ corresponds to $f_{mob} = 1 - f_{ads}$. Indeed, in Fig. 3.9 we see for instance that the red curve gives $D_z(0)/D \approx 0.8$, which corresponds to the red curve value $f_{ads} \approx 0.2$ in Fig. 3.5. Furthermore, the more tracers adsorb, the longer it takes for them to relax. Similarly, as we can see in Fig. 3.10, $D_z(t)$ decays faster for positive

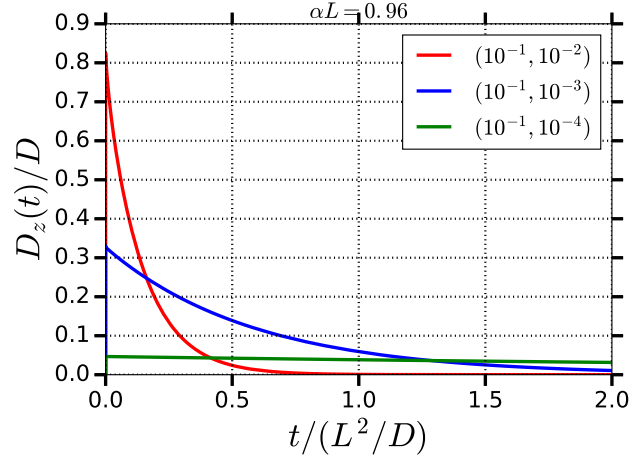


Figure 3.9 – Time-dependent diffusion coefficient in the direction normal to the surfaces $D_z(t) = \int_0^t dt' Z_z(t')$ for neutral tracers, for $\alpha L = 0.96$ and $\beta e E_y \Delta x = 0.1$. The adsorption/desorption rates are $k_a \Delta t / \Delta x = 10^{-1}$ and $k_d \Delta t = 10^{-2}, 10^{-3}$ and 10^{-4} .

tracers, for lower values $k_d \Delta x$, which correspond to more adsorption. We also observe that as αL increases, the relaxation time also increases. Indeed, as the walls are negatively charged, tracers experience an electrostatic attraction towards them and thus diffuse longer. Once again we verified that at $t = 0$, $D_z(t)/D$ corresponds to $f_{mob} = 1 - f_{ads}$. In addition, we can see in Fig. 3.5 that the red and blue curve increase as αL increases, which implies that $D_z(0)$ should decrease as αL increases and indeed this is what is observed in Fig. 3.10.

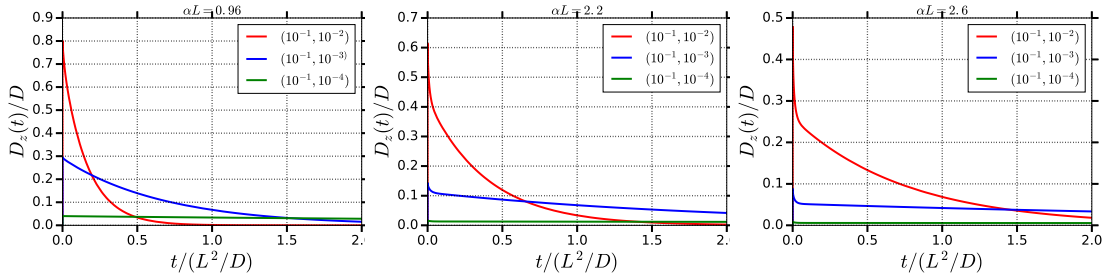


Figure 3.10 – Time-dependent diffusion coefficient in the direction normal to the surfaces $D_z(t) = \int_0^t dt' Z_z(t')$ for positive tracers, for $\alpha L = 0.96$ (left figure), 2.2 (centre figure) and 2.6 (right figure) and $\beta e E_y \Delta x = 0.1$. The adsorption/desorption rates are $k_a \Delta t / \Delta x = 10^{-1}$ and $k_d \Delta t = 10^{-2}, 10^{-3}$ and 10^{-4} .

Likewise, we can see in Fig. 3.5 that for negative tracers all the curves decrease as αL increases, implying that $D_z(0)$ should increase as αL increases. Once again this is what we observe in Fig. 3.11. Furthermore, as we can see in Fig. 3.11, negative tracers are repelled by the negatively charged walls and thus take less time to diffuse in the z -direction, as αL increases. Overall, both adsorption/desorption and the tracer's charge strongly affect the time for them to relax and reach steady state. It is thus clear that these effects cannot be neglected.

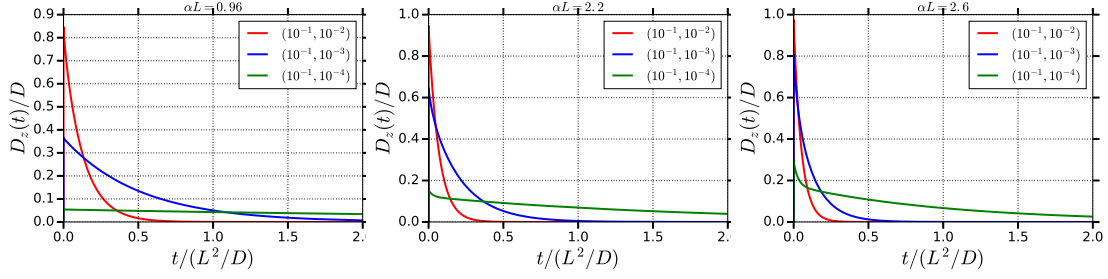


Figure 3.11 – Time-dependent diffusion coefficient in the direction normal to the surfaces $D_z(t) = \int_0^t dt' Z_z(t')$ for negative tracers, for $\alpha L = 0.96$ (left figure), 2.2 (centre figure) and 2.6 (right figure) and $\beta e E_y \Delta x = 0.1$. The adsorption/desorption rates are $k_a \Delta t / \Delta x = 10^{-1}$ and $k_d \Delta t = 10^{-2}, 10^{-3}$ and 10^{-4} .

3.3.8 Dispersion coefficient

Due to their diffusion in the direction perpendicular to the surface, tracers experience various streamlines with different velocities. The adsorption/desorption processes also participate in the dispersion since they offer other possibilities for tracers to adopt different states (here the adsorbed species are considered as immobile, but surface diffusion would also contribute). The dispersion coefficient in the direction of the flow, D_y , normalized by the diffusion coefficient D , as a function of the Péclet number $\bar{u}L/D$, is shown for tracers with $q \in \{-1, 0, 1\}$, for a surface charge density corresponding to $\alpha L = 2.63$. In this geometry the dispersion coefficient behaves according to Eq. 3.22, while in the absence of electric field ($E_y = 0$) the dispersion coefficient is simply $D_y = f_{mob}D$, this is not the case in the presence of an applied field.

The simulation results reported as symbols in Figure 3.12 are in good agreement with this analytical result, reported as the dashed lines. In this no-adsorption case, also discussed in Section 3.3.2, counterions ($q = +1$) are more dispersed than neutral tracers ($q = 0$) because they are mainly located near the walls, where the velocity profile is more inhomogeneous (see Figure 3.6). The opposite behaviour is observed for co-ions ($q = -1$), which are mainly located near the center where the flow is more homogeneous.

In the general case with adsorption, Eq. 3.24 does not apply, and the “curvature” $f(\alpha L, q)$ must be determined numerically by fitting the simulation results to Eq. 3.22. Note that in each case the only fitting parameter is $f(\alpha L, q)$ since $f_{mob} = 1 - f_{ads}$ is known independently (see Figure 3.5). The solid lines in Figure 3.12 illustrate in this particular case that the behaviour remains indeed quadratic with applied field (hence Pe) and that the effect of adsorption depends strongly on the valency of the tracer. For example, in this case dispersion is increased by adsorption/desorption for neutral and negative tracers, while it is decreased for positive ones. This dependence is shown in more detail in Figure 3.13 which reports $f(\alpha L, q)$ for the same adsorption/desorption rates as for the discussion of the average velocity (Figure 3.8). It is less easy to understand than the average velocity, which boils down to the combined effects of the fraction of mobile species and their individual mobility.

In the limit of small surface charges ($\alpha L \rightarrow 0$) where the flow profile is almost parabolic and where the tracer distribution is (almost) flat even for charged tracers, one recovers the result for a Poiseuille flow, namely $f = \frac{1}{210}$. Already in this regime the effect of adsorption/desorption is not simple: Consistently with the analytical result for Taylor-Aris dispersion by a Poiseuille flow^[155–157], f does not vary monotonically with *e.g.* decreasing desorption

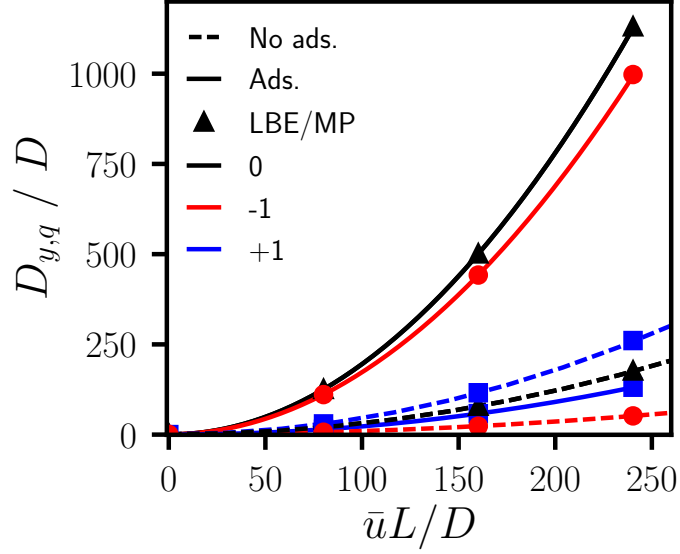


Figure 3.12 – Dispersion coefficient, normalized by the diffusion coefficient, $D_{y,q}L/D$ as a function of the Péclet number $\bar{u}L/D$, for tracers with valency $q \in \{-1, 0, 1\}$, for a surface charge density corresponding to $\alpha L = 2.63$, without adsorption (dashed lines) and with adsorption/desorption rates $(k_a \Delta t / \Delta x, k_d \Delta t) = (10^{-1}, 10^{-3})$ (solid lines). The simulation results are shown as symbols, while the lines correspond to the quadratic form Eq. 3.22. In this equation, the value at zero-field $f_{mob} = 1 - f_{ads}$ corresponds to Figure 3.5; the curvature is known analytically in the no-adsorption case, see Eq. 3.24 and fitted numerically in the presence of adsorption/desorption. Results of this fitting are discussed in Figure 3.13.

rate k_d at fixed adsorption rate k_a . In this case (without any effect of charge), it further depends separately on the ratios $k_a/k_d L$ and $D/k_d L^2$ ^[84]. In the present case of charged tracers and electro-osmotic flows, the situation is even more complicated, even though one can note similar trends for all tracers in the limit $\alpha L \rightarrow 0$.

For very large surface charge densities ($\alpha L \rightarrow \pi$), f tends to decrease with increasing αL for both co- and counterions, because their distribution becomes increasingly concentrated near or away from the surface, respectively, while the electro-osmotic velocity profiles becomes flatter near the center (which also explains the less pronounced decrease of f for neutral tracers). For counterions (resp. co-ions), this is likely due to the fact that the fraction of mobile tracers then becomes very small (resp. large), see Figure 3.5, so that the average velocity becomes dominated by adsorbed (resp. mobile) tracers, which have the same vanishing (resp. large) velocity. In the cases with smaller desorption rates k_d , this decrease with αL is observed for relatively small values in the case of co-ions ($q = +1$), it is preceded for counter-ions ($q = -1$) by an increase with αL and is almost not visible for neutral tracers. For the largest desorption rate, one observes for all tracers a maximum as a function of αL . Overall, the interplay between adsorption/desorption, migration and advection by the electro-osmotic flow results in a very rich behaviour of the dispersion coefficient – more difficult to interpret than the average mobility. This underlines the usefulness of a numerical simulation tool to investigate the combined effects of all processes.

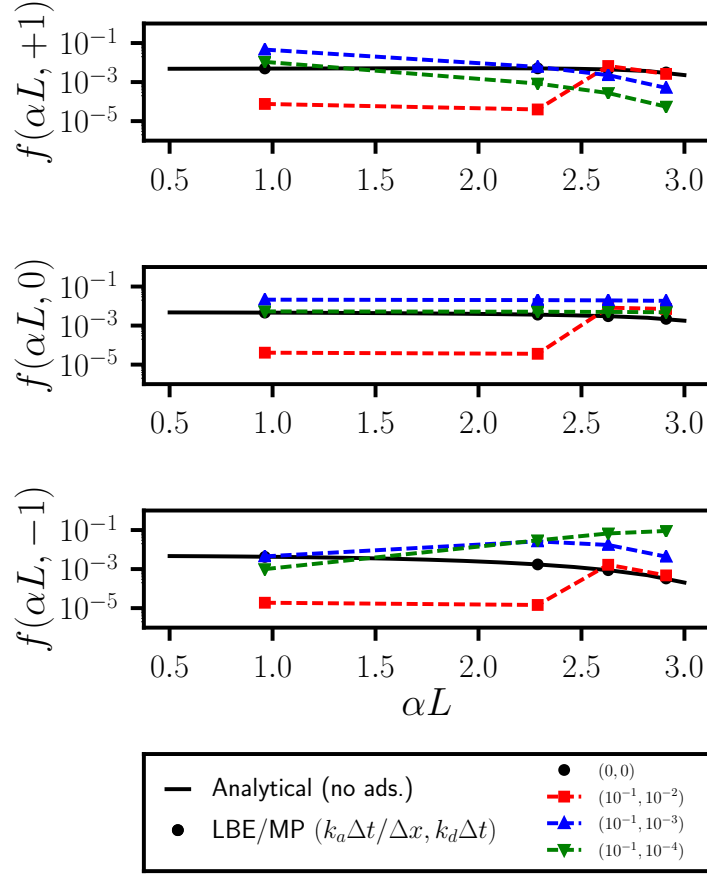


Figure 3.13 – Prefactor of the dispersion coefficient vs Péclet number, $f(\alpha L, q)$ defined by Eq. 3.22, for $q = +1$ (top), 0 (middle) and -1 (bottom). In the no-adsorption case (black), simulation results are compared to the analytical expression Eq. 3.24 (solid line). The other simulation results are for finite adsorption rate $k_a \Delta t / \Delta x = 10^{-1}$ and three desorption rates: $k_d \Delta t = 10^{-2}$ (red), 10^{-3} (blue) and 10^{-4} (green). The dashed-lines are only guide for the eyes.

3.4 Conclusion

We have extended the Moment Propagation (MP) method to capture the combined effects of adsorption/desorption of charged tracers, their migration under local and applied electric fields, as well as their advection by the local velocity of the fluid. We validated our modification with previous works^[113,114]. We thus combined previous developments for the separate description of these phenomena in particular (adsorption/desorption and charged tracers), taking advantage of the Lattice Boltzmann Electrokinetics method to capture electrokinetic effects in the underlying fluid. As a further validation, we examined the simple case of dispersion by an electro-osmotic flow in a slit-pore with charged walls and counterions in the absence of added salt, for which some properties can be determined analytically. We computed with MP the velocity auto-correlation function (VACF) of charged and neutral tracers, from which we extracted their average mobility, time-dependent diffusion coefficient and dispersion coefficient. Comparison with analytical results for the average mobility allowed to validate

Chapter 3. Moment propagation method for adsorbing/desorbing charged species

the algorithm; the diffusion coefficient for charged tracers and the dispersion coefficient then illustrates examples of property which can be provided by the MP method when no analytical results are available. For both properties, we discussed the combined effects of the surface charge, of the tracer valency and of the adsorption/desorption rates.

Futhermore, the time-dependent diffusion coefficient $D(t)$ is of particular interest in porous materials since it reflects how each tracer explores the porosity accessible to it (which depends on its valency in charged porous materials) and can be measured experimentally using NMR^[153]. As also mentioned previously, the MP method is not limited to the VACF and can be used *e.g.* to compute NMR spectra of species diffusing in porous materials^[158]. The present algorithm allows the computation of such properties for charged species undergoing adsorption/desorption, migration and advection, in simple geometries as presented here but also in more complex media. Finally, we note that we have considered here the coupling of adsorption/desorption with transport of charged tracers only, so that these processes do not influence the dynamics of the underlying fluid. While in the present case of steady-state in an infinite slit pore this would only result in the renormalization of the surface charge density, this is not true in general and a richer behaviour is expected, especially in the transient regime. In order to do this and hence describe the interplay between adsorption/desorption and electrokinetic effects, the present development of the MP method would need to be also extended to the Lattice Boltzmann Electrokinetics scheme.

From Surface Charge to Constant Potential Simulations in LBE

Contents

4.1	Ion distribution on the microscopic scale	81
4.2	Capacitor imposing a surface charge $\pm\sigma$	81
4.2.1	No salt solution	81
4.2.2	Added salt solution	83
4.2.3	Electro-osmotic flow	86
4.3	Capacitor with a constant potential difference	87
4.3.1	Boundary conditions	88
4.3.2	Case of a slit channel	89
4.3.2.1	Electrostatic Potential	89
4.3.2.2	Concentration profiles and errors	90
4.3.2.3	Electrode Capacitance	93
4.3.2.4	Electro-osmotic flow	95
4.3.3	Case of a coaxial cylindrical channel	97
4.3.3.1	Electrostatic potential	98
4.3.3.2	Electrode capacitance	101
4.3.3.3	Electro-osmotic flow	101
4.4	Conclusion	102

SO FAR the LBE method was used in order to simulate fluids confined at the nanoscale between walls bearing an identical surface charge. Indeed, it is common in the literature that the simulated systems have always an identical surface charge density in the solid region, whether colloids or channels are taken into consideration. During this PhD we extended the LBE method to simulate capacitors: as a first step we considered opposite surface charge densities at the walls. Then we modified the method to impose a constant potential difference, which is closer to the experimental situation. In this Chapter we present the development of this modification, limiting ourselves to the stationary regime. The transient regime will be addressed in the following chapter.

4.1 Ion distribution on the microscopic scale

In Chapter 2 we have extensively discussed how ions distribute in a channel and what is their corresponding electrostatic potential. Once steady state is reached, ions are distributed according to the Boltzmann distribution

$$\rho_k = n_k \exp(-z_k \phi) \quad (4.1)$$

where $\phi := \beta e \psi$ and n_k denotes a constant corresponding to the concentration where the potential reference is taken. Plugging it in the Poisson equation yields

$$\varepsilon \Delta \psi = - \sum_{k=1}^N e z_k n_k \exp(-z_k \phi) \quad (4.2)$$

which is the so-called Poisson-Boltzmann (PB) equation. In the case of a symmetric 1:1 electrolyte (*i.e.* with a monovalent salt), the PB equation may be written as

$$\nabla^2(\beta e \phi) = \kappa^2 \sinh(\beta e \phi). \quad (4.3)$$

the inverse of the Debye screening length κ is defined according to $\kappa^2 = 8\pi l_B n_{\pm}$ with the Bjerrum length $l_B = \beta e^2 / 4\pi \varepsilon$ being the distance at which the electrostatic energy between two unit charges is equal to the thermal energy. $l_B = 0.7 \text{ nm}$ in water at room temperature. When $\beta e \phi \ll 1$ the PB equation may be linearized resulting in

$$\nabla^2 \phi = \kappa^2 \phi. \quad (4.4)$$

4.2 Capacitor imposing a surface charge $\pm\sigma$

4.2.1 No salt solution

We now restrict ourselves to a slit channel whose walls are separated by a distance L and in order to simulate a capacitor, we apply an equal but opposite surface charge density on each wall respectively (*i.e.* $\pm\sigma$ on $\pm L/2$ respectively given $\sigma > 0$). In the absence of added salt the system is equivalent to a capacitor with a dielectric permittivity ε inside the channel. The PB equation then reads

$$\Delta \phi = \frac{\partial^2 \phi}{\partial z^2} = 0 \quad (4.5)$$

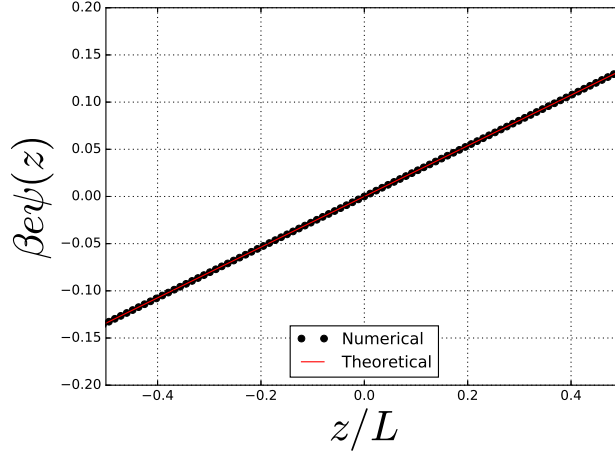


Figure 4.1 – Electrostatic potential in a slit channel due to the surface charge density $\pm\sigma\Delta x^2/e = \pm 0.11111$, for a distance $L/\Delta x = 89$ between the walls in the absence of salt. The potential is non-dimensionalized with $\beta e = e/k_B T$ and z is normalized with respect to L . The theoretical solution under PBCs is given by Eq. 4.7

L	$5.54 \times 10^{-8} \text{ m}$
$L_x = L_y$	$1.75 \times 10^{-9} \text{ m}$
ν	$1.06 \times 10^{-6} \text{ m}^2/\text{s}$
l_B	$0.7 \times 10^{-9} \text{ m}$
σ	$-8.16 \times 10^{15} \text{ m}^{-2}$

Table 4.1 – Physical data for an Electro-osmotic flow without salt in a slit channel. L is the length of the channel separating the walls, ν is the kinematic viscosity, l_B the Bjerrum length, σ the surface charge.

Gauss' law provides an information on the potential derivative at the wall, which leads to the final solution

$$\phi(z) = -4\pi l_B \sigma z \quad (4.6)$$

However, as we are working with PBCs, the solution given in Eq. 4.6 is affected and thus needs to be corrected. Indeed, in order to ensure PBCs, the electrical field $-\nabla\psi$ maintains its continuity thanks to a linear correction term. Considering that each wall has a width $d/2$ (see Fig. 4.2), *i.e.* that d is the total width of the walls, the electrostatic potential corresponding to our simulations is in fact

$$\phi_{PBC}(z) = \frac{-4\pi l_B \sigma z}{(L+d)/d}. \quad (4.7)$$

The scaling factor is then $(L+d)/d$. Fig. 4.1 illustrates the numerical result obtained and the solution given by Eq. 4.7. Perfect agreement is found between the two. The simulation was performed on $N_x \times N_y \times N_z = 3 \times 3 \times 95$ lattice points with three solid layers on each side. The distance between walls is thus $L = 89\Delta x$. A surface charge $\pm\sigma\Delta x^2 = \pm 0.11111$ was imposed at the walls and a Bjerrum length $l_B/\Delta x = 1.2$ was fixed. The corresponding physical data is shown in Table 4.1.

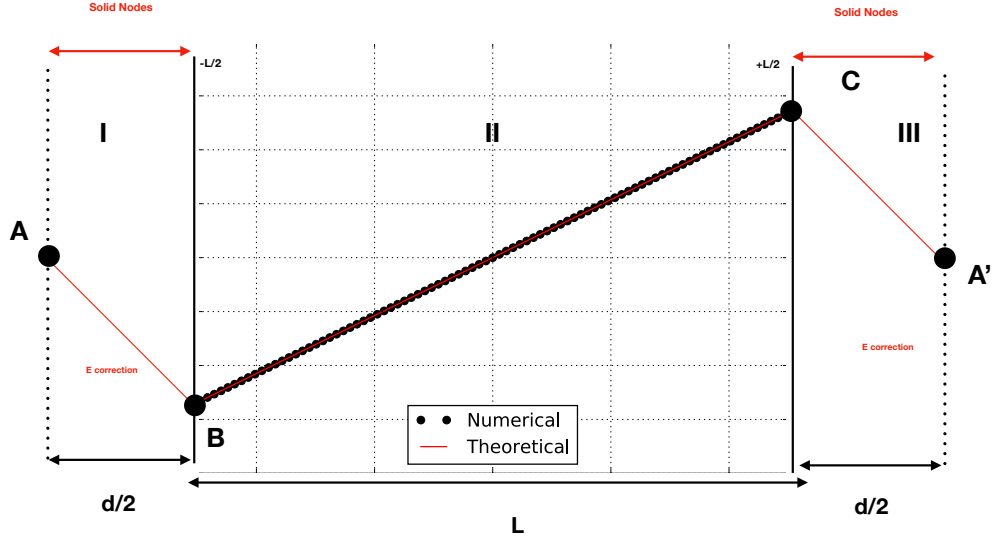


Figure 4.2 – Sketch of PBC corrections for no-salt case

4.2.2 Added salt solution

If salt is added in the slit channel, we can solve Eq. 4.4 in the low potential regime, for which a solution can be written as:

$$\phi(z) = A \exp(\kappa z) + B \exp(-\kappa z) \quad (4.8)$$

Considering the boundary conditions $\partial_z \psi(z = \pm L/2) = 4\pi l_B \sigma$, we obtain

$$\begin{cases} A\kappa \exp(\kappa L/2) - B\kappa \exp(-\kappa L/2) = 4\pi l_B \sigma \\ A\kappa \exp(-\kappa L/2) - B\kappa \exp(\kappa L/2) = 4\pi l_B \sigma \end{cases} \quad (4.9)$$

Let $\gamma := \kappa L/2$. We solve the system using Cramer's rule, *i.e.*

$$D = \begin{vmatrix} \kappa \exp(\gamma) & -\kappa \exp(-\gamma) \\ \kappa \exp(-\gamma) & -\kappa \exp(\gamma) \end{vmatrix} = -2\kappa^2 \sinh(2\gamma) \quad (4.10)$$

$$D_A = \begin{vmatrix} 4\pi l_B \sigma & -\kappa \exp(-\gamma) \\ 4\pi l_B \sigma & -\kappa \exp(\gamma) \end{vmatrix} = -8\pi l_B \sigma \kappa \sinh(\gamma) \quad (4.11)$$

$$D_B = \begin{vmatrix} \kappa \exp(\gamma) & 4\pi l_B \sigma \\ \kappa \exp(-\gamma) & 4\pi l_B \sigma \end{vmatrix} = 8\pi l_B \sigma \kappa \sinh(\gamma) \quad (4.12)$$

Hence,

$$A = \frac{D_A}{D} = \frac{4\pi l_B \sigma}{\kappa} \frac{\sinh(\gamma)}{\sinh(2\gamma)} \quad (4.13)$$

$$B = \frac{D_B}{D} = -\frac{4\pi l_B \sigma}{\kappa} \frac{\sinh(\gamma)}{\sinh(2\gamma)} \quad (4.14)$$

Therefore the solution for the potential is

$$\psi(z) = \frac{2\pi l_B \sigma}{\kappa} \frac{\sinh(\kappa z)}{\cosh(\kappa L/2)} \quad (4.15)$$

PBC Corrections

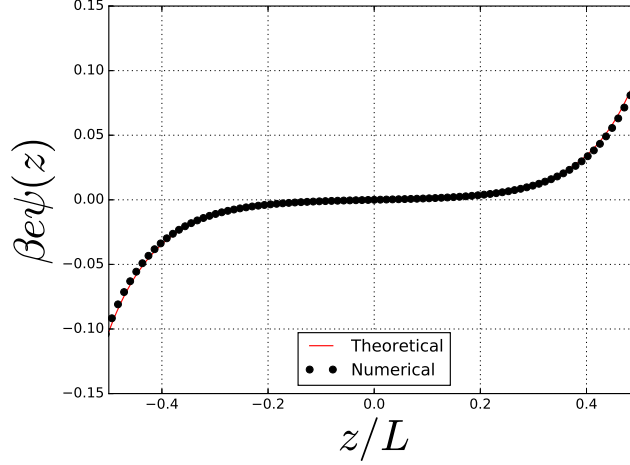


Figure 4.3 – Electrostatic potential in a slit channel due to the surface charge density $\pm\sigma\Delta x^2/e = \pm 0.05$, for a distance $L/\Delta x = 89$ between the walls, when salt is added. The salt concentration corresponds to a Debye screening length $\lambda_D/\Delta x = 8.0$. The potential is non-dimensionalized with $\beta e = e/k_B T$ and z is normalized with respect to L

Similarly to the case with no salt PBCs modify the solution of the electrostatic potential. We can write the solution for the reduced potential ϕ as:

$$\phi(z) = \beta e \psi(z) = \zeta \sinh(\kappa z) \quad (4.16)$$

where ζ is a prefactor to be determined according to the effects of the PBCs. Indeed, in order to ensure PBCs, a linear contribution of the electric field connects points B and C as illustrated in Fig. 4.4.

Let I and III denote the solid nodes of the left and right wall respectively, as shown in Fig. 4.4, and II denote the region with fluid nodes. Then in region I and III

$$\frac{\partial \psi}{\partial z} = - \frac{\psi(L/2) - \psi(-L/2)}{d} \quad (4.17)$$

where $d/2$ is the width of each wall and thus d is the distance between the two walls across the boundary conditions.

Therefore, the electric field may be written, using Gauss' law, as the difference of the electric field from both sides of the charged plane. For instance, at $z = +L/2$

$$\left. \frac{\partial \psi}{\partial z} \right|_{z=(L/2)^+} - \left. \frac{\partial \psi}{\partial z} \right|_{z=(L/2)^-} = \frac{\sigma}{\epsilon}. \quad (4.18)$$

The first term on the left-hand-side may be evaluated with Eq. 4.17, whilst the second term on the left-hand-side is computed using the derivative of Eq. 4.16 resulting in

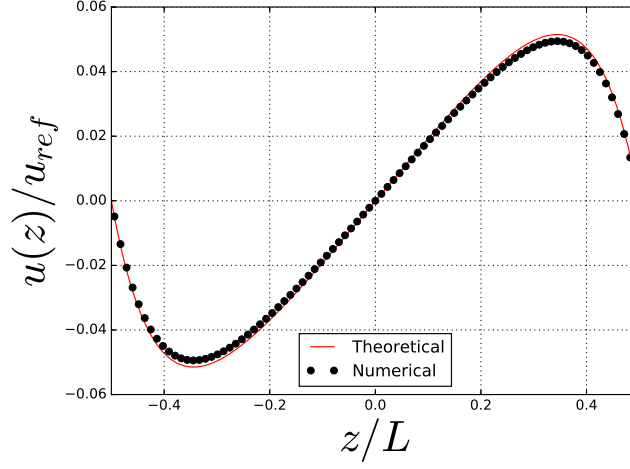


Figure 4.5 – Electro-osmotic flow profile in a slit channel with added salt due to the surface charge density $\pm\sigma\Delta x^2/e = \pm 0.05$. The flow is induced by an external electric field $\beta e\Delta x E = 1 \times 10^{-3}$ parallel to the walls. The velocity u is normalized with respect to the reference velocity $u_{ref} = \varepsilon E_y/\eta$, whereas z , which denotes the position in the fluid region, is normalized with respect to the distance L between the walls.

4.2.3 Electro-osmotic flow

As discussed in Chapter 2, if an EOF is considered in the case of a slit channel, the resulting flow is written as:

$$u(z) = \frac{\varepsilon}{\eta} E_y \psi(z) + Az + B \quad (4.22)$$

where A and B are integration constants to be determined. Given the following boundary conditions

- At $z = L/2$, $u = 0$ and $\psi = \psi(\kappa L/2)$
- At $z = -L/2$, $u = 0$ and $\psi = \psi(-\kappa L/2)$

Thus the system of equations reads

$$\begin{cases} \frac{\varepsilon E_y \zeta}{\eta} \sinh(\kappa L/2) + \frac{AL}{2} + B = 0 \\ -\frac{\varepsilon E_y \zeta}{\eta} \sinh(\kappa L/2) - \frac{AL}{2} + B = 0 \end{cases} \quad (4.23)$$

Adding the two equations yields $B = 0$ and the first equation can then be rewritten as

$$A = -\frac{2\varepsilon E_y \zeta}{\eta L} \sinh(\kappa L/2). \quad (4.24)$$

Then the velocity profile is written as follows

$$u(z) = \frac{\varepsilon E_y \zeta}{\eta} \sinh(\kappa z) - \frac{2\varepsilon E_y \zeta}{\eta L} \sinh(\kappa L/2) z, \quad (4.25)$$

which can be rearranged as

$$u(z) = \frac{\varepsilon E_y \zeta}{\eta} \left[\sinh(\kappa z) - \frac{2}{L} \sinh(\kappa L/2) z \right]. \quad (4.26)$$

Fig. 4.5 shows the electro-osmotic flow induced by an electric field $\beta e \Delta x E = 1 \times 10^{-3}$ parallel to the walls. Theoretical and numerical results are in good agreement except for the *extrema*, which are slightly overestimated by the theory. One could think that the numerical solution did not converge completely meaning that the profile is not fully developed. However, decrease of the converge criterion C (see Chapter 2), for the velocity profile, from $C = 10^{-10}$ to 10^{-15} did not show major changes in the final result.

At this point we have successfully simulated a nano-capacitor consisting of an electrolyte with monovalent salt confined between oppositely charged surfaces. However, in a real capacitor we impose the potential difference rather than the electrode charges.

4.3 Capacitor with a constant potential difference

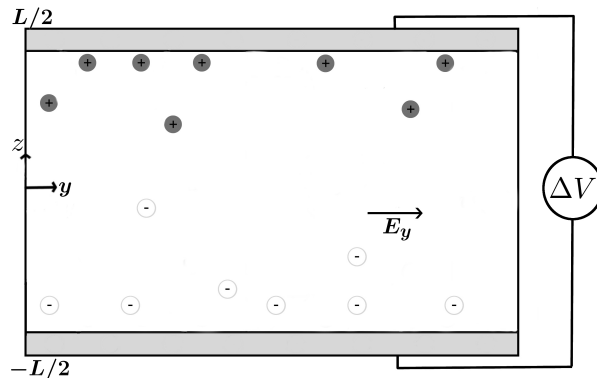


Figure 4.6 – Sketch of a capacitor

One of the aims of this work is to create a framework to simulate electrochemical experiments. Given that the experimentalists do not control the surface charge, but rather apply a potential difference between electrodes, it is necessary to allow the computational scientist to do the same. This can be achieved in the LBE method, by changing the electrostatic boundary conditions. Instead of fixing a surface charge $\pm\sigma$ on each wall, we impose two different reduced fixed potential values ϕ_1 and ϕ_2 , resulting in a reduced potential difference $\Delta V = \phi_2 - \phi_1$. This is shown schematically in Fig. 4.6. This implementation is a complete novelty in the field of LBE, although an attempt at implementing constant potential simulations coupling LB with finite differences was previously achieved^[159]. Instead of using the LF method, they resolve the PNP equations via finite differences and the NS equation via LBM. They incorporate a body force term, which creates the interaction of the EDL field with the externally applied electrical field into the discrete Boltzmann equation using the method described by Guo *et al.*^[160]. Therefore, to the best of our knowledge, we present here the first implementation of the LBE method coupling LB with LF with constant potential boundary conditions.

4.3.1 Boundary conditions

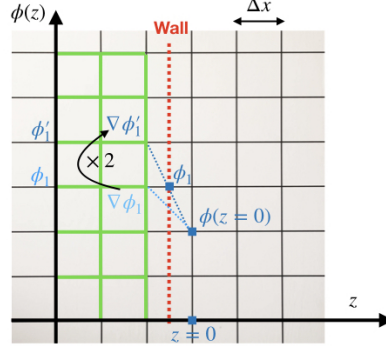


Figure 4.7 – Electrostatic potential values as a function of the position. The discretized green region denotes the solid part, whereas the remaining region on the right corresponds to the fluid region, where the Poisson equation is solved. The potential of one electrode is fixed at a constant value ϕ_1 . The wall is located half-way between the discretized solid region and liquid region. The resolution is Δx .

The boundary conditions of the LB part do not change. On the other hand, the LF part does need a change. It still requires the ions fluxes penetrating (*i.e.* such that $\mathbf{r} + \mathbf{c}_i \Delta t$ is a solid node) to be canceled. However, the new feature of this LBE method is that the electrodes are kept at a constant potential instead of bearing a uniform surface charge σ .

The most natural way to implement this constant-potential boundary condition is to simply assign the target value to solid nodes and not to update them during the resolution of the Poisson equation via the SOR algorithm. This is however not sufficiently accurate. Indeed, in that case the potential at the true interface, which is located half-way between the solid and fluid nodes, differs from that on the solid nodes. This observation provides a simple solution to cure this problem, as illustrated in Fig. 4.7 for the 1D-case. In order to correctly compute the potential gradient at the interface, *i.e.* so that the value of the potential at the true interface is the target value ϕ_1 , it is necessary to double its natural estimate (*i.e.* divide the difference $\phi_1 - \phi(z=0)$ by $\Delta x/2$ instead of Δx only).

We generalize this fix to the 3D case with the LB lattice velocities and weights, by modifying the estimate of the Laplacian on the lattice (Eq. 2.46), by doubling all contribution of links which cross the interface. This is achieved by introducing the characteristic function of the solution defined as:

$$\chi(\mathbf{r}) := \begin{cases} 0, & \text{if } \mathbf{r} \in \mathcal{F}. \\ 1, & \text{if } \mathbf{r} \in \mathcal{S}. \end{cases} \quad (4.27)$$

where \mathcal{S} denotes the solid region, whereas \mathcal{F} denotes the fluid region, and replacing in SOR the estimate of the Laplacian by:

$$\nabla^2 \psi = \frac{2}{c_s^2 \Delta t^2} \sum_i w_i [\psi(\mathbf{r} + \mathbf{c}_i \Delta t) - \psi(\mathbf{r})] \times [1 + \chi(\mathbf{r} + \mathbf{c}_i \Delta t) - \chi(\mathbf{r})]. \quad (4.28)$$

Note that the potential is computed only on the fluid nodes and that the values of ψ are kept constant on all of the solid nodes.

Once the SOR algorithm has converged with this modification, it is possible to estimate the surface charge density from Eq. 4.28 now computed on the interfacial solid nodes. By summing on the nodes corresponding to each electrode we obtain their total charge at every time step. Once steady-state is reached, we can compute the capacitance of the capacitor, dividing the electrode charge by the applied voltage.

4.3.2 Case of a slit channel

We now consider two planar electrodes separated by a distance L under a reduced potential difference ΔV .

4.3.2.1 Electrostatic Potential

No salt solution

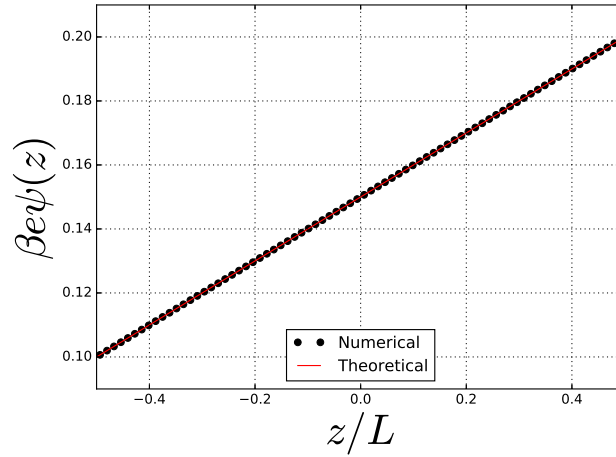


Figure 4.8 – Electrostatic potential profile in a slit channel of separation $L/\Delta x = 82$ without salt. The resolution is fixed by the Bjerrum length $l_B/\Delta x = 1.44$ and $\Delta V = 0.1$.

In the absence of added salt the system is equivalent to a capacitor with a dielectric permittivity ε inside the channel. The PB equation then reads

$$\Delta\phi = \frac{d^2\phi}{dz^2} = 0 \quad (4.29)$$

with Neumann boundary conditions

$$\begin{aligned} \phi(z = L/2) &= \phi_2 \\ \phi(z = -L/2) &= \phi_1 \end{aligned} \quad (4.30)$$

where ϕ_1 and ϕ_2 are reduced fixed potentials at the walls so that $\Delta V = \phi_2 - \phi_1$.

The solution for the electrostatic potential reads

$$\boxed{\phi(z) = \frac{\phi_2 - \phi_1}{L}z = \frac{\Delta V}{L}z} \quad (4.31)$$

The corresponding numerical result is shown in Fig. 4.8. The simulation was performed on $N_x \times N_y \times N_z = 3 \times 3 \times 82$ lattice points with three solid sheets on each side. The distance

between the walls is thus $L = 76\Delta x = 4.0 \times 10^{-8} \text{ m}$. A potential difference $\Delta V = 0.1$ was imposed and the Bjerrum length $l_B/\Delta x = 1.44$ was fixed.

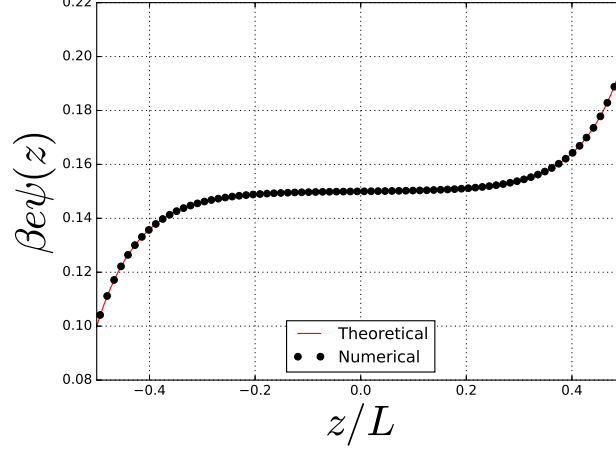


Figure 4.9 – Electrostatic potential profile in a slit channel of separation $L/\Delta x = 82$ with added salt. The resolution is fixed by the Bjerrum length $l_B/\Delta x = 1.44$, the salt concentration corresponds to a Debye screening length $\lambda_D/\Delta x = 6.0$ and $\Delta V = 0.1$

Added salt solution

When salt is added, using the linearized version of PB equation with the same boundary conditions results in the following electrostatic potential

$$\psi(z) = \frac{(\psi_1 \exp(\gamma) - \psi_2 \exp(-\gamma)) \exp(\kappa z) + (\psi_2 \exp(\gamma) - \psi_1 \exp(-\gamma)) \exp(-\kappa z)}{2 \sinh(2\gamma)} \quad (4.32)$$

where $\gamma := \kappa L/2$. Since $\Delta V = \beta e(\psi_2 - \psi_1)$,

$$\phi(z) = \beta e \psi(z) = \frac{\Delta V}{2 \sinh(\kappa L/2)} \sinh(\kappa z) + \frac{\beta e(\psi_1 + \psi_2)}{2} \quad (4.33)$$

The simulation was performed under the same conditions as in the no-salt case, except for the salt concentration, which corresponds to a Debye screening length $\lambda_D/\Delta x = 6.0$. Excellent agreement between the theoretical and numerical results is found, as we can see in Fig. 4.9.

4.3.2.2 Concentration profiles and errors

Substituting Eq. 4.33 in Eq. 4.1 yields the ionic distributions, which are shown in Fig. 4.10. We can clearly see that the cations move to one wall and the anions to the opposite one. Furthermore, we have electroneutrality in the middle of the channel.

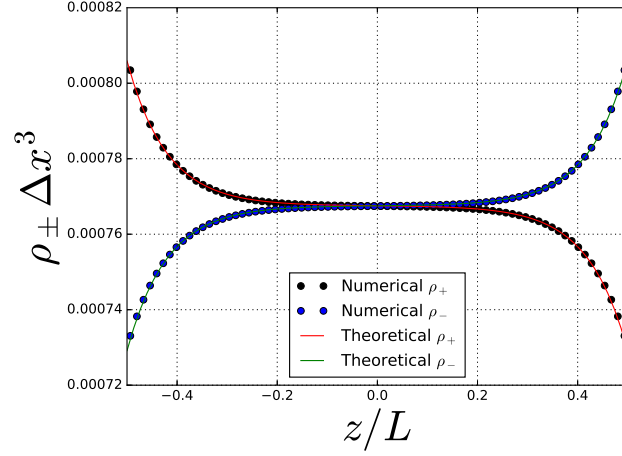


Figure 4.10 – Ion concentration profile in a capacitor of width $L/\Delta x = 82$ with added salt under a reduced voltage $\Delta V = \beta e \Delta \psi = 0.1$ (cations are in black and red and anions are in blue and green). The resolution is fixed by the Bjerrum length $l_B/\Delta x = 1.44$ and the salt concentration corresponds to a Debye screening length $\lambda_D/\Delta x = 6.0$.

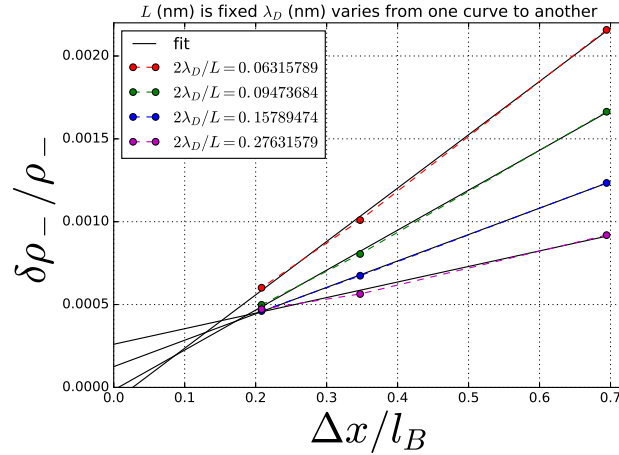


Figure 4.11 – Effect of the resolution on the relative error of the anions concentration profile. The error is defined as $\frac{\delta\rho}{\rho} = \sqrt{\frac{1}{N} \sum_{\omega} \left(\frac{\rho_n}{\rho_a} - 1 \right)^2}$, where ρ_n and ρ_a denote the numerical and analytical concentration respectively. The study was carried out by fixing the distance $L = 3.7 \times 10^{-8} \text{ m}$ between the walls and varying the Debye screening length λ_D (nm) from a curve to another (see Table 4.2). The fit is $f(x) = \frac{ALx}{2\lambda_D} + B$ where A and B are the fitting parameters, whose numerical values are illustrated in Table 4.3.

Nevertheless, a difference between the two solutions (numerical and analytical) exists. We quantify this error $\delta\rho/\rho$ on the concentration profiles as:

$$\frac{\delta\rho}{\rho} = \sqrt{\frac{1}{N} \sum_{\omega} \left(\frac{\rho_n}{\rho_a} - 1 \right)^2} \quad (4.34)$$

where ρ_n and ρ_a denote the numerical and analytical error respectively; $N = N_x \times N_y \times N_z$ and

$2\lambda_D/L$							
0.06		0.09		0.16		0.28	
$L/\Delta x$	$\lambda_D/\Delta x$	$L/\Delta x$	$\lambda_D/\Delta x$	$L/\Delta x$	$\lambda_D/\Delta x$	$L/\Delta x$	$\lambda_D/\Delta x$
76	2.4	76	3.6	76	6	76	10.5
152	4.8	152	7.2	152	12	152	21
253	8	253	12	253	20	253	35

Table 4.2 – Simulations parameters used to obtain the results shown in Fig. 4.11. All of the simulations were carried out for $l_B/\Delta x = 1.44, 2.88$ and 4.8 , under a reduced voltage $\Delta V = 0.1$, to ensure that the distance between the wall is always the same $L = 3.7 \times 10^{-8} m$.

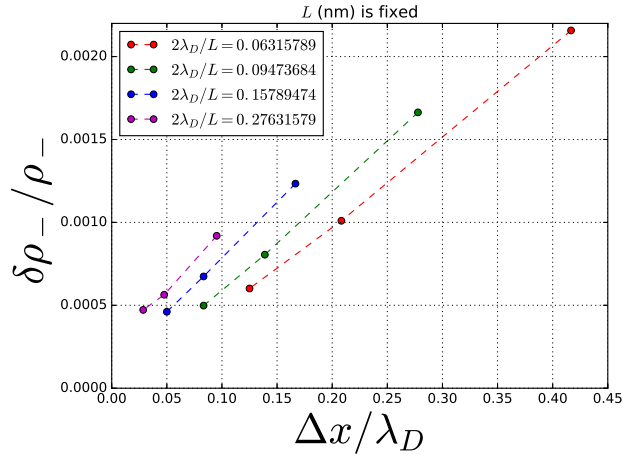


Figure 4.12 – Effect of the Debye screening length λ_D on the relative error of the anions concentration profile. The error is defined as $\frac{\delta\rho}{\rho} = \sqrt{\frac{1}{N} \sum_{\omega} \left(\frac{\rho_n}{\rho_a} - 1 \right)^2}$, where ρ_n and ρ_a denote the numerical and analytical error respectively. The study was carried out by fixing the distance L (nm) between the walls and varying the Debye screening length λ_D , as shown in Table 4.2.

$2\lambda_D/L$	A	B
0.06	2.0×10^{-4}	-8.6×10^{-5}
0.09	2.3×10^{-4}	-1.6×10^{-5}
0.16	2.5×10^{-4}	1.3×10^{-4}
0.28	2.6×10^{-4}	2.6×10^{-4}

Table 4.3 – Fitting parameters corresponding to the fit $f(x) = \frac{ALx}{2\lambda_D} + B$ as illustrated in Fig. 4.11.

ω is the domain of the fluid nodes. All simulations were carried out with $N_x \times N_y = 1 \times 1$ and varying $\lambda_D/\Delta x$ as well as N_z under a reduced potential difference $\Delta V = 0.1$. Furthermore, all simulations have three solid layers on each side. We fixed the distance $L = 3.7 \times 10^{-8} m$ and varied λ_D according to the data presented in Table 4.2. Fig. 4.11 shows how $\delta\rho/\rho$ varies with respect to λ_D and how it varies when increasing the resolution Δx , choosing $l_B/\Delta x = 1.44, 2.88$ and 4.8 . We do observe a decrease in the error as the resolution is increased (*i.e.* as Δx decreases). Besides, for all ratios $2\lambda_D/L$ the error scales linearly, which is why a fit $f(x) = Ax + B$ was carried out on each curve. The computed parameters A and B are presented in Table 4.3. We notice that the slope A increases as $2\lambda_D/L$ increases.

Fig. 4.12 shows the same data plotted as a function of λ_D , for a fixed $L = 3.7 \times 10^{-8} \text{ m}$. The error decreases when increasing λ_D (decreasing the salt concentration). This is probably due to the fact that the errors between the ρ_n and ρ_a mostly occur close to the walls. Hence, as λ_D increases for a fixed Δx , the Debye layer is better resolved and therefore the errors close to the wall decrease. The data used comes from the same simulations corresponding to the parameters in Table 4.2.

$2\lambda_D/L$							
0.171		0.092		0.083		0.075	
$L/\Delta x$	$\lambda_D/\Delta x$	$L/\Delta x$	$\lambda_D/\Delta x$	$L/\Delta x$	$\lambda_D/\Delta x$	$L/\Delta x$	$\lambda_D/\Delta x$
28	2.4	52	2.4	58	2.4	64	2.4
56	4.8	104	4.8	116	4.8	128	4.8
93	8.0	173	8.0	193	8	213	8.0

Table 4.4 – Simulations were carried out for $l_B/\Delta x = 1.44, 2.88$ and 4.8 , to ensure that the Debye screening length is always the same, *i.e.* $\lambda_D = 1.17 \times 10^{-9} \text{ m}$.

On the other hand, if we vary L instead of λ_D (see Fig. 4.13), we observe again a linear scaling for $\delta\rho/\rho$ both for increasing resolution (*i.e.* decreasing $\Delta x/l_B$) and as a function of the inverse box size $\Delta x/L$ (see Fig. 4.14). Contrary to the previous case, the error does go to zero as $1/\Delta x$ or L increases. Thus a fit $f(x) = Ax$ is here appropriate. The input parameters corresponding to Fig. 4.13 are shown in Table 4.4. Moreover, if we look at the computed parameters A presented in Table 4.5, we notice that as $2\lambda_D/L$ increases, the slope A increases.

$2\lambda_D/L$	A
0.171	8.4×10^{-4}
0.092	3.4×10^{-4}
0.083	2.9×10^{-4}
0.075	2.5×10^{-4}

Table 4.5 – Fitting parameters corresponding to the fit $f(x) = \frac{ALx}{2\lambda_D}$ as illustrated in Fig. 4.13.

4.3.2.3 Electrode Capacitance

A fundamental property of the capacitors is their integral capacitance, which is defined as

$$C = \frac{Q}{\Delta V} \quad (4.35)$$

In the absence of added salt the capacitance reads

$$C_0 = \frac{\varepsilon_0 \varepsilon_r S}{L}, \quad (4.36)$$

where S is the surface of the electrode. In the presence of added salt, in the low voltage regime, the Debye-Hückel capacitance reads,

$$C_{DH} = \frac{\beta e^2 S}{8\pi l_B \lambda_D}. \quad (4.37)$$

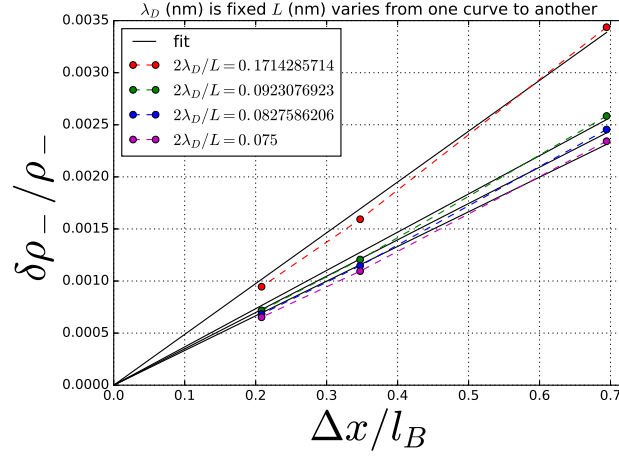


Figure 4.13 – Effect of the resolution $\Delta x/l_B$ on the relative error of the anions concentration profile.

The error is defined as $\frac{\delta\rho}{\rho} = \sqrt{\frac{1}{N} \sum_{\omega} \left(\frac{\rho_n}{\rho_a} - 1\right)^2}$, where ρ_n and ρ_a denote the numerical and analytical concentrations respectively. The study was carried out by fixing the distance $\lambda_D = 1.1 \times 10^{-9} m$ between the walls and varying L (nm) from a curve to another, as shown in Table 4.4. The fit is $f(x) = \frac{ALx}{2\lambda_D}$, where A is the fitting parameter.

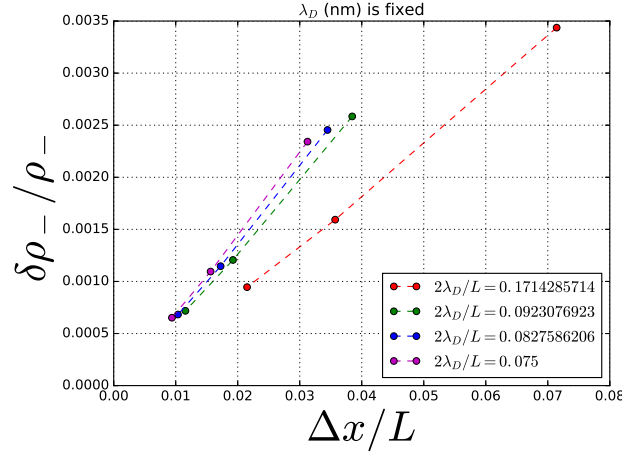


Figure 4.14 – Effect of the Debye screening length λ_D on the relative error of the anions concentration profile. The error is defined as $\frac{\delta\rho}{\rho} = \sqrt{\frac{1}{N} \sum_{\omega} \left(\frac{\rho_n}{\rho_a} - 1\right)^2}$, where ρ_n and ρ_a denote the numerical and analytical concentrations respectively. The study was carried out by fixing the distance $\lambda_D = 1.1 \times 10^{-9} m$ and varying the distance L between the walls, as shown in Table 4.4.

In our simulations of capacitors, we compute the capacitance from the steady-state charge of the electrodes, as described in Section 4.3.1.

Concentration Study

We study the effect of the concentration *i.e.* λ_D on the relative error for the calculations

of the capacitance $\frac{\delta C}{C}$, which is defined as:

$$\frac{\delta C}{C} = \frac{C_n}{C_a} - 1 \quad (4.38)$$

where C_n is the numerical result for the capacitance and $C_a = C_{DH}$ as given by Eq. 4.37. We observe that as the resolution of the grid increases, whenever salt is added, the error scales linearly as $\Delta x/2\lambda_D$.

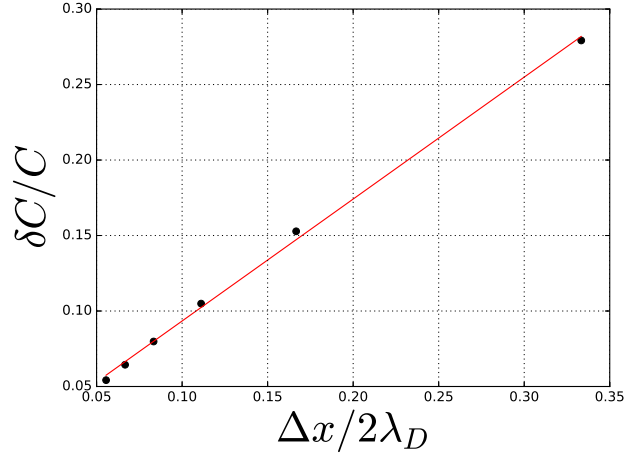


Figure 4.15 – Effect of the concentration (*i.e.* λ_D) on the capacitance error $\frac{\delta C}{C} = \frac{C_n}{C_a} - 1$ for a fixed distance $L = 7.35 \times 10^{-8} \text{ m}$ between the walls and fixed $l_B/\Delta x = 1.2$. $\delta C/C$ scales linearly following $\delta C/C = \Delta x/2\lambda_D$. The fit is shown in red and the numerical simulations are shown as black dots.

Fig. 4.15 is an example of how the relative error varies when λ_D changes. More specifically, $\lambda_D/\Delta x = 1.5, 4.5, 6, 7.5$ and 9 . We repeated this analysis for different l_B values and plot the corresponding slope values on Fig. 4.16. The simulations were performed with a stencil $N_x \times N_y = 1 \times 1$ and $N_z = 42, 84, 124, 168, 210$ and 252 (with three solid layers on each side), for each concentration $\lambda_D/\Delta x$ and for $l_B/\Delta x = 0.4, 0.8, 1.2, 1.6, 2$ and 4 . This ensures that $L = 7.35 \times 10^{-8} \text{ m}$. The slope is then computed from the linear fit (red line on Fig. 4.15). The value of the slope is close to one and in fact the slope varies according to the following scaling law:

$$\frac{\delta C}{C} = \frac{\Delta x}{2\lambda_D} \left[1 - A \left(\frac{\lambda_D}{l_B} \right)^B \right] \quad (4.39)$$

where A and B are fitting parameters whose values are 0.12 and 0.40 respectively. We do not have yet an interpretation.

4.3.2.4 Electro-osmotic flow

We recall from Chapter 2 that when an external electric field is applied parallel to the walls a flow called electro-osmotic flow (EOF) is induced. When the EOF is fully developed, *i.e.* $d\mathbf{u}/dt = \mathbf{0}$, with no external pressure gradient across the charged surface and in the limit of

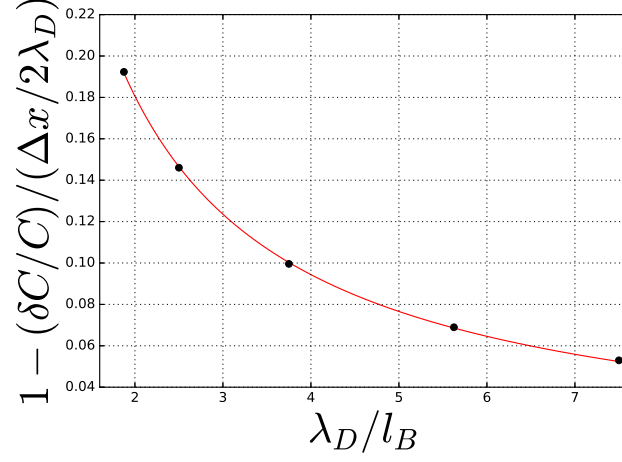


Figure 4.16 – Scaling of the slope of $\delta C/C$ vs. $\Delta x/(2\lambda_D)$ as a function of λ_D/l_B . The numerical data obeys to Eq. 4.39. The fit is shown in red and the numerical simulations are in shown as black dots.

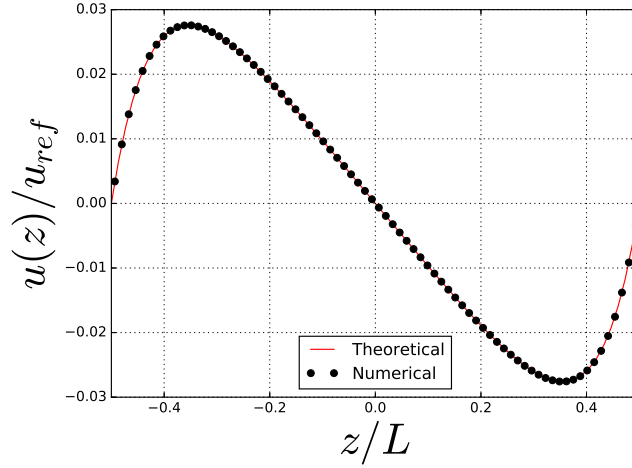


Figure 4.17 – Electro-osmotic flow profile in a slit channel of width $L/\Delta x = 82$ with added salt. The salt concentration corresponds to a Debye screening length $\lambda_D/\Delta x = 6.0$ and a reduced voltage $\Delta V = 0.1$ is applied. The EOF flow is induced by an external electric field $\beta e \Delta x E_y = 0.01$ parallel to the walls. The resolution is fixed by the Bjerrum length $l_B/\Delta x = 1.44$.

low Reynolds number ($\Rightarrow (\mathbf{u} \cdot \nabla) \mathbf{u} = \mathbf{0}$) the NS equation reduces to

$$\eta \frac{d^2 u}{dz^2} = \varepsilon \frac{d^2 \psi}{dz^2} E_y . \quad (4.40)$$

Integration yields,

$$u(z) = \frac{\varepsilon E_y}{\eta} \psi(z) + Az + B \quad (4.41)$$

where A and B are constant to be determined with the following boundary conditions

- $\phi(z = L/2) = \phi_2$

- $\phi(z = -L/2) = \phi_1$

- $u(z = \pm L/2) = 0$

yielding the final solution

$$u(z) = \frac{\varepsilon E_y}{\eta} \left[\phi(z) - \frac{\Delta V}{L} z \right] \times \frac{k_B T}{e} \quad (4.42)$$

We carry out a simulation with the same parameters as in Section 4.31, in the case where salt is added to the system, with an external electric field $\beta e \Delta x E_y = 0.01$ parallel to the walls, as shown in Fig. 4.17. We recover the solution given in Eq. 4.42 (see Fig. 4.17). The fact that cations and anions are in excess on opposite walls creates a sort of shear flow: the anions move opposite to the electric field direction, whilst the cations move in its direction. This represents an exotic type of motion, which could be considered for possible experimental applications that would for instance allow to separate cations from anions. Indeed, if we were to consider a pore connecting two reservoirs, we could consider to insert KBr in the reservoir and NaCl in the pore. Then, if we induced an EOF in the pore, we could collect K^+ on one side and Br^- on the other. Hence, this could be an alternative technique for ions separation.

4.3.3 Case of a coaxial cylindrical channel

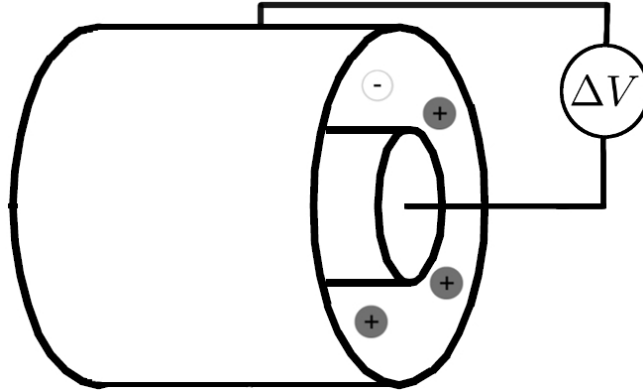


Figure 4.18 – Sketch of a coaxial cylindrical channel

We now consider the case of a coaxial cylindrical channel, as shown in Fig. 4.18, with an inner cylindrical electrode of radius R_1 and an outer cylindrical electrode of radius R_2 . In this case the PB equation reads

$$\frac{1}{r} \frac{d}{dr} \left[r \frac{d\psi}{dr} \right] = -\frac{e}{\varepsilon} \sum_k n_k z_k \exp[-z_k \beta e \psi] \quad (4.43)$$

In the linear (Debye-Hückel) regime, the corresponding ionic concentrations are written as

$$\rho_{\pm}(r) = n_{\pm} [1 \mp \phi(r)], \quad (4.44)$$

with $\phi := \beta e \psi$ and n_{\pm} the concentrations of reference, which need to be expressed as a function of n_s (the salt concentration), ϕ_1 and ϕ_2 (the electrodes reduced potentials).

4.3.3.1 Electrostatic potential

No salt solution

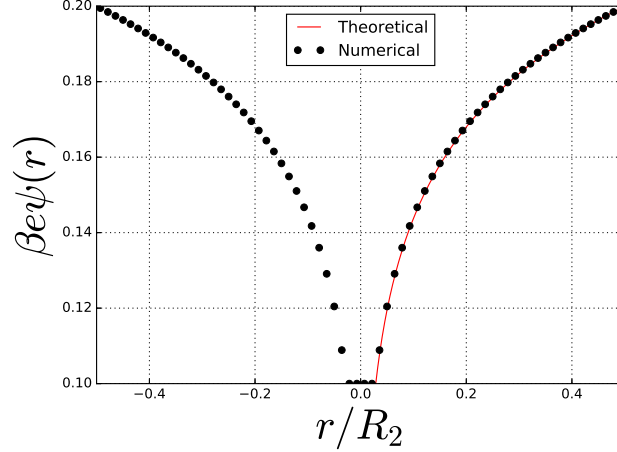


Figure 4.19 – Electrostatic potential profile in a coaxial cylindrical channel with radii $R_1/\Delta x = 2$ and $R_2/\Delta x = 35$ without salt. The resolution is fixed by the Bjerrum length $l_B/\Delta x = 1.2$ and a potential difference $\Delta V = 0.1$ was imposed between the two cylinders. The separation between the external boundary of the outer cylinder and the box of simulation is $w = 4\Delta x$.

If no salt is added between the two cylinders, Eq. 4.43 may be simplified as

$$\frac{1}{r} \frac{d}{dr} \left[r \frac{d\phi}{dr} \right] = 0 \quad (4.45)$$

with Neumann boundary conditions

$$\begin{aligned} \phi(r = R_1) &= \phi_1 \\ \phi(r = R_2) &= \phi_2 \end{aligned} \quad (4.46)$$

the solution is given by

$$\phi(r) = \frac{\Delta V}{\ln(R_2/R_1)} \ln(r/R_2) + \phi_2 \quad (4.47)$$

The simulation was performed on $N_x \times N_y \times N_z = 74 \times 74 \times 1$ lattice points. The radii of the inner and outer cylinder are $R_1 = 2$ and $R_2 = 35$ lattice points respectively. The separation between the external boundary of the outer cylinder and the box of simulation is $w = 4\Delta x$. A reduced potential difference $\Delta V = 0.1$ was imposed between the two cylinders and a Bjerrum length $l_B/\Delta x = 1.2$ was fixed. The corresponding physical data is shown in Table 4.6. The numerical result corresponding to Eq. 4.47 is shown in Fig. 4.19. The agreement with the theoretical result is excellent despite the small radius of the inner cylinder. In particular, the potential is correctly imposed at the hydrodynamic interface (midway between the solid and fluid nodes) by the method introduced in Section 2.2.10.

R_1	$1.16 \times 10^{-9} \text{ m}$
R_2	$2.04 \times 10^{-8} \text{ m}$
L_{PBC}	$5.83 \times 10^{-10} \text{ m}$
ν	$1.0 \times 10^{-6} \text{ m}^2/\text{s}$
l_B	$0.7 \times 10^{-9} \text{ m}$

Table 4.6 – Physical data for a coaxial cylindrical channel with a constant reduced potential difference of $\Delta V = 0.1$. R_1 and R_2 are the inner and outer cylinder radii respectively. ν and l_B denote the dynamic viscosity and the Bjerrum length.

Added salt solution

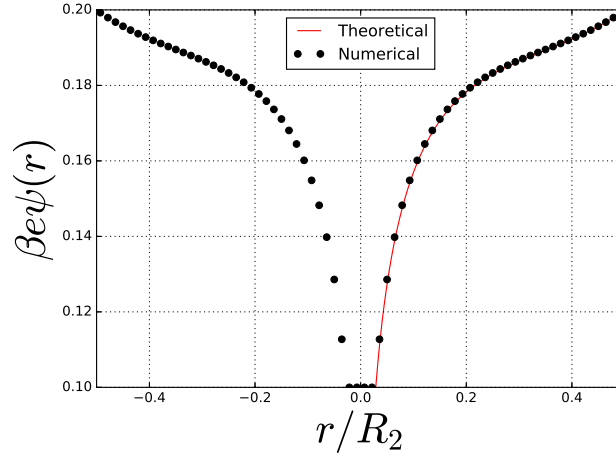


Figure 4.20 – Electrostatic potential profile in a coaxial cylindrical channel with radii $R_1/\Delta x = 2$ and $R_2/\Delta x = 35$ with added salt. The resolution is fixed by the Bjerrum length $l_B/\Delta x = 1.2$ and a reduced potential difference $\Delta V = 0.1$ was imposed between the two cylinders. The separation between the external boundary of the outer cylinder and the box of simulation is $w = 4\Delta x$. The salt concentration corresponds to a Debye screening length $\lambda_D/\Delta x = 9.0$.

On the other hand, when salt is added, the linearized PB equation reads

$$\Delta\phi = -4\pi l_B(\rho_+ - \rho_-) \quad (4.48)$$

$$= -4\pi l_B(n_+ - n_-) + 4\pi l_B(-n_- + n_-)\phi \quad (4.49)$$

which can be rewritten as

$$\Delta\phi = \kappa^2\phi - \kappa^2\delta \quad (4.50)$$

where $\kappa^2 = 4\pi l_B(n_+ + n_-) = f(n_s, \phi_1, \phi_2)$ and $\delta = \frac{n_+ - n_-}{n_+ + n_-}$.

A solution for this equation is:

$$\phi(r) = AK_0(\kappa r) + BI_0(\kappa r) + D \quad (4.51)$$

Chapter 4. From Surface Charge to Constant Potential Simulations in LBE

where A , B and D are constants to be determined. Using the same boundary conditions and Gauss' law

$$R_1 \frac{d\phi}{dr} \Big|_{r=R_1} = R_2 \frac{d\phi}{dr} \Big|_{r=R_2} \quad (4.52)$$

we obtain:

$$A = \frac{(\phi_1 - \phi_2)(R_1 K_1^1 - R_2 K_1^2)}{\xi} \quad (4.53)$$

and

$$B = \frac{(\phi_1 - \phi_2)(R_1 I_1^1 - R_2 I_1^2)}{\xi} \quad (4.54)$$

where

$$\begin{aligned} \xi := & (I_0^1 - I_0^2)(R_1 K_1^1 - R_2 K_1^2) \\ & + (R_1 I_1^1 - R_2 I_1^2)(K_0^1 - K_0^2). \end{aligned} \quad (4.55)$$

and where we defined

$$I_\alpha^\beta := I_\alpha(\kappa R_\beta) \quad (4.56)$$

$$K_\alpha^\beta := K_\alpha(\kappa R_\beta) \quad (4.57)$$

for $\alpha \in \{0, 1\}$ and $\beta \in \{1, 2\}$. Finally, the constant D can be expressed using the boundary conditions so that

$$D = \phi_1 - AK_0^1 + BI_0^1. \quad (4.58)$$

The concentration n_s can then be expressed in terms of the average of the ionic concentrations, *i.e.*

$$\bar{\rho}_\pm = n_\pm [1 \mp \bar{\phi}] = n_s \quad (4.59)$$

which means that

$$\frac{\kappa^2}{4\pi l_B} = n_+ + n_- \quad (4.60)$$

$$= n_s \left[\frac{1}{1 - \bar{\phi}} + \frac{1}{1 + \bar{\phi}} \right] \quad (4.61)$$

$$= \frac{2n_s}{1 - \bar{\phi}^2} \quad (4.62)$$

In other words, when $\bar{\phi} \ll 1$ we recover

$$n_s = \frac{n_+ + n_-}{2}. \quad (4.63)$$

The simulation was carried out with the same parameters as in the no-salt case and the salt concentration corresponds to a Debye screening length $\lambda_D/\Delta x = 9.0$. Fig. 4.20 compares the resulting electrostatic potential to the analytical result in Eq. 4.51. Once again excellent agreement is found between the two.

4.3.3.2 Electrode capacitance

When no salt is added, the capacitance per unit length can be easily derived from Gauss' law^[161] so that

$$C_0 = \frac{2\pi\epsilon}{\ln(R_2/R_1)}, \quad (4.64)$$

or using the Bjerrum length:

$$C_0 = \frac{\beta e^2/l_B}{2\ln(R_2/R_1)}. \quad (4.65)$$

On the other hand, when salt is added and in the Debye-Hückel regime limit the capacitance per unit length reads:

$$\begin{aligned} C_{DH} &= \frac{2\pi R_1 \epsilon}{\Delta V} \left. \frac{d\psi}{dr} \right|_{r=R_1} \\ &= \frac{2\pi R_1 \epsilon}{\Delta V} [\kappa A I_1(\kappa R_1) - \kappa B K_1(\kappa R_1)] \end{aligned} \quad (4.66)$$

with A and B defined in Eq. 4.53 and 4.54 respectively.

We performed a set of simulations to see if the capacitance values are recovered correctly. We used $N_x \times N_y \times N_z = 54 \times 54 \times 3$ lattice points. The radii of the inner and outer cylinders are $R_1 = 2$ and $R_2 = 25$ lattice points respectively. The separation between the external boundary of the outer cylinder and the box of simulation is $w = 4\Delta x$. A reduced potential difference $\Delta V = 0.1$ was imposed between the two cylinders and a Bjerrum length $l_B/\Delta x = 1.2$ was fixed. We varied the concentrations which correspond to Debye screening lengths $\lambda_D = 3, 6, 9$ and 12 . Table 4.7 illustrates the relative error between the numerical data and the theoretical result given by Eq. 4.66. We notice that the error decreases as λ_D increases, which is probably due to the fact that the Debye layer is better resolved. We notice that even with only three nodes resolving the Debye layer (which is rather small), we recover a value for the capacitance with a relative error of only 2.3%.

$\lambda_D/\Delta x$	3	6	9	12
$\delta C_{DH}/C_{DH}$	2.3%	1.2%	1%	0.94%

Table 4.7 – Error the capacitance for a coaxial cylindrical channel with added salt (see Eq. 4.66), when varying λ_D (see text for details on parameters).

4.3.3.3 Electro-osmotic flow

Considering the radial and swirl components of the velocity to be zero, *i.e.* $u_r = u_\theta = 0$, the flow fully developed, *i.e.* $\partial u_z/\partial t = 0$, and the flow to be axisymmetric, *i.e.* $\partial(\cdot)/\partial\theta = 0$, the

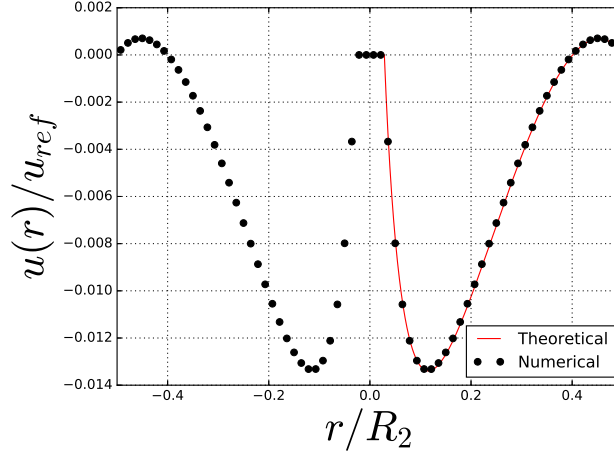


Figure 4.21 – Velocity profile in a coaxial cylindrical channel with radii $R_1/\Delta x = 2$ and $R_2/\Delta x = 35$ with added salt, corresponding to a Debye screening length $\lambda_D/\Delta x = 9.0$. The flow is induced by an external electric field $\beta e \Delta x E = 0.0001$ parallel to the walls resulting in an EOF. The resolution is fixed by the Bjerrum length $l_B/\Delta x = 1.2$.

NS equation can be simplified as

$$\eta \left[\frac{1}{r} \frac{\partial}{\partial r} \left(r \frac{\partial u_z}{\partial r} \right) \right] = \varepsilon E_z \left[\frac{1}{r} \frac{\partial}{\partial r} \left(r \frac{\partial \phi}{\partial r} \right) \right] \quad (4.67)$$

Using the following boundary conditions

- $\phi(r = R_1) = \phi_1$
- $\phi(r = R_2) = \phi_2$
- $u(r = R_1) = u(r = R_2) = 0$

yields the solution

$$u(r) = \frac{\varepsilon E_z}{\eta} [\phi(r) + A \ln(r) + B] \quad (4.68)$$

with $A = (\phi_1 - \phi_2)/\ln(R_1/R_2)$ and $B = \phi_1 + (\phi_1 - \phi_2) \ln(R_1)/\ln(R_1/R_2)$.

As we can see in Fig. 4.21 there is perfect agreement between the analytical solution and the numerical data obtained with an external electric field $\beta e \Delta x E = 0.0001$ parallel to the walls.

4.4 Conclusion

In this Chapter we have successfully simulated a nano-capacitor in two different geometries, with two different kinds of boundary conditions. The first one, which is in a similar fashion as in the two previous chapter, imposes opposite surface charges on the two electrodes (*i.e.*

Chapter 4. From Surface Charge to Constant Potential Simulations in LBE

walls). The second involved a modification of the boundary conditions in order to apply a constant potential difference between the two electrodes. Electrostatic potentials, concentrations and velocity profiles (at steady state) were tested with and without added salt with analytical results which we derived. This change in the LBE method allows the *Laboetie* code to reproduce more faithfully electrokinetic experiments, as discussed in the Introduction of this thesis, and is a first step towards modelling the fluctuations of the electrostatic potential. In order to do so, we analyse in the next chapter the transient regime of a charging capacitor, which (as we will show in the last chapter of this thesis) can be related to the equilibrium fluctuations of the system.

*"It does not say in the Bible that all laws of nature are expressible linearly!"
- Enrico Fermi*

Transient regime in constant potential simulations

Contents

5.1	Debye relaxation time	106
5.1.1	Macroscopic point of view	107
5.1.2	Microscopic point of view	108
5.1.3	From bulk to confined electrolytes	109
5.2	Case of a slit channel	110
5.2.1	Results	110
	5.2.1.1 Resolution and concentration study	113
	5.2.1.2 Non-linear analysis	113
5.3	Case of a coaxial cylindrical channel	116
5.3.1	Results	116
5.4	Conclusion	117

THE EXPERIMENTAL community has drawn a growing interest to the transient regime as the time-dependent applied voltages have encountered different applications, such as pumping liquid electrolytes^[162-170], separation or self-assembly of colloidal particles^[170-174] and manipulation of biological cells and vesicles^[175-177]. Furthermore, pressure driven flows were observed to produce a frequency-dependent streaming potential, which can be used to determine the structure of porous media^[178]. This is why double-layer charging, which is a phenomenon not as well understood as one may think^[42], and its corresponding time scales need to be explored. Indeed, the community long thought that the only time scale at play for the relaxation of the electrolytes was the Debye characteristic length $\tau_D = \lambda_D^2/D$, which is a material property of the electrolyte (τ_D being of the order of $ns/\mu s$ for a Debye screening length ranging from 1 – 100 nm - for aqueous solutions - with $D \approx 10^{-9}m^2 \cdot s^{-1}$). We shall discuss more in details the origin of this time scale in the next sections and show how this description is in fact partially inaccurate. Usually electrochemists describe their theoretical problem by doing an analogy between the system studied and its equivalent electrical circuit^[179,180]. In fact, it was Helmholtz himself who suggested to treat the electrolyte interface as a thin capacitor^[181,182] (this is why he used the term "double layer"). From this analysis it was found that the relaxation time needed to charge the double layers depends on the electrode separation, via the bulk resistance of the electrolyte^[183]. The study of diffuse charge in the double layer allowed Gouy to link the excess ionic charge near the electrode to a capacitance per unit area $C_D = \varepsilon/\lambda_D$. Eventually, he considered the ions screening on a flat surface, from which he derived the exact solution of the electrostatic potential profile at steady state, for the full nonlinear equations^[184].

In the same spirit as the electrochemical community we can consider that the charge time response at one electrode has an exponential nature as in a RC circuit, *i.e.*

$$Q(t) = Q_\infty(1 - e^{t/\tau}) \tag{5.1}$$

where $\tau = RC$ is the characteristic time and R and C are the resistance (of the interface, *i.e.* the conductivity inverse) and the capacitance respectively. Q_∞ is the steady state value for $Q(t)$. As Bazant *et al.* pointed out, over the last century τ was thought to be equivalent to the Debye characteristic time. However, using an equivalent circuit model, they showed that this is not the case and that the electrolyte experiences several characteristic times.

In Section 5.1 we derive the Debye time to point out the origin and prior assumptions of this time scale, as well as showing the difference with the result obtained by Bazant *et al.*^[42]. In Section 5.2 we present a new numerical approach, which we validate in the linear response regime with a new theoretical prediction, carried out by our collaborator Ivan Palaia. This approach is more precise than the analysis of Bazant *et al.*^[42], whose result is limited to the case where $\lambda_D \ll L/2$, with L denoting the distance between the electrodes. We thus obtain the charge time response and its corresponding relaxation characteristic time. We also extend the analysis to the non-linear regime, to prove the efficiency of the method beyond theoretical predictions. Finally, In Section 5.3 we extend the analysis and validation to the case of a coaxial cylindrical channel, which was not tackled previously.

5.1 Debye relaxation time

For the purpose of clarity we shall briefly derive the Debye time with two different methods.

5.1.1 Macroscopic point of view

The first method is a macroscopic approach. Let ψ be a disturbing potential applied at time zero to a system whose conductance is χ and where the free charge density is ρ_f . The current density is thus given by

$$\mathbf{i} = -\chi \nabla \psi. \quad (5.2)$$

The equation of continuity can then be written as

$$\frac{\partial \rho_f}{\partial t} = -\nabla \cdot \mathbf{i} = \chi \Delta \psi \quad (5.3)$$

Combined with Poisson equation

$$\Delta \psi = -\frac{\rho_f}{\varepsilon} \quad (5.4)$$

we find

$$\frac{d\rho_f}{dt} = -\chi \frac{\rho_f}{\varepsilon}. \quad (5.5)$$

Integration then leads to

$$\rho_f(t) = \rho_f(0) \exp(-t/\tau) \quad (5.6)$$

with τ defined as:

$$\tau = \frac{\varepsilon}{\chi}. \quad (5.7)$$

Neglecting ion-correlations, the conductance can be expressed with the Nernst-Einstein relation:

$$\chi = \sum_k \beta e^2 \rho_k D_k z_k^2 \quad (5.8)$$

If all the ionic mobilities are the same, the expression may be simplified as

$$\chi \simeq \varepsilon D \kappa^2 \quad (5.9)$$

Plugging this result in Eq. 5.7 yields

$$\tau_D = \frac{1}{D \kappa^2} = \frac{\lambda_D^2}{D}, \quad (5.10)$$

which is the so-called Debye-time, which corresponds to the diffusion of ions over the Debye screening length.

5.1.2 Microscopic point of view

The relaxation time can also be obtained from a more microscopic approach. We can use start from Eq. 2.1 to write

$$\frac{\partial \rho_+}{\partial t} + \nabla \cdot \mathbf{j}_+ = 0 \quad (5.11)$$

$$\frac{\partial \rho_-}{\partial t} + \nabla \cdot \mathbf{j}_- = 0 \quad (5.12)$$

where + and – denote the physical quantity corresponding to cations and anions. Advection was here neglected. Ionic fluxes include migrational effects beside diffusional ones. Thus we can use Eq. 2.8 to write

$$\mathbf{j}_+ = -D_+ \left(\nabla \rho_+ + \frac{z_+ e}{k_B T} \rho_+ \nabla \psi \right) \quad (5.13)$$

$$\mathbf{j}_- = -D_- \left(\nabla \rho_- + \frac{z_- e}{k_B T} \rho_- \nabla \psi \right). \quad (5.14)$$

The expression does not consider deviations from Einstein's relation, such as the electrophoretic contribution or the gradient of the activity coefficient. Then, considering only first order terms of the perturbation in Eq. 5.11 and 5.12 yields the following relations

$$\frac{\partial(\delta \rho_+)}{\partial t} + \nabla \cdot (\delta \mathbf{j}_+) = 0 \quad (5.15)$$

$$\frac{\partial(\delta \rho_-)}{\partial t} + \nabla \cdot (\delta \mathbf{j}_-) = 0 \quad (5.16)$$

Macroscopic and microscopic diffusion processes originate simply due the distribution of charge inhomogeneities. Considering electroneutrality of the ion equilibrium distribution the potential is computed using the Poisson equation

$$\Delta \psi = \frac{e}{\varepsilon} \sum_{k=+,-} (\rho_k^0 + \delta \rho_k) z_k \quad (5.17)$$

Since $\sum_{+,-} \rho_k^0 z_k = 0$ the equation reduces to

$$\nabla \cdot \delta \mathbf{j}_+ = -D_+ \nabla \cdot [\nabla(\delta \rho_+)] + \kappa_+^2 D_+ \delta \rho_+ + \kappa_+^2 D_+ \frac{z_-}{z_+} \quad (5.18)$$

$$\nabla \cdot \delta \mathbf{j}_- = -D_- \nabla \cdot [\nabla(\delta \rho_-)] + \kappa_-^2 D_- \delta \rho_- + \kappa_-^2 D_- \frac{z_+}{z_-} \quad (5.19)$$

where the Debye screening lengths are defined as:

$$\kappa^2 = \kappa_+^2 + \kappa_-^2 \quad (5.20)$$

$$= \frac{\beta e^2}{\varepsilon} (\rho_+ z_+^2 + \rho_- z_-^2) \quad (5.21)$$

$$= 4\pi l_B \sum_{k=+,-}^N \rho_k z_k^2 \quad (5.22)$$

Chapter 5. Transient regime in constant potential simulations

Eq. 5.11 and 5.12 are subsequently written as

$$\left[\frac{\partial}{\partial t} - D_+ \Delta + \kappa_+^2 D_+ \right] \delta \rho_+ + \kappa_+^2 D_+ \frac{z_-}{z_+} \delta \rho_- = 0 \quad (5.23)$$

$$\kappa_-^2 D_- \frac{z_+}{z_-} \delta \rho_+ + \left[\frac{\partial}{\partial t} - D_- \Delta + \kappa_-^2 D_- \right] \delta \rho_- = 0 \quad (5.24)$$

Taking a Fourier and a Laplace tanformations yields,

$$[s + (q^2 + \kappa_+^2) D_+] \delta \rho_+(q, s) + \kappa_+^2 D_+ \frac{z_-}{z_+} \delta \rho_-(q, s) = \delta \rho_+(q, t = 0) \quad (5.25)$$

$$\kappa_-^2 D_- \frac{z_+}{z_-} \delta \rho_+(q, s) + [s + (q^2 + \kappa_-^2) D_-] \delta \rho_-(q, s) = \delta \rho_-(q, t = 0) \quad (5.26)$$

The roots of the principal determinant can then be determined with

$$\begin{bmatrix} s + (q^2 + \kappa_+^2) D_+ & \kappa_+^2 D_+ \frac{z_-}{z_+} \\ \kappa_-^2 D_- \frac{z_+}{z_-} & s + (q^2 + \kappa_-^2) D_- \end{bmatrix} = 0 \quad (5.27)$$

The matrix system has two independent solutions for s, which yields to the nondiffusional modes when q^2 goes to zero.

$$s^2 + s[\kappa_+^2 D_+ + \kappa_-^2 D_-] = 0 \quad (5.28)$$

the roots are

$$s_1 = 0, \quad s_2 = -[\kappa_+^2 D_+ + \kappa_-^2 D_-] \quad (5.29)$$

The first root corresponds to an overall mass conservation. The second corresponds to the Debye relaxation time, which in the general case (more than two species) reads:

$$\boxed{\frac{1}{\tau_D} = 4\pi l_B \sum_k \rho_k z_k^2 D_k} \quad (5.30)$$

If we further assume $D_+ = D_-$ and use the definition of κ we recover the simple expression

$$\boxed{\tau_D = s_2^{-1} = (\kappa^2 D)^{-1}} \quad (5.31)$$

5.1.3 From bulk to confined electrolytes

However, when the electrolyte is confined between walls, in particular between electrodes, the presence of an additional length scale results in the emergence of additional time scales. In particular, the slowest relaxation time for the charge reads:

$$\tau_\rho = \frac{\lambda_D L}{2D} - \frac{\lambda_D^2}{D} \quad (5.32)$$

Since the screening length is usually much smaller than half of the distance separating the electrodes (*i.e.* $\lambda_D \ll L/2$) the expression typically reduces to

$$\tau_p = \frac{\lambda_D L}{2D}. \quad (5.33)$$

These lengths scales were originally derived by Bazant *et al.* [42].

5.2 Case of a slit channel

We now want to compute numerically the characteristic relaxation time of a confined electrolyte with our constant potential LBE simulations. In order to do that we compute the charge accumulating on an electrode with respect to time.

5.2.1 Results

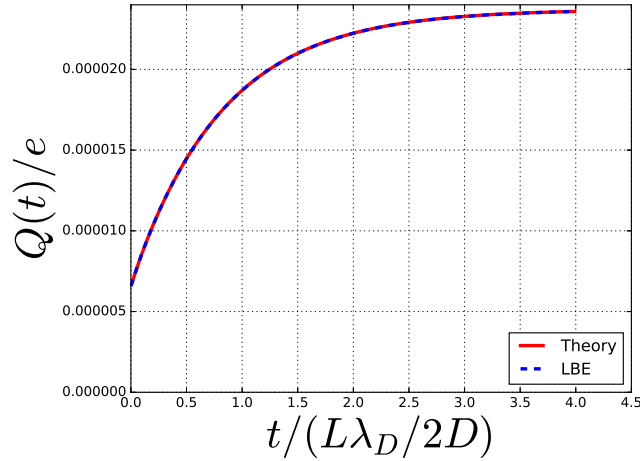


Figure 5.1 – Evolution of the electrode charge for a capacitor, submitted to a voltage step $\psi(t) = \psi_0\theta(t)$, with θ denoting the Heaviside step function. The charge accumulates in a monoexponential manner analog to a RC circuit. The distance between the solid-liquid interfaces is $L = 253\Delta x$. The resolution is fixed with the Bjerrum length $l_B/\Delta x = 4.8$. The reduced potential difference applied at the walls is $\Delta V = 0.1$, the salt concentration corresponds to a Debye screening length of $\lambda_D/\Delta x = 35.0$ and the ions have a bulk diffusion coefficient $D = 0.05 (\Delta x^2/\Delta t)$.

We consider the time-dependent response of a capacitor initially uncharged and submitted to a voltage

$$\psi(t) = \psi_0\theta(t), \quad (5.34)$$

with θ denoting the Heaviside step function, in the linear regime (*i.e.* $\psi_0 \ll k_B T/e$). In the LBE simulations, the charge is computed on a node according to Eq. ??; the total charge is then obtained summing on all the solid nodes constituting the electrode. Fig. 5.1 shows numerical simulations results for a system with $\epsilon = 2\lambda_D/L = 0.28$ and a reduced voltage $\beta e\psi_0 = 0.1$. The results are in excellent agreement with the analytical results carried out by our collaborator I. Palaia (see Appendix A.2). This validates our extension of the LBE

Chapter 5. Transient regime in constant potential simulations

method both to simulate the time-dependent response to an applied voltage and to determine the induced surface charge on the electrodes.

As we can see on Fig. 5.1 the charge at $t = 0$ is not equal to zero. This can be explained because the ions present in the fluid do not have enough time to move and therefore the profile of the potential is equivalent to the case where no salt is present in the solution (see *e.g.* Fig. 4.8). Hence, the analytical solution for the electrostatic potential at $t = 0$ can be computed from the capacitance without salt (*i.e.* Eq. 4.36), which yields:

$$Q(0) = \frac{\varepsilon \Delta \psi S}{L}, \quad (5.35)$$

whereas for $t \rightarrow \infty$, Q can be expressed using Eq. 4.37, *i.e.*

$$Q_\infty = \frac{\beta e^2 \Delta \psi S}{8\pi l_B \lambda_D}. \quad (5.36)$$

$\lambda_D/\Delta x$	8	12	20	35
$\delta Q_\infty/Q_\infty$	0.19%	0.08%	0.04%	0.04%
$\delta Q(0)/Q(0)$	0.50%	0.22%	0.21%	0.21%

Table 5.1 – Error on Q_∞ and $Q(0)$ when varying λ_D (see text for details on parameters)

Comparison of the relative error on Q_∞ and $Q(0)$ to the analytical results given by Eq. 5.35 and 5.36 is shown in Table 5.1 and 5.2. Simulations were carried out for a resolution fixed by the Bjerrum length $l_B/\Delta x = 4.8$ and with $N_x = N_y = 1 \times 1$ lattice points. In Table 5.1 we fix $N_z = 259$ lattice points, with three solid nodes on each side, and the salt concentration corresponds to a Debye screening length $\lambda_D/\Delta x = 8, 12, 20$ and 35. In Table 5.2 we fix $\lambda_D/\Delta x = 8$ and the distance between the electrodes varied so that $N_z = 99, 179, 199, 219$ and 259 lattice points. The reduced potential applied at the electrodes is $\Delta V = 0.1$. We observe that the error on $Q(0)$ seems to decrease as λ_D increases, whereas it increases as N_z increases. It is expected that as the Debye length is more discretized the error would decrease and similarly, for a given resolution value, as the distance L increases, less details are captured and therefore the error increases. However, contrary to the capacitance study in the previous chapter, the simulations were all carried out at a high resolution value (fixed by $l_B/\Delta x = 4.8$) and we can thus observe that the errors for both $Q(0)$ and Q_∞ are all below 0.5%, which is extremely precise.

$L/\Delta x$	93	173	193	213	253
$\delta Q_\infty/Q_\infty$	0.189%	0.189%	0.188%	0.187%	0.186%
$\delta Q(0)/Q(0)$	0.068%	0.234%	0.291%	0.354%	0.500%

Table 5.2 – Error on Q_∞ and $Q(0)$ when varying L , for a fixed resolution $l_B/\Delta x = 4.8$ and salt concentration corresponding to $\lambda_D/\Delta x = 8$.

Fig. 5.1 showed that $Q(0) \neq 0$ and therefore the usual exponential response of an electric circuit needs to be modified in order to take into account the shift $Q(0)$ at $t = 0$. We can

thus write the charge temporal response of the system as:

$$Q(t) = Q_\infty + (Q(0) - Q_\infty) \exp[-t/\tau]. \quad (5.37)$$

In order to compute the characteristic time we replot our results according to

$$-\frac{t}{\tau} = \ln \left[\frac{Q(t) - Q_\infty}{Q(0) - Q_\infty} \right], \quad (5.38)$$

as shown on Fig. 5.2, meaning that the characteristic time is given by the inverse of the slope:

$$\tau = \frac{1}{d \left(-\ln \left[\frac{Q(t) - Q_\infty}{Q(0) - Q_\infty} \right] \right) / dt} \quad (5.39)$$

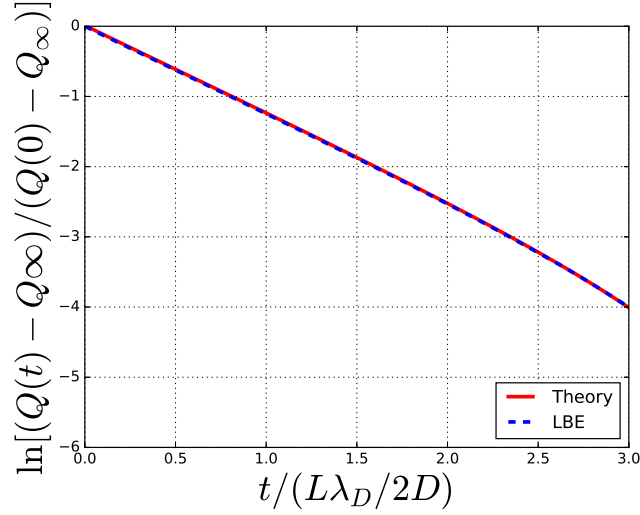


Figure 5.2 – Natural logarithm of the temporal charge evolution of Fig. 5.1 as described by Eq. 5.38. The inverse of the slope of the straight line corresponds to the characteristic time at which the capacitor relaxes (see Eq. 5.39).

We use $N_x \times N_y \times N_z = 1 \times 1 \times 259$ lattice points, with three layers of solid nodes on each side for the simulation shown in Fig. 5.1. The distance between the solid-liquid interfaces is thus $L = (N_z - 6)\Delta x = 253\Delta x$. Periodic boundary conditions are used in all directions. The resolution is fixed with the Bjerrum length $l_B/\Delta x = 4.8$. The reduced potential difference applied at the walls is $\Delta V = 0.1$, the salt concentration corresponds to a Debye screening length of $\lambda_D/\Delta x = 35.0$ and the ions have a bulk diffusion coefficient $D = 0.05 (\Delta x^2/\Delta t)$. The resulting charge evolution with respect to time is shown in Fig. 5.1. The numerical data is presented with the theoretical prediction discussed in Section A.2. The theoretical curve was obtained doing an inverse Laplace transform numerically (with Mathematica) of Eq. A.27 and applying the residue theorem truncated up to the 8th pole (the first pole would have been enough considering that we have a monoexponential function). As we can see there is a perfect agreement between the two sets of data.

On the other hand, Fig. 5.3 illustrates how the characteristic time evolves as $2\lambda_D/L$ changes. The simulations carried out are the same as the ones used to compute the data in

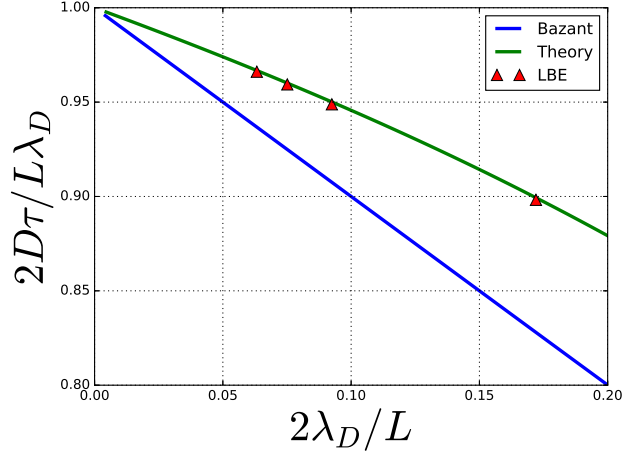


Figure 5.3 – Characteristic time in a slit when varying $\epsilon := 2\lambda_D/L$. The simulations were carried out under a reduced potential difference of $\Delta V = 0.1$ with a fixed L while λ_D varies so that $L/\Delta x = 253$ and the concentration corresponds to Debye screening lengths $\lambda_D/\Delta x = 8, 12, 20$ and 35 . The analytical results described in Appendix A.2 is shown with a green solid line, our numerical results with red triangles and Bazant’s results *i.e.* Eq. 5.32 with a blue solid line.

Table 5.1. Numerical LBE results perfectly match the theoretical prediction. Also shown on this figure is the simpler result corresponding to Eq. 5.32, depicted with a blue solid line, to illustrate the deviation between the correct relaxation time and the one predicted by Bazant *et al.* [42], which is only valid for low values of $\epsilon = 2\lambda_D/L$.

5.2.1.1 Resolution and concentration study

We studied the effect of the resolution on the characteristic relaxation time relative error. This is illustrated in Fig. 5.4. The simulations were carried out in the same conditions as for Fig. 5.1. The Bjerrum length values used to fix the resolution are $l_B/\Delta x = 1.44, 2.88$ and 4.8 . As we can see the maximum errors are close to 2% and as the resolution increases (*i.e.* as $\Delta x/l_B \rightarrow 0$) the error goes to zero.

Similarly, Fig. 5.5 illustrates the effect of the concentration (*i.e.* when λ_D varies) on the characteristic time relative error for a fixed $l_B/\Delta x = 4.8$. The Debye screening lengths used are $\lambda_D/\Delta x = 8, 12, 20$ and 35 . Once again, whenever λ_D increases, the error also goes to zero.

Overall, the results of the present section demonstrate the ability of the LBE method to quantitatively predict the time-dependent response of an electrolyte confined between planar electrodes in the linear regime.

5.2.1.2 Non-linear analysis

We mentioned in the previous chapters that we usually validate our algorithms and their implementation with analytical results in the linear regime. However, the LBE method is not limited to this regime and can actually carry out non-linear simulations. Indeed, this is one of the assets of this computational method and now that we validated the linear response part, we can explore the physics beyond this regime.

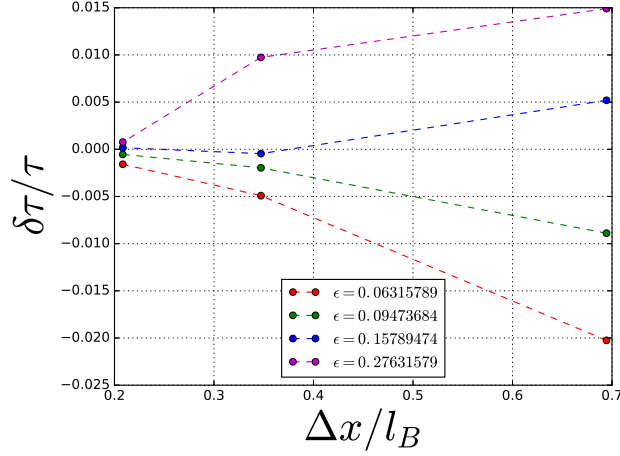


Figure 5.4 – Relative error on the characteristic time τ for $l_B/\Delta x = 1.44, 2.88$ and 4.8 , for a fixed L/l_B ratio. Four different values of $\epsilon := 2\lambda_D/L$ were tested: $0.06, 0.09, 0.16, 0.28$.

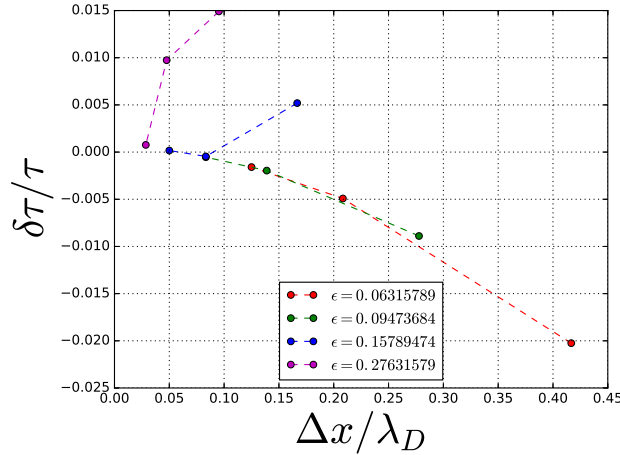


Figure 5.5 – Relative error on the characteristic time τ for $\lambda_D/\Delta x = 8, 12, 20$ and 35 , for a fixed L/l_B ratio. Four different values of $\epsilon := 2\lambda_D/L$ were tested: $0.06, 0.09, 0.16, 0.28$.

We use again $N_x \times N_y \times N_z = 1 \times 1 \times 259$ lattice points, with three layers of solid nodes on each side for the simulation shown in Fig. 5.1. The distance between the solid-liquid interfaces is thus $L = (N_z - 6)\Delta x = 253\Delta x$. The resolution is fixed with the Bjerrum length $l_B = 4.8/\Delta x$. The salt concentration corresponds to a Debye screening length of $\lambda_D/\Delta x = 35.0$ and the ions have a bulk diffusion coefficient $D = 0.05 (\Delta x^2/\Delta t)$. We then vary the reduced potential difference so that $\Delta V = 0.5, 1, 2, 3, 4, 5, 6, 8, 10$ and 20 .

Fig. 5.6 shows how the characteristic time τ varies according to the applied potential difference. We notice that for reduced voltages lower than 6 the electrolyte takes more time than in the linear regime ($\Delta V \rightarrow 0$). However, above this threshold value, the characteristic time drastically decreases. In order to understand this phenomenon we looked at the electrostatic potential profiles at steady-state, which are illustrated in Fig. 5.7. We observe that as ΔV increases the corresponding potential profile is flattened, to eventually resemble a straight line similar to the case when no salt is inserted (*e.g.* Fig. 4.8). In fact, if we look

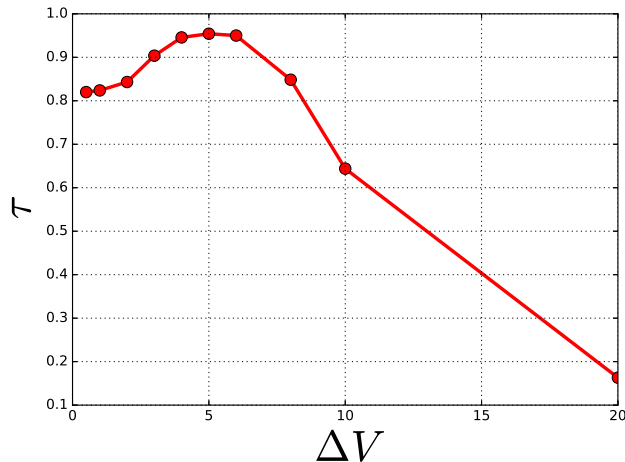


Figure 5.6 – Characteristic time in a slit when varying the reduced potential $\Delta V = 0.5, 1, 2, 3, 4, 5, 6, 8, 10$ and 20 . The distance between the solid-liquid interfaces is $L = 253\Delta x$. The resolution is fixed with the Bjerrum length $l_B/\Delta x = 4.8$. The salt concentration corresponds to a Debye screening length of $\lambda_D/\Delta x = 35.0$ and the ions have a bulk diffusion coefficient $D = 0.05 (\Delta x^2/\Delta t)$. The time for the electrolyte to relax increases for $\Delta V \leq 6/\beta e$, whereas it decreases for higher values.

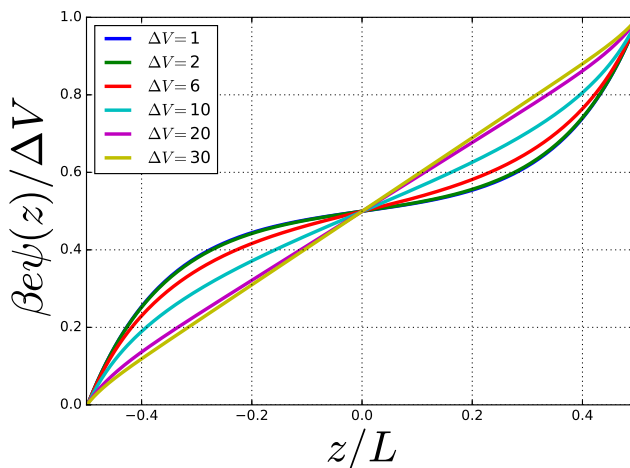


Figure 5.7 – Steady-state electrostatic potential profile for $\Delta V = 1, 2, 6, 10, 20$ and 30 . As ΔV increases the potential profile becomes more and more linear and therefore resembles the case where no salt is added.

at the cations concentration profiles shown in Fig. 5.8, we see that as the potential difference increases, cations move towards the electrode on the left until leaving almost no ions in the centre of the channel. We are actually observing a phenomenon of depletion. Hence, for large ΔV values the ions move fast towards the electrodes, forming a positive and negative layer on the anode and cathode respectively and thereby acting like a new capacitor, with no salt, and with a slightly shorter separation between the electrodes. We know that when no salt is added the relaxation time is almost instantaneous (at this level of description, which does not include the solvent relaxation explicitly) and thus it is normal to observe that τ is incredibly fastened in the case of depletion. It is worth mentioning that this phenomenon takes place because we are in the canonical ensemble. Such a depletion effect should also be observed in

the more general grand-canonical case, when the time needed to repopulate the capacitor by ions from the reservoir is long compared to the charging time (*e.g.* when the lateral extension of the electrodes is much larger than the inter-electrode distance). We now turn to the case of a coaxial cylindrical channel and test this geometry in the linear regime.

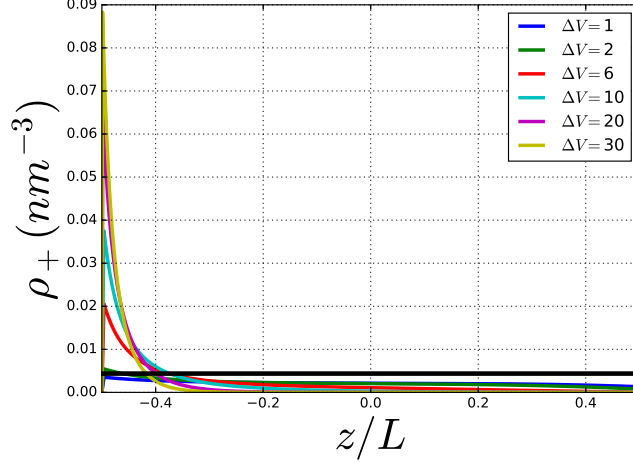


Figure 5.8 – Steady-state cation density profiles for $\Delta V = 1, 2, 6, 10, 20$ and 30 . As ΔV increases, the ions move away from the bulk region, eventually leaving almost no salt, to stick to the walls. The initial salt concentration is shown with a black solid line.

5.3 Case of a coaxial cylindrical channel

5.3.1 Results

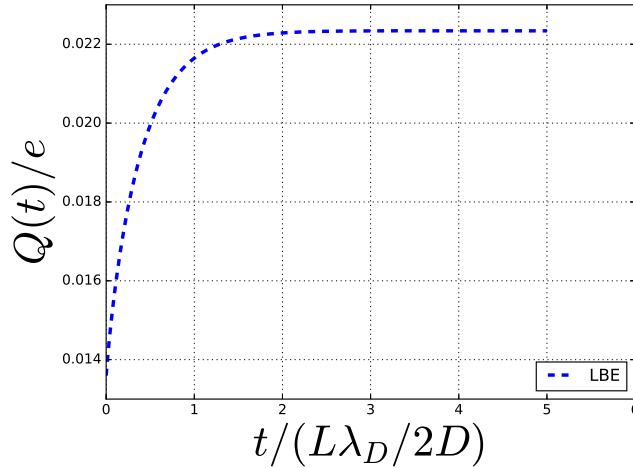


Figure 5.9 – Temporal charge evolution at one electrode of a coaxial channel. The charge accumulates in a monoexponential manner analog to a RC circuit. The distance between the electrodes is $L/\Delta x = (R_2 - R_1)/\Delta x = 40$, with the inner and outer cylinder $R_1 = 2\Delta x$ and $R_2 = 42\Delta x$ respectively. The resolution is fixed by $l_B/\Delta x = 1.2$. The reduced potential difference applied at the walls is $\Delta V = 0.1$, the salt concentration corresponds to a Debye screening length $\lambda_D/\Delta x = 8.0$ and the ions have a bulk diffusion coefficient $D = 0.05 (\Delta x^2/\Delta t)$.

Chapter 5. Transient regime in constant potential simulations

Similarly to the slit channel case, we perform a set of simulations in order to recover the theoretical prediction of I. Palaia (see Appendix A.3), for this geometry, for the charge evolution at one electrode, as well as the characteristic time, as shown in Fig. A.2.

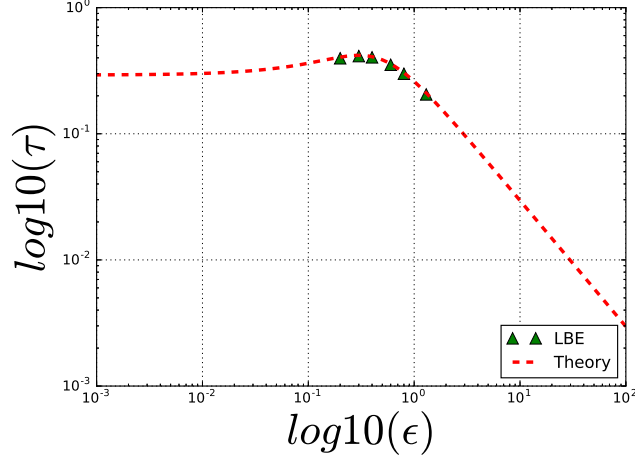


Figure 5.10 – Characteristic time in a coaxial cylindrical channel when varying $\epsilon := 2\lambda_D/L$. The simulations were carried out under a reduced potential difference of $\Delta V = 0.1$ with a fixed L while λ_D varies so that the inner and outer cylinder are $R_1 = 2\Delta x$ and $R_2 = 42\Delta x$ respectively. The salt concentration corresponds to Debye screening lengths $\lambda_D/\Delta x = 4, 6, 8, 12, 16$ and 26 .

We recover again an exponential response as described by Eq. 5.37 (see Fig. 5.9). We use $N_x \times N_y \times N_z = 134 \times 134 \times 1$ lattice points. The separation between the external boundary of the outer cylinder and the box of simulation is $w = 4\Delta x$. The radii of the inner and outer cylinder are $R_1 = 2\Delta x$ and $R_2 = 42\Delta x$ respectively. Periodic boundary conditions are used in all directions. The resolution is fixed with the Bjerrum length $l_B/\Delta x = 1.2$. The reduced potential difference applied at the walls is $\Delta V = 0.1$, the salt concentration corresponds to a Debye screening length $\lambda_D/\Delta x = 8.0$ and the ions have a bulk diffusion coefficient $D = 0.05 (\Delta x^2/\Delta t)$.

In order to validate the results in Fig. A.2, we carry out six simulations in the same conditions as in Fig. 5.9 except for $\lambda_D/\Delta x = 4, 6, 8, 12, 16$ and 26 . We compute the characteristic times in the same fashion as for the slit channel case and compare it to the corresponding theoretical curve (see Fig. 5.10). We observe that we recover perfectly the theoretical prediction (numerical data shown in green triangles) and in particular the LBE simulations are able to capture the small "bump" on the curve. It is important to point out that the theoretical curve not only depends on the distance between the two electrodes, as in the slit channel case, but also has an important dependence on the inner radius R_1 as discussed in Section A.3.

5.4 Conclusion

In this chapter we have extended the analysis of constant potential simulations of the previous chapter to the transient regime. The charge fluctuations at the electrodes are at the heart of the understanding of current fluctuations and thus of electrical noise. We verified that our numerical results correspond to the theoretical analysis carried out by I. Palaia (see Appendix A.2 and A.3) of the charge response and in particular of the electrolyte relaxation

time. In the spirit of Bazant *et al.* we showed that the relaxation time differs from the Debye time and we underlined the deviation from Bazant's result for larger values of ϵ . We pushed the analysis of the relaxation time to the non-linear regime, leading to interesting physical phenomena not obviously expected. Hence we could observe a phenomenon of depletion for large values of ΔV , which drastically accelerate the relaxation time of the electrolytes, which we could link to the depletion of the electrolyte in the bulk due to the concentration of ions near the electrodes. This is but one example of the rich physical phenomena that we will be able to investigate thanks to this new numerical tool. A first natural step in this direction would be to identify the key physical parameters controlling the transition between the two regimes (increasing/decreasing with voltage) observed for the relaxation time in a single system (fixed distance and salt concentration). Furthermore, from the point of view of the Lattice Boltzmann community, to the best of our knowledge, this is the first analysis of the charge response on an electrode for fluids confined at the nanoscale. We will see in the next chapter how a general response can be linked to electrical or thermal fluctuations. Finally we extended the analysis of the slit geometry to the case of a coaxial cylindrical channel, which was never tackled before. Once again the numerical values verified the theoretical predictions.

We have thus successfully developed a new computational method to analyse the charge response at the mesoscale. In the next Chapter we turn to the linear response theory to show that it can be applied to LB simulations to extract microscopic information (such as ion diffusion) from macroscopic quantities like a potential perturbation or any other external force. Indeed, now that this computational development was achieved, we need to test our method to available theoretical tools for the study of electrical noise arising from nanofluids.

Transient hydrodynamic finite size effects in simulations under periodic boundary conditions

Contents

6.1	Diffusion and mobility	121
6.2	Perturbation in a fluid and its linear response	124
6.3	Algorithm	125
6.4	Validation of the method	126
6.5	Finite size effects in the transient regime	127
6.5.1	Velocity auto-correlation of the local velocity field	127
6.5.2	Propagation of acoustic modes	129
6.6	Conclusion	131
6.7	Perspectives	134

Chapter 6. Transient hydrodynamic finite size effects in simulations under periodic boundary conditions

THIS PhD thesis aims at providing a theoretical and numerical framework to study thermal fluctuations in electrolytes. During the previous chapters, we have studied the response of a system to an external perturbation, which was either purely mechanical (via a pressure gradient), or electrical (via an external electric field, an imposed surface charge or a potential difference). The response to such perturbations provides information on the equilibrium fluctuations of the unperturbed system. Linear response theory can be used to derive the essential relations such as the fluctuation-dissipation theorem^[185], which we shall discuss more in details in Section 6.1. For example the response of the differential capacitance can inform us on the fluctuations in the electric charge

$$C_{\text{diff}} = \frac{\partial \langle Q \rangle}{\partial \Delta \psi} = \beta \langle \delta Q^2 \rangle \quad (6.1)$$

where $\langle \cdot \rangle$ denotes the average, Q the charge and $\delta Q = Q - \langle Q \rangle$. Eq. 6.1 is an example of a fluctuation-dissipation relation^[186] known in electronics as the Johnson-Nyquist relation^[57,58]. Fluctuations of the electric current can also be linked to the conductivity. If a time dependent electric field is applied to a system of charged particles, such field will create a current

$$e \mathbf{j}^Z(t) = \sum_{k=1}^N z_k e \dot{\mathbf{r}}_k(t) = \dot{\mathbf{M}}(t) \quad (6.2)$$

where $\dot{(\cdot)}$ denotes the time derivative and $\dot{\mathbf{M}}(t)$ is the total dipole moment of the sample. An hamiltonian describing the interaction of the system with such field can then be written as

$$\mathcal{H}'(t) = - \sum_{k=1}^N \mathbf{M}(t) \cdot \mathbf{E}(t) \quad (6.3)$$

Supposing that the electric field is applied in the x -direction and that the system is isotropic, then only the current in the x -direction will survive. Therefore, the linear response to a real, periodic field reads

$$e \langle j_x^Z(t) \rangle = \text{Re } \sigma(\omega) E_0 \exp(-i\omega t) \quad (6.4)$$

Finally, using an *after-effect function* and a complex *dynamic susceptibility*, which is also called a *dynamic response function* (see Ref. 185 for further details on these functions), one can write a Green-Kubo formula for the frequency-dependent conductivity, *i.e.*

$$\sigma(\omega) = \frac{\beta e}{V} \int_0^\infty \sum_{k=1}^N \langle j_x^Z(t) z_k e \dot{x}_k \rangle \exp(i\omega t) dt \quad (6.5)$$

$$= \frac{\beta e^2}{V} \int_0^\infty \langle j_x^Z(t) j_x^Z \rangle \exp(i\omega t) dt \quad (6.6)$$

The usual static electrical conductivity σ can be computed as $\sigma = \lim_{\omega \rightarrow 0} \sigma(\omega)$. The statistical average in Eq. 6.6 is the autocorrelation function of the fluctuating charge current in the absence of the electric field. As we will see in Section 6.1, Einstein made an argument relating the diffusion coefficient to the mobility, which can be extended to yield a correlation

Chapter 6. Transient hydrodynamic finite size effects in simulations under periodic boundary conditions

function expression for the thermal conductivity. In the present chapter, we show how linear response theory can be used together with hydrodynamic LB simulations to investigate equilibrium velocity fluctuations and the related transport coefficient, namely the diffusion coefficient.

In Section 6.1 we discuss the links between diffusion and mobility. Later, in section 6.2 and 6.3 we present the formalism of linear response theory for the specific case studied, *i.e.* a singular perturbation in a fluid, and the algorithm used to study such a perturbation. We validate the method in Section 6.4 with known results on diffusion coefficients, present in the literature. Finally, Section 6.5 illustrates the new results considering both steady state and transient regimes.

6.1 Diffusion and mobility

In the introduction we mentioned that Einstein proved the existence of Brownian motion. More specifically, Einstein imagined that particles move due to a force \mathbf{F} , whose nature is not specified, acting on them, which can depend on the position but is independent of time. As particles move in a medium, namely the fluid, they experience a viscous force (*i.e.* friction), which limits them to a maximum velocity $\mathbf{u}_{max} = \mathbf{F}/\zeta$, where ζ is the viscous friction coefficient. At equilibrium, the particle flux is compensated by a diffusion flux, which is linked to the concentration gradient so that

$$\frac{\rho_k \mathbf{F}}{\zeta_k} - D_k \nabla \rho_k = 0 \quad (6.7)$$

Furthermore, Einstein makes use of the Van't Hoff law and applies it to a suspension so that the sum of the external and osmotic forces per unit volume vanish, *i.e.*

$$\rho_k \mathbf{F} - \frac{RT}{\mathcal{N}_A} \nabla \rho_k = 0 \quad (6.8)$$

where \mathcal{N}_A is Avogadro's constant, T the temperature and R is the perfect gas constant. Using Eq. 6.7 and 6.8 yields

$$D_k = \frac{k_B T}{\zeta_k}. \quad (6.9)$$

Historically, this is the first formulation of a fluctuation-dissipation relation. If the particles are assumed to be spherical with radius R , one can use Stokes formula for the friction coefficient, resulting in a new expression for the diffusion coefficient

$$D = \frac{k_B T}{c\pi\eta R} \quad (6.10)$$

where c is a constant which depends on the prior assumptions of the problem. Integration of the stress tensor over all the sphere leads to the friction force, yielding $c = 6$ and 4 for no-slip and slip boundary conditions respectively.

Einstein finally concludes his calculations on a more probabilistic basis. Indeed, particles at positions $\{\mathbf{r}(0)\}$ diffuse over a time t to eventually reach a new positions $\{\mathbf{r}(t)\}$. The probability density to find a given particle at a position \mathbf{r} at a time t is given by the solution

Chapter 6. Transient hydrodynamic finite size effects in simulations under periodic boundary conditions

of the diffusion equation. Therefore, the mean square value of the displacement is linked to the diffusion coefficient at long times giving

$$D = \lim_{t \rightarrow +\infty} \frac{1}{6t} \langle |\mathbf{r}(t) - \mathbf{r}(0)|^2 \rangle \quad (6.11)$$

the average is here taken on the initial conditions. This relation is the result of a random walk where the mean square displacement of the walker becomes a linear time function after a sufficient large number of random steps. Smoluchowski established a relation between this random walk and Brownian motion^[187,188]. Eq. 6.11 implies that the thermodynamical limit is taken before the limit $t \rightarrow +\infty$. For a finite volume V , the diffusion coefficient is strictly zero considering that the maximum of the mean square displacement is of the order to $V^{2/3}$. In fact, the right hand side of Eq. 6.11 reaches a plateau for times shorter than the ones necessary for the particle to reach the edges of the system of reference. It is thus this plateau value that allows us to define the diffusion coefficient for a finite system. For a given particle we may write

$$\mathbf{r}(t) - \mathbf{r}(0) = \int_0^t \mathbf{v}(t') dt', \quad (6.12)$$

which yields

$$\langle |\mathbf{r}(t) - \mathbf{r}(0)|^2 \rangle = \int_0^t dt' \int_0^{t'} dt'' \langle \mathbf{v}(t') \cdot \mathbf{v}(t'') \rangle \quad (6.13)$$

$$= \int_0^t dt' \int_0^{t'} dt'' \langle \mathbf{v}(t' - t'') \cdot \mathbf{v}(0) \rangle \quad (6.14)$$

$$= 2 \int_0^t (t - t') \langle \mathbf{v}(t') \cdot \mathbf{v}(0) \rangle dt' \quad (6.15)$$

which is obtained using the stationary property of the correlation function and applying a change of variable. Plugging Eq. 6.15 in 6.11 and remembering that it only applies for large time scales we can write

$$D = \frac{1}{3} \int_0^{+\infty} \langle \mathbf{v}(t) \cdot \mathbf{v}(0) \rangle dt \quad (6.16)$$

Eq. 6.16 is a typical example of a Green-Kubo formula^[189–191], which is a class of relations where the dynamical properties are written in the form of a time integral of microscopic correlation functions. At long times (*i.e.* longer than relaxation times) the initial and final velocities are completely decorrelated. Hence, when $t \rightarrow +\infty$, $\langle \mathbf{v}(t) \cdot \mathbf{v}(0) \rangle = 0$. It was until the 1960s that the scientific community believed the velocity autocorrelation function to decay exponentially, as this result was predicted by the linearized Boltzmann equation^[121], the Fokker-Planck equation^[192], as well as the Enskog equation.

Thanks to the pioneering work of Alder and Wainwright, who studied the behaviour of the velocity autocorrelation function on a model of disks or hard spheres, the community understood that the decay had a slow asymptotic behaviour in $t^{-d/2}$, where d is the dimension of the system. They also provided a simple hydrodynamical explanation of such a decay^[193]. Shortly after, other types of theoretical explanations, on for instance a kinetic basis, were

Chapter 6. Transient hydrodynamic finite size effects in simulations under periodic boundary conditions

formulated^[194–196]. A review with other types of theoretical formulations, which include Brownian motion and group renormalisation, was carried out by Pomeau and Resibois^[197]. Eq. 6.11 and 6.16 are relations which can be easily computed via trajectories obtained experimentally or with a numerical simulation. This is a quantity obtained at equilibrium, but when simulations are used, it can be affected by finite size effects. Indeed, it is by now well established that hydrodynamic finite size effects arise in simulations due to the use of periodic boundary conditions (PBC). These effects can be understood as the result of spurious hydrodynamic interactions between particles and their periodic images.

Following Dünweg and Kremer^[198], Yeh and Hummer^[199] proposed a complete analysis of the finite size effect on the diffusion coefficient of fluid particles in a cubic box based on the mobility tensor \mathbb{T} (see below):

$$\mathbb{D}_{\text{PBC}} = D_{\infty} \mathbb{1} + k_B T \lim_{r \rightarrow 0} [\mathbb{T}_{\text{PBC}}(\mathbf{r}) - \mathbb{T}_{\infty}(\mathbf{r})], \quad (6.17)$$

where PBC and ∞ subscripts denote properties under periodic and unbounded conditions, respectively, while $\mathbb{1}$ is the identity matrix. This results in a finite size scaling of the diffusion coefficient

$$D(L) = D_{\infty} - \xi k_B T / 6\pi\eta L \quad (6.18)$$

for a cubic box of size L , with $\xi \approx 2.837$ a constant and η the fluid viscosity. The same scaling was found independently^[200] and has been confirmed in molecular dynamics simulations of simple fluids^[199], including several water models^[201,202], ionic liquids^[203] or more complex fluids such as solutions of star polymers^[204]. More recently, the extension to anisotropic boxes was also investigated^[205,206] and interpreted in terms of the same hydrodynamic arguments^[207,208].

The distortion of the flow field due to the finite size of the system (and the associated use of PBC) does not only affect the diffusion coefficient of particles, but in principle all dynamical properties. In particular, hydrodynamic flows in an unbounded fluid result in long-time tails of correlations functions, *e.g.* as $t^{-3/2}$ for the velocity autocorrelation function (VACF) in three dimensions^[185,209]. Such long time tails have been reported in molecular simulations for the VACF since the pioneering work of Ref. 210 (see *e.g.*^[211]) as well as in purely hydrodynamic lattice simulations for the VACF or other correlation functions^[133,135,148,212].

They have further been observed experimentally on colloidal particles^[213–215]. Their trapping in a harmonic potential by optical tweezers modifies the decay of the VACF which remains however algebraic^[216]. Such slow hydrodynamic modes also manifest themselves in the non-Markovian dynamics of solutes, which includes a deterministic component of the force exerted by the suspending fluid, well described for colloidal spheres by the Basset-Boussinesq force^[217,218]. Simulations displaying such a hydrodynamic memory, either on a coarse-grained^[213] or molecular^[219] scale, may therefore suffer from artefacts associated with the use of PBC, at least on long time scales. This was already recognized by Alder and Wainwright in their seminal paper where they reported their results “up to the time where serious interference between neighbouring periodically repeated systems is indicated”^[193].

Here we address this issue of finite size effects on the transient regime by revisiting the above hydrodynamic approach. We investigate the transient response to a singular perturbation of the fluid, previously considered to predict the steady-state mobility^[199,220]. More

Chapter 6. Transient hydrodynamic finite size effects in simulations under periodic boundary conditions

precisely, we determine numerically the time-dependent Green's function for the Navier-Stokes (NS) equation using Lattice Boltzmann (LB) simulations^[125]. We validate this new approach in the steady-state by comparison with known results, before turning to the transient hydrodynamic response. We show that the multiple features of these finite size effects can be rationalized analytically by considering the decay of the relevant hydrodynamic modes.

6.2 Perturbation in a fluid and its linear response

The dynamics of an incompressible fluid of mass density ρ_m and shear viscosity η can be described by the mass conservation $\partial_t \rho_m + \nabla \cdot (\rho_m \mathbf{v}) = 0$ and NS equation:

$$\rho_m \frac{\partial \mathbf{v}}{\partial t} + \rho_m (\mathbf{v} \cdot \nabla) \mathbf{v} = \eta \nabla^2 \mathbf{v} - \nabla p + \mathbf{f} \quad (6.19)$$

where \mathbf{v} is the velocity field, p is the pressure and \mathbf{f} is a force density. In the limit of small Reynolds number ($\text{Re} = \frac{\|\rho_m (\mathbf{v} \cdot \nabla) \mathbf{v}\|}{\|\eta \nabla^2 \mathbf{v}\|} \sim \frac{uL}{\nu}$ with u and L the typical velocity and length, and $\nu = \eta/\rho_m$ the kinematic viscosity), both tensors in Eq. 6.17 can be obtained by determining the Green's function for the Stokes equation. This corresponds to a vanishing left hand side in Eq. 6.19 and a perturbation:

$$\mathbf{f}(\mathbf{r}') = \left[\delta(\mathbf{r}' - \mathbf{r}) - \frac{1}{V} \right] \mathbf{F}, \quad (6.20)$$

with δ the Dirac distribution, \mathbf{F} a force and V the volume of the system, *i.e.* a singular point force at \mathbf{r} and a uniform compensating background. The mobility tensor then follows from the steady state velocity as $\mathbf{v}(\mathbf{r}') = \mathbb{T}(\mathbf{r}', \mathbf{r}) \cdot \mathbf{F}$. Note that the limit in Eq. 6.17 corresponds to $\mathbf{r}' \rightarrow \mathbf{r}$. The result for the unbounded case is the well-known Oseen tensor

$$\mathbb{T}_\infty(\mathbf{r}) = \frac{1}{8\pi\eta r} \left(\mathbb{1} + \frac{\mathbf{r}\mathbf{r}}{r^2} \right), \quad (6.21)$$

while under PBC it is more conveniently expressed in Fourier space^[199].

Similarly, the full dynamical response can be obtained by considering a perturbation of the form $\mathbf{f}(\mathbf{r}')\Theta(t)$, where $\Theta(t)$ is the Heaviside function and the spatial dependence is given by Eq. 6.20, applied on a fluid initially at rest. The Green's function for the time-dependent NS equation, which corresponds to a perturbation $\mathbf{f}(\mathbf{r}')\delta(t)$ is obtained as the time-derivative of the solution $\mathbf{v}(\mathbf{r}', t)$. In the limit $\text{Re} \ll 1$, the response to $\mathbf{f}(\mathbf{r}')\Theta(t)$ converges at long times toward the stationary field corresponding to the mobility tensor.

The transient hydrodynamic regime, as quantified by the Green's function, is also related to the equilibrium fluctuations of the velocity field. Using linear response theory^[185], we can perturb the system with a small Hamiltonian expressed as:

$$H(t) = - \int d\mathbf{r} A(\mathbf{r}, t) \mathbf{f}(\mathbf{r}, t). \quad (6.22)$$

where $\mathbf{f}(\mathbf{r}, t)$ is a force density and $A(\mathbf{r}, t)$ the conjugate field. Its corresponding linear response is then written as

$$\frac{d\langle \Delta B(\mathbf{r}, t) \rangle}{dt} = \frac{1}{k_B T} \int d\mathbf{r}' \langle B(\mathbf{r}, t) \dot{A}(\mathbf{r}', 0) \rangle \mathbf{f}(\mathbf{r}', t) \quad (6.23)$$

Chapter 6. Transient hydrodynamic finite size effects in simulations under periodic boundary conditions

where B is an observable and $\Delta B = B(t) - B(0)$. We can then take $\mathbf{f}(\mathbf{r}, t)$ to be equal to Eq. 6.20 and its conjugate field A corresponds to

$$\dot{A}(\mathbf{r}, t) = v(\mathbf{r}, t). \quad (6.24)$$

For the particular choice of observable

$$B(\mathbf{r}, t) = \rho v(\mathbf{r}, t), \quad (6.25)$$

and noting that the initial velocity vanishes, Eq. 6.23 shows that the average velocity v (canonical average over initial configurations) in the direction of the force at the position where it is applied, evolves as:

$$\frac{d}{dt} \langle v(\mathbf{r}, t) \rangle = \frac{1}{k_B T} \int d\mathbf{r}' \langle v(\mathbf{r}, t) v(\mathbf{r}', 0) \rangle f(\mathbf{r}', t) \quad (6.26)$$

This simplifies for the perturbation considered in Eq. 6.20, since the total applied force vanishes and so does the total momentum $\int d\mathbf{r}' v(\mathbf{r}', 0)$. One can finally express the velocity auto-correlation of the local velocity field (LVACF) as:

$$Z(t) \equiv \langle v(\mathbf{r}, t) v(\mathbf{r}, 0) \rangle = \frac{k_B T}{F} \frac{d \langle v(\mathbf{r}, t) \rangle}{dt}, \quad (6.27)$$

where $\langle v(\mathbf{r}, t) \rangle$ is the response to the perturbation Eq. 6.20. This expression, although similar to the one for the velocity of a particle under a constant force F , has in fact a very different meaning: Here a perturbation is applied at a fixed position \mathbf{r} (together with the compensating background) and the fluid velocity is followed at that position. Indeed, the average and auto-correlation functions are taken for the local fluid velocity defined by $\rho(\mathbf{r}, t) \mathbf{v}(\mathbf{r}, t) = \langle \sum_i \delta[\mathbf{r}_i(t) - \mathbf{r}] \mathbf{u}_i(t) \rangle$, with $\rho(\mathbf{r}, t) = \langle \sum_i \delta[\mathbf{r}_i(t) - \mathbf{r}] \rangle$ the number density, \mathbf{r}_i and \mathbf{u}_i the position and velocity of particle i .

Integrating between 0 and infinity, one obtains the steady state velocity:

$$v_\infty(\mathbf{r}) = \lim_{t \rightarrow \infty} \langle v(\mathbf{r}, t) \rangle = \frac{F}{k_B T} \int_0^\infty \langle v(\mathbf{r}, t) v(\mathbf{r}, 0) \rangle dt \quad (6.28)$$

This relation is analogous to Einstein's relation for the mobility of a particle, $\mu = v/F = D/k_B T$, with the diffusion coefficient $D = \int_0^\infty Z(t) dt$. In the following we will therefore refer to the integral of the LVACF as the diffusion coefficient.

6.3 Algorithm

Here we use LB simulations^[125], with the *Laboetie* code, to solve the above hydrodynamic problem, *i.e.* the NS equation for a fluid initially at rest on which the perturbation Eq. 6.20 is applied. As mentioned in the previous Chapters, the LB method evolves the one-particle velocity distribution $f(\mathbf{r}, \mathbf{c}, t)$ from which the hydrodynamic moments (density, momentum, stress tensor) can be computed. In practice, a kinetic equation is discretized in space (lattice spacing Δx) and time (time step Δt) and so are the velocities, which belong to a finite set

Chapter 6. Transient hydrodynamic finite size effects in simulations under periodic boundary conditions

$\{\mathbf{c}_i\}$ (here we use the D3Q19 lattice). The populations $f_i(\mathbf{r}, t) \equiv w_i f(\mathbf{r}, \mathbf{c}_i, t)$ are updated following:

$$f_i(\mathbf{r} + \mathbf{c}_i \Delta t, t + \Delta t) = f_i(\mathbf{r}, t) - \frac{\Delta t}{\tau} [f_i(\mathbf{r}, t) - f_i^{eq}(\mathbf{r}, t)] + F_i^{ext}(\mathbf{r}, t), \quad (6.29)$$

where $f_i^{eq}(\mathbf{r}, t)$ corresponds to the local Maxwell-Boltzmann equilibrium with density $\rho(\mathbf{r}, t) = \sum_i f_i(\mathbf{r}, t)$ and momentum $\rho \mathbf{v}(\mathbf{r}, t) = \sum_i f_i(\mathbf{r}, t) \mathbf{c}_i$, expanded to second-order in the velocity to minimize discretization effects resulting *e.g.* in numerical viscosity. The relaxation time τ controls the fluid viscosity. Here we use $\tau = \Delta t$, which results in a kinematic viscosity $\nu = \frac{c_s^2 \Delta t}{2} = \frac{1}{6} \frac{\Delta x^2}{\Delta t}$ since for the D3Q19 lattice the speed of sound is $c_s = \frac{1}{\sqrt{3}} \frac{\Delta x}{\Delta t}$ and F_i^{ext} accounts for the external force acting on the fluid^[125]. We perform simulations for orthorhombic cells with one length (L_\perp) different from the other two (L_\parallel), as illustrated in Figure 6.1a, in order to analyze the effect of both the system size and shape.

Starting from f_i^{eq} for a uniform fluid at rest, we apply the singular perturbation to a single node (an extension to arbitrary singular forces, including off-lattice, has been proposed in Ref. 221) with the compensating background everywhere and monitor the velocity on that node (see Figure 6.1b). The same force F is applied for all systems (10^{-4} lattice units to ensure that the Mach number is always small: $\text{Ma} = \frac{v}{c_s} < 10^{-3}$) whose sizes are chosen to remain in the limit of small Knudsen numbers ($\text{Kn} \sim \frac{\text{Ma}}{\text{Re}} = \frac{\nu}{c_s L} \sim \frac{\Delta x}{L} < 0.1$), with Re at most $\mathcal{O}(1)$.

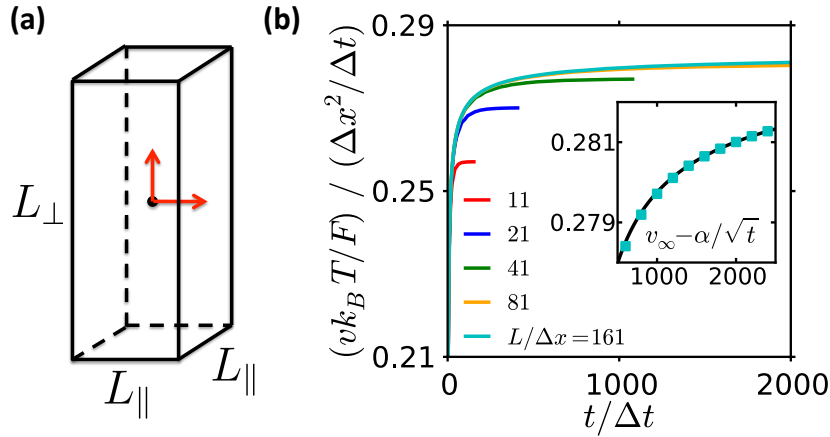


Figure 6.1 – a. A bulk fluid in an orthorhombic cell with one length different from the other two is submitted to a perturbation Eq. 6.20 which corresponds to a singular point force (in one of the two relevant directions indicated by red arrows) and a uniform compensating background. Both elongated ($L_\perp > L_\parallel$, as shown) and flat ($L_\perp < L_\parallel$) boxes are considered. b. Velocity at point \mathbf{r} where the perturbation is applied, as a function of time, from Lattice Boltzmann simulations with various cubic boxes of size $L = L_{\perp, \parallel}$. The inset shows the scaling at long times used to extrapolate the steady-state velocity, for the largest system.

6.4 Validation of the method

As a validation of this new approach for the computation of hydrodynamic Green’s functions, we first describe the results for the diffusion coefficient, obtained from the steady-state velocity as $D = k_B T v_\infty(\mathbf{r}) / F$. Here the diffusion tensor is anisotropic and the two independent

Chapter 6. Transient hydrodynamic finite size effects in simulations under periodic boundary conditions

components $D_{\parallel,\perp}$ are determined by applying the perturbation Eq. 6.20 in the corresponding directions. Continuum hydrodynamics predicts a scaling with system size^[207]:

$$D_{\parallel,\perp} = D_\infty + \frac{k_B T}{6\pi\eta L_\parallel} h_{\parallel,\perp} \left(\frac{L_\perp}{L_\parallel} \right), \quad (6.30)$$

where the two functions $h_{\parallel,\perp}$ depend only on the aspect ratio L_\perp/L_\parallel (see Ref. 207). For the isotropic case $h_{\parallel,\perp}(1) = -\xi \approx -2.837$. The inset of Figure 6.2 shows the diffusion coefficient for a cubic box as a function of the size $L_\perp = L_\parallel$. For reasons discussed below, the velocity $\langle v(\mathbf{r}, t) \rangle$ converges slowly to its steady-state value, as $v_\infty - \alpha/\sqrt{t}$ (see the inset of Figure 6.1b). Therefore we used a fit to this expression at long times to determine v_∞ for the larger systems.

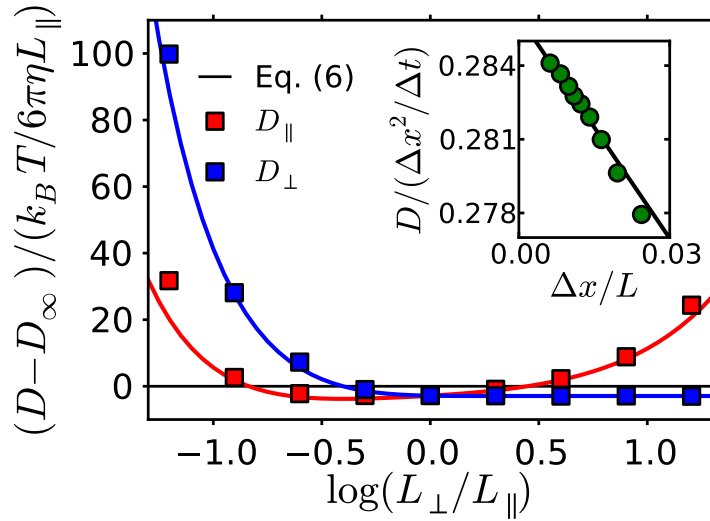


Figure 6.2 – Scaling functions $h_{\parallel,\perp} = (D_{\parallel,\perp} - D_\infty)/(k_B T/6\pi\eta L_\parallel)$ defined in Eq. 6.30 as a function of the aspect ratio L_\perp/L_\parallel . Lattice Boltzmann results (symbols) are compared to analytical results (lines) from Ref. 207. Note the logarithmic scale on the x -axis. Each point corresponds to the slope of a scaling with system size at fixed aspect ratio, as illustrated in the inset for a cubic box ($L = L_{\perp,\parallel}$), where the line again corresponds to Eq. 6.30.

The LB results are in excellent agreement with the slope expected from Eq. 6.30, even though some deviations are observed for the smaller box sizes ($\sim 10\Delta x$) as expected. The extrapolated value for an infinite system is $D_\infty \approx 0.286\Delta x^2/\Delta t$. By performing similar size scalings for various aspect ratios (see Table 6.1), we can compute the scaling functions $h_{\parallel,\perp}$ for both components of the diffusion tensor. The results, shown in the main part of Figure 6.2, are also in excellent agreement with Eq. 6.30. This validates the present approach combining linear response and LB simulations to determine hydrodynamic finite size effects on the steady-state dynamics.

6.5 Finite size effects in the transient regime

6.5.1 Velocity auto-correlation of the local velocity field

We now turn to the the finite size effects in the transient regime. As explained above, the Green’s function for the time-dependent NS equation is obtained from the derivative of the

Chapter 6. Transient hydrodynamic finite size effects in simulations under periodic boundary conditions

Size ratio α	Lengths	Values (in lattice unit Δx)								
1/16	\mathbf{L}_{\parallel}	175	271	337	429					
	\mathbf{L}_{\perp}	11	17	21	27					
1/8	\mathbf{L}_{\parallel}	103	119	135	151	169				
	\mathbf{L}_{\perp}	13	15	17	19	21				
1/4	\mathbf{L}_{\parallel}	85	115	125	155	165	175			
	\mathbf{L}_{\perp}	21	29	31	39	41	43			
1/2	\mathbf{L}_{\parallel}	31	41	51	61	71	101			
	\mathbf{L}_{\perp}	15	21	25	31	35	51			
1	\mathbf{L}_{\parallel}	11	21	41	81	161				
	\mathbf{L}_{\perp}	11	21	41	81	161				
2	\mathbf{L}_{\parallel}	11	17	23	29	35	41	47	53	59
	\mathbf{L}_{\perp}	22	35	47	59	71	83	95	107	119
4	\mathbf{L}_{\parallel}	11	17	23	29	35	41	47		
	\mathbf{L}_{\perp}	45	69	93	117	141	165	189		
8	\mathbf{L}_{\parallel}	11	17	23	29	35				
	\mathbf{L}_{\perp}	89	137	185	233	281				
16	\mathbf{L}_{\parallel}	11	17	23	29	35				
	\mathbf{L}_{\perp}	175	273	369	465	561				

Table 6.1 – The simulated systems correspond to orthorhombic boxes with $L_x = L_y = L_{\parallel}$ and $L_z = L_{\perp}$. For each size ratio $\alpha = L_{\perp}/L_{\parallel}$, we compute the steady-state velocity as a function of $k_B T/6\pi\eta L_{\parallel}$, for a singular force applied either in the x or z directions. The corresponding slopes provide the scaling functions $h_{\parallel,\perp}$ reported in Figure 6.2.

response $v(\mathbf{r}, t)$ to the perturbation $\mathbf{f}(\mathbf{r}')\Theta(t)$. More precisely, we discuss here the LVACF defined by Eq. 6.27 which is proportional to this Green’s function and quantifies the equilibrium hydrodynamic fluctuations. In an unbounded medium, such fluctuations result in the long-time tail of the VACF in simple fluids according to^[185]:

$$Z_{\infty}(t) = \frac{2}{3} \frac{k_B T}{\rho_m} [4\pi\nu t]^{-3/2} . \quad (6.31)$$

Mode-coupling theory predicts in fact a scaling with $D + \nu$ instead of ν , but here the Green’s function is not associated with the diffusion of a tagged particle, so that D is not involved.

Figure 6.3 reports the LVACF computed from Eq. 6.27 using the present LB approach, for various cubic boxes of size L . For the larger systems, the simulation results coincide exactly with the hydrodynamic scaling Eq. 6.31 over several orders of magnitude, without any adjustable parameter. This scaling, together with Eq. 6.27, justifies a posteriori the fit of the velocity as $v_{\infty} - \alpha/\sqrt{t}$ to extrapolate the steady-state value. However, we observe a cross-over from the algebraic decay to an exponential regime (and oscillations discussed in more detail below), with a cross-over time that decreases with decreasing L .

The algebraic decay Eq. 6.31 arises from the superposition of an infinite number of modes (corresponding to the hydrodynamic limit of vanishing wave numbers $k \rightarrow 0$) for momentum diffusion, which in Fourier space decay as $\sim e^{-\nu k^2 t}$. The exponential decay therefore results from the cut-off at low wave numbers introduced by the PBC, with the slowest mode corresponding to $k_L = 2\pi/L$ and a characteristic time $\tau_L = 1/\nu k_L^2$. The vertical arrows in

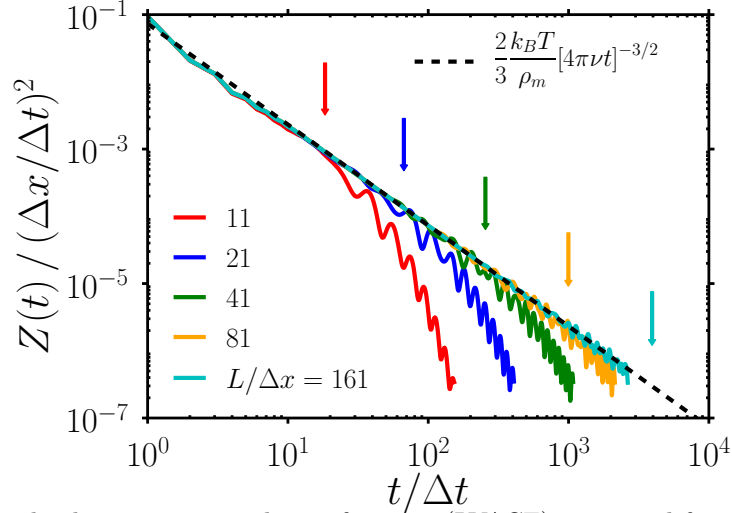


Figure 6.3 – Local velocity auto-correlation function (LVACF) computed from Lattice Boltzmann simulations in a cubic cell, for various cell sizes $L/\Delta x$. The double logarithmic scale underlines the algebraic decay expected from hydrodynamics in an unbounded fluid, Eq. 6.31. The finite size results in a cross-over to an exponential decay, analyzed in further detail in Figure 6.4. The arrows indicate the diffusion time for the slowest mode, $\tau_L = 1/\nu k_L^2$, with $k_L = 2\pi/L$, which corresponds to the exponential decay rate and is also typical of the cross-over between the algebraic and exponential regimes.

Figure 6.3, which indicate this time, show that it is also typical of the cross-over from algebraic to exponential decay $A_L e^{-\nu k_L^2 t}$ of the LVACF. The scaling of the cross-over time τ_L is consistent with that reported for the velocity decay of a particle submitted to an impulsive force in LB simulations with fixed system size and varying viscosity^[221]. The prefactor A_L can be roughly estimated by assuming the continuity between the two regimes at $t = \tau_L$. Using Eq. 6.31, this results in:

$$A_L = \frac{2e}{3} \frac{k_B T}{[4\pi]^{3/2} \rho_m} k_L^3. \quad (6.32)$$

6.5.2 Propagation of acoustic modes

Another striking feature in Figure 6.3 is the presence of oscillations, with a frequency which depends on the size of the simulation box. This is clearly another finite size effect, which can be understood in terms of the slight compressibility of the fluid. Indeed, in the LB method the fluid is only quasi-incompressible. In such a case, while the transverse mode decays as $\sim e^{-\nu k^2 t}$ (as for an incompressible fluid), the longitudinal modes follow a dispersion relation which can be obtained by linearizing the mass conservation and compressible NS equation, for an isothermal perturbation of the form $e^{i(\omega t - \mathbf{k} \cdot \mathbf{r})}$. Since the equation of state of the LB fluid is that of an ideal gas ($p = \rho k_B T = \rho_m c_s^2$), one obtains:

$$(i\omega)^2 + i\omega k^2 \left(\frac{4}{3} \nu + \nu' \right) + c_s^2 k^2 = 0, \quad (6.33)$$

with $\nu' = \zeta/\rho_m$ the kinematic bulk viscosity. In the case of the D3Q19 lattice, for which

Chapter 6. Transient hydrodynamic finite size effects in simulations under periodic boundary conditions

$\nu' = \frac{2}{3}\nu$, the solutions are of the form

$$i\omega = -\nu k^2 \pm ikc_s \sqrt{1 - \nu^2 k^2 / c_s^2} \sim -\nu k^2 \pm ikc_s \quad (6.34)$$

(for $k \ll c_s/\nu$), *i.e.* attenuated sound waves. Such a dispersion relation had already been considered for the LB simulation of acoustic waves, see *e.g.* [222–224].

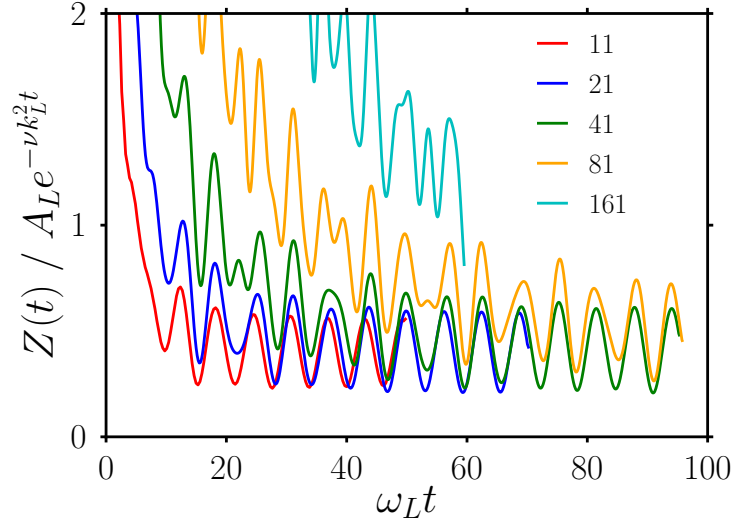


Figure 6.4 – LVACF computed from Lattice Boltzmann simulations in a cubic cell, for various cell sizes $L/\Delta x$, normalized by the expected exponential scaling at long times $A_L e^{-\nu k_L^2 t}$ with $k_L = 2\pi/L$ and A_L given by Eq. 6.32, as a function of time rescaled by the frequency $\omega_L = kc_s \sqrt{1 - \nu^2 k^2 / c_s^2}$. The oscillations are due to the small compressibility of the LB fluid, which results in damped acoustic waves. For the larger systems the contribution of faster modes nk_L is still visible on the time scale of the simulations.

For periodic systems, the slowest modes correspond to $k_L = 2\pi/L$ and longitudinal modes decay as $\sim e^{-\nu k_L^2 t} \cos \omega_L t$, with a frequency

$$\omega_L = k_L c_s \sqrt{1 - \nu^2 k_L^2 / c_s^2} \sim k_L c_s. \quad (6.35)$$

Figure 6.4 reports the LVACF normalized by the exponential decay $A_L e^{-\nu k_L^2 t}$, as a function of the rescaled time $\omega_L t$, for various system sizes spanning more than one order of magnitude. It clearly shows that the above analysis captures all the main features of the finite size effects on the transient hydrodynamic response: 1) the rate of the exponential decay, since at long times the curves oscillate around a plateau; 2) the order of magnitude A_L of the exponential regime, since the value of the plateau is the same for all system sizes; 3) the frequency of the oscillations, which are in phase after rescaling by ω_L . While only the slowest mode contributes to the oscillations for the smallest system ($L = 11\Delta x$), others are increasingly visible in this time range as the system size increases. Indeed, the other modes nk_L decay as $\sim e^{-\nu n^2 k_L^2 t} = e^{-\frac{\nu n^2 k_L^2}{\omega_L} \omega_L t}$, *i.e.* $\frac{\nu n^2 k_L^2}{\omega_L} = n^2 \frac{\nu k_L}{c_s}$ times faster – a difference which decreases with increasing L . Using more elaborate LB schemes for compressible thermal flows [225] or any other hydrodynamic simulation algorithm (or even the continuous Boltzmann equation from which the LB algorithm follows), will also result in the cross-over to the exponential regime, which is an inevitable consequence of the finite size of the system and the associated PBC.

It should also manifest itself with strictly incompressible flow simulations, even though we do not expect oscillations in the VACF in that case.

6.6 Conclusion

In this Chapter, we have used Lattice Boltzmann and analytical calculations to investigate transient hydrodynamic finite size effects induced by the use of periodic boundary conditions. These effects are inevitable in simulations at the molecular, mesoscopic or continuum levels of description. We analyzed the transient response to a local perturbation in the fluid and obtained the local velocity correlation function via linear response theory. This new approach was validated by comparing the finite size effects on the steady-state velocity with the known results for the diffusion coefficient. We next investigated the full time-dependence of the local velocity auto-correlation function. We found at long times a cross-over between the expected $t^{-3/2}$ hydrodynamic tail and an oscillatory exponential decay, and studied the scaling with the system size of the cross-over time, exponential rate and amplitude, and oscillation frequency. We interpreted these results from the analytic solution of the compressible Navier-Stokes equation for the slowest modes, which are set by the system size. The present work not only provides a comprehensive analysis of hydrodynamic finite size effects in bulk fluids, which arise regardless of the level of description and simulation algorithm, but also establishes the Lattice Boltzmann method as a suitable tool to investigate such effects in general. More specifically, the present work shows that it is possible to rationalize all finite size effects in terms of the cut-off of hydrodynamic modes at small wave numbers introduced by the use of PBC. Coming back to Alder and Wainwright's quote^[193], the time where neighbouring periodically repeated systems seriously interfere corresponds to momentum diffusion for the slowest mode, $\tau_L = 1/\nu k_L^2$. It is crucial for the setup and analysis of molecular simulations to control these finite size effects, which can be efficiently computed from the present approach combining linear response and LB simulations. In turn, such an analysis is useful to extrapolate the macroscopic limit without actually performing the simulations for too large systems. One could exploit these effects further to determine material properties, not only the viscosity from the slope of the diffusion coefficient vs inverse box size (as for water in first principles molecular dynamics simulations^[226]), but also *e.g.* the speed of sound from the oscillation frequency of the LVACF, as shown here.

The systematic finite size analysis of the transient response could also be extended to other situations. For example, the long-time decay of the VACF under confinement or near a boundary, in an otherwise unbounded fluid, scales as $t^{-5/2}$ instead of $t^{-3/2}$ in the bulk^[136,227], but PBC in the directions parallel to the interface will also result in deviations from the algebraic decay. Similarly, the diffusion coefficient of lipids and carbon nanotubes embedded in a membrane diverges logarithmically with system size^[208] and one should also observe the impact of PBC on the transient dynamics. This may also prove important for extracting from finite size simulations other dynamical properties for which hydrodynamics play an important role, such as memory kernels^[219].

Therefore, we may consider this Chapter as a first form of validation to prove the effectiveness of the LB method to tackle analysis involving linear response theory, which in the future will help us to understand the origin of electrical noise via macroscopic quantities such as the fluctuations of electric current, by readapting this problem to the case presented in

Chapter 6. Transient hydrodynamic finite size effects in simulations under periodic boundary conditions

Eq. 6.6, but also to the electrokinetic response, related to the cross-correlation between mass and electric currents^[74,79].

General Conclusion

OUR work is inscribed in a succession of attempts at understanding fluctuations, nanofluidic sensings or simply nanoelectrodes from different angles (*i.e.* different computational tools). Lattice Boltzmann Electrokinetics (LBE) and more specifically its implementation in the *Laboetie* code represents another brick in the wall with the other available algorithms which simulate electrodes maintained at fixed electrical potentials (*e.g.* Ref. 228).

Our contribution within the Lattice Boltzmann community was to extend the moment propagation method to include the combined effects of adsorption/desorption of charged tracers, their migration under local and applied electric fields, as well as their advection by the local velocity of the fluid. Furthermore, we modified the algorithm to simulate nano-capacitors in different geometries - we only tested two different kinds but the method can be applied to any arbitrary geometry - under a constant potential difference between the electrodes. This moved the LBE method in the community of algorithms simulating electrodes maintained at fixed electrical potentials, as mentioned above. Besides, the constant potential method and more generally the LBE method was used for the first time to analyse the transient regime of nanocapacitors charging. By doing so, we could retrieve the temporal evolution of the charge at an electrode (*i.e.* the charge response to a perturbation) and point out that, in the case of small applied potential differences, the electrolytes relaxation time present characteristic times more complex than the simple Debye time or even the time found by Bazant. Furthermore we could extend the analysis to the non-linear regime and show an interesting depletion phenomenon taking place, which leads to a more complex temporal response. Contrary to the other methods mentioned (*e.g.* Ref. 228) LBE is a mesoscopic method and has thus the advantage of simulating large systems ~ 100 nm, which reinforces the idea that it provides a useful computational framework for the experimentalists, allowing them to better understand their results. Finally we showed the efficiency of the LB method to study confined electrolytes using linear response theory and the link between response and fluctuations. This will enable us to understand the origin of electrical noise, via macroscopic quantities, such as the fluctuations of electric current. Indeed, Nyquist gave an expression for the generalized noise for devices with a partially reactive response, such as a capacitor, and showed that the power spectral density of the series noise voltage can be linked to a frequency-dependent complex electrical impedance. A Fourier transform of the temporal charge response would provide us with the capacitor impedance. Hence, the charge response can be linked to the impedance and thus to the electrical fluctuations. Furthermore, we will also be able to study the electrokinetic response related to the cross correlation response between mass and electric currents.

Therefore, we provided the basis of a computational framework, which in a compact form can model a large variety of physical phenomena, coupling different dynamics, and can be applied to available theories to understand intrinsic microscopic mechanisms from macroscopic quantities. This is the first note of this noisy symphony, which we are trying to listen. Let us listen carefully...

6.7 Perspectives

Because of the prior assumptions of PNP theory, excluded volume effects are not taken into account at this stage (in the *Laboetie* code). Moreover, we have considered only symmetric electrolytes so far. However, we could consider modifying the method with other available theories to include volume effects^[229] or simulate N -component electrolytes^[230] *i.e.* for tracers which do not influence the dynamics of the other species. In addition, as the sorption dynamics is only present in the moment propagation method, it would be interesting to also include it in the LB part of the code. This would help us understanding the interplay between adsorption/desorption and electrokinetic effects during the transient regime for instance.

From a general perspective, the study of electrical fluctuations in a number of geometries and conditions, corresponding to the available experimental literature, would allow us to predict the expected signal (*i.e.* the experimentally measured signal). The problem can be viewed in two different directions: experimentalists measure a signal and try to understand the underlying mechanisms, whereas we can predict the expected signal and its noise characteristics as a function of the geometrical and physical parameters defining the experimental system. This allows in turn to extract the latter from the experimental data, as the noise footprint is unique for any given molecule or atom. We can thus consider an inverse approach to the problem and provide noisy signals to the experimentalists, which correspond to a system of reference. We could then explore new strategies and optimise the available setups in order to push the detection limits, allowing experimentalists and engineers to exploit their tools beyond the current state-of-the-art, *e.g.* working at low ionic strength, at higher frequencies or with smaller devices.

During this PhD we focused on modelling electric charge and current fluctuations. However, it would be interesting to introduce thermal fluctuations into LBE simulations. This would then provide the right computational tools to directly simulate single molecule detection and nano-electrochemical experiments, as described in the introduction.

On the longer term, the basis of this work could have implications for the development of nanofluidic sensors. Simulations related to the development of nanoISFETs (Nanoscale Ion Sensitive Field Effect transistors) could be considered. Our methodological development would provide a basis for further developments that would create simulation tools which could be transferable to other scientific and technological contexts, such as biological sensors or the production of "Blue energy" from salinity gradients (*e.g.* between salty sea water and fresh river water) and sea water desalination.

Appendix

Mathematical derivations and algorithms

A.1 Successive Over Relaxation Algorithm

The electrostatic potential ψ is solved via Poisson equation, which is computed at each time step using the Successive Over Relaxation algorithm, namely SOR. It is a numerical recipe which solves linear systems such as

$$Ax = b \tag{A.1}$$

where $A \in \mathbb{R}^{n,m}$, $b \in \mathbb{R}^n$. In our case A corresponds to the Laplacian operator, x to the electrostatic potential ψ and b to the charge density.

It is an iterative algorithm which constructs a series of vectors $x^{(k)} \in \mathbb{R}^n$ such that $\lim_{k \rightarrow \infty} x^{(k)} = x = A^{-1}b$. $x^{(k)}$ is a serie convergent in x for all $k \in \mathbb{N}$.

More specifically, SOR is based on a Gauss-Seidel algorithm. It makes use of a matrix Ω_ω , which depends on a chosen parameter ω which is picked so that the spectral radius $\rho(\Omega_\omega)$ is as small as possible. We decompose the matrix A according to $A = M - N$ with $M = 1/\omega(D - \omega E) \Rightarrow A = D - E - F$. The *a priori* assumption is that $(D - \omega E)$ is invertible (*i.e.* $a_{i,i} \neq 0 \ \forall i$). We define Ω_ω with $\Omega_\omega = M^{-1}(M - A) = I - M^{-1}A$, where $\Omega_\omega = (D - \omega E)^{-1}[(1 - \omega)D + \omega F] = (I - \omega L)^{-1}[(1 - \omega)I + \omega U]$, with $L = D^{-1}E$, $U = D^{-1}F$ and $C_\omega = M^{-1}b$ where $C_\omega = \omega(D - \omega E)^{-1}b = \omega(I - \omega L)^{-1}(D^{-1}b)$.

The method works then as follows,

$$M = \frac{1}{\omega}D - E \Rightarrow N = \left(\frac{1}{\omega} - 1\right)D + F \ ; \quad \mathcal{L}_\omega = (D - \omega E)^{-1}[(1 - \omega)D + \omega F] \tag{A.2}$$

then we solve

$$\left(\frac{1}{\omega}D - E\right)x^{k+1} = \left[\left(\frac{1}{\omega} - 1\right)D + F\right]x^k + b \tag{A.3}$$

Proposition : If $\omega \notin (0, 2)$ then SOR diverges $\Rightarrow \rho(\mathcal{L}_\omega) \geq 1$

$$\det(\mathcal{L}_\omega) = \det[D - \omega E]^{-1} \det[(1 - \omega)D + \omega F] \tag{A.4}$$

$$= \det[D]^{-1} \det[D]^{-1} \det[(1 - \omega)D] \tag{A.5}$$

$$= (1 - \omega)^n \tag{A.6}$$

Appendix A. Mathematical derivations and algorithms

Let $W = \mathcal{L}_\omega^t \mathcal{L}_\omega$, then ν_i are the eigenvalues of $W \Rightarrow \rho(\mathcal{L}_\omega) = \sup_{1 \leq i \leq n} \sqrt{\nu_i}$. We have

$$\det(W) = [\det(\mathcal{L}_\omega)]^2 \quad (\text{A.7})$$

$$= \prod_{i=1}^n \nu_i \quad (\text{A.8})$$

$$\leq [\rho(\mathcal{L}_\omega)]^{2n} \quad (\text{A.9})$$

and thus,

$$(1 - \omega)^{2n} \leq [\rho(\mathcal{L}_\omega)]^{2n} \quad (\text{A.10})$$

If $\omega \leq 0 \Rightarrow (1 - \omega) \geq 1 \Rightarrow \rho(\mathcal{L}_\omega)$

If $\omega \geq 2 \Rightarrow -1 \geq (1 - \omega) \Rightarrow (1 - \omega)^2 \geq 1 \Rightarrow \rho(\mathcal{L}_\omega)$

Hence, in order for SOR to converge we need to have $0 < \omega < 2$. For our purposes we use $\omega = 1.4$.

A.2 Ions dynamics and relaxation times, linear regime - slit channel case

The following section corresponds to the analytical derivations carried out by Ivan Palaia to estimate the electrolyte relaxation time, in the linear regime, in a slit channel. The corresponding numerical comparisons are discussed in Section 5.2.

The dynamics is determined by the Nernst-Planck drift-diffusion equations,

$$\frac{\partial \rho_\pm}{\partial t} = -D \frac{\partial}{\partial x} \left(-\frac{\partial \rho_\pm}{\partial x} \mp \beta e \rho_\pm \frac{\partial \psi}{\partial x} \right) \quad (\text{A.11})$$

The electric potential is linked to the volumic density of charge $\rho_f = e(\rho_+ - \rho_-)$ through the Poisson equation

$$-\nabla^2 \psi = \frac{\rho_f}{\epsilon_r \epsilon_0} \quad (\text{A.12})$$

The fact that ions are confined within the two slabs of the capacitor imposes that the current of cations and anions at $+L/2$ and $-L/2$ be vanishing:

$$\begin{aligned} -\frac{\partial \rho_\pm}{\partial x}(-L/2, t) \mp \beta e \rho_\pm(-L/2, t) \frac{\partial \psi}{\partial x}(-L/2, t) &= 0 \\ -\frac{\partial \rho_\pm}{\partial x}(+L/2, t) \mp \beta e \rho_\pm(+L/2, t) \frac{\partial \psi}{\partial x}(+L/2, t) &= 0 \end{aligned} \quad (\text{A.13})$$

Finally, the potential must be continuous between slab and solution, so

$$\psi(\pm L/2, t) = \pm V(t) \quad (\text{A.14})$$

Appendix A. Mathematical derivations and algorithms

Eq. A.11 can be linearised around the equilibrium values of ψ and ρ_{\pm} when the voltage source is off: namely, $\psi = 0$ and $\rho_{\pm} = n_s$, n_s being the uniform initial concentration of the two ionic species (salt concentration). The linearisation will give accurate results as long as $|\psi(x, t)| \ll (\beta e)^{-1}$ and $|\rho_{\pm}(x, t) - n_s| \ll n_s$ during the evolution of the system; these conditions logically translate into $|V(t)| \ll (\beta e)^{-1}$ and $|\rho_f(x, t)| \ll 2n_s e$, respectively. Subtracting the linearised equation for ρ_- from the linearised equation for ρ_+ yields the so-called Debye-Falkenhagen equation for ρ_f :

$$\frac{\partial \rho_f}{\partial t} = D \left(\frac{\partial^2 \rho_f}{\partial x^2} + 2\beta e^2 n_s \frac{\partial^2 \psi}{\partial x^2} \right) \quad (\text{A.15})$$

Using Eq. A.12, we get

$$\frac{\partial \rho_f}{\partial t} = D \left(\frac{\partial^2 \rho_f}{\partial x^2} - \kappa^2 \rho_f \right) \quad (\text{A.16})$$

We now make the equations adimensional: we measure lengths in units of $L/2$, times in units of $\frac{L\lambda_D}{2D}$, potentials in units of $\frac{1}{\beta e}$, electric charge density in units of $2en_s$, and denote ϵ the adimensional ratio $\frac{2\lambda_D}{L} = \frac{2}{\kappa L}$. Note that ϵ can but need not be a small quantity. From now onwards, x and t will denote the adimensional coordinates, $\rho_f(x, t)$ and $\psi(x, t)$ will be adimensional functions of adimensional coordinates, and ϵ will be the only adimensional parameter of the system. Eq. A.16 can be rewritten as

$$\epsilon \frac{\partial \rho_f}{\partial t} = \epsilon^2 \frac{\partial^2 \rho_f}{\partial x^2} - \rho_f \quad (\text{A.17})$$

The Poisson equation reads

$$-\epsilon^2 \frac{\partial^2 \psi}{\partial x^2} = \rho_f \quad (\text{A.18})$$

The boundary condition given in Eq. A.13 can be written in terms of the charge density upon linearization; its dimensionless version reads

$$-\frac{\partial \rho_f}{\partial x}(\pm 1, t) - \frac{\partial \psi}{\partial x}(\pm 1, t) = 0 \quad (\text{A.19})$$

Finally, boundary condition given in Eq. A.14 still reads

$$\psi(\pm 1, t) = \pm V(t) \quad (\text{A.20})$$

We present two equivalent derivations of the exact relaxation times in the linear regime: in the first one we make use of the Laplace transform to solve the PNP equation, in the second one we start from an ansatz about its solution and work in the time domain.

A.2.0.1 Laplace domain

Eq. A.17 can be easily solved by using Laplace transforms (as in^[42]), that we denote by hats and define as follows:

$$\widehat{\rho}_f(x, s) = \mathcal{L}\{\rho_f(x, t)\} = \int_0^{\infty} \rho_f(x, t) e^{-st} dt \quad (\text{A.21})$$

Appendix A. Mathematical derivations and algorithms

In the Laplace domain, knowing that $\rho_f(x, 0) = 0$ since we start from a discharged EDLC, Eq. A.17 reads

$$\frac{1 + \epsilon s}{\epsilon^2} \widehat{\rho}_f = \frac{\partial^2 \widehat{\rho}_f}{\partial x^2} \quad (\text{A.22})$$

Any x -antisymmetric solution will be of the type

$$\widehat{\rho}_f(x, s) = A(s) \sinh(kx) \quad (\text{A.23})$$

where k is in principle any of the two solutions of the equation

$$k^2 = \frac{1 + \epsilon s}{\epsilon^2} \quad (\text{A.24})$$

In the following, we will always assume k to be the solution with positive imaginary part (thus operating a branch cut of the square-root function along the positive real axis) and we will see in a while that the complementary choice gives the same results. Using the the Laplace-domain version of Eq. A.18, one gets the general form of $\widehat{\psi}$. Fixing the null-potential plane at $x = 0$, and imposing boundary conditions of Eq. A.19 and A.20, again, in their Laplace-domain version, the following result can be obtained:

$$\widehat{\psi}(x, s) = \frac{\sinh(kx) + xk(\epsilon^2 k^2 - 1) \cosh(k)}{\sinh(k) + k(\epsilon^2 k^2 - 1) \cosh(k)} \widehat{V}(s) \quad (\text{A.25})$$

$$\widehat{\rho}_f(x, s) = -\frac{\epsilon^2 k^2 \sinh(kx)}{\sinh(k) + k(\epsilon^2 k^2 - 1) \cosh(k)} \widehat{V}(s) \quad (\text{A.26})$$

Other interesting adimensional quantities are the superficial density of charge $\sigma(t)$ on the left plate, expressed in unites of $\frac{2e}{L \frac{\beta e^2}{\epsilon_r \epsilon_0}}$, the integrated charge density $Q(t) = \int_{-1}^0 \rho_f(x, t) dx$, of course in unites of $2n_s e L / 2 = \frac{eL}{2\lambda_D^2 \frac{\beta e^2}{\epsilon_r \epsilon_0}}$, and the electric field $E(0, t)$ at $x = 0$, in unites of $\frac{2}{L\beta e}$. Their Laplace transforms read

$$\begin{aligned} \widehat{\sigma}(s) &= -\frac{\partial \widehat{\psi}}{\partial x}(-1, s) \\ &= -k \coth(k) \frac{\epsilon^2 k^2}{1 + k(\epsilon^2 k^2 - 1) \coth(k)} \widehat{V}(s) \end{aligned} \quad (\text{A.27})$$

$$\begin{aligned} \widehat{Q}(s) &= \int_{-1}^0 \widehat{\rho}_f(x, s) dx \\ &= \frac{\tanh(\frac{k}{2})}{k} \frac{\epsilon^2 k^2}{1 + k(\epsilon^2 k^2 - 1) \coth(k)} \widehat{V}(s) \end{aligned} \quad (\text{A.28})$$

$$\begin{aligned} \widehat{E}(0, s) &= -\frac{\partial \widehat{\psi}}{\partial x}(0, s) \\ &= \left[\frac{\tanh(\frac{k}{2})}{\epsilon^2 k} - k \coth(k) \right] \frac{\epsilon^2 k^2}{1 + k(\epsilon^2 k^2 - 1) \coth(k)} \widehat{V}(s) \end{aligned} \quad (\text{A.29})$$

Appendix A. Mathematical derivations and algorithms

Note that these three quantities satisfy exactly Gauss' theorem, in the form

$$\hat{\sigma}(s) + \frac{1}{\epsilon^2} \hat{Q}(s) = \hat{E}(0, s) \quad (\text{A.30})$$

All these expressions for Laplace transforms of real observables are invariant under the transformation $k \rightarrow -k$, meaning that considering the second solution of Eq. A.24 gives the exact same results.

To study the time relaxation of the system to equilibrium, we recall that by the Bromwich-Mellin inversion formula

$$\rho_f(x, t) = \mathcal{L}^{-1}\{\hat{\rho}(x, s)\} = \int_{S-i\infty}^{S+i\infty} \hat{\rho}(x, s) e^{st} ds \quad (\text{A.31})$$

for some real S such that $\hat{\rho}(x, s)$ has no pole lying on the right of S . We observe that, if the integrand function is such that its integral over the semi-circumference of infinite radius in a left half-plane goes to zero, the integral amounts to the sum of the residues of the integrand itself. Hence, each non-zero pole of the function $\hat{\rho}(x, s)$ will contribute to the inverse Laplace transform with a term $e^{s_n t} \text{Res}_{\hat{\rho}(x, s)}(s_n)$. The non-zero poles of $\hat{\rho}$, $\hat{\sigma}$, \hat{Q} or $\hat{E}0$ are thus the relaxation rates of our system.

For a step potential $V(t) = v$ for $t > 0$, the non-zero poles of functions in Eq. A.25 to A.29 all coincide. Indeed, such quantities can all be expressed as products of entire functions (except in 0) times the following $H(s)$:

$$H(s) = \frac{\epsilon^2 k^2}{1 + k(\epsilon^2 k^2 - 1) \coth(k)} = \frac{1 + \epsilon s}{1 + s\sqrt{1 + \epsilon s} \coth\left(\frac{\sqrt{1 + \epsilon s}}{\epsilon}\right)} \quad (\text{A.32})$$

The same branch cut introduced before for the square root is used.

We denote the poles of $H(s)$ by s_n , with $n \in \{0, 1, 2, \dots\}$, and we order them such that the highest their index n , the most distant they are from the origin. They all lie on the negative real axis and are all of order 1. To identify them, we analyse first the case $s < -\frac{1}{\epsilon}$ and then the case $s > -\frac{1}{\epsilon}$; notice that $s = -\frac{1}{\epsilon}$ is not a pole but a removable singularity.

In the case $s < -\frac{1}{\epsilon}$, $\sqrt{1 + \epsilon s} = iy(s)$ with y real and positive. Finding the zeroes of Eq. A.32 amounts therefore to finding the roots of the transcendental equation

$$\tan\left(\frac{y(s)}{\epsilon}\right) = \frac{y(s)}{\epsilon} (y(s)^2 + 1) \quad (\text{A.33})$$

They can be easily found graphically and numerically and they are included in the interval $\epsilon\pi n < y_n < \epsilon\pi(n + \frac{1}{2})$, with $n \geq 1$ if $\epsilon \leq \frac{1}{\sqrt{3}}$ or $n \geq 0$ if $\epsilon > \frac{1}{\sqrt{3}}$. This corresponds to poles s_n such that

$$-\frac{1}{\epsilon} - \epsilon\pi^2 \left(n + \frac{1}{2}\right)^2 < s_n < -\frac{1}{\epsilon} - \epsilon\pi^2 n^2 \quad (\text{A.34})$$

$$\text{with } \begin{cases} n \geq 1, & \text{if } \epsilon \leq \frac{1}{\sqrt{3}} \\ n \geq 0, & \text{if } \epsilon > \frac{1}{\sqrt{3}} \end{cases} \quad (\text{A.35})$$

Appendix A. Mathematical derivations and algorithms

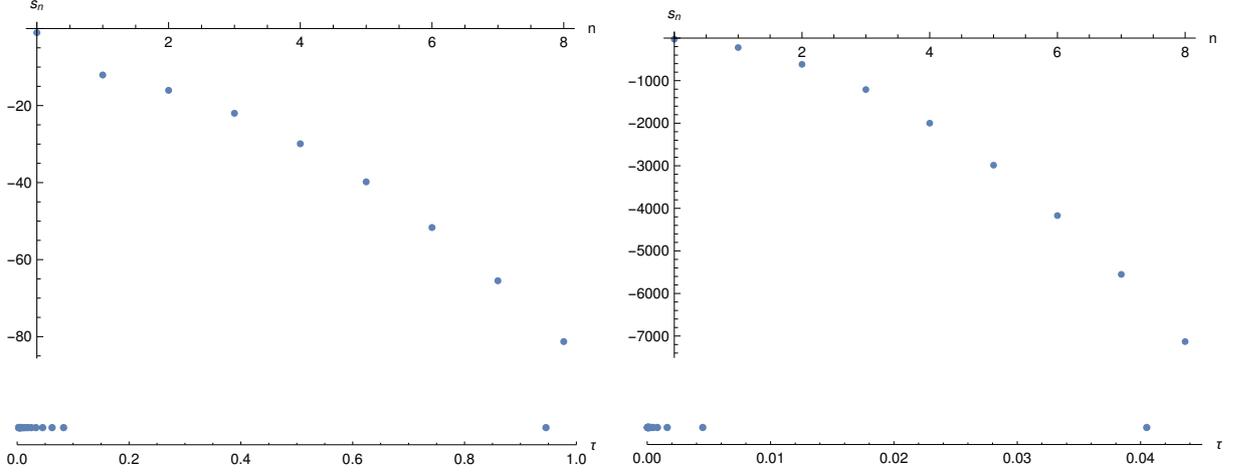


Figure A.1 – On the left, poles s_n and corresponding relaxation times τ_n for $\epsilon = 0.1$; the first pole is $s_0 = -1.057$ and the longest relaxation time is $\tau_0 = -s_0^{-1} = 0.946$. On the right, the same thing for $\epsilon = 10$; in this case the first pole is $s_0 = -24.693 = -10.008 \frac{\pi^2}{4}$ and the longest relaxation time is $\tau_0 = -s_0^{-1} = 0.04050$.

As $n \rightarrow \infty$, s_n approaches the left extremum of the interval and scales as n^2 .

In the case $s > -\frac{1}{\epsilon}$, we take $\sqrt{1 + \epsilon s} = z(s)$ with z real and positive. Now, finding the zeroes of the denominator of $H(s)$ amounts to finding the roots of another transcendental equation:

$$\tanh\left(\frac{z(s)}{\epsilon}\right) = -\frac{z(s)}{\epsilon} (z(s)^2 - 1) \quad (\text{A.36})$$

If $\epsilon \leq \frac{1}{\sqrt{3}}$, this equation has only one root $-\frac{1}{\epsilon} < s_0 < 0$. If $\epsilon > \frac{1}{\sqrt{3}}$, it has no roots.

Summarising, the infinitely many poles s_n of quantities in Eq. A.25 to A.29 are to be found as follows. For $n \geq 1$, the poles s_n are the roots of Eq. A.33 over the intervals Eq. A.34; for $n = 0$, the pole s_0 corresponds to the root of Eq. A.33 over the interval $-\frac{1}{\epsilon} - \frac{\epsilon\pi^2}{4} < s < -\frac{1}{\epsilon}$ if $\epsilon \geq \frac{1}{\sqrt{3}}$, and to the root of Eq. A.36 if $\epsilon < \frac{1}{\sqrt{3}}$.

Studying numerically the value of these relaxation rates, one can identify two limits. When $\epsilon \ll 1$, as in [42], $s_0 \sim -1$, so the slowest time scale $\tau_0 = -s_0^{-1}$ tends to 1 (in dimensioned time $\frac{L\lambda_D}{2D}$); all the other s_n lie on the left of $-\frac{1}{\epsilon}$, corresponding to infinitely many very short relaxation times τ_n , smaller than or of the order of ϵ (in dimensioned time $\frac{\lambda_D^2}{D}$) and accumulating around 0. When $\epsilon \gg 1$, $s_0 \sim -\epsilon \frac{\pi^2}{4}$, so the slowest time scale τ_0 tends to $\frac{4}{\pi^2 \epsilon}$ (in dimensioned time $\frac{4L^2}{4\pi^2 D}$); 0 is again an accumulation point for the other time scales τ_n . For $\epsilon = 0.1$ and 10, the first few poles s_n and time scales τ_n are represented in Fig. A.1.

This derivation, although with a much heavier notation, can be found in [231], whose authors arrived independently to the same results.

Finally, computing explicitly the residue

$$\text{Res}_{H(s)}(s_n) = \frac{2s_n(1 + \epsilon s_n)}{3 - s_n^2} \quad (\text{A.37})$$

Appendix A. Mathematical derivations and algorithms

allows to retrieve immediately expressions such as

$$\rho_f(x, t) = -v \frac{\sinh \frac{x}{\epsilon}}{\sinh \frac{1}{\epsilon}} - v \sum_{n=0}^{\infty} \frac{2(1 + \epsilon s_n)}{3 - s_n^2} \frac{\sinh \frac{\sqrt{1 + \epsilon s_n} x}{\epsilon^2}}{\sinh \frac{\sqrt{1 + \epsilon s_n}}{\epsilon^2}} e^{s_n t} \quad (\text{A.38})$$

which can be shown to be equivalent to Eq. 40 in Ref. 231.

A.2.0.2 Time domain

We here make the ansatz that potential $\psi(x, t)$ and electric density $\rho_f(x, t)$ relax to equilibrium as

$$\psi(x, t) = v \frac{\sinh \left(\frac{x}{\epsilon} \right)}{\sinh \left(\frac{1}{\epsilon} \right)} + v \sum_{n=0}^{\infty} b_n(x) e^{s_n t} \quad (\text{A.39})$$

$$\rho_f(x, t) = -v \frac{\sinh \left(\frac{x}{\epsilon} \right)}{\sinh \left(\frac{1}{\epsilon} \right)} + v \sum_{n=0}^{\infty} B_n(x) e^{s_n t} \quad (\text{A.40})$$

with $B_n(x) = -\epsilon^2 b_n''(x)$ by Eq. A.18, and s_n real. Putting Eq. A.40 in Eq. A.17 and enforcing asymmetry gives

$$B_n(x) = c_n \sinh \left(\frac{\sqrt{1 + \epsilon s_n}}{\epsilon} x \right) \quad (\text{A.41})$$

This expression can be integrated to get the corresponding $b_n(x)$. Fixing the gauge $\psi(0) = 0$ and imposing Eq. A.19 one finds

$$b_n(x) = -c_n \left[\frac{\sinh \left(\frac{\sqrt{1 + \epsilon s_n}}{\epsilon} x \right)}{1 + \epsilon s_n} + x \frac{s_n \cosh \left(\frac{\sqrt{1 + \epsilon s_n}}{\epsilon} x \right)}{\sqrt{1 + \epsilon s_n}} \right] \quad (\text{A.42})$$

Finally, Eq. A.20 gives, for any n , either $c_n = 0$ or

$$1 + s_n \sqrt{1 + \epsilon s_n} \coth \left(\frac{\sqrt{1 + \epsilon s_n}}{\epsilon} \right) = 0 \quad (\text{A.43})$$

which is exactly the defining equation for the poles of Eq. A.32. Notice that we have taken the same branch cut for the square root as in the previous section; when $s < -\frac{1}{\epsilon}$ the hyperbolic cotangent has imaginary argument and a situation like the one of Eq. A.33 is recovered (infinitely many solutions), while when $s > -\frac{1}{\epsilon}$ the situation is analogous to Eq. A.36 (one or no solution, depending on the value of ϵ).

An approximation for s_0 can also be found in a simpler way by assuming a monoexponential relaxation. This leads to the correct $B_0(x)$, as in Eq. A.41, and to the following approximate version of

$$1 + s_0 \coth \frac{\sqrt{1 + \epsilon s_0}}{\epsilon} = 0 \quad (\text{A.44})$$

which is correct in the small ϵ limit, when s_0 is well separated from the other relaxation rates.

A.3 Ions dynamics and relaxation times - cylindrical channel case

The following section corresponds to the analytical derivations carried out by Ivan Palaia to estimate the electrolyte relaxation time, in the linear regime, in a coaxial cylindrical channel. The corresponding numerical comparisons are discussed in Section 5.3.

The Debye-Falkenhagen equation for charge, equivalent to Eq. A.16 reads

$$\frac{\partial \rho_f}{\partial t} = D \left[\frac{1}{r} \frac{\partial}{\partial r} \left(r \frac{\partial \rho_f}{\partial r} \right) - \kappa^2 \rho_f \right] \quad (\text{A.45})$$

We here use the same nondimensional units as in Section A.2, choosing as reference length $L = R_2 - R_1$. The two adimensional parameters that describe the system are now $\epsilon = \frac{2\lambda_D}{L}$ and $\eta = \frac{2R_1}{L}$. Now Eq. A.45 reads

$$\epsilon \frac{\partial \rho_f}{\partial t} = \epsilon^2 \frac{1}{r} \frac{\partial}{\partial r} \left(r \frac{\partial \rho_f}{\partial r} \right) - \rho_f \quad (\text{A.46})$$

In terms of the Laplace transform of the charge density, $\widehat{\rho}(r, s)$, this becomes

$$k^2 \widehat{\rho} = \frac{1}{r} \rho_f + \frac{\partial^2 \rho_f}{\partial r^2} \quad (\text{A.47})$$

In cylindrical coordinates, boundary conditions of Eq. A.19 and A.20 read

$$\frac{\partial \rho_f}{\partial r}(\eta) + \frac{\partial \psi}{\partial r}(\eta) = 0 \quad (\text{A.48})$$

$$\frac{\partial \rho_f}{\partial r}(\eta + 2) + \frac{\partial \psi}{\partial r}(\eta + 2) = 0 \quad (\text{A.49})$$

$$\psi(\eta) = -\widehat{V}(s) \quad (\text{A.50})$$

$$\psi(\eta + 2) = \widehat{V}(s) \quad (\text{A.51})$$

Solving for the charge density gives

$$\begin{aligned} \widehat{\rho}(r, s) = & \\ & - 2k^3 \widehat{V}(s) \epsilon^2 \left(\eta I_1(k\eta) K_0(kr) - (\eta + 2) I_1(k(\eta + 2)) K_0(kr) \right. \\ & \left. + (\eta K_1(k\eta) - (\eta + 2) K_1(k(\eta + 2))) I_0(kr) \right) / \\ & \left[k \left(\eta I_1(k\eta) \left((\eta + 2) k \log \left(\frac{\eta}{\eta + 2} \right) (k^2 \epsilon^2 - 1) K_1(k(\eta + 2)) \right. \right. \right. \\ & \left. \left. \left. + K_0(k(\eta + 2)) \right) \right) \right. \\ & \left. + (\eta + 2) I_1(k(\eta + 2)) (2\eta k \coth^{-1}(\eta + 1) (k^2 \epsilon^2 - 1) K_1(k\eta) + K_0(k\eta)) \right. \\ & \left. \left. + \eta I_0(k(\eta + 2)) K_1(k\eta) + (\eta + 2) I_0(k\eta) K_1(k(\eta + 2)) \right) - 2 \right] \quad (\text{A.52}) \end{aligned}$$

Appendix A. Mathematical derivations and algorithms

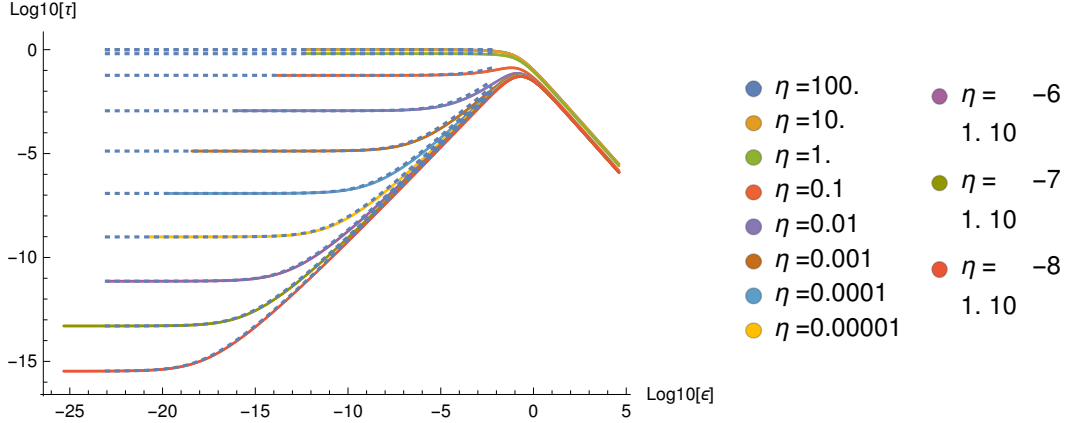


Figure A.2 – In continuous lines, τ as a function of ϵ , for different values of η . In dotted blue lines, the circuit-model approximation for τ (Eq. A.57), for the same values of η .

Eq. A.52 gives the correct steady state behavior at infinite time, for a step applied potential. It also tends to Eq. A.26 as $\eta \rightarrow \infty$.

As before, we can retrieve at least numerically the poles of this function. Starting from $\eta \rightarrow \infty$ and going toward $\eta \rightarrow 0$, one can see that a slight curvature splits each zero of Eq. A.32 into two zeros with a pole in between. These poles s_n correspond to the relaxation rates of the system. In Fig. A.2 we plot the slowest timescale $\tau_0 = s_0^{-1}$ as a function of ϵ , for different values of η .

For $\epsilon \gg 1$, the relaxation process is diffusive: $\tau_0 = \frac{1}{a^2\epsilon}$, or $\frac{L^2}{4a^2D}$ in physical units. For arbitrary η , a is given by the solution of

$$I_1(a(\eta+2))K_1(a\eta) - I_1(a\eta)K_1(a(\eta+2)) = 0 \quad (\text{A.53})$$

and it is equal to $\pi/2$ in the planar limit and to 3.67049... in the $\eta \rightarrow 0$ limit. It represents a purely geometrical effect of curvature in diffusion problems, see for instance^[7].

For $\epsilon \ll \eta \ll 1$, the double layer width is smaller than the radius of curvature and the cylinders appear as locally flat. In this regime τ is constant with respect to ϵ , as in the planar case, but its value crucially depends on η . For $\eta \ll \epsilon \ll 1$, the double layer is oddly defined around the inner cylinder.

A simple circuit model explains well the whole $\eta \ll 1$ and $\epsilon \ll 1$ regime. We model each charged cylinder with its double layer ($\epsilon \ll 1$) as a regular cylindrical capacitor, whose electrodes are at distance ϵ . The capacitance (per unit length), in units of $2\pi\epsilon_0\epsilon_r$, turns out to be

$$\frac{1}{\ln \frac{\eta+\epsilon}{\eta}} \quad (\text{A.54})$$

for the inner cylinder, and

$$\frac{1}{\ln \frac{2+\eta}{2+\eta-\epsilon}} \quad (\text{A.55})$$

for the outer cylinder. We model the whole ionic solution, as a resistance with conductivity $2n_s\beta D e^2$. Assuming a certain potential difference across the resistance, one can derive the electric field from Gauss' theorem, in cylindrical geometry. Ohm's law then gives the resistance

Appendix A. Mathematical derivations and algorithms

(per unit inverse length), that measured in unit of $\frac{\lambda_D L}{4\pi\epsilon_0\epsilon_r D}$ reads

$$\epsilon \frac{\ln(2 + \eta)}{\ln(\eta)} \tag{A.56}$$

We compute the characteristic time of the circuit as the product of this resistance and the total capacitance. The result is

$$\tau = \frac{\epsilon \ln\left(\frac{2+\eta}{\eta}\right)}{\ln\left(\frac{(\eta+2)(\eta+\epsilon)}{\eta(\eta-\epsilon+2)}\right)} \tag{A.57}$$

This approximation performs spectacularly in the whole regime $\epsilon \ll 1$ (see Fig. A.2).

Bibliography

- [1] Dekker, C. Solid-state nanopores. *Nature Nanotechnology*, 2(4):209–215, **2007**. URL <https://www.nature.com/articles/nnano.2007.27>. *Cited on page 1*
- [2] Li, J., Stein, D., McMullan, C., Branton, D., Aziz, M. J. & Golovchenko, J. A. Ion-beam sculpting at nanometre length scales. *Nature*, 412(6843):166–169, **2001**. URL <https://www.nature.com/articles/35084037>. *Cited on page 1*
- [3] Choi, W., Ulissi, Z. W., Shimizu, S. F. E., Bellisario, D. O., Ellison, M. D. & Strano, M. S. Diameter-dependent ion transport through the interior of isolated single-walled carbon nanotubes. *Nature Communications*, 4:2397, **2013**. *Cited on page 1*
- [4] Siria, A., Poncharal, P., Bianco, A.-L., Fulcrand, R., Blase, X., Purcell, S. T. & Bocquet, L. Giant osmotic energy conversion measured in a single transmembrane boron nitride nanotube. *Nature*, 494(7438):455–458, **2013**. URL http://www.nature.com/nature/journal/v494/n7438/full/nature11876.html?WT.ec_id=NATURE-20130228. *Cited on pages 1 & 62*
- [5] Zevenbergen, M. A. G., Wolfrum, B. L., Goluch, E. D., Singh, P. S. & Lemay, S. G. Fast Electron-Transfer Kinetics Probed in Nanofluidic Channels. *Journal of the American Chemical Society*, 131(32):11471–11477, **2009**. URL <http://dx.doi.org/10.1021/ja902331u>. *Cited on pages 1, 8, & 16*
- [6] Singh, P. S., Kätelhön, E., Mathwig, K., Wolfrum, B. & Lemay, S. G. Stochasticity in Single-Molecule Nanoelectrochemistry: Origins, Consequences, and Solutions. *ACS Nano*, 6(11):9662–9671, **2012**. URL <https://doi.org/10.1021/nm3031029>. *Cited on page 1*
- [7] Hüske, M., Stockmann, R., Offenhäusser, A. & Wolfrum, B. Redox cycling in nanoporous electrochemical devices. *Nanoscale*, 6(1):589–598, **2014**. *Cited on page 1*
- [8] Chen, S., Bommer, J. G., Carlen, E. T. & van den Berg, A. Al₂O₃/Silicon NanoISFET with Near Ideal Nernstian Response. *Nano Letters*, 11(6):2334–2341, **2011**. URL <https://doi.org/10.1021/nl200623n>. *Cited on page 1*
- [9] Bocquet, L. & Charlaix, E. Nanofluidics, from bulk to interfaces. *Chemical Society Reviews*, 39(3):1073–1095, **2010**. URL <https://pubs.rsc.org/en/content/articlelanding/2010/cs/b909366b>. *Cited on pages iv, 2, 7, & 24*
- [10] Eijkel, J. C. T. & Berg, A. v. d. Nanofluidics: what is it and what can we expect from it? *Microfluidics and Nanofluidics*, 1(3):249–267, **2005**. URL <https://doi.org/10.1007/s10404-004-0012-9>. *Cited on page 2*
- [11] Sparreboom, W., van den Berg, A. & Eijkel, J. C. T. Principles and applications of nanofluidic transport. *Nature Nanotechnology*, 4(11):713–720, **2009**. URL <http://www.nature.com/accesdistant.upmc.fr/nnano/journal/v4/n11/full/nnano.2009.332.html>. *Cited on page 2*
- [12] Plecis, A., Schoch, R. B. & Renaud, P. Ionic transport phenomena in nanofluidics: Experimental and theoretical study of the exclusion-enrichment effect on a chip. *Nano Letters*, 5(6):1147–1155, **2005**. URL <https://doi.org/10.1021/nl050265h>. *Cited on page 2*

Bibliography

- [13] Schasfoort, R. B. M., Schlautmann, S., Hendrikse, J. & Berg, A. v. d. Field-Effect Flow Control for Microfabricated Fluidic Networks. *Science*, 286(5441):942–945, **1999**. URL <http://science.sciencemag.org/content/286/5441/942>. Cited on pages 2 & 7
- [14] Karnik, R., Fan, R., Yue, M., Li, D., Yang, P. & Majumdar, A. Electrostatic Control of Ions and Molecules in Nanofluidic Transistors. *Nano Letters*, 5(5):943–948, **2005**. URL <https://doi.org/10.1021/nl050493b>. Cited on pages 2 & 7
- [15] Karnik, R., Duan, C., Castelino, K., Daiguji, H. & Majumdar, A. Rectification of Ionic Current in a Nanofluidic Diode. *Nano Letters*, 7(3):547–551, **2007**. URL <https://doi.org/10.1021/nl062806o>. Cited on pages 2 & 7
- [16] Siwy, Z. & Fulinski, A. Fabrication of a Synthetic Nanopore Ion Pump. *Physical Review Letters*, 89(19):198103, **2002**. URL <https://link.aps.org/doi/10.1103/PhysRevLett.89.198103>. Cited on pages 2 & 7
- [17] Sui, H., Han, B. G., Lee, J. K., Walian, P. & Jap, B. K. Structural basis of water-specific transport through the AQP1 water channel. *Nature*, 414(6866):872–878, **2001**. Cited on page 2
- [18] Murata, K., Mitsuoka, K., Hirai, T., Walz, T., Agre, P., Heymann, J. B., Engel, A. & Fujiyoshi, Y. Structural determinants of water permeation through aquaporin-1. *Nature*, 407(6804):599–605, **2000**. Cited on page 2
- [19] Chan, D. Y. C. & Horn, R. G. The drainage of thin liquid films between solid surfaces. *The Journal of Chemical Physics*, 83(10):5311–5324, **1985**. URL <https://aip.scitation.org/doi/abs/10.1063/1.449693>. Cited on page 2
- [20] Georges, J. M., Millot, S., Loubet, J. L. & Tonck, A. Drainage of thin liquid films between relatively smooth surfaces. *The Journal of Chemical Physics*, 98(9):7345–7360, **1993**. URL <https://aip.scitation.org/doi/abs/10.1063/1.465059>. Cited on page 2
- [21] Raviv, U. & Klein, J. Fluidity of Bound Hydration Layers. *Science*, 297(5586):1540–1543, **2002**. URL <http://science.sciencemag.org/content/297/5586/1540>. Cited on page 2
- [22] Li, T.-D., Gao, J., Szoszkiewicz, R., Landman, U. & Riedo, E. Structured and viscous water in subnanometer gaps. *Physical Review B*, 75(11):115415, **2007**. URL <https://link.aps.org/doi/10.1103/PhysRevB.75.115415>. Cited on page 2
- [23] Maali, A., Cohen-Bouhacina, T., Couturier, G. & Aimé, J.-P. Oscillatory Dissipation of a Simple Confined Liquid. *Physical Review Letters*, 96(8):086105, **2006**. URL <https://link.aps.org/doi/10.1103/PhysRevLett.96.086105>. Cited on pages 2 & 3
- [24] Becker, T. & Mugele, F. Nanofluidics: Viscous Dissipation in Layered Liquid Films. *Physical Review Letters*, 91(16):166104, **2003**. URL <https://link.aps.org/doi/10.1103/PhysRevLett.91.166104>. Cited on pages 2 & 3
- [25] Thomas, J. A. & McGaughey, A. J. H. Water Flow in Carbon Nanotubes: Transition to Subcontinuum Transport. *Physical Review Letters*, 102(18):184502, **2009**. URL <https://link.aps.org/doi/10.1103/PhysRevLett.102.184502>. Cited on page 3
- [26] Leng, Y. & Cummings, P. T. Fluidity of Hydration Layers Nanoconfined between Mica Surfaces. *Physical Review Letters*, 94(2):026101, **2005**. URL <https://link.aps.org/doi/10.1103/PhysRevLett.94.026101>. Cited on page 3

Bibliography

- [27] Bocquet, L. & Barrat, J.-L. Flow boundary conditions from nano- to micro-scales. *Soft Matter*, 3(6):685–693, **2007**. URL <https://pubs.rsc.org/en/content/articlelanding/2007/sm/b616490k>. *Cited on page 3*
- [28] Joly, L., Ybert, C., Trizac, E. & Bocquet, L. Liquid friction on charged surfaces: From hydrodynamic slippage to electrokinetics. *The Journal of Chemical Physics*, 125(20):204716–204716–14, **2006**. URL http://jcp.aip.org/resource/1/jcpsa6/v125/i20/p204716_s1?isAuthorized=no. *Cited on pages 3 & 12*
- [29] Saugey, A., Joly, L., Ybert, C., Barrat, J. L. & Bocquet, L. Diffusion in pores and its dependence on boundary conditions. *Journal of Physics: Condensed Matter*, 17(49):S4075, **2005**. URL <http://stacks.iop.org/0953-8984/17/i=49/a=005>. *Cited on page 3*
- [30] Goyon, J., Colin, A., Ovarlez, G., Ajdari, A. & Bocquet, L. Spatial cooperativity in soft glassy flows. *Nature*, 454(7200):84–87, **2008**. URL <https://www.nature.com/articles/nature07026>. *Cited on page 3*
- [31] J. H Masliyah & S. Bhattacharjee. *Electrokinetic and Colloid Transport Phenomena*. New York: Wiley, new york: wiley édition, **2006**. *Cited on page 4*
- [32] Henry, D. C. The Cataphoresis of Suspended Particles. Part I. The Equation of Cataphoresis. *Proceedings of the Royal Society of London A: Mathematical, Physical and Engineering Sciences*, 133(821):106–129, **1931**. URL <http://rspa.royalsocietypublishing.org/content/133/821/106>. *Cited on page 5*
- [33] H. A. Pohl. *Dielectrophoresis*. Cambridge University Press, Cambridge UK, **1978**. *Cited on page 5*
- [34] G. Karniadakis, A. Beskok & N. Aluru. *Microflows and Nanoflows: Fundamentals and Simulation*. New York: Springer, **2005**. *Cited on page 6*
- [35] Al-Jarro, A., Paul, J., Thomas, D. W. P., Crowe, J., Sawyer, N., Rose, F. R. A. & Shakesheff, K. M. Direct calculation of Maxwell stress tensor for accurate trajectory prediction during DEP for 2d and 3d structures. *Journal of Physics D: Applied Physics*, 40(1):71, **2007**. URL <http://stacks.iop.org/0022-3727/40/i=1/a=S11>. *Cited on page 6*
- [36] Schoch, R. B., Han, J. & Renaud, P. Transport phenomena in nanofluidics. *Reviews of Modern Physics*, 80(3):839–883, **2008**. URL <https://link.aps.org/doi/10.1103/RevModPhys.80.839>. *Cited on page 7*
- [37] Stein, D., Kruithof, M. & Dekker, C. Surface-Charge-Governed Ion Transport in Nanofluidic Channels. *Physical Review Letters*, 93(3):035901, **2004**. URL <https://link.aps.org/doi/10.1103/PhysRevLett.93.035901>. *Cited on page 7*
- [38] Bouzigues, C. I., Tabeling, P. & Bocquet, L. Nanofluidics in the Debye Layer at Hydrophilic and Hydrophobic Surfaces. *Physical Review Letters*, 101(11):114503, **2008**. URL <https://link.aps.org/doi/10.1103/PhysRevLett.101.114503>. *Cited on page 7*
- [39] Storm, A. J., Storm, C., Chen, J., Zandbergen, H., Joanny, J.-F. & Dekker, C. Fast DNA Translocation through a Solid-State Nanopore. *Nano Letters*, 5(7):1193–1197, **2005**. URL <http://dx.doi.org/10.1021/nl048030d>. *Cited on page 7*
- [40] Lathrop, D. K., Ervin, E. N., Barrall, G. A., Keehan, M. G., Kawano, R., Krupka, M. A., White, H. S. & Hibbs, A. H. Monitoring the Escape of DNA from a Nanopore Using an Alternating Current Signal. *Journal of the American Chemical Society*, 132(6):1878–1885, **2010**. URL <http://dx.doi.org/10.1021/ja906951g>. *Cited on page 7*

Bibliography

- [41] Green, N. G. & Morgan, H. Dielectrophoretic separation of nano-particles. Journal of Physics D: Applied Physics, 30(11):L41, **1997**. URL <http://stacks.iop.org/0022-3727/30/i=11/a=001>. *Cited on page 7*
- [42] Bazant, M. Z. & Squires, T. M. Induced-Charge Electrokinetic Phenomena: Theory and Microfluidic Applications. Physical Review Letters, 92(6):066101, **2004**. URL <http://link.aps.org/doi/10.1103/PhysRevLett.92.066101>. *Cited on pages 8, 106, 110, 113, 138, & 141*
- [43] Bazant, M. Z. & Squires, T. M. Induced-charge electrokinetic phenomena. Current Opinion in Colloid & Interface Science, 15(3):203–213, **2010**. URL <http://www.sciencedirect.com/science/article/pii/S135902941000004X>. *Cited on page 8*
- [44] Wu, Z. & Li, D. Mixing and flow regulating by induced-charge electrokinetic flow in a microchannel with a pair of conducting triangle hurdles. Microfluidics and Nanofluidics, 5(1):65–76, **2007**. URL <http://link.springer.com/article/10.1007/s10404-007-0227-7>. *Cited on page 8*
- [45] Wu, Z. & Li, D. Micromixing using induced-charge electrokinetic flow. Electrochimica Acta, 53(19):5827–5835, **2008**. URL <http://www.sciencedirect.com/science/article/pii/S0013468608003939>. *Cited on page 8*
- [46] Jain, M., Yeung, A. & Nandakumar, K. Efficient Micromixing Using Induced-Charge Electroosmosis. Journal of Microelectromechanical Systems, 18(2):376–384, **2009**. *Cited on page 8*
- [47] Rahul Dhopeswarkar, Dzmityr Hlushkou, Mark Nguyen, Ulrich Tallarek & Richard M. Crooks. Electrokinetics in Microfluidic Channels Containing a Floating Electrode. Journal of American Chemical Society, 130:10480–10481, **2008**. *Cited on page 8*
- [48] Yalcin, S. E., Sharma, A., Qian, S., Joo, S. W. & Baysal, O. On-demand particle enrichment in a microfluidic channel by a locally controlled floating electrode. Sensors and Actuators B: Chemical, 153(1):277–283, **2011**. URL <http://www.sciencedirect.com/science/article/pii/S0925400510008324>. *Cited on page 8*
- [49] Pullman, B. L'Atome dans l'histoire de la pensée humaine. Fayard édition, **1995**. URL <https://www.fayard.fr/sciences-humaines/latome-dans-lhistoire-de-la-pensee-humaine-9782213594637>. *Cited on page 8*
- [50] Nye, M. J. Molecular reality: a perspective on the scientific work of Jean Perrin. Macdonald, 1st édition, **1972**. *Cited on pages 8 & 9*
- [51] Lindley, D. Boltzmanns Atom: The Great Debate That Launched A Revolution In Physics. Simon and Schuster, 2nd édition, **2015**. *Cited on page 9*
- [52] Einstein, A. über die von der molekularkinetischen theorie der warme geforderte bewegung von in ruhenden flüssigkeiten suspendierten teilchen. Annalen der Physik, 322(8):549–560, **1905**. URL <https://onlinelibrary.wiley.com/doi/abs/10.1002/andp.19053220806>. *Cited on page 9*
- [53] Einstein, A. Elementare theorie der Brownschen Bewegung. Zeitschrift für elektrochemie und angewandte physikalische chemie, 14(17):235–239, **1908**. URL <https://onlinelibrary.wiley.com/doi/abs/10.1002/bbpc.19080141703>. *Cited on page 9*
- [54] Einstein, A. Méthode pour la détermination de valeurs statistiques d'observations concernant des grandeurs soumises à des fluctuations irrégulières. Archives des Sciences, 37, **1914**. URL <http://adsabs.harvard.edu/abs/1914ArS...37..254E>. *Cited on page 9*
- [55] Langevin, P. Sur la théorie du mouvement Brownien. Compt. Rendus, 146:530–533, **1908**. URL <https://ci.nii.ac.jp/naid/10020793023/>. *Cited on page 10*

Bibliography

- [56] Schottky, W. Über spontane Stromschwankungen in verschiedenen elektrizitätsleitern. Annalen der Physik, 362(23):541–567, **1918**. URL <https://onlinelibrary.wiley.com/doi/abs/10.1002/andp.19183622304>. Cited on page 10
- [57] Johnson, J. B. Thermal Agitation of Electricity in Conductors. Phys. Rev., 32:97, **1928**. Cited on pages 10 & 120
- [58] Nyquist, H. Thermal Agitation of Electric Charge in Conductors. Physical Review, 32(1):110–113, **1928**. URL <https://link.aps.org/doi/10.1103/PhysRev.32.110>. Cited on pages 10 & 120
- [59] Einstein, A. Zur Theorie der Brownschen Bewegung. Annalen der Physik, 324(2):371–381, **1906**. URL <https://onlinelibrary.wiley.com/doi/abs/10.1002/andp.19063240208>. Cited on page 10
- [60] van Zon, R., Ciliberto, S. & Cohen, E. G. D. Power and Heat Fluctuation Theorems for Electric Circuits. Physical Review Letters, 92(13):130601, **2004**. URL <https://link.aps.org/doi/10.1103/PhysRevLett.92.130601>. Cited on page 10
- [61] Landauer, R. Condensed-matter physics: The noise is the signal. Nature, 392(6677):658–659, **1998**. URL <https://www.nature.com/articles/33551>. Cited on page 11
- [62] Bérut, A., Arakelyan, A., Petrosyan, A., Ciliberto, S., Dillenschneider, R. & Lutz, E. Experimental verification of Landauer’s principle linking information and thermodynamics. Nature, 483(7388):187–189, **2012**. URL <https://www.nature.com/articles/nature10872>. Cited on page 11
- [63] Bertocci, U. & Huet, F. Noise Analysis Applied to Electrochemical Systems. CORROSION, 51(2):131–144, **1995**. URL <http://corrosionjournal.org/doi/10.5006/1.3293585>. Cited on page 11
- [64] Garcia-Morales, V. & Krischer, K. Fluctuation enhanced electrochemical reaction rates at the nanoscale. Proceedings of the National Academy of Sciences, 107(10):4528–4532, **2010**. URL <http://www.pnas.org/content/107/10/4528>. Cited on page 11
- [65] Marcus, R. A. On the Theory of Oxidation-Reduction Reactions Involving Electron Transfer. i. The Journal of Chemical Physics, 24(5):966–978, **1956**. URL <https://aip.scitation.org/doi/abs/10.1063/1.1742723>. Cited on pages 11 & 16
- [66] Lemay, S. G., Kang, S., Mathwig, K. & Singh, P. S. Single-molecule electrochemistry: present status and outlook. Accounts of Chemical Research, 46(2):369–377, **2013**. Cited on pages iv & 12
- [67] Enno Kätelhon, Kay J. Krause, Klaus Mathwig, Serge G. Lemay & Bernhard Wolfrum. Noise Phenomena Caused by Reversible Adsorption in Nanoscale Electrochemical Devices. American Chemical Society, 8(5):4924 – 4930, **2014**. Cited on pages iv, 11, 12, & 13
- [68] Marcel A. G. Zevenbergen, Pradyumna S. Singh, Edgar D. Goluch, Bernhard L. Wolfrum & Serge G. Lemay. Stochastic Sensing of Single Molecules in a Nanofluidic Electrochemical Device. Nano Letters, 11:2881 – 2886, **2011**. Cited on page 11
- [69] Magnussen, O. M. Ordered Anion Adlayers on Metal Electrode Surfaces. Chemical Reviews, 102(3):679–726, **2002**. URL <http://pubs.acs.org/doi/abs/10.1021/cr000069p>. Cited on pages 12 & 13

Bibliography

- [70] Tripkovic, D. V., Strmcnik, D., Vliet, D. v. d., Stamenkovic, V. & Markovic, N. M. The role of anions in surface electrochemistry. *Faraday Discussions*, 140(0):25–40, **2008**. URL <http://pubs.rsc.org/en/content/articlelanding/2009/fd/b803714k>. Cited on pages 12 & 13
- [71] Morrison, F. A. & Osterle, J. F. Electrokinetic Energy Conversion in Ultrafine Capillaries. *The Journal of Chemical Physics*, 43(6):2111–2115, **1965**. URL <http://scitation.aip.org/content/aip/journal/jcp/43/6/10.1063/1.1697081>. Cited on page 12
- [72] Siria, A., Bocquet, M.-L. & Bocquet, L. New avenues for the large-scale harvesting of blue energy. *Nature Reviews Chemistry*, 1:91, **2017**. URL <https://www.nature.com/articles/s41570-017-0091>. Cited on page 12
- [73] Jouniaux, L. & Ishido, T. Electrokinetics in Earth Sciences: A Tutorial. *International Journal of Geophysics*, 2012:1–16, **2012**. URL <http://www.hindawi.com/journals/ijge/2012/286107/>. Cited on page 12
- [74] Marry, V., Dufrêche, J.-F., Jardat, M. & Turq, P. Equilibrium and electrokinetic phenomena in charged porous media from microscopic and mesoscopic models: electro-osmosis in montmorillonite. *Molecular Physics*, 101(20):3111–3119, **2003**. URL <http://www.tandfonline.com/doi/abs/10.1080/00268970310001626432>. Cited on pages 12 & 132
- [75] Qiao, R. & Aluru, N. R. Charge Inversion and Flow Reversal in a Nanochannel Electro-osmotic Flow. *Physical Review Letters*, 92(19):198301, **2004**. URL <http://link.aps.org/doi/10.1103/PhysRevLett.92.198301>. Cited on page 12
- [76] Storey, B. D. & Bazant, M. Z. Effects of electrostatic correlations on electrokinetic phenomena. *Physical Review E*, 86(5):056303, **2012**. URL <http://link.aps.org/doi/10.1103/PhysRevE.86.056303>. Cited on page 12
- [77] Schmitz, R. & Dünweg, B. Numerical electrokinetics. *Journal of Physics: Condensed Matter*, 24(46):464111, **2012**. URL <http://stacks.iop.org/0953-8984/24/i=46/a=464111>. Cited on pages 12 & 16
- [78] Botan, A., Marry, V., Rotenberg, B., Turq, P. & Noetinger, B. How Electrostatics Influences Hydrodynamic Boundary Conditions: Poiseuille and Electro-osmotic Flows in Clay Nanopores. *The Journal of Physical Chemistry C*, 117(2):978–985, **2013**. URL <http://dx.doi.org/10.1021/jp3092336>. Cited on page 12
- [79] Yoshida, H., Mizuno, H., Kinjo, T., Washizu, H. & Barrat, J.-L. Molecular dynamics simulation of electrokinetic flow of an aqueous electrolyte solution in nanochannels. *The Journal of Chemical Physics*, 140(21):214701, **2014**. URL <http://scitation.aip.org/content/aip/journal/jcp/140/21/10.1063/1.4879547>. Cited on pages 12 & 132
- [80] Rotenberg, B. & Pagonabarraga, I. Electrokinetics: insights from simulation on the microscopic scale. *Molecular Physics*, 111(7):827–842, **2013**. URL <http://www.tandfonline.com/doi/abs/10.1080/00268976.2013.791731>. Cited on page 12
- [81] Pagonabarraga, I., Rotenberg, B. & Frenkel, D. Recent advances in the modelling and simulation of electrokinetic effects: bridging the gap between atomistic and macroscopic descriptions. *Phys. Chem. Chem. Phys.*, 12(33):9566–9580, **2010**. URL <http://pubs.rsc.org/en/content/articlepdf/2010/cp/c004012f>. Cited on page 12

Bibliography

- [82] Altmann, S., Tournassat, C., Goutelard, F., Parneix, J.-C., Gimmi, T. & Maes, N. Diffusion-driven transport in clayrock formations. *Applied Geochemistry*, 27(2):463–478, **2012**. URL <http://www.sciencedirect.com/science/article/pii/S0883292711004057>. *Cited on page 13*
- [83] Hlushkou, D., Khirevich, S., Apanasovich, V., Seidel-Morgenstern, A. & Tallarek, U. Pore-Scale Dispersion in Electrokinetic Flow through a Random Sphere Packing. *Analytical Chemistry*, 79(1):113–121, **2007**. URL <http://pubs.acs.org/doi/abs/10.1021/ac061168r>. *Cited on page 13*
- [84] Brenner, H. & Edwards, D. *Macrotransport Processes*. Butterworth-Heinemann Series I. Butterworth-Heinemann, London, **1993**. *Cited on pages 13 & 77*
- [85] Pradyumna S. Singh, Hui-Shan M. Chan, Shuo Kang & Serge G. Lemay. Stochastic Amperometric Fluctuations as a Probe for Dynamic Adsorption in Nanofluidic Electrochemical Systems. *Journal of American chemical Society*, 133:18289 – 18295, **2011**. *Cited on pages 13 & 14*
- [86] Marcel A. G. Zevenbergen, Pradyumna S. Singh, Edgar D. Goluch, Bernhard L. Wolfrum & Serge G. Lemay. Electrochemical Correlation Spectroscopy in Nanofluidic Cavities. *American Chemical Society*, 81:8203–8212, **2009**. *Cited on page 14*
- [87] Mathwig, K., Mampallil, D., Kang, S. & Lemay, S. G. Electrical Cross-Correlation Spectroscopy: Measuring Picoliter-per-Minute Flows in Nanochannels. *Physical Review Letters*, 109(11):118302, **2012**. URL <http://link.aps.org/doi/10.1103/PhysRevLett.109.118302>. *Cited on page 14*
- [88] Meller, A., Nivon, L. & Branton, D. Voltage-Driven DNA Translocations through a Nanopore. *Physical Review Letters*, 86(15):3435–3438, **2001**. URL <https://link.aps.org/doi/10.1103/PhysRevLett.86.3435>. *Cited on page 14*
- [89] Auger, T., Mathe, J., Viasnoff, V., Charron, G., Di Meglio, J.-M., Auvray, L. & Montel, F. Zero-Mode Waveguide Detection of Flow-Driven DNA Translocation through Nanopores. *Physical Review Letters*, 113(2):028302, **2014**. URL <http://link.aps.org/doi/10.1103/PhysRevLett.113.028302>. *Cited on page 14*
- [90] Parsons, R. The electrical double layer: recent experimental and theoretical developments. *Chemical Reviews*, 90(5):813–826, **1990**. URL <https://pubs.acs.org/doi/abs/10.1021/cr00103a008>. *Cited on page 14*
- [91] Kornyshev, A. A. Double-Layer in Ionic Liquids: Paradigm Change? *The Journal of Physical Chemistry B*, 111(20):5545–5557, **2007**. URL <https://doi.org/10.1021/jp067857o>. *Cited on page 15*
- [92] Bazant, M. Z., Storey, B. D. & Kornyshev, A. A. Double Layer in Ionic Liquids: Overscreening versus Crowding. *Physical Review Letters*, 106(4), **2011**. URL <https://link.aps.org/doi/10.1103/PhysRevLett.106.046102>. *Cited on page 15*
- [93] di Caprio, D., Stafiej, J. & Badiali, J. P. Field theory for ionic systems. From fluctuations and structure at a hard wall to thermodynamics. *Electrochimica Acta*, 48(20):2967–2974, **2003**. URL <http://www.sciencedirect.com/science/article/pii/S0013468603003621>. *Cited on page 15*
- [94] Samaj, L. & Trizac, E. Wigner-crystal formulation of strong-coupling theory for counterions near planar charged interfaces. *Physical Review E*, 84(4):041401, **2011**. URL <https://link.aps.org/doi/10.1103/PhysRevE.84.041401>. *Cited on page 15*

Bibliography

- [95] Naji, A., Kanduc, M., Forsman, J. & Podgornik, R. Perspective: Coulomb fluids-Weak coupling, strong coupling, in between and beyond. *The Journal of Chemical Physics*, 139(15):150901, **2013**. URL <https://aip.scitation.org/doi/abs/10.1063/1.4824681>. *Cited on page 15*
- [96] Horbach, J. & Succi, S. Lattice Boltzmann versus Molecular Dynamics Simulation of Nanoscale Hydrodynamic Flows. *Physical Review Letters*, 96(22):224503, **2006**. URL <http://link.aps.org/doi/10.1103/PhysRevLett.96.224503>. *Cited on page 15*
- [97] Kätelhön, E., Krause, K. J., Singh, P. S., Lemay, S. G. & Wolfrum, B. Noise characteristic of nanoscaled redox-cycling sensors: Investigations based on random walks. *Journal of American Chemical Society*, 135:8874 – 8881, **2012**. *Cited on page 16*
- [98] Chandra, A. & Bagchi, B. Microscopic free energy functional for polarization fluctuations: Generalization of Marcus-Felderhof expression. *The Journal of Chemical Physics*, 94(3):2258–2261, **1991**. URL <https://aip.scitation.org/doi/10.1063/1.459896>. *Cited on page 16*
- [99] Karlström, G. & Halle, B. A fluctuation approach to solvation in polar fluids. *The Journal of Chemical Physics*, 99(10):8056–8062, **1993**. URL <https://aip.scitation.org/doi/abs/10.1063/1.465632>. *Cited on page 16*
- [100] Stenhammar, J., Linse, P. & Karlström, G. A unified treatment of polar solvation using electrostatic fluctuations. *Chemical Physics Letters*, 501(4):364–368, **2011**. URL <http://www.sciencedirect.com/science/article/pii/S0009261410015782>. *Cited on page 16*
- [101] Song, X., Chandler, D. & Marcus, R. A. Gaussian Field Model of Dielectric Solvation Dynamics. *The Journal of Physical Chemistry*, 100(29):11954–11959, **1996**. URL <https://doi.org/10.1021/jp960887e>. *Cited on page 16*
- [102] Abragam, A. *The Principles of Nuclear Magnetism*. International Series of Monographs on Physics. Oxford University Press, Oxford, New York, **1983**. *Cited on page 16*
- [103] van Dorp, S., Keyser, U. F., Dekker, N. H., Dekker, C. & Lemay, S. G. Origin of the electrophoretic force on DNA in solid-state nanopores. *Nature Physics*, 5(5):347–351, **2009**. URL <https://www.nature.com/articles/nphys1230>. *Cited on page 16*
- [104] Reboux, S., Capuani, F. & Frenkel, D. Lattice-Boltzmann Simulations of Ionic Current Modulation by DNA Translocation. *Journal of Chemical Theory and Computation*, 2(3):495–503, **2006**. URL <https://doi.org/10.1021/ct050340g>. *Cited on page 16*
- [105] Marconi, U. M. B. & Melchionna, S. Ionic conduction in non-uniform nanopores and DNA translocation: a Nernst-Planck-Jacobs one-dimensional description. *Molecular Physics*, 111(22-23):3493–3501, **2013**. URL <https://doi.org/10.1080/00268976.2013.826828>. *Cited on page 16*
- [106] Gabrielli, C., Huet, F. & Keddam, M. Fluctuations in electrochemical systems. I. General theory on diffusion limited electrochemical reactions. *The Journal of Chemical Physics*, 99(9):7232–7239, **1993**. URL <https://aip.scitation.org/doi/10.1063/1.465440>. *Cited on page 16*
- [107] Hassibi, A., Navid, R., Dutton, R. W. & Lee, T. H. Comprehensive study of noise processes in electrode electrolyte interfaces. *Journal of Applied Physics*, 96(2):1074–1082, **2004**. URL <https://aip.scitation.org/doi/10.1063/1.1755429>. *Cited on page 16*
- [108] Kätelhön, E., Krause, K. J., Singh, P. S., Lemay, S. G. & Wolfrum, B. Noise Characteristics of Nanoscaled Redox-Cycling Sensors: Investigations Based on Random Walks. *Journal of the American Chemical Society*, 135(24):8874–8881, **2013**. URL <https://doi.org/10.1021/ja3121313>. *Cited on page 16*

Bibliography

- [109] Grün, F., Jardat, M., Turq, P. & Amatore, C. Relaxation of the electrical double layer after an electron transfer approached by Brownian dynamics simulation. *The Journal of Chemical Physics*, 120(20):9648–9655, **2004**. URL <http://scitation.aip.org/content/aip/journal/jcp/120/20/10.1063/1.1718201>. *Cited on page 16*
- [110] Siepmann, J. I. & Sprik, M. Influence of surface topology and electrostatic potential on water/electrode systems. *The Journal of Chemical Physics*, 102(1):511–524, **1995**. URL <https://aip.scitation.org/doi/abs/10.1063/1.469429>. *Cited on page 17*
- [111] Reed, S. K., Lanning, O. J. & Madden, P. A. Electrochemical interface between an ionic liquid and a model metallic electrode. *The Journal of Chemical Physics*, 126(8):084704, **2007**. URL <https://aip.scitation.org/doi/abs/10.1063/1.2464084>. *Cited on page 17*
- [112] Gingrich, T. R. & Wilson, M. On the Ewald summation of Gaussian charges for the simulation of metallic surfaces. *Chemical Physics Letters*, 500(1):178–183, **2010**. URL <http://www.sciencedirect.com/science/article/pii/S0009261410013606>. *Cited on page 17*
- [113] Rotenberg, B., Pagonabarraga, I. & Frenkel, D. Dispersion of charged tracers in charged porous media. *EPL (Europhysics Letters)*, 83(3):34004, **2008**. URL <http://stacks.iop.org/0295-5075/83/i=3/a=34004>. *Cited on pages 17, 33, 62, 63, 64, 66, 67, 69, 72, 73, & 78*
- [114] Levesque, M., Duvail, M., Pagonabarraga, I., Frenkel, D. & Rotenberg, B. Accounting for adsorption and desorption in lattice Boltzmann simulations. *Physical Review E*, 88(1):013308, **2013**. URL <http://link.aps.org/doi/10.1103/PhysRevE.88.013308>. *Cited on pages 17, 62, 63, 64, 66, 69, 70, & 78*
- [115] Limbach, H. J., Arnold, A., Mann, B. A. & Holm, C. Espresso - an extensible simulation package for research on soft matter systems. *Computer Physics Communications*, 174(9):704–727, **2006**. URL <http://www.sciencedirect.com/science/article/pii/S001046550500576X>. *Cited on pages 24 & 37*
- [116] Desplat, J.-C., Pagonabarraga, I. & Bladon, P. LUDWIG: A parallel Lattice-Boltzmann code for complex fluids. *Computer Physics Communications*, 134(3):273–290, **2001**. URL <http://www.sciencedirect.com/science/article/pii/S0010465500002058>. *Cited on pages 24 & 37*
- [117] Frisch, U., Hasslacher, B. & Pomeau, Y. Lattice - Gas Automata for the Navier - Stokes Equation. *Physical Review Letters*, 56(14):1505–1508, **1986**. URL <https://link.aps.org/doi/10.1103/PhysRevLett.56.1505>. *Cited on page 25*
- [118] Wolfram, S. Cellular automaton fluids 1: Basic theory. *Journal of Statistical Physics*, 45(3):471–526, **1986**. URL <https://doi.org/10.1007/BF01021083>. *Cited on page 25*
- [119] Bhatnagar, P. L., Gross, E. P. & Krook, M. A Model for Collision Processes in Gases. I. Small Amplitude Processes in Charged and Neutral One-Component Systems. *Physical Review*, 94(3):511–525, **1954**. URL <https://link.aps.org/doi/10.1103/PhysRev.94.511>. *Cited on page 26*
- [120] Boltzmann, L. *Vorlesungen über Gastheorie*. Leipzig Johann Ambrosius Barth, **1896**. URL <https://trove.nla.gov.au/work/2995281>. *Cited on page 26*
- [121] Chapman, S., Cowling, T. G. & Burnett, D. *The Mathematical Theory of Non-uniform Gases: An Account of the Kinetic Theory of Viscosity, Thermal Conduction and Diffusion in Gases*. Cambridge University Press, **1990**. *Cited on pages 28 & 122*

Bibliography

- [122] Chapman, S. Vi on the law of distribution of molecular velocities, and on the theory of viscosity and thermal conduction, in a non-uniform simple monatomic gas. Phil. Trans. R. Soc. Lond. A, 216(538-548):279–348, **1916**. URL <http://rsta.royalsocietypublishing.org/content/216/538-548/279>. *Cited on page 28*
- [123] Chapman, S. V on the kinetic theory of a gas. Part II. - A composite monatomic gas: diffusion, viscosity, and thermal conduction. Phil. Trans. R. Soc. Lond. A, 217(549-560):115–197, **1918**. URL <http://rsta.royalsocietypublishing.org/content/217/549-560/115>. *Cited on page 28*
- [124] Enskog, D. The numerical calculation of phenomena in fairly dense gases. Arkiv Mat. Astr. Fys., 16, **1921**. *Cited on page 28*
- [125] Succi, S. The Lattice Boltzmann Equation for Fluid Dynamics and Beyond. Oxford University Press, **2001**. *Cited on pages 28, 70, 124, 125, & 126*
- [126] Peng, G., Xi, H., Duncan, C. & Chou, S.-H. Lattice Boltzmann method on irregular meshes. Physical Review E, 58(4):R4124–R4127, **1998**. URL <https://link.aps.org/doi/10.1103/PhysRevE.58.R4124>. *Cited on page 28*
- [127] Zou, Q. & He, X. On pressure and velocity boundary conditions for the lattice Boltzmann BGK model. Physics of Fluids, 9(6):1591–1598, **1997**. URL <https://aip.scitation.org/doi/10.1063/1.869307>. *Cited on page 32*
- [128] Kuron, M., Rempfer, G., Schornbaum, F., Bauer, M., Godenschwager, C., Holm, C. & de Graaf, J. Moving charged particles in lattice Boltzmann-based electrokinetics. The Journal of Chemical Physics, 145(21):214102, **2016**. URL <http://aip.scitation.org/doi/full/10.1063/1.4968596>. *Cited on page 33*
- [129] Chen, X.-P. Applications of Lattice Boltzmann Method to Turbulent Flow Around Two-Dimensional Airfoil. Engineering Applications of Computational Fluid Mechanics, 6(4):572–580, **2012**. URL <https://doi.org/10.1080/19942060.2012.11015443>. *Cited on page 33*
- [130] Meghdadi Isfahani, A. H., Tasdighi, I., Karimipour, A., Shirani, E. & Afrand, M. A joint lattice Boltzmann and molecular dynamics investigation for thermohydraulical simulation of nano flows through porous media. European Journal of Mechanics - B/Fluids, 55, Part 1:15–23, **2016**. URL <http://www.sciencedirect.com/science/article/pii/S0997754615000989>. *Cited on page 33*
- [131] Capuani, F., Pagonabarraga, I. & Frenkel, D. Discrete solution of the electrokinetic equations. The Journal of Chemical Physics, 121(2):973–986, **2004**. *Cited on pages iv, 33, 34, & 35*
- [132] Warren, P. B. Electroviscous transport problems via Lattice-Boltzmann. International Journal of Modern Physics C, 8(4):889, **1997**. *Cited on pages 33, 62, & 63*
- [133] Lowe, C. P. & Frenkel, D. The super long-time decay of velocity fluctuations in a two-dimensional fluid. Physica A: Statistical Mechanics and its Applications, 220(3):251–260, **1995**. URL <http://www.sciencedirect.com/science/article/pii/0378437195002080>. *Cited on pages 33, 62, 63, & 123*
- [134] Lowe, C. P., Frenkel, D. & Hoef, M. A. v. d. Deviations from Fick’s law in Lorentz gases. Journal of statistical physics, 87(5):1229–1244, **1997**. URL <http://www.springerlink.com/index/P17T87T8JK707181.pdf>. *Cited on pages 33 & 62*

Bibliography

- [135] van der Hoef, M. A. & Frenkel, D. Long-time tails of the velocity autocorrelation function in two- and three-dimensional lattice-gas cellular automata: A test of mode-coupling theory. Physical Review A, 41(8):4277–4284, **1990**. URL <http://link.aps.org/doi/10.1103/PhysRevA.41.4277>. Cited on pages 33, 62, & 123
- [136] Hagen, M. H. J., Pagonabarraga, I., Lowe, C. P. & Frenkel, D. Algebraic decay of velocity fluctuations in a confined fluid. Physical Review Letters, 78(19):3785, **1997**. URL <http://journals.aps.org/prl/abstract/10.1103/PhysRevLett.78.3785>. Cited on pages 33, 62, & 131
- [137] Merks, R., Hoekstra, A. & Slood, P. The Moment Propagation Method for Advection–Diffusion in the Lattice Boltzmann Method: Validation and Péclet Number Limits. Journal of Computational Physics, 183(2):563–576, **2002**. URL <http://linkinghub.elsevier.com/retrieve/pii/S0021999102972098>. Cited on pages 33, 62, & 63
- [138] Press, W. H., Teukolsky, S. A., Vetterling, W. T. & Flannery, B. P. Numerical Recipes in C: The Art of Scientific Computing. Cambridge University Press, Cambridge, 2nd édition, **1993**. Cited on page 36
- [139] Obliger, A., Duvail, M., Jardat, M., Coelho, D., Békri, S. & Rotenberg, B. Numerical homogenization of electrokinetic equations in porous media using lattice-Boltzmann simulations. Physical Review E, 88(1):013019, **2013**. URL <https://link.aps.org/doi/10.1103/PhysRevE.88.013019>. Cited on pages 37 & 53
- [140] Reuss, F. F. Notice sur un nouvel effet de l’électricité galvanique. Mémoires de la Société Impériale des Naturalistes de Moscou, 2:327–337, **1809**. Cited on page 55
- [141] Wang, M. & Chen, S. Electroosmosis in homogeneously charged micro- and nanoscale random porous media. Journal of Colloid and Interface Science, 314(1):264–273, **2007**. URL <http://www.sciencedirect.com/science/article/pii/S0021979707007217>. Cited on page 57
- [142] Horinek, D. & Netz, R. R. Specific ion adsorption at hydrophobic solid surfaces. Physical Review Letters, 99(22):226–104, **2007**. URL <http://link.aps.org/doi/10.1103/PhysRevLett.99.226104>. Cited on page 62
- [143] Schwierz, N., Horinek, D., Sivan, U. & Netz, R. R. Reversed Hofmeister series: The rule rather than the exception. Current Opinion in Colloid & Interface Science, 23:10–18, **2016**. URL <http://www.sciencedirect.com/science/article/pii/S1359029416300474>. Cited on page 62
- [144] Bonthuis, D. J. & Netz, R. R. Unraveling the Combined Effects of Dielectric and Viscosity Profiles on Surface Capacitance, Electro-Osmotic Mobility, and Electric Surface Conductivity. Langmuir, 28(46):16049–16059, **2012**. URL <http://dx.doi.org/10.1021/la3020089>. Cited on page 62
- [145] Grosjean, B., Pean, C., Siria, A., Bocquet, L., Vuilleumier, R. & Bocquet, M.-L. Chemisorption of Hydroxide on 2d Materials from DFT Calculations: Graphene versus Hexagonal Boron Nitride. The Journal of Physical Chemistry Letters, 7(22):4695–4700, **2016**. URL <http://dx.doi.org/10.1021/acs.jpcllett.6b02248>. Cited on page 62
- [146] Secchi, E., Marbach, S., Niguès, A., Stein, D., Siria, A. & Bocquet, L. Massive radius-dependent flow slippage in carbon nanotubes. Nature, 537(7619):210–213, **2016**. URL <https://www.nature.com/nature/journal/v537/n7619/abs/nature19315.html>. Cited on page 62

Bibliography

- [147] Huang, D. M., Cottin-Bizonne, C., Ybert, C. & Bocquet, L. Aqueous electrolytes near hydrophobic surfaces: Dynamic effects of ion specificity and hydrodynamicslip. *Langmuir*, 24(4):1442–1450, **2008**. URL <http://pubs.acs.org/doi/abs/10.1021/la7021787>. *Cited on page 62*
- [148] Lowe, C. P., Frenkel, D. & Masters, A. J. Long-time tails in angular momentum correlations. *The Journal of Chemical Physics*, 103(4):1582–1587, **1995**. URL http://jcp.aip.org/resource/1/jcpsa6/v103/i4/p1582_s1. *Cited on pages 63 & 123*
- [149] Vanson, J.-M., Coudert, F.-X., Rotenberg, B., Levesque, M., Tardivat, C., Klotz, M. & Boutin, A. Unexpected coupling between flow and adsorption in porous media. *Soft Matter*, 11(30):6125–6133, **2015**. *Cited on page 63*
- [150] Vanson, J.-M., Boutin, A., Klotz, M. & Coudert, F.-X. Transport and adsorption under liquid flow: the role of pore geometry. *Soft Matter*, 13(4):875–885, **2017**. URL <http://pubs.rsc.org/en/content/articlelanding/2017/sm/c6sm02414a>. *Cited on page 63*
- [151] Vanson, J.-M., Coudert, F.-X., Klotz, M. & Boutin, A. Kinetic Accessibility of Porous Material Adsorption Sites Studied through the Lattice Boltzmann Method. *Langmuir*, 33(6):1405–1411, **2017**. URL <http://dx.doi.org/10.1021/acs.langmuir.6b04472>. *Cited on page 63*
- [152] Benzi, R., Succi, S. & Vergassola, M. The lattice Boltzmann equation: theory and applications. *Physics Reports*, 222(3):145–197, **1992**. URL <http://www.sciencedirect.com/science/article/pii/037015739290090M>. *Cited on page 64*
- [153] Sen, P. N. Time-dependent diffusion coefficient as a probe of geometry. *Concepts in Magnetic Resonance Part A*, 23A(1):1–21, **2004**. URL <http://onlinelibrary.wiley.com/doi/10.1002/cmr.a.20017/abstract>. *Cited on pages 68 & 79*
- [154] De Leebeeck, A. & Sinton, D. Ionic dispersion in nanofluidics. *Electrophoresis*, 27(24):4999–5008, **2006**. URL <http://onlinelibrary.wiley.com/doi/10.1002/elps.200600264/abstract>. *Cited on page 68*
- [155] Taylor, G. Dispersion of soluble matter in solvent flowing slowly through a tube. *P. Roy. Soc. A*, 219(1137):186–203, **1953**. URL <http://rspa.royalsocietypublishing.org/cgi/doi/10.1098/rspa.1953.0139>. *Cited on pages 69 & 76*
- [156] Aris, R. On the dispersion of a solute in a fluid flowing through a tube. *P. Roy. Soc. A*, 235(1200):67–77, **1956**. URL <http://rspa.royalsocietypublishing.org/cgi/doi/10.1098/rspa.1956.0065>. *Cited on pages 69 & 76*
- [157] Levesque, M., Bénichou, O., Voituriez, R. & Rotenberg, B. Taylor dispersion with adsorption and desorption. *Phys. Rev. E*, 86(3):036–316, **2012**. URL <http://link.aps.org/doi/10.1103/PhysRevE.86.036316>. *Cited on page 76*
- [158] Merlet, C., Forse, A. C., Griffin, J. M., Frenkel, D. & Grey, C. P. Lattice simulation method to model diffusion and NMR spectra in porous materials. *The Journal of Chemical Physics*, 142(9):094701, **2015**. URL <http://scitation.aip.org/content/aip/journal/jcp/142/9/10.1063/1.4913368>. *Cited on page 79*
- [159] Hlushkou, D., Kandhai, D. & Tallarek, U. Coupled lattice-Boltzmann and finite-difference simulation of electroosmosis in microfluidic channels. *International Journal for Numerical Methods in Fluids*, 46(5):507–532, **2004**. URL <https://onlinelibrary.wiley.com/doi/abs/10.1002/flid.765>. *Cited on page 87*

Bibliography

- [160] Guo, Z. Discrete lattice effects on the forcing term in the lattice Boltzmann method. Physical Review E, 65(4), **2002**. *Cited on page 87*
- [161] Tipler, P. A. Physics. Worth Publishers, 1st édition, **1976**. *Cited on page 101*
- [162] Ramos, A., Morgan, H., Green, N. G. & Castellanos, A. Ac electrokinetics: a review of forces in microelectrode structures. Journal of Physics D: Applied Physics, 31(18):2338, **1998**. URL <http://stacks.iop.org/0022-3727/31/i=18/a=021>. *Cited on page 106*
- [163] Ramos, A., Morgan, H., Green, N. G. & Castellanos, A. AC Electric-Field-Induced Fluid Flow in Microelectrodes. Journal of Colloid and Interface Science, 217, **1999**. URL <https://eprints.soton.ac.uk/372372/>. *Cited on page 106*
- [164] Green, N. G., Ramos, A., González, A., Morgan, H. & Castellanos, A. Fluid flow induced by nonuniform ac electric fields in electrolytes on microelectrodes. I. Experimental measurements. Physical Review E, 61(4):4011–4018, **2000**. URL <https://link.aps.org/doi/10.1103/PhysRevE.61.4011>. *Cited on page 106*
- [165] González, A., Ramos, A., Green, N. G., Castellanos, A. & Morgan, H. Fluid flow induced by nonuniform ac electric fields in electrolytes on microelectrodes. II. A linear double-layer analysis. Physical Review E, 61(4):4019–4028, **2000**. URL <https://link.aps.org/doi/10.1103/PhysRevE.61.4019>. *Cited on page 106*
- [166] Green, N. G., Ramos, A., González, A., Morgan, H. & Castellanos, A. Fluid flow induced by nonuniform ac electric fields in electrolytes on microelectrodes. III. Observation of streamlines and numerical simulation. Physical Review E, 66(2):026305, **2002**. URL <https://link.aps.org/doi/10.1103/PhysRevE.66.026305>. *Cited on page 106*
- [167] Ramos, A., González, A., Castellanos, A., Green, N. G. & Morgan, H. Pumping of liquids with ac voltages applied to asymmetric pairs of microelectrodes. Physical Review E, 67(5):056302, **2003**. URL <https://link.aps.org/doi/10.1103/PhysRevE.67.056302>. *Cited on page 106*
- [168] Ajdari, A. Pumping liquids using asymmetric electrode arrays. Physical Review E, 61(1):R45–R48, **2000**. URL <https://link.aps.org/doi/10.1103/PhysRevE.61.R45>. *Cited on page 106*
- [169] Brown, A. B. D., Smith, C. G. & Rennie, A. R. Pumping of water with ac electric fields applied to asymmetric pairs of microelectrodes. Physical Review E, 63(1):016305, **2000**. URL <https://link.aps.org/doi/10.1103/PhysRevE.63.016305>. *Cited on page 106*
- [170] Nadal, F., Argoul, F., Hanusse, P., Pouligny, B. & Ajdari, A. Electrically induced interactions between colloidal particles in the vicinity of a conducting plane. Physical Review E, 65(6):061409, **2002**. URL <https://link.aps.org/doi/10.1103/PhysRevE.65.061409>. *Cited on page 106*
- [171] Yeh, S.-R., Seul, M. & Shraiman, B. I. Assembly of ordered colloidal aggregates by electric-field-induced fluid flow. Nature, 386(6620):57–59, **1997**. URL <https://www.nature.com/articles/386057a0>. *Cited on page 106*
- [172] Faure, C., Decoster, N. & Argoul, F. AC field induced two-dimensional aggregation of multilamellar vesicles. The European Physical Journal B - Condensed Matter and Complex Systems, 5(1):87–97, **1998**. URL <https://doi.org/10.1007/s100510050422>. *Cited on page 106*
- [173] Green, N. G., Ramos, A. & Morgan, H. Ac electrokinetics: a survey of sub-micrometre particle dynamics. Journal of Physics D: Applied Physics, 33(6):632, **2000**. URL <http://stacks.iop.org/0022-3727/33/i=6/a=308>. *Cited on page 106*

Bibliography

- [174] Ristenpart, W. D., Aksay, I. A. & Saville, D. A. Electrically Guided Assembly of Planar Superlattices in Binary Colloidal Suspensions. Physical Review Letters, 90(12):128303, **2003**. URL <https://link.aps.org/doi/10.1103/PhysRevLett.90.128303>. Cited on page 106
- [175] Helfrich, W. Deformation of Lipid Bilayer Spheres by Electric Fields. Zeitschrift für Naturforschung C, 29(3-4):182–183, **2014**. URL <https://www.degruyter.com/view/j/znc.1974.29.issue-3-4/znc-1974-3-417/znc-1974-3-417.xml>. Cited on page 106
- [176] Mitov, M. D., Méléard, P., Winterhalter, M., Angelova, M. I. & Bothorel, P. Electric-field-dependent thermal fluctuations of giant vesicles. Physical Review E, 48(1):628–631, **1993**. URL <https://link.aps.org/doi/10.1103/PhysRevE.48.628>. Cited on page 106
- [177] Pethig, R. Dielectrophoresis: Using Inhomogeneous AC Electrical Fields to Separate and Manipulate Cells. Critical Reviews in Biotechnology, 16(4):331–348, **1996**. URL <https://doi.org/10.3109/07388559609147425>. Cited on page 106
- [178] Reppert, P. M. & Morgan, F. D. Frequency-Dependent Electroosmosis. Journal of Colloid and Interface Science, 254(2):372–383, **2002**. URL <http://linkinghub.elsevier.com/retrieve/pii/S0021979702985966>. Cited on page 106
- [179] Macdonald, J. R. Impedance spectroscopy: old problems and new developments. Electrochimica Acta, 35(10):1483–1492, **1990**. URL <http://www.sciencedirect.com/science/article/pii/0013468690800026>. Cited on page 106
- [180] Geddes, L. A. Historical evolution of circuit models for the electrode-electrolyte interface. Annals of Biomedical Engineering, 25(1):1, **1997**. URL <https://doi.org/10.1007/BF02738534>. Cited on page 106
- [181] Helmholtz, H. Über einige Gesetze der Vertheilung elektrischer Ströme in körperlichen Leitern, mit Anwendung auf die thierisch-elektrischen Versuche (Schluss.). Annalen der Physik, 165(7):353–377, **1853**. URL <https://onlinelibrary.wiley.com/doi/abs/10.1002/andp.18531650702>. Cited on page 106
- [182] Helmholtz, H. Studien über electrische Grenzschichten. **1879**. URL <https://onlinelibrary.wiley.com/doi/abs/10.1002/andp.18792430702>. Cited on page 106
- [183] Randles, J. E. B. Kinetics of rapid electrode reactions. Discussions of the Faraday Society, 1:11–19, **1947**. URL <https://pubs.rsc.org/en/content/articlelanding/1947/df/df9470100011>. Cited on page 106
- [184] Gouy, M. Sur la constitution de la charge électrique á la surface d'un électrolyte. J. Phys. Theor. Appl., 9(1):457–468, **1910**. URL <https://hal.archives-ouvertes.fr/jpa-00241565/document>. Cited on page 106
- [185] Hansen, J.-P. & McDonald, I. R. Theory of Simple Liquids: with Applications to Soft Matter. Academic Press, **2013**. Google-Books-ID: pbJfOUqZVSgC. Cited on pages 120, 123, 124, & 128
- [186] Limmer, D. T., Merlet, C., Salanne, M., Chandler, D., Madden, P. A., van Roij, R. & Rotenberg, B. Charge Fluctuations in Nanoscale Capacitors. Physical Review Letters, 111(10):106102, **2013**. URL <http://link.aps.org/doi/10.1103/PhysRevLett.111.106102>. Cited on page 120
- [187] Smoluchowski, M. v. Zur kinetischen Theorie der Brownschen Molekularbewegung und der Suspensionen. Annalen der Physik, 326(14):756–780, **1906**. URL <https://onlinelibrary.wiley.com/doi/abs/10.1002/andp.19063261405>. Cited on page 122

Bibliography

- [188] Smoluchowski, M. v. Sur le chemin parcouru par les molécules d'un gaz et sur son rapport avec la théorie de la diffusion. pages 202–213, **1906**. *Cited on page 122*
- [189] Green, M. S. Markoff random processes and the statistical mechanics of time-dependent phenomena. The Journal of Chemical Physics, 20(8):1281–1295, **1952**. URL <https://aip.scitation.org/doi/10.1063/1.1700722>. *Cited on page 122*
- [190] Green, M. S. Comment on a Paper of Mori on Time-Correlation Expressions for Transport Properties. Physical Review, 119(3):829–830, **1960**. URL <https://link.aps.org/doi/10.1103/PhysRev.119.829>. *Cited on page 122*
- [191] Kubo, R. Statistical-Mechanical Theory of Irreversible Processes. I. General Theory and Simple Applications to Magnetic and Conduction Problems. Journal of the Physical Society of Japan, 12(6):570–586, **1957**. URL <https://journals.jps.jp/doi/10.1143/JPSJ.12.570>. *Cited on page 122*
- [192] Chandrasekhar, S. Stochastic Problems in Physics and Astronomy. Reviews of Modern Physics, 15(1):1–89, **1943**. URL <https://link.aps.org/doi/10.1103/RevModPhys.15.1>. *Cited on page 122*
- [193] Alder, B. J. & Wainwright, T. E. Decay of the Velocity Autocorrelation Function. Physical Review A, 1(1):18–21, **1970**. URL <https://link.aps.org/doi/10.1103/PhysRevA.1.18>. *Cited on pages 122, 123, & 131*
- [194] Dorfman, J. R. & Cohen, E. G. D. Velocity-Correlation Functions in Two and Three Dimensions: Low Density. Physical Review A, 6(2):776–790, **1972**. URL <https://link.aps.org/doi/10.1103/PhysRevA.6.776>. *Cited on page 123*
- [195] Dorfman, J. R. & Cohen, E. G. D. Velocity-correlation functions in two and three dimensions. II. Higher density. Physical Review A, 12(1):292–316, **1975**. URL <https://link.aps.org/doi/10.1103/PhysRevA.12.292>. *Cited on page 123*
- [196] Theodosopulu, M. & Résibois, P. Kinetic approach to the long-time behaviour in fluids: III. The one-particle propagator. Physica A: Statistical Mechanics and its Applications, 82(1):47–71, **1976**. URL <http://www.sciencedirect.com/science/article/pii/0378437176900911>. *Cited on page 123*
- [197] Pomeau, Y. & Résibois, P. Time dependent correlation functions and mode-mode coupling theories. Physics Reports, 19(2):63–139, **1975**. URL <http://www.sciencedirect.com/science/article/pii/0370157375900198>. *Cited on page 123*
- [198] Dünweg, B. & Kremer, K. Molecular dynamics simulation of a polymer chain in solution. The Journal of Chemical Physics, 99(9):6983–6997, **1993**. URL <https://aip.scitation.org/doi/10.1063/1.465445>. *Cited on page 123*
- [199] Yeh, I-C. & Hummer, G. System-Size Dependence of Diffusion Coefficients and Viscosities from Molecular Dynamics Simulations with Periodic Boundary Conditions. The Journal of Physical Chemistry B, 108(40):15873–15879, **2004**. URL <http://dx.doi.org/10.1021/jp0477147>. *Cited on pages 123 & 124*
- [200] Fushiki, M. System size dependence of the diffusion coefficient in a simple liquid. Physical Review E, 68(2):021203, **2003**. URL <https://link.aps.org/doi/10.1103/PhysRevE.68.021203>. *Cited on page 123*

Bibliography

- [201] Tazi, S., Botan, A., Salanne, M., Marry, V., Turq, P. & Rotenberg, B. Diffusion coefficient and shear viscosity of rigid water models. *Journal of Physics: Condensed Matter*, 24(28):284117, **2012**. URL <http://stacks.iop.org/0953-8984/24/i=28/a=284117>. *Cited on page 123*
- [202] Rozmanov, D. & Kusalik, P. G. Transport coefficients of the TIP4p-2005 water model. *The Journal of Chemical Physics*, 136(4):044507, **2012**. URL <https://aip.scitation.org/doi/10.1063/1.3677196>. *Cited on page 123*
- [203] Gabl, S., Schröder, C. & Steinhauser, O. Computational studies of ionic liquids: Size does matter and time too. *The Journal of Chemical Physics*, 137(9):094501, **2012**. URL <https://aip.scitation.org/doi/10.1063/1.4748352>. *Cited on page 123*
- [204] Singh, S. P., Huang, C.-C., Westphal, E., Gompper, G. & Winkler, R. G. Hydrodynamic correlations and diffusion coefficient of star polymers in solution. *The Journal of Chemical Physics*, 141(8):084901, **2014**. URL <https://aip.scitation.org/doi/10.1063/1.4893766>. *Cited on page 123*
- [205] Kikugawa, G., Ando, S., Suzuki, J., Naruke, Y., Nakano, T. & Ohara, T. Effect of the computational domain size and shape on the self-diffusion coefficient in a Lennard-Jones liquid. *The Journal of Chemical Physics*, 142(2):024503, **2015**. URL <https://aip.scitation.org/doi/abs/10.1063/1.4905545>. *Cited on page 123*
- [206] Kikugawa, G., Nakano, T. & Ohara, T. Hydrodynamic consideration of the finite size effect on the self-diffusion coefficient in a periodic rectangular parallelepiped system. *The Journal of Chemical Physics*, 143(2):024507, **2015**. URL <https://aip.scitation.org/doi/abs/10.1063/1.4926841>. *Cited on page 123*
- [207] Botan, A., Marry, V. & Rotenberg, B. Diffusion in bulk liquids: finite-size effects in anisotropic systems. *Molecular Physics*, 113(17-18):2674–2679, **2015**. URL <http://dx.doi.org/10.1080/00268976.2015.1021730>. *Cited on pages xi, 123, & 127*
- [208] Vögele, M. & Hummer, G. Divergent Diffusion Coefficients in Simulations of Fluids and Lipid Membranes. *The Journal of Physical Chemistry B*, 120(33):8722–8732, **2016**. URL <https://doi.org/10.1021/acs.jpcc.6b05102>. *Cited on pages 123 & 131*
- [209] Ernst, M. H., Hauge, E. H. & van Leeuwen, J. M. J. Asymptotic Time Behavior of Correlation Functions. I. Kinetic Terms. *Physical Review A*, 4(5):2055–2065, **1971**. URL <https://link.aps.org/doi/10.1103/PhysRevA.4.2055>. *Cited on page 123*
- [210] Alder, B. J. & Wainwright, T. E. Velocity Autocorrelations for Hard Spheres. *Physical Review Letters*, 18(23):988–990, **1967**. URL <https://link.aps.org/doi/10.1103/PhysRevLett.18.988>. *Cited on page 123*
- [211] Levesque, D. & Ashurst, W. T. Long-Time Behavior of the Velocity Autocorrelation Function for a Fluid of Soft Repulsive Particles. *Physical Review Letters*, 33(5):277–280, **1974**. URL <https://link.aps.org/doi/10.1103/PhysRevLett.33.277>. *Cited on page 123*
- [212] Hoef, M. A. v. d. & Frenkel, D. Computer simulations of long-time tails: What’s new? *Transport Theory and Statistical Physics*, 24(6-8):1227–1247, **1995**. URL <https://doi.org/10.1080/00411459508203951>. *Cited on page 123*
- [213] Franosch, T., Grimm, M., Belushkin, M., Mor, F. M., Foffi, G., Forro, L. & Jeney, S. Resonances arising from hydrodynamic memory in Brownian motion. *Nature*, 478(7367):85–88, **2011**. URL <https://www.nature.com/articles/nature10498>. *Cited on page 123*

Bibliography

- [214] Li, T. & Raizen, M. G. Brownian motion at short time scales. *Annalen der Physik*, 525(4):281–295, **2013**. URL <https://onlinelibrary.wiley.com/doi/abs/10.1002/andp.201200232>. Cited on page 123
- [215] Kheifets, S., Simha, A., Melin, K., Li, T. & Raizen, M. G. Observation of Brownian Motion in Liquids at Short Times: Instantaneous Velocity and Memory Loss. *Science*, 343(6178):1493–1496, **2014**. URL <http://science.sciencemag.org/content/343/6178/1493>. Cited on page 123
- [216] Clercx, H. J. H. & Schram, P. P. J. M. Brownian particles in shear flow and harmonic potentials: A study of long-time tails. *Physical Review A*, 46(4):1942–1950, **1992**. URL <https://link.aps.org/doi/10.1103/PhysRevA.46.1942>. Cited on page 123
- [217] Boussinesq, J. *Théorie analytique de la chaleur*, vol. 2. **1901**. URL <https://gallica.bnf.fr/ark:/12148/bpt6k61635r>. Cited on page 123
- [218] Chow, T. S. & Hermans, J. J. Effect of Inertia on the Brownian Motion of Rigid Particles in a Viscous Fluid. *The Journal of Chemical Physics*, 56(6):3150–3154, **1972**. URL <https://aip.scitation.org/doi/10.1063/1.1677653>. Cited on page 123
- [219] Lesnicki, D., Vuilleumier, R., Carof, A. & Rotenberg, B. Molecular Hydrodynamics from Memory Kernels. *Physical Review Letters*, 116(14):147804, **2016**. URL <https://link.aps.org/doi/10.1103/PhysRevLett.116.147804>. Cited on pages 123 & 131
- [220] Hasimoto, H. On the periodic fundamental solutions of the Stokes equations and their application to viscous flow past a cubic array of spheres. *Journal of Fluid Mechanics*, 5(2):317–328, **1959**. URL <https://www.cambridge.org/core/journals/journal-of-fluid-mechanics/article/on-the-periodic-fundamental-solutions-of-the-stokes-equations-and-their-application-to-viscous-flow-past-a-cubic-array-of-spheres/F0F666CB13F9F4508FF24329E5589709>. Cited on page 123
- [221] Nash, R. W., Adhikari, R. & Cates, M. E. Singular forces and pointlike colloids in lattice Boltzmann hydrodynamics. *Physical Review E*, 77(2):026709, **2008**. URL <https://link.aps.org/doi/10.1103/PhysRevE.77.026709>. Cited on pages 126 & 129
- [222] Dellar, P. J. Bulk and shear viscosities in lattice Boltzmann equations. *Physical Review E*, 64(3):031203, **2001**. URL <https://link.aps.org/doi/10.1103/PhysRevE.64.031203>. Cited on page 130
- [223] Li, Y. & Shan, X. Lattice Boltzmann method for adiabatic acoustics. *Philosophical Transactions of the Royal Society of London A: Mathematical, Physical and Engineering Sciences*, 369(1944):2371–2380, **2011**. URL <http://rsta.royalsocietypublishing.org/content/369/1944/2371>. Cited on page 130
- [224] Viggen, E. M. Viscously damped acoustic waves with the lattice Boltzmann method. *Philosophical Transactions of the Royal Society of London A: Mathematical, Physical and Engineering Sciences*, 369(1944):2246–2254, **2011**. URL <http://rsta.royalsocietypublishing.org/content/369/1944/2246>. Cited on page 130
- [225] Prasianakis, N. I. & Karlin, I. V. Lattice Boltzmann method for simulation of compressible flows on standard lattices. *Physical Review E*, 78(1):016704, **2008**. URL <https://link.aps.org/doi/10.1103/PhysRevE.78.016704>. Cited on page 130

Bibliography

- [226] Kuhne, T. D., Krack, M. & Parrinello, M. Static and Dynamical Properties of Liquid Water from First Principles by a Novel Car - Parrinello - like Approach. Journal of Chemical Theory and Computation, 5(2):235–241, **2009**. URL <https://doi.org/10.1021/ct800417q>. *Cited on page 131*
- [227] Huang, K. & Szlufarska, I. Effect of interfaces on the nearby Brownian motion. Nature Communications, 6:8558, **2015**. URL <https://www.nature.com/articles/ncomms9558>. *Cited on page 131*
- [228] Siepmann, J. I. & Sprik, M. Influence of surface topology and electrostatic potential on water/electrode systems. The Journal of Chemical Physics, 102(1):511–524, **1995**. URL <https://aip.scitation.org/doi/10.1063/1.469429>. *Cited on page 133*
- [229] Dufrêche, J.-F., Bernard, O., Durand-Vidal, S. & Turq, P. Analytical theories of transport in concentrated electrolyte solutions from the MSA. The Journal of Physical Chemistry. B, 109(20):9873–9884, **2005**. *Cited on page 134*
- [230] Allaire, G., Brizzi, R., Dufrêche, J.-F., Mikelic, A. & Piatnitski, A. Ion transport in porous media: derivation of the macroscopic equations using upscaling and properties of the effective coefficients. Computational Geosciences, 17(3):479–495, **2013**. URL <https://doi.org/10.1007/s10596-013-9342-6>. *Cited on page 134*
- [231] Janssen, M. & Bier, M. Transient dynamics of electric double layer capacitors: Exact expressions within the Debye-Falkenhagen approximation. arXiv:1802.02777 [cond-mat, physics:physics], **2018**. URL <http://arxiv.org/abs/1802.02777>. ArXiv: 1802.02777. *Cited on pages 141 & 142*

*"Physics is like sex: sure, it may give some practical results,
but that's not why we do it." - Richard Feynman*

